

# Dissertation

submitted to the

Combined Faculty of the Natural Sciences and  
Mathematics of the Ruperto-Carola-University of  
Heidelberg, Germany

for the degree of

Doctor of Natural Sciences

Put forward by

**M.Sc. Jiahan Shi**

born in

Hebei, China

Oral examination: 04 May 2023



KINETIC FIELD THEORY APPLIED TO  
PLANETESIMAL FORMATION

Refereed by:

Prof. Dr Matthias Bartelmann

Prof. Dr. Thomas Henning



## ABSTRACT

---

Recently, a kinetic field theory for ensembles of point-like classical particles in or out of equilibrium has been applied to cosmic structure formation. This theory encodes the dynamics of a classical particle ensemble by a generating functional which is completely specified by the initial probability distribution of particles in phase space and their equations of motion. In this work, we apply kinetic field theory to planetesimal formation.

The initial probability distribution of dust particles in phase space is obtained by Gaussianizing the density and momentum fields of a three-dimensional local streaming-instability shearing box simulation. The particle trajectories are calculated by considering their interaction by friction with the constant background gas field and the self-gravitational interaction with each other.

We calculate the non-linearly evolved density and momentum-density power spectra of dust particles and find that their power spectra develop a universal  $k^{-3}$  tail at small scales independent of the form of the initial spectrum, suggesting scale-invariant structure formation and particle kinetic energy accumulation below a characteristic and time-dependent length scale in the protoplanetary disk. Furthermore, the analysis of the amplitude for the small-scale  $k^{-3}$  tails shows a critical particle size  $\tau_s \approx 3.03$  which corresponds to the strongest structure formation and the maximal kinetic energy accumulation at small scales of a system when considering only the friction between dust particles and the constant background gas field. Finally, we discuss the "meter-size barrier" problem. And for particles as small as Stokes number  $\tau_s \approx 10^{-5}$ , we provide evidence that accumulated self-gravitational interaction among the dust particles over a long evolution time is strong enough for them to successfully "jump the barrier" and lead to a final gravitational collapse.

## ZUSAMMENFASSUNG

---

Vor kurzem wurde eine kinetische Feldtheorie für Ensembles punktförmiger klassischer Teilchen, die sich im oder außerhalb des Gleichgewichts befinden, auf die kosmische Strukturbildung angewandt. Diese Theorie kodiert die Dynamik eines klassischen Teilchenensembles durch ein erzeugendes Funktional, das vollständig durch die anfängliche Wahrscheinlichkeitsverteilung der Teilchen im Phasenraum und ihre Bewegungsgleichungen spezifiziert ist. In dieser Arbeit wenden wir die kinetische Feldtheorie auf die Bildung von Planetesimalen an.

Die anfängliche Wahrscheinlichkeitsverteilung der Staubteilchen im Phasenraum wird durch Gaussianisierung der Dichte- und Impulsfelder einer dreidimensionalen lokalen Shearing-Box-Simulation der Streaming-Instabilität erhalten. Die Trajektorien der Teilchen werden unter Berücksichtigung ihrer Wechselwirkung durch Reibung mit dem konstanten Hintergrundgasfeld und der selbstgravitativen Wechselwirkung untereinander berechnet.

Wir berechnen die nichtlinear entwickelten Dichte- und Impulsdichte-Leistungsspektren der Staubteilchen und stellen fest, dass ihre Leistungsspektren ein universelles  $k^{-3}$ -Verhalten auf kleinen Skalen entwickeln, das unabhängig von der Form des Anfangsspektrums ist, was auf skaleninvariante Strukturbildung und kinetische Energieakkumulation der Teilchen unterhalb einer charakteristischen und zeitabhängigen Längenskala in der protoplanetaren Scheibe hinweist. Darüber hinaus zeigt die Analyse der Amplitude der kleinskaligen  $k^{-3}$ -Verläufe eine kritische Teilchengröße  $\tau_s \approx 3.03$ , die der ausgeprägtesten Strukturbildung und der maximalen kinetischen Energieakkumulation auf kleinen Skalen eines Systems entspricht, wenn man nur die Reibung zwischen Staubteilchen und dem konstanten Hintergrundgasfeld berücksichtigt. Schließlich diskutieren wir das Problem der "Meter-Size Barrier". Für Teilchen mit einer Stokes-Zahl von  $\tau_s \approx 10^{-5}$  weisen wir nach, dass die akkumulierte selbstgravitative Wechselwirkung zwischen den Staubteilchen über eine lange Entwicklungszeit stark genug ist, um die "Meter-Size-Barrier" erfolgreich zu überwinden und zu einem endgültigen gravitativen Kollaps zu führen.

*For the endless love, support, and encouragement from my parents*



## ACKNOWLEDGEMENTS

---

First and foremost, my greatest thanks goes to my supervisor and teacher Matthias Bartelmann. Without his fantastic ideas, his guidance, his warm character, and his patience, this work would not have been possible. Whenever I felt stuck, he had an idea for how to proceed. His brilliant and unique way of viewing the physics framework deeply impresses me and drives me to becoming a better physicist every single day. Additionally, I have to mention that his most effective working style has influenced me to become healthier and more organized through life, and for that, I'm eternally grateful.

Next, I would like to thank my second supervisors Cornelis Dullemond and Hubert Klahr for the numerous extended and enlightening conversations about the foundations of planetary formation and teaching me that seemingly simple things in physics are often much more complex and exciting.

I also want to thank all my fellow field workers for the great and inspiring discussions about KFT. I thank Dr. Sara Konrad and Leif Seute for the fruitful discussions on the novel asymptotic analysis and calculations. I thank Dr. Carsten Littek for the development of the momentum-density power spectra. Furthermore, a special thanks goes to my old office mates Dr. Johannes Schwinn and Dr. Martin Feix for tossing inspiring ideas at the beginning of this work. I also thank my current office mate Christophe Pixus for the mean field discussions and for providing the template and the title page of this thesis.

A warm thanks goes to Joanna Cichecka, Nadja Weigel and Dr. May-Britt Becker from the excellence cluster STRUCTURES for taking care of all the administrative problems.

I am most grateful for my parents and my family who always saw the scientist in me and love and support me in every life situation. Three years away from home during the pandemic, their constant warm and caring words have always reminded me that home is never far away.

Furthermore, I sincerely thank my best friend Song Wei for the numerous phone calls and messages from China to help pick me up from the deep doubting hell I put myself through, and for reminding me of who I was and who I want to be in this great life journey.

A special thanks goes to my cat Xiaoqi, for being the warmest and cutest little creature who takes away my daily ups and downs and always puts a big smile on my face.

Finally, I would like to express my genuine thanks to my husband Andrzej Chrobak for loving, caring and supporting me every step of the way, and for reminding me that there is as well beautiful life outside of the appealing physics world worth living for.

# CONTENTS

---

1	INTRODUCTION	1
<b>I</b>	<b>FOUNDATIONS</b>	<b>5</b>
2	DUST DYNAMICS IN PROTOPLANETARY DISKS	7
2.1	Gas Dynamics . . . . .	7
2.1.1	Keplerian rotation . . . . .	8
2.1.2	Gas disk pressure scale-height . . . . .	8
2.1.3	Global pressure gradient . . . . .	10
2.2	Particle Friction and Stokes Number . . . . .	12
2.2.1	Friction . . . . .	12
2.2.2	The streaming instability . . . . .	14
2.3	Dust Equation of motion in the shearing sheet approximation . . . . .	14
2.3.1	Shearing Box Approximation . . . . .	15
2.3.2	Shearing Periodic Condition . . . . .	15
2.3.3	Euler Equations . . . . .	16
2.4	Hill Stability of A Particle Cloud . . . . .	20
2.5	Summary and Discussion . . . . .	22
3	KINETIC FIELD THEORY IN A NUTSHELL	25
3.1	Notations . . . . .	25
3.2	Generating Functional . . . . .	27
3.2.1	The Generating Functional . . . . .	27
3.2.2	Similarities to Equilibrium Statistical Physics . . . . .	30
3.3	Simplified Dust Particle Trajectories . . . . .	31
3.3.1	Complications with the Full Equation of Motion . . . . .	31
3.3.2	Dust Particles Trajectory . . . . .	32
3.4	Operators . . . . .	35
3.4.1	Density Operator . . . . .	36
3.4.2	Momentum-Density Operator . . . . .	37
3.5	Summary and Discussion . . . . .	38
<b>II</b>	<b>RESULTS</b>	<b>41</b>
4	INITIAL PROBABILITY DISTRIBUTION FUNCTION IN PHASE SPACE	43
4.1	Simulation Specification . . . . .	43
4.2	Initial Probability Distribution Function . . . . .	45
4.2.1	Density and Momentum Distribution . . . . .	46
4.2.2	Gaussianization of the Density Field . . . . .	48
4.2.3	Inverse Density Transformation . . . . .	49

4.2.4	The Final Expression . . . . .	51
4.3	Covariance Matrix . . . . .	58
4.3.1	Initial Power Spectra and Correlation Functions . . . . .	58
4.3.2	The Pipeline . . . . .	59
4.3.3	The Final Results . . . . .	63
4.3.4	Approximating The Correlation Operator . . . . .	68
4.3.5	Rotate Momentum Covariance Matrix . . . . .	69
4.4	Summary and Discussion . . . . .	73
5	DUST DENSITY POWER SPECTRUM BY KFT . . . . .	75
5.1	Analytical Derivation of Density Power Spectrum . . . . .	76
5.1.1	KFT Nonlinear Density Power Spectrum . . . . .	76
5.1.2	Average The Gravitational Interaction . . . . .	79
5.2	Freely Streaming Particles . . . . .	83
5.2.1	Linear Density Power Spectrum . . . . .	83
5.2.2	Free Density Power Spectrum . . . . .	85
5.2.3	Time Dependence of Small Scale Behaviours . . . . .	88
5.3	Friction Density Power Spectrum . . . . .	90
5.3.1	Linear Power Spectrum At Small $\tau_s$ . . . . .	91
5.3.2	Non Linear Power Spectrum At Large $\tau_s$ . . . . .	93
5.3.3	Time and Particle-Size Dependence At Small Scales . . . . .	94
5.4	Gravitational Density Power Spectrum . . . . .	100
5.4.1	Proper Approximation for $P(k, t)$ . . . . .	101
5.4.2	Linear Power Spectrum at Small $\tau_s$ . . . . .	104
5.4.3	Non Linear Power Spectrum at Large $\tau_s$ . . . . .	110
5.4.4	Determine Gravitational Collapse at Small $\tau_s$ . . . . .	115
5.5	Further Discussion of $k^{-3}$ Behaviour . . . . .	123
5.6	Summary and Discussion . . . . .	123
6	DUST MOMENTUM-DENSITY POWER SPECTRA BY KFT . . . . .	127
6.1	Analytical Derivation of Momentum-Density Power Spectra . . . . .	128
6.1.1	Factorize Generating Functional . . . . .	128
6.1.2	Three Scalar Momentum-Density Power Spectra . . . . .	133
6.2	Interlude: Asymptotics Of Certain Types of Integrals . . . . .	137
6.3	Free Streaming Particles . . . . .	146
6.3.1	Linear Momentum-Density Power Spectra . . . . .	147
6.3.2	Nonlinear Momentum-Density Power Spectra . . . . .	149
6.4	Friction Momentum-Density Power Spectra . . . . .	157
6.4.1	Linear Momentum-Density Power Spectra at Small $\tau_s$ . . . . .	158
6.4.2	Nonlinear Momentum-Density Power Spectra at Large $\tau_s$ . . . . .	160
6.5	Gravitational Momentum-Density Power Spectra . . . . .	175
6.5.1	Linear Momentum-Density Power Spectra at Small $\tau_s$ . . . . .	177
6.5.2	Nonlinear Momentum-Density Power Spectra at Large $\tau_s$ . . . . .	183

6.6	Summary and Discussion . . . . .	190
7	CONCLUSIONS AND DISCUSSIONS	195
III	APPENDIX	201
A	MORE DISCUSSIONS OVER KFT POWER SPECTRA	203
A.1	Small-Scale Asymptotics of Linear Power Spectra . . . . .	203
A.1.1	Linear Density Power spectrum . . . . .	203
A.1.2	Linear Free Momentum-Density Power Spectra Elements . . . . .	204
A.2	Verify Modified Nonlinear Density Power Spectrum . . . . .	207
B	SMALL-SCALE ASYMPTOTICS OF MOMENTUM-DENSITY TRACE POWER SPECTRUM	211
B.1	Time and Particle Size Dependence of $\bar{\mathcal{P}}_{\text{lin1}}(k_1, t)$ . . . . .	211
B.2	Time and Particle Size Dependence of $\bar{\mathcal{P}}_{\text{ftr}}(k_1, t)$ . . . . .	214
	BIBLIOGRAPHY	219

## LIST OF FIGURES

---

Figure 2.1	In this drawing the shearing box coordinate system is the primed system with coordinates $x'$ and $y'$ . It is a coordinate system that orbits around the star with the Keplerian velocity at its origin. Hence, unity vectors in $\hat{\phi}$ transform into $\hat{y}$ of the primed system. Consequently, the Keplerian shear has to be linearised in the shearing sheet coordinate system. In order to have the radial boundary condition periodic, we include a shear periodic boundary condition that adjusts the azimuthal velocity when surpassing the radial boundary. . . . .	15
Figure 2.2	Example for the shear periodic boundary condition for a shearing box of size $L$ . At the initial time step $t_0$ (top), the radial periodicity is similar to a normal periodic boundary condition. But, with evolving time, the linear shear moves this periodic boundary in azimuthal direction. A particle leaving the radial inner boundary re-enters the simulation domain shifted by the shear-offset, see orange arrow, and its azimuthal velocity is shear corrected. . . . .	17
Figure 2.3	The Hill criterion is a criterion for internal stability. It looks for the boundedness of a test mass $\mu$ to a smaller mass $m$ , in the vicinity of a larger mass $M$ . The Hill analysis assumes the smaller mass to orbit around the larger mass. The Hill analysis leads to a Hill sphere, which is the sphere of zero acceleration around the mass $m$ . Everything inside this sphere is bound, under the assumption of not having escape velocity or other perturbations occurring. . . . .	21
Figure 3.1	Illustration of the main idea of KFT. An initial probability distribution on the phase space is mapped to any later time by classical particle trajectories. Since phase-space trajectories do not cross, this approach avoids the notorious shell-crossing problem by construction. . . . .	28

Figure 4.1	The shearing sheet approximation allows to simulate a patch (blue box) out of a protoplanetary disk (black grid). The center of the shearing box has a distance $R_0$ from the star and moves with Keplerian velocity $v_K = \Omega R_0$ around it. This motion is translated by the coordinate transformation and shear linearisation into a linear shearing motion, see <a href="#">Section 2.3</a> . In this shearing box coordinate system, the center of the domain is at rest. Everything closer to the star ( $x < 0$ ) moves forward in an azimuthal direction, and everything towards the outside of the domain ( $x > 0$ ) moves backward. . . . .	44
Figure 4.2	This plot shows the dust particles' density distribution $\rho$ in an $x - y$ slice of the simulation snapshot discussed in this paper. The overall density distribution throughout the whole plot is more or less equal, suggesting a nearly homogeneous and isotropic simulation domain. . . . .	45
Figure 4.3	Momentum distributions in the $x, y, z$ directions with double-logarithmic scaling. The purple dotted lines represent actual data, the red lines are the curves of the Gaussian fitting functions described by <a href="#">Equation 4.2</a> . The curves show that the momentum distributions can individually be well described by Gaussians. Notice that the mean values $p_{1c}$ and $p_{2c}$ are set to zero here. . . . .	46
Figure 4.4	Density distribution function in double-logarithm scaling. The data points in the plot are represented by the purple dots, and the orange curve shows the fit function by <a href="#">Equation 4.4</a> . . . . .	47
Figure 4.5	This figure shows how the cumulative distribution function (CDF) of the original density variable $F_\rho(\rho)$ changes from 0 to 1. The purple dots come from the numerical counts for particle number density in phase space, while the orange line represents the curve of <a href="#">Equation 4.9</a> which is the analytical integration of the original density distribution by <a href="#">Equation 4.4</a> . . . . .	49
Figure 4.6	Probability distribution of the centred and normalized density variable $\tilde{\rho}$ in double-logarithmic scaling. The purple dots show the data points transformed as in <a href="#">Equation 4.8</a> . The orange curve shows a Gaussian fit to these points. Their agreement illustrates that $\tilde{\rho}$ does indeed follow a Gaussian distribution. . . . .	49
Figure 4.7	This plot shows the quadratic polynomial fitting result of the inverse density relation $\rho = g(\tilde{\rho})$ . The purple dots are obtained by switching the axis of <a href="#">Equation 4.8</a> . The orange line represents the quadratic fitting function by <a href="#">Equation 4.10</a> . . . . .	50

Figure 4.8	This is the relative difference plot between original density field $\rho_{\text{data}}$ and the approximate original density field $\rho_{\text{aprx}}$ obtained by <a href="#">Equation 4.12</a> . . . . .	51
Figure 4.9	This plot shows the numerical results of the integration $I_{1j}(t_{\bar{\rho}_j}) = \int_{\bar{\rho}_{\min}}^{\bar{\rho}_{\max}} d\bar{\rho}_j \exp(it_{\bar{\rho}_j} \bar{\rho}_j)$ within the range $-0.3 < t_{\bar{\rho}_j} < 0.3$ , where $\bar{\rho}_{\min} \approx 0$ , we choose $\bar{\rho}_{\max} \approx 10^7$ according to the initial particle number $N$ . The fact that the nonzero values of this curve are all occur near $t_{\bar{\rho}} \approx 0$ satisfies the definition of a Dirac Delta distribution, which validates our integration result in <a href="#">Equation 4.28</a> . . . . .	54
Figure 4.10	This picture is given to illustrate the concept of the <a href="#">CIC</a> code. Suppose we have a two-dimensional grid, the black grid points represent the center of cells and the small red dots mimic particles, the side length of each cell is set to be unity, the mass of each particle is one unit mass, for a particle at $p = (x_p, y_p)$ , we can assign its mass to the four grid points next to it, which are the points $(i, j), (i + 1, j), (i, j + 1), (i + 1, j + 1)$ . The weight assigned to each point depends only on its relative position to this particle. For example, for grid point $(i, j)$ , the mass it gains from particle $p$ is: $\Delta m_{i,j} = t_x t_y$ . . . . .	61
Figure 4.11	The six independent components of the momentum power spectrum are shown here. The red vertical line at $k = 17.5$ represents the dissipation scale $l_d$ and the grey vertical line at $k = 42$ represents the correlation scale $l_c$ . . . . .	63
Figure 4.12	Momentum power spectra measured from the simulation (purple dots) together with the individual fit functions of the form of <a href="#">Equation 4.56</a> (orange lines). The blue dashed lines illustrate the $k^{-2/3}$ slope for reference. . . . .	65
Figure 4.13	Density power spectra extracted from the simulation (purple points) and modeled by the fit function <a href="#">Equation 4.57</a> (orange line). Left: complete $k$ range allowed by the simulation data; right: small scales, i.e. large wave numbers. The blue dashed line represents the $k^{-3}$ slope. . . . .	65
Figure 4.14	Cross power spectra between the density and the momentum components. Similar to the momentum power spectra shown in <a href="#">Figure 4.11</a> , the orange vertical line at $k = 17.5$ represents the dissipation scale $l_d$ , and the yellow vertical line at $k = 42$ the correlation scale $l_c$ . . . . .	66
Figure 4.15	Density-momentum cross power spectra overlaid with the fit function <a href="#">Equation 4.58</a> , with exponents $\beta_{0i} = 4/3$ and $\alpha_{0i} = 1/3$ . The purple dots are the data points, the green lines show the fits with parameters listed in <a href="#">Table 4.4</a> . . . . .	67

Figure 4.16	The density, momentum, and density-momentum correlation functions of Equation 4.59 are shown here in the left, center, and right panels, respectively. The horizontal axes are scaled in $L = 0.1H$ , i.e. with the same length scale as the simulation boxes.	67
Figure 4.17	The function of $\zeta_{pp}(r)$ (blue line), $ m_1(r) $ (green line) and $ m_2(r) $ (purple line) are shown together with their approximations $\zeta(r)$ (yellow line), $\alpha_1(r)$ (red line) and $\alpha_2(r)$ (orange line) given by Equation 4.76-4.78.	71
Figure 4.18	The function of $P_0(k)$ (orange line) given by Equation 4.67 is shown together with its asymptotic behavior $k^{-\frac{2}{3}}$ (blue dashed line).	72
Figure 5.1	Illustration of the shape of the linear density power spectrum $\mathcal{P}_{lin}(k_1, t)$ (blue line) and its asymptotic behavior at small (yellow dashed line) and large scales (green dashed line).	85
Figure 5.2	The radial integrand of the free power spectrum, $r^2 l(r)$ , is shown here for $k_1 = 1.0$ , $k_1 = 25.0$ and $k_1 = 80.0$ (blue lines) at time $t = 4\pi$ . The yellow dashed lines indicate the $r^{-4/3}$ slope.	86
Figure 5.3	The linearly evolved density power spectrum $\mathcal{P}_{lin}(k_1, t)$ (blue line) compared to the free non-linear density power spectrum $\mathcal{P}_{free}(k_1, t)$ (yellow line). The asymptotic behaviour at large (green dashed line) and small scales is also indicated. At small scales, the linear power spectrum falls off like $k^{-1}$ (red dashed line), while the free non-linear power spectrum develops a $k^{-3}$ slope (purple dashed line).	86
Figure 5.4	Non-linear density power spectra $\mathcal{P}_{free}(k_1, t)$ together with their small scale asymptotic behavior (orange dash-dotted lines) at the four different times $t = 0.6\pi$ (purple line), $t = 1\pi$ (yellow line), $t = 2.5\pi$ (green line) and $t = 4\pi$ (blue line).	89
Figure 5.5	Left: Power $k_1^3 \mathcal{P}_{free}(k_1, t)$ as a function of $k_1$ at the four different times $t = 0.6\pi$ (purple line), $t = 1\pi$ (yellow line), $t = 2.5\pi$ (green line) and $t = 4\pi$ (blue line). The red dots mark the wave number $k_0$ where the $k^{-3}$ slope is reached. Dependence of $k_0$ on time, with the points indicating $k_0$ for the four different times given.	89
Figure 5.6	Amplitude $\mathcal{P}^{(0)}(t)$ for the asymptotic $k^{-3}$ tail of the free, non-linear power spectrum as a function of time $t$ . The blue point indicates its maximum $\mathcal{P}_{max}^{(0)}$ at time $t_{max}$ according to Equation 5.60. The yellow points are obtained by direct integration of Equation 5.20. The four red points mark the amplitudes at the times $t = 0.6\pi$ , $t = 1.0\pi$ , $t = 2.5\pi$ , and $t = 4.0\pi$ .	90

Figure 5.7	This plot compares the propagator $g_{qp}(t)$ in Equation 3.39 respectively at $\tau_s = 0.25$ (blue line), $\tau_s = 0.5$ (yellow line), $\tau_s = 1.0$ (green line), $\tau_s = 5.0$ (red line) and $\tau_s = 10.0$ (purple line) together with the freely streaming propagator $g_0(t) = t$ (brown line). . . . .	91
Figure 5.8	This plot illustrates the shape of linear density power spectrum $\mathcal{P}_{\text{lin}}(k_1, t)$ with $\tau_s = 0.01$ at evolution time $t = 0.001$ (blue line) and $t = 10.0$ (yellow line). Their asymptotic behavior at small and large scales are represented by the green and red dashed lines. . . . .	92
Figure 5.9	This plot illustrates the shape of linear density power spectrum $\mathcal{P}_{\text{lin}}(k_1, t)$ at evolution time $t = 10.0$ with friction coefficient $\tau_s = 0.1$ (blue line), $\tau_s = 0.01$ (yellow line) and $\tau_s = 0.001$ (green line). Their asymptotic behavior at small and large scales are represented by the red and purple dashed lines. . . . .	93
Figure 5.10	This plot compares the linear density power spectrum $\mathcal{P}_{\text{lin}}(k_1, t)$ (blue line) with the nonlinear density power spectrum $\mathcal{P}_f(k_1, t)$ (yellow line) together with their asymptotic behavior at large (green dashed line) and small scales. At small scales, the asymptotic behavior of the linear power spectrum is proportional to $k^{-1}$ (red dashed line), while the nonlinear power spectrum develops a different $k^{-3}$ slope (purple dashed line). . . . .	94
Figure 5.11	This plot shows the density power spectrum $\mathcal{P}_f(k_1, t)$ with friction at evolution times $t = 2.0$ (blue line), $t = 10.0$ (yellow line) and $t = 100.0$ (green line) with the friction coefficient $\tau_s = 5.0$ . At small scales, they all develop $k^{-3}$ slopes (red dashed lines). . . . .	95
Figure 5.12	These two plots show the shape of the nonlinear density power spectrum $\mathcal{P}_f(k_1, t)$ at evolution times $t = 2.0$ (left panel) and $t = 10.0$ (right panel) with the friction coefficients $\tau_s = 5.0$ (blue line), $\tau_s = 10.0$ (yellow line) and $\tau_s = 20.0$ (green line) together with their small scale $k^{-3}$ asymptotic behavior (red dashed lines). . . . .	96
Figure 5.13	This plot shows the value of $t_m$ as a function of the friction coefficient $\tau_s$ . . . . .	97
Figure 5.14	This plot illustrates the evolution of the amplitude $\mathcal{P}_f^{(0)}(t)$ for the $k^{-3}$ slope as a function of time $t$ with friction coefficients $\tau_s = 1.0$ (purple line), $\tau_s = 2.0$ (yellow line) and $\tau_s = 3.0$ (burgundy line). . . . .	97

- Figure 5.15 This plot shows the density power spectrum  $\mathcal{P}_f(k_1, t)$  with friction at evolution times  $t = 2.0$  (blue line),  $t = 3.0$  (yellow line) and  $t = 10.0$  (green line) with the friction coefficient  $\tau_s = 3.0$ . At small scales, they all develop  $k^{-3}$  slopes (red dashed lines). As time proceeds, the power spectrum grows at both large and small scales. . . . . 98
- Figure 5.16 This plot illustrates the shape of the amplitude  $\mathcal{P}_f^{(0)}(t)$  for the  $k^{-3}$  slope as a function of time  $t$  with friction coefficient  $\tau_s = 5.0$  (purple line),  $\tau_s = 10.0$  (yellow line) and  $\tau_s = 20.0$  (light blue line). The crosses of the same color on each curve represent their maximum value  $\mathcal{P}_{fm}^{(0)}$  at time  $t_m$  by Equation 5.60. . . . . 98
- Figure 5.17 This plot illustrates the shape of the amplitude  $\mathcal{P}_f^{(0)}(t)$  for the  $k^{-3}$  slope as a function of friction coefficient  $\tau_s$  at two different time  $t = 2.0$  (purple line) and  $t = 100.0$  (burgundy line). The same color dot on the burgundy curve represents its maximal  $\mathcal{P}_{fm}^{(0)}$  at friction coefficient  $\tau_{sm}$  calculated by Equation 5.71. . . . . 99
- Figure 5.18 This plot compares the linear friction density power spectrum  $\mathcal{P}_{lin}(k, t_0)$  (solid lines) and the initial density power spectrum  $\mathcal{P}_{ini}(k, t_0)$  (dashed lines) at evolution time  $t_0 = 10.0$  with two different friction coefficient  $\tau_s = 0.01$  (blue, green) and  $\tau_s = 0.001$  (yellow, red). . . . . 102
- Figure 5.19 This plot compares the density power spectrum  $\mathcal{P}_f(k, t_0)$  with friction (solid lines) and the initial density power spectrum  $\mathcal{P}_{ini}(k, t_0)$  (dashed lines) at evolution time  $t_0 = 2.0$  (blue, green) and at  $t_0 = 10.0$  (yellow, red) with the friction coefficient  $\tau_s = 3.0$ . . . . . 104
- Figure 5.20 This plot shows the shape of  $J(y)$  in Equation 5.36 together with its asymptotic constant  $J(0) = 2$  at small  $y$  from Equation 5.85 and the  $y^{-2}$  slope at larger  $y$  from Equation 5.86. . . . . 105
- Figure 5.21 This plot illustrates the shape of the mean interaction term  $i\langle S_I \rangle(k_1, t)$  as a function of wave number  $k_1$  (solid lines) with gravitational parameter  $f = 1$  at initial time  $t_0 = 10.0$  and evolution time  $t = 11.0$  (blue, red),  $t = 20.0$  (yellow, purple) and  $t = 100.0$  (green, brown) with two different friction coefficients  $\tau_s = 0.01$  (blue, yellow, green) and  $\tau_s = 0.001$  (red, purple, brown). Their  $k^2$  asymptotic behaviors at large scales are represented by the purple dashed lines. The asymptotic constants at small scales are illustrated in green dashed lines. . . . . 106

- Figure 5.22 These two plots show the shape of the mean interaction term  $i\langle S_I \rangle(k_1, t)$  in Equation 5.83 as a function of evolution time  $t$  (left panel) and small valued friction coefficient  $\tau_s$  (right panel). The red dashed line in the left panel represents the  $t^1$  asymptotic slope from Equation 5.88. The red dashed line in the right panel represents the  $\tau_s^3$  asymptotic slope from Equation 5.89. The upper limit for  $\tau_s$  in the right panel plot is roughly chosen to be 1 for studying small valued  $\tau_s$ . . . . . 107
- Figure 5.23 These two plots illustrate the shape of the full linear density power spectrum  $\mathcal{P}_{\text{glin}}(k_1, t)$  as a function of wave number  $k_1$  with the initial time  $t_0 = 10.0$  and the friction coefficients  $\tau_s = 0.01$  (left panel) and  $\tau_s = 0.001$  (right panel) at three evolution time  $t = 11.0$  (orange),  $t = 20.0$  (green) and  $t = 100.0$  (red) with the parameter  $f = 1$ . The blue lines represent the corresponding initial linear friction density power spectrum  $\mathcal{P}_{\text{flin}}(k_1, t_0)$  in both plots. And the yellow dashed lines illustrate the small scale  $k^{-1}$  asymptotic behavior. . . . . 108
- Figure 5.24 These plots zoom in to the very small scales of Figure 5.23 and illustrate their small scale  $k^{-1}$  asymptotic behaviors (yellow dashed line). The linear density power spectrum  $\mathcal{P}_{\text{glin}}(k_1, t)$  at evolution time  $t = 20.0$  with  $\tau_s = 0.01$  (green line) is given in the left panel,  $\mathcal{P}_{\text{g}}(k_1, t)$  at evolution time  $t = 100.0$  with  $\tau_s = 0.001$  (red line) is given in the right panel. . . . . 108
- Figure 5.25 This plot illustrates the shape of the full nonlinear density power spectrum  $\mathcal{P}_{\text{glin}}(k_1, t)$  as a function of wave number  $k_1$  with the friction coefficients  $\tau_s = 0.001$  and initial time  $t_0 = 10.0$  at three different evolution times  $t = 11.0$  (yellow, purple lines),  $t = 20.0$  (green, brown lines) and  $t = 100$  (red, light blue lines) with two different gravitational parameters  $f = 8$  (yellow, green, red lines) and  $f = 1$  (purple, brown, light blue lines). The initial friction power spectrum  $\mathcal{P}_{\text{flin}}(k_1, t)$  is represented by the blue line. . . . . 109
- Figure 5.26 This plot illustrates the ratio between the full linear density power spectrum  $\mathcal{P}_{\text{glin}}(k_1, t)$  and the initial linear density power spectrum  $\mathcal{P}_{\text{flin}}(k_1, t)$  as a function of evolution time  $t$  with initial time  $t_0 = 10.0$  and the friction coefficients  $\tau_s = 0.01$  (blue) and  $\tau_s = 0.001$  (yellow, green) at two different gravitational parameters  $f = 1$  (blue, yellow) and  $f = 8$  (green). The upper limit of the  $t$  axis  $t_{\text{max}} = 10^6$  is chosen according to the dynamic lifetime of an average PPD. . . . . 110

- Figure 5.27 This plot illustrates the shape of the mean interaction term  $i\langle S_I \rangle(k_1, t)$  as a function of wave number  $k_1$  (solid lines) with the friction coefficient  $\tau_s = 3.0$  at four sets of initial times  $t_0$  and evolution times  $t$ , which respectively are:  $t_0 = 2.0, t = 3.0$  (blue);  $t_0 = 10.0, t = 11.0$  (yellow);  $t_0 = 2.0, t = 7.0$  (green);  $t_0 = 10.0, t = 15.0$  (red). Their  $k^2$  asymptotic behavior at large scales is represented by the purple dashed lines. Their asymptotic constant at small scales is represented by the green dashed lines. . . . . 111
- Figure 5.28 These two plots show the shape of the mean interaction term  $i\langle S_I \rangle(k_1, t)$  in Equation 5.90 as a function of evolution time  $t$  (left panel) and large valued friction coefficient  $\tau_s$  (right panel). The red dashed line in the left panel represents the  $t^1$  asymptotic slope from Equation 5.88. The red dashed line in the right panel represents the asymptotic constant from Equation 5.92. . . . . 112
- Figure 5.29 This plot shows the mean interaction term  $i\langle S_I \rangle(k_1, t)$  in Equation 5.90 as a function of  $\tau_s$  with gravitational parameter  $f = 1$  and initial time  $t_0 = 10.0$  and evolution time  $t = 11.0$  at six different scales respectively are  $k_1 = 10.0$  (blue line),  $k_1 = 30.0$  (orange line),  $k_1 = 100.0$  (green line),  $k_1 = 1000.0$  (red line),  $k_1 = 10000.0$  (purple line) and  $k_1 = 100000.0$  (brown line). . . . . 113
- Figure 5.30 This plot shows the mean interaction term  $i\langle S_I \rangle(k_1, t)$  in Equation 5.90 as a function of  $\tau_s$  at scale  $k_1 = 1000.0$  with parameter  $f = 1$  and initial time  $t_0 = 10.0$  at five different evolution time respectively are  $t = 11, t = 15, t = 20, t = 30$  and  $t = 40$ . . . . . 113
- Figure 5.31 These two plots show the shape of  $\mathcal{P}_g(k_1, t)$  as a function of  $k_1$  at two different evolution times  $t = 3.0$  (orange line) and  $t = 7.0$  (green lines) with the initial time  $t_0 = 2.0$  (blue line) and the friction coefficient  $\tau_s = 3.0$  while the density of the dust particles is set to be the Hill density ( $f = 1$ ). Their small-scale  $k^{-3}$  asymptotic behavior is illustrated by the yellow dashed lines. The right panel zoom-in plot shows the small scale  $k^{-3}$  tail of  $\mathcal{P}_g(k_1, t)$  at  $t = 7.0$ . . . . . 114

Figure 5.32	This plot illustrates the shape of the full nonlinear density power spectrum $\mathcal{P}_g(k_1, t)$ as a function of wave number $k_1$ with the friction coefficients $\tau_s = 3.0$ and initial time $t_0 = 2.0$ at two different evolution times $t = 3.0$ (yellow, red lines) and $t = 7.0$ (green, purple lines) with two different gravitational parameters $f = 1$ (yellow, green lines) and $f = 5$ (red, purple lines). The initial friction power spectrum $\mathcal{P}_f(k_1, t)$ is represented by the blue line. The $k^{-3}$ tail at small scales is illustrated by the yellow dashed lines. . . . .	115
Figure 5.33	This plot compares the mean interaction term $i\langle S_I \rangle(\vec{k}_1, t)$ in Equation 5.83 with its numerical fitting function $S_{\text{fit}}(k_1, t)$ in Equation 5.96 (gray dashed lines) as a function of wave number $k_1$ (solid lines) with gravitational parameter $f = 1$ at initial time $t_0 = 10.0$ and evolution times $t = 11.0$ (blue, red), $t = 20.0$ (yellow, purple) and $t = 100.0$ (green, brown) with two different friction coefficients $\tau_s = 0.01$ (blue, yellow, green) and $\tau_s = 0.001$ (red, purple, brown). . . . .	117
Figure 5.34	These two plots show the shape of the mean interaction term $i\langle S_I \rangle(k_1, t)$ in Equation 5.83 and its fitting function $S_{\text{fit}}(k_1, t)$ (gray dashed lines) in Equation 5.96 as a function of evolution time $t$ at small (left panel) and large (right panel) scales with gravitational parameter $f = 1$ and initial time $t_0 = 10.0$ and two different friction coefficients $\tau_s = 0.01$ (blue lines) and $\tau_s = 0.001$ (yellow lines). . . . .	118
Figure 5.35	These two plots show the shape of the mean interaction term $i\langle S_I \rangle(k_1, t)$ in Equation 5.83 and its fitting function $S_{\text{fit}}(k_1, t)$ (gray dashed lines) in Equation 5.96 as a function of friction coefficient $\tau_s$ at small (left panel) and large (right panel) scales with gravitational parameter $f = 1$ and initial time $t_0 = 10.0$ and two different evolution times $t = 11.0$ (blue lines) and $t = 100.0$ (red lines). . . . .	118
Figure 5.36	These two plots show the shape of the density ration $\delta^2(t, \tau_s, f)$ in Equation 5.103 as a function of evolution time $t$ at parameters $f = 1, \tau_s = 0.01$ and $t_0 = 10.0$ (blue line), together with its numerical fitting function $\delta^2 \approx \chi_0^{t-t_0}$ (yellow dashed line). The gray dashed lines in both plots represent the lower limit $\delta^2_{\text{min}}$ in Equation 5.104. . . . .	120

Figure 5.37 These two plots show the shape of the density ration  $\delta^2(t, \tau_s, f)$  in Equation 5.103 as a function of friction coefficient  $\tau_s$  at parameters  $f = 1$ ,  $t_0 = 10.0$  and  $t = 20.0$  (blue line), together with its numerical fitting function  $\delta^2 \approx \chi_1^{\tau_s^3}$  (yellow dashed line). The gray dashed lines in both plots represent the lower limit  $\delta_-^2$  in Equation 5.104. . . . . 120

Figure 5.38 These two plots show the shape of the density ratio  $\delta^2(t, \tau_s, f)$  in Equation 5.103 as a function of gravitational parameter  $f$  at parameters  $t_0 = 10.0$ ,  $\tau_s = 0.001$  and  $t = 20.0$  (blue line), together with its numerical fitting function  $\delta^2 \approx \chi_2^f$  (yellow dashed line). The gray dashed lines in both plots represent the lower limit  $\delta_-^2$  in Equation 5.104. . . . . 121

Figure 6.1 *Left panel:* This plot shows the shape of integral (2) in Equation 6.86 as a function of  $g_{qp}(t)$ . *Right panel:* This plot shows the shape of integral (3) in Equation 6.87 as a function of  $g_{qp}(t)$ . 143

Figure 6.2 This figure shows the shape of absolute values of  $\bar{\mathcal{P}}_{\text{lin}1}^{\text{free}}(k_1)$  (left panel),  $\bar{\mathcal{P}}_{\text{lin}2}^{\text{free}}(k_1)$  (middle panel) and  $\bar{\mathcal{P}}_{\text{lin}3}^{\text{free}}(k_1)$  (right panel) in terms of wavenumber  $k_1$  (blue lines), together with their small scale asymptotic behaviors (yellow dashed lines) and the large scale  $k^{-1}$  asymptotic slopes (green dashed lines) of  $\bar{\mathcal{P}}_{\text{lin}2}^{\text{free}}(k_1)$  and  $\bar{\mathcal{P}}_{\text{lin}3}^{\text{free}}(k_1)$ . . . . . 149

Figure 6.3 This plot shows the free momentum-density trace power spectrum  $\bar{\mathcal{P}}_{\text{tr}}^{\text{free}}(k_1, t) = T_{10} + T_{20} + T_{30}$  (yellow line) and its elements  $T_{10}$  (purple line),  $T_{20}$  (green line),  $T_{30}$  (blue line) in terms of wave number  $k_1$  at evolution time  $g_0(t) = t = 2.0$ , together with their large scales asymptotic behaviors by Equation 6.125, Equation 6.131, Equation 6.132 and small-scale asymptotic behaviors by Equation 6.103-6.105. The negative values of  $T_{20}$  and  $T_{30}$  are represented by the same color dashed lines. . . . . 151

Figure 6.4	<p><i>Left panel:</i> This plot shows the free momentum-density divergence power spectrum elements <math>T_{50}</math> (purple line), <math>T_{20}</math> (green line), <math>T_{30}</math> (blue line) and <math>T_{50} + T_{20} + T_{30}</math> (yellow line) in terms of wave number <math>k_1</math> at evolution time <math>g_0(t) = t = 2.0</math>, together with their large scales asymptotic behaviors by Equation 6.126, Equation 6.131, Equation 6.132 and small-scale asymptotic behaviors by Equation 6.104-6.106. The negative values of <math>T_{20}</math>, <math>T_{30}</math>, <math>T_{50}</math> and <math>T_{50} + T_{20} + T_{30}</math> are represented by the same color dashed lines. <i>Right panel:</i> This plot shows the free momentum-density divergence power spectrum <math>\bar{\mathcal{P}}_{\text{div}}^{\text{free}}(k_1, t)</math> (yellow line) as a function of <math>k_1</math> at the same evolution time <math>g_0(t) = t = 2.0</math>, together with its large scale <math>k_1^{4/3}</math> asymptotic slope (black dash-dotted line) in Equation 6.137 and its small scale <math>k_1^{-1}</math> asymptotic slope (black dashed line) in Equation 6.138. . . . .</p>	153
Figure 6.5	<p>This plot shows the shape of amplitude <math>\mathcal{P}_{\text{frdiv}}^{(0)}(t)</math> in equation 6.138 as a function of evolution time <math>t</math>. The yellow dot marks its value at evolution time <math>t = 2.0</math> which corresponds to Figure 6.4. The green cross represents the example extreme points of the curve given in Equation 6.139. . . . .</p>	154
Figure 6.6	<p><i>Left panel:</i> This plot shows the free momentum-density curl power spectrum elements <math>T_{60}</math> (yellow line) in terms of wave number <math>k_1</math> at evolution time <math>g_0(t) = t = 2.0</math>, together with its large scales asymptotic behaviors by Equation 6.127 (black dashed line) and small-scale asymptotic behaviors by Equation 6.107 (black dash-dotted line). <i>Right panel:</i> This plot shows the free momentum-density curl power spectrum <math>\bar{\mathcal{P}}_{\text{curl}}^{\text{free}}(k_1, t)</math> (yellow line) as a function of <math>k_1</math> at the same evolution time <math>g_0(t) = t = 2.0</math>, together with its large scale <math>k_1^{4/3}</math> asymptotic slope (black dashed line) in Equation 6.140 and its small scale <math>k_1^{-1}</math> asymptotic slope (black dash-dotted line) in Equation 6.141. . . . .</p>	155
Figure 6.7	<p>This plot shows the shape of amplitude <math>\mathcal{P}_{\text{frcurl}}^{(0)}(t)</math> in Equation 6.141 as a function of evolution time <math>t</math>. The yellow dot marks its value at evolution time <math>t = 2.0</math> which corresponds to Figure 6.6. The green cross represents the example extreme point of the curve given in Equation 6.142. . . . .</p>	155

Figure 6.8 This plot shows the free momentum-density power spectra elements  $T_{10}$  (purple line),  $T_{50}$  (green line),  $T_{60}$  (blue line) and sum  $T_{50} + T_{60}$  (yellow line) in terms of wave number  $k_1$  at evolution time  $g_0(t) = t = 2.0$ , together with their large scales asymptotic behaviors by Equation 6.125, Equation 6.126, Equation 6.127 and small-scale asymptotic behaviors by Equation 6.103, Equation 6.106, Equation 6.107. The negative values of  $T_{50}$  is represented by the same color dashed lines. . . . . 156

Figure 6.9 This plot shows the shape of the linear momentum-density trace (top panel), divergence (middle panel) and curl (bottom panel) power spectra as functions of wave number  $k_1$  with very small friction coefficient  $\tau_s = 0.01$  (blue lines) and  $\tau_s = 0.1$  (yellow lines) at evolution time  $t = 10.0$ . Their large scales asymptotic behaviors are marked by the green dashed lines, and their small-scale asymptotic behaviors are represented by the red dashed lines. . . . . 159

Figure 6.10 This plot gives the shape of the first term in Equation 6.144  $\bar{\mathcal{P}}_{\text{lin1}}(k_1, t)$  as a function of wave number  $k_1$  with parameters:  $\tau_s = 1.0, t = 2.0$  (blue line);  $\tau_s = 2.0, t = 2.0$  (yellow line);  $\tau_s = 3.0, t = 2.0$  (green line);  $\tau_s = 3.0, t = 2.0$  (red line). At small scales, the  $k_1^{-3}$  slopes are marked by the purple dashed lines. . . . . 161

Figure 6.11 These four plots show the momentum-density trace power spectrum elements  $T_1$  (purple line),  $T_2$  (green line),  $T_3$  (blue line) and  $T_1 + T_2 + T_3$  (yellow line) as functions of wave number  $k_1$ , together with there large scales asymptotic behaviors by Equation 6.125, 6.131, 6.132 and small scales asymptotic behaviors by Equation 6.103-6.105, respectively at parameters:  $\tau_s = 1.0, t = 2.0$  (top left);  $\tau_s = 2.0, t = 2.0$  (top right);  $\tau_s = 3.0, t = 2.0$  (bottom left);  $\tau_s = 3.0, t = 3.0$  (bottom right). The negative values of  $T_2$  and  $T_3$  are represented by the same color dashed lines. . . . 162

Figure 6.12 This plot shows the total momentum-density trace power spectrum  $\bar{\mathcal{P}}_{\text{ftr}}(k_1, t)$  as a function of wave number  $k_1$  at the parameters:  $\tau_s = 1.0, t = 2.0$  (blue line);  $\tau_s = 2.0, t = 2.0$  (yellow line);  $\tau_s = 3.0, t = 2.0$  (green line);  $\tau_s = 3.0, t = 3.0$  (red line). At small scales, the  $k_1^{-3}$  asymptotic behaviors are marked by purple dashed lines. . . . . 163

Figure 6.13 This plot shows the amplitude  $\mathcal{P}^{\text{tot}}(t)$  of  $\bar{\mathcal{P}}_{\text{ftr}}(k_1, t)$  at small scales as a function of friction coefficient  $\tau_s$  (left panel) and evolution time (right panel). The green points in both plots mark the value of  $\mathcal{P}^{(0)}(t)$  corresponding to the  $\tau_s$  and  $t$  in Figure 6.12. . . . . 163

- Figure 6.14 This plot shows the momentum-density trace power spectrum ratio  $\text{ratio}_1(k_1, t)$  in Equation 6.162 as a function of wave number  $k_1$  with parameters as:  $\tau_s = 1.0, t = 2.0$  (blue line);  $\tau_s = 2.0, t = 2.0$  (yellow line);  $\tau_s = 3.0, t = 2.0$  (green line);  $\tau_s = 3.0, t = 3.0$  (red line). The purple dashed lines represent the asymptotic constant  $R_1$  in Equation 6.163 at small scales. . . . . 164
- Figure 6.15 This plot gives the shape of the first term in Equation 6.145  $\bar{\mathcal{P}}_{\text{lin}2}(k_1, t)$  as a function of wave number  $k_1$  with parameters:  $\tau_s = 1.0, t = 2.0$  (blue line);  $\tau_s = 2.0, t = 2.0$  (yellow line);  $\tau_s = 3.0, t = 2.0$  (green line);  $\tau_s = 3.0, t = 2.0$  (red line). At small scales, the  $k_1^{-1}$  slopes are marked by the purple dashed lines. . . . . 166
- Figure 6.16 These four plots show the momentum-density power spectra elements  $T_5$  (purple line),  $T_2$  (green line),  $T_3$  (blue line) and  $T_5 + T_2 + T_3$  (yellow line) as a function of wave number  $k_1$ , together with their large scales asymptotic behaviors by Equation 6.126, Equation 6.131, Equation 6.132 and small scales asymptotic behaviors by Equation 6.106, Equation 6.104, Equation 6.105 respectively at parameters:  $\tau_s = 1.0, t = 2.0$  (top left);  $\tau_s = 2.0, t = 2.0$  (top right);  $\tau_s = 3.0, t = 2.0$  (bottom left);  $\tau_s = 3.0, t = 3.0$  (bottom right). The negative values of  $T_5, T_2, T_3$  and  $T_5 + T_2 + T_3$  are represented by the same color dashed lines. . . . . 167
- Figure 6.17 This plot shows the total momentum-density divergence power spectrum  $\bar{\mathcal{P}}_{\text{div}}(k_1, t)$  as a function of wave number  $k_1$  at the parameters:  $\tau_s = 1.0, t = 2.0$  (blue line);  $\tau_s = 2.0, t = 2.0$  (yellow line);  $\tau_s = 3.0, t = 2.0$  (green line);  $\tau_s = 3.0, t = 3.0$  (red line), the same color dotted-straight lines represent positive values, otherwise are negative values. At small scales, the  $k_1^{-1}$  asymptotic behaviors are marked by the purple dashed lines. At large scales, the  $k_1^{\frac{4}{3}}$  slopes are marked by the borrow dashed line. . . . . 168
- Figure 6.18 This plot shows the amplitude  $\mathcal{P}_2^{\text{tot}}(t)$  of  $\bar{\mathcal{P}}_{\text{div}}(k_1, t)$  at small scales as a function of evolution time  $t$  (left panel) and friction coefficient  $\tau_s$  (right panel). The yellow points in both plots mark the value of  $\mathcal{P}_2^{\text{tot}}(t)$  corresponding to the  $\tau_s$  and  $t$  in Figure 6.17. 168
- Figure 6.19 This plot shows the momentum-density divergence power spectrum ratio  $\text{ratio}_2(k_1, t)$  in Equation 6.170 as a function of wave number  $k_1$  with parameters as:  $\tau_s = 1.0, t = 2.0$  (blue line);  $\tau_s = 2.0, t = 2.0$  (yellow line);  $\tau_s = 3.0, t = 2.0$  (green line);  $\tau_s = 3.0, t = 3.0$  (red line). The purple dashed lines represent the asymptotic constant  $R_2$  in Equation 6.171 at small scales. . . 169

Figure 6.20 This plot gives the shape of the first term in Equation 6.146  $\bar{\mathcal{P}}_{\text{lin}3}(k_1, t)$  as a function of wave number  $k_1$  with parameters:  $\tau_s = 1.0, t = 2.0$  (blue line);  $\tau_s = 2.0, t = 2.0$  (yellow line);  $\tau_s = 3.0, t = 2.0$  (green line);  $\tau_s = 3.0, t = 2.0$  (red line). At small scales, the  $k_1^{-1}$  slopes are marked by the purple dashed lines. . . . . 170

Figure 6.21 This plot shows the momentum-density power spectra element  $T_6$  as a function of wave number  $k_1$  at parameters:  $\tau_s = 1.0, t = 2.0$  (purple line);  $\tau_s = 2.0, t = 2.0$  (green line);  $\tau_s = 3.0, t = 2.0$  (blue line);  $\tau_s = 3.0, t = 3.0$  (yellow line). Their large scale  $k^{-\frac{2}{3}}$  asymptotic behavior is represented by the black dashed line, and their small scale  $k^{-3}$  asymptotic behavior is represented by the black dash-dotted line. . . . . 171

Figure 6.22 This plot shows the total momentum-density divergence power spectrum  $\bar{\mathcal{P}}_{\text{div}}(k_1, t)$  as a function of wave number  $k_1$  at the parameters:  $\tau_s = 1.0, t = 2.0$  (blue line);  $\tau_s = 2.0, t = 2.0$  (yellow line);  $\tau_s = 3.0, t = 2.0$  (green line);  $\tau_s = 3.0, t = 3.0$  (red line), the same color dotted-straight lines represent positive values, otherwise are negative values. At small scales, the  $k_1^{-1}$  asymptotic behaviors are marked by purple dashed lines. At large scales, the  $k_1^{\frac{4}{3}}$  slopes are marked by the borrow dashed line. . . . . 172

Figure 6.23 This plot shows the amplitude  $\mathcal{P}_3^{\text{tot}}(t)$  of  $\bar{\mathcal{P}}_{\text{fcurl}}(k_1, t)$  at small scales as a function of evolution time  $t$  (left panel) and friction coefficient  $\tau_s$  (right panel). The yellow points in both plots mark the value of  $\mathcal{P}_3^{\text{tot}}(t)$  corresponding to the  $\tau_s$  and  $t$  in Figure 6.22. 172

Figure 6.24 This plot shows the momentum-density curl power spectrum ratio  $\text{ratio}_3(k_1, t)$  in Equation 6.177 as a function of wave number  $k_1$  with parameters as:  $\tau_s = 1.0, t = 2.0$  (blue line);  $\tau_s = 2.0, t = 2.0$  (yellow line);  $\tau_s = 3.0, t = 2.0$  (green line);  $\tau_s = 3.0, t = 3.0$  (red line). The purple dashed lines represent the asymptotic constant  $R_3$  in Equation 6.178 at small scales. . . . . 173

- Figure 6.25 These four plots show the momentum-density power spectrum elements  $T_1$  (purple line),  $T_5$  (green line),  $T_6$  (blue line) and  $T_5 + T_6$  (yellow line) as a function of wave number  $k_1$ , together with their  $k^{-\frac{2}{3}}$  large scales asymptotic behaviors by Equation 6.125, Equation 6.126, Equation 6.127 and  $k^{-3}$  small scales asymptotic behaviors by Equation 6.103, Equation 6.106, Equation 6.107 respectively at parameters:  $\tau_s = 1.0, t = 2.0$  (top left);  $\tau_s = 2.0, t = 2.0$  (top right);  $\tau_s = 3.0, t = 2.0$  (bottom left);  $\tau_s = 3.0, t = 3.0$  (bottom right). The negative values of  $T_5$  are represented by the same color dashed lines. . . . . 175
- Figure 6.26 This plot shows the shape of  $\text{ratio}_1$  as a function  $k_1$  with parameters:  $\tau_s = 1, t = 2$  (blue line);  $\tau_s = 2, t = 2$  (green line);  $\tau_s = 3, t = 2$  (yellow line);  $\tau_s = 3, t = 3$  (red line), together with the corresponding values of  $\frac{1}{3}(\text{Ratio}_2(t) + 2 \cdot \text{Ratio}_3(t))$ . At very small scales, the values of  $R_1$  in Equation 6.163 are marked by the purple dashed lines. . . . . 176
- Figure 6.27 This plot shows the shape of  $i\langle S_1 \rangle(k_1, t)$  in Equation 5.83 as a function of  $k_1$  at different particle sizes  $\tau_s = 0.01$  (blue, yellow lines),  $\tau_s = 0.1$  (green, red lines) with different evolution time  $t = 11.0$  (blue, green lines),  $t = 20.0$  (yellow, red lines) at the same initial time  $t_0 = 10.0$  and the same gravitational parameter  $f = 1.0$ . Their large scale  $k_1^2$  asymptotic slopes are marked by the burgundy dashed lines, and their small scale asymptotic constants are represented by the light green dashed lines. . . . 178
- Figure 6.28 This plot shows the shape of  $\vec{F} \cdot \vec{F}$  (left panel) and  $\vec{k}_1 \cdot \vec{F}$  (right panel) in Equation 6.193 and Equation 6.194 as functions of wavenumber  $k_1$  at the initial time  $t_0 = 10.0$  and gravitational parameter  $f = 1.0$  with different parameters:  $\tau_s = 0.1, t - t_0 = 1.0$  (blue lines);  $\tau_s = 0.1, t - t_0 = 10.0$  (green dashed lines);  $\tau_s = 0.01, t - t_0 = 1.0$  (yellow lines);  $\tau_s = 0.01, t - t_0 = 10.0$  (red dashed lines). At large scales, their asymptotic behaviors are marked by the purple dashed lines, and at small scales, their asymptotic behaviors are marked by brown dashed lines. . . . 181

- Figure 6.29 These two plots shows the shape of the full linear momentum-density trace power spectra  $\bar{\mathcal{P}}_{\text{glin1}}(k_1, t)$  as functions of wave number  $k_1$  with parameters:  $\tau_s = 0.01, t = 11.0$  (yellow line);  $\tau_s = 0.01, t = 20.0$  (green line);  $\tau_s = 0.1, t = 11.0$  (purple line);  $\tau_s = 0.1, t = 20.0$  (brown line), together with their corresponding initial trace power spectrum  $\bar{\mathcal{P}}_{\text{lin1}}(k_1, t)$  in Equation 6.152 at initial time  $t_0 = 10.0$  (blue, red lines) at the same gravitational parameter  $f = 1.0$ . The gray dashed line marks the curve of  $(1 - g_{\text{pp}}(t))^2 u_0^2 \mathcal{P}_{\text{glin}}(k_1, t)$ . The right panel plot shows the zoom plot of  $\bar{\mathcal{P}}_{\text{glin1}}(k_1, t)$  at higher values. . . . . 182
- Figure 6.30 These two plots show the shape of the full linear momentum-density divergence power spectra  $\bar{\mathcal{P}}_{\text{glin2}}(k_1, t)$  as functions of wave number  $k_1$  with parameters:  $\tau_s = 0.01, t = 11.0$  (yellow line);  $\tau_s = 0.01, t = 20.0$  (green line);  $\tau_s = 0.1, t = 11.0$  (purple line);  $\tau_s = 0.1, t = 20.0$  (brown line), together with their corresponding initial divergence power spectrum  $\bar{\mathcal{P}}_{\text{lin2}}(k_1, t)$  in Equation 6.153 at initial time  $t_0 = 10.0$  (blue, red lines) at the same gravitational parameter  $f = 1.0$ . The gray dashed line marks the curve of  $\frac{1}{3}(1 - g_{\text{pp}}(t))^2 u_0^2 k_1^2 \mathcal{P}_{\text{glin}}(k_1, t)$ . The right panel plot shows the zoom plot of  $\bar{\mathcal{P}}_{\text{glin2}}(k_1, t)$  at higher values. 182
- Figure 6.31 This plot shows the shape of the full linear momentum-density curl power spectra  $\bar{\mathcal{P}}_{\text{glin3}}(k_1, t)$  as functions of wave number  $k_1$  with parameters:  $\tau_s = 0.01, t = 11.0$  (yellow line);  $\tau_s = 0.01, t = 20.0$  (green line);  $\tau_s = 0.1, t = 11.0$  (purple line);  $\tau_s = 0.1, t = 20.0$  (brown line), together with their corresponding initial curl power spectrum  $\bar{\mathcal{P}}_{\text{lin3}}(k_1, t)$  in Equation 6.154 at initial time  $t_0 = 10.0$  (blue, red lines) at the same gravitational parameter  $f = 1.0$ . The gray dashed line marks the curve of  $\frac{2}{3}(1 - g_{\text{pp}}(t))^2 u_0^2 k_1^2 \mathcal{P}_{\text{glin}}(k_1, t)$ . The right panel plot shows the zoom plot of  $\bar{\mathcal{P}}_{\text{glin3}}(k_1, t)$  at higher values. . . . . 183
- Figure 6.32 This plot shows the shape of  $i\langle S_I \rangle(k_1, t)$  in Equation 5.90 as a function of  $k_1$  at different particle sizes  $\tau_s = 1$  (blue line),  $\tau_s = 2$  (yellow line),  $\tau_s = 3.0$  (green line) with different initial time  $t_0 = 2.0$  (blue, yellow, green lines),  $t = 3.0$  (red lines) at the same evolution time time  $t = 10.0$  and the same gravitational parameter  $f = 1.0$ . Their large scale  $k_1^2$  asymptotic slopes are marked by the burgundy dashed lines, and their small scale asymptotic constants are represented by the light green dashed lines. . . . . 184

- Figure 6.33 This plot shows the shape of  $\vec{F} \cdot \vec{F}$  (left panel) and  $\vec{k}_1 \cdot \vec{F}$  (right panel) in Equation 6.202 and Equation 6.203 as functions of wavenumber  $k_1$  at the evolution time  $t = 10.0$  and gravitational parameter  $f = 1.0$  with different parameters:  $\tau_s = 1.0, t_0 = 2.0$  (blue lines);  $\tau_s = 2.0, t_0 = 2.0$  (yellow lines);  $\tau_s = 3.0, t_0 = 2.0$  (green lines);  $\tau_s = 3.0, t_0 = 3.0$  (red lines). Their  $k_1^{-2}$  and  $k_1^2$  asymptotic slopes are marked by the purple dashed lines, and their asymptotic constants are marked by brown dashed lines. 187
- Figure 6.34 *Left panel:* This plot shows the momentum-density power spectra element  $T_7$  as a function of wave number  $k_1$  at parameters:  $\tau_s = 1.0, t = 2.0$  (purple line);  $\tau_s = 2.0, t = 2.0$  (green line);  $\tau_s = 3.0, t = 2.0$  (blue line);  $\tau_s = 3.0, t = 3.0$  (yellow line). The negative values of  $T_7$  at different  $\tau_s$  and  $t$  are represented by the same color dashed lines. Their large scale  $k_1^{\frac{4}{3}}$  asymptotic behaviors are represented by the black dash-dotted lines, and their small scale  $k_1^{-3}$  asymptotic behaviors are represented by the black dashed lines. *Right panel:* This plot shows the shape of momentum-density elements  $T_5$  (green line) and  $T_7$  (purple line) at the same time as functions of  $k_1$  with parameters  $\tau_s = 2.0$  and  $t = 2.0$ . Their negative values are represented by the same color dashed lines. . . . . 188
- Figure 6.35 These four plots show the full nonlinear momentum-density trace power spectra  $\bar{\mathcal{P}}_{\text{gr}}(k_1, t)$  as functions of wave number  $k_1$  at evolution time  $t = 10.0$  (yellow lines) with parameters  $\tau_s = 1.0, t_0 = 2.0$ ;  $\tau_s = 2.0, t_0 = 2.0$ ;  $\tau_s = 3.0, t_0 = 2.0$ ;  $\tau_s = 3.0, t_0 = 3.0$  with the same gravitational parameter  $f = 1.0$ . Their corresponding initial trace power spectrum  $\bar{\mathcal{P}}_{\text{tr}}(k_1, t)$  in Equation 6.144 at initial times  $t_0$  are marked by blue lines. The gray dashed lines mark the curve of  $\exp(i\langle S_I \rangle) \cdot \bar{\mathcal{P}}_{\text{tr}}(k_1, t)$ . . . . . 190
- Figure 6.36 These four plots show the full nonlinear momentum-density divergence power spectra  $\bar{\mathcal{P}}_{\text{div}}(k_1, t)$  as functions of wave number  $k_1$  at evolution time  $t = 10.0$  (yellow lines) with parameters  $\tau_s = 1.0, t_0 = 2.0$ ;  $\tau_s = 2.0, t_0 = 2.0$ ;  $\tau_s = 3.0, t_0 = 2.0$ ;  $\tau_s = 3.0, t_0 = 3.0$  with the same gravitational parameter  $f = 1.0$ . Their corresponding initial trace power spectra  $\bar{\mathcal{P}}_{\text{div}}(k_1, t)$  in Equation 6.145 at initial times  $t_0$  are marked by blue lines. The gray dashed lines mark the curve of  $\exp(i\langle S_I \rangle) \cdot \bar{\mathcal{P}}_{\text{div}}(k_1, t)$ . . . . . 191

Figure 6.37 These four plots show the full nonlinear momentum-density curl power spectra  $\bar{\mathcal{P}}_{\text{gcurl}}(k_1, t)$  as functions of wave number  $k_1$  at evolution time  $t = 10.0$  (yellow lines) with parameters  $\tau_s = 1.0, t_0 = 2.0$ ;  $\tau_s = 2.0, t_0 = 2.0$ ;  $\tau_s = 3.0, t_0 = 2.0$ ;  $\tau_s = 3.0, t_0 = 3.0$  with the same gravitational parameter  $f = 1.0$ . Their corresponding initial trace power spectrum  $\bar{\mathcal{P}}_{\text{fcurl}}(k_1, t)$  in Equation 6.146 at initial times  $t_0$  are marked by blue lines. The gray dashed lines mark the curve of  $\exp(i\langle S_I \rangle) \cdot \bar{\mathcal{P}}_{\text{fcurl}}(k_1, t)$ . . . 192

Figure 7.1 The spiral galaxy IC 5332, as captured by the James Webb Space Telescope’s Mid-Infrared Instrument. . . . . 196

Figure A.1 This plot shows the shape of integral  $I_{\text{lin}0}(k_1)$  in (A.3) as a function of wavenumber  $k_1$  (blue line), together with its large scale  $k_1^{7/3}$  asymptotic behavior (yellow dashed line) and small scale asymptotic constant (green dashed line). . . . . 204

Figure A.2 This figure shows the shape of absolute values of  $I_{\text{lin}1}(k_1)$  (left panel),  $I_{\text{lin}5}(k_1)$  (middle panel) and  $I_{\text{lin}6}(k_1)$  (right panel) in terms of wavenumber  $k_1$  (blue lines), together with their small scale  $k_1^{7/3}$  asymptotic behaviors (yellow dashed lines) and the large scale asymptotic constants (green dashed lines) of  $I_{\text{lin}5}(k_1)$  and  $I_{\text{lin}6}(k_1)$ . . . . . 206

Figure A.3 These 2 plots illustrate the function of  $r^2 l_0(r)$  respectively at  $k_1 = 1.0$  and  $k_1 = 50.0$  at time  $t = 4\pi$  (blue lines). The orange dashed lines represent the  $r^2$  slope. The green dashed lines represent the  $r$  slope. . . . . 208

Figure A.4 This plot compares the nonlinear density power spectrum  $\mathcal{P}_0(k_1, t)$  (purple line) with  $\mathcal{P}_{\text{free}}(k_1, t)$  (green line) together with their asymptotic behaviour at large scales (blue dashed line). . . . . 209

Figure A.5 This plot shows the relative difference between  $\mathcal{P}_0(k_1, t)$  and  $\mathcal{P}_{\text{free}}(k_1, t)$  defined in Equation A.29. . . . . 209

Figure B.1 This plot shows the amplitude  $\mathcal{P}_{\text{lin}1}^{(0)}(t)$  of  $\bar{\mathcal{P}}_{\text{lin}1}(k_1, t)$  at small scales as a function of friction coefficient  $\tau_s$  (left panel) and evolution time (right panel). The green points in both plots mark the value of  $\mathcal{P}^{(0)}(t)$  corresponding to the  $\tau_s$  and  $t$  in Figure 6.10. The blue point in the left panel represents the maximal point of this curve by Equation B.3 and Equation B.4. . . . . 212

Figure B.2	This plot shows the shape of $L_1\left(\frac{t}{\tau_{sm}}\right)$ (blue line) and $R_1\left(\frac{t}{\tau_{sm}}\right)$ (yellow line) as a function of $\frac{t}{\tau_{sm}}$ . At small $\frac{t}{\tau_{sm}}$ , $L_1$ is proportional to $\left(\frac{t}{\tau_{sm}}\right)^{-1}$ (green dashed line) and $R_1$ is proportional to $\left(\frac{t}{\tau_{sm}}\right)^{-2}$ (red dashed line). At large $\frac{t}{\tau_{sm}}$ , $L_1$ reaches its asymptotic constant at $L_{1\infty}$ in Equation B.5 (purple dashed line) and $R_1$ reaches its asymptotic constant at $R_{1\infty}$ in Equation B.5 (brown dashed line). . . . .	212
Figure B.3	This plot shows the shape of amplitude $\mathcal{P}_{\text{linI}}^{(0)}(t)$ as a function of evolution time $t$ at different particle size $\tau_s$ . . . . .	213
Figure B.4	This plot shows shape of $L^{\text{tot}}(y)$ (blue line) and $R^{\text{tot}}(y)$ (yellow line). At large $y$ , both curves reach their asymptotic constant $L_{\infty}^{\text{tot}}$ (green dashed line) and $R_{\infty}^{\text{tot}}$ (red dashed line). . . . .	215
Figure B.5	This plot shows shape of $L^{\tau}(z)$ (blue line) and $R^{\tau}(z)$ (yellow line). At large $z$ , both curves reach their asymptotic constant $L_{\infty}^{\tau}$ (green dashed line) and $R_{\infty}^{\tau}$ (red dashed line). . . . .	216
Figure B.6	This plot shows shape of $\mathcal{P}^{\text{tot}}(t)$ as a function of $t$ at different particle sizes $\tau_s$ . . . . .	217

## LIST OF TABLES

---

Table 4.1	Best-fitting parameters of the momentum distributions in all spatial directions. Notice that the mean values for the momenta in the $x$ and $y$ directions do not vanish due to drift motion. We set them to zero for the calculations later. . . . .	47
Table 4.2	Best-fitting parameters for all six independent momentum power spectra. The small but nonzero first value for all curves reflects the shot noise. . . . .	64
Table 4.3	This table shows the fitting coefficient for the density spatial power spectrum $P_{00}(k)$ . . . . .	64
Table 4.4	Fit parameters for all density-momentum cross power spectra. .	66
Table 5.1	This table gives the values for the fitting coefficients $c_0 g_{qp}^2(t_0)$ and $c_2$ in <a href="#">Equation 5.81</a> for $\tau_s = 3.0$ at the initial time $t_0 = 2.0$ and at $t_0 = 10.0$ . . . . .	103

## ACRONYMS

---

KFT kinetic field theory

PPD protoplanetary disk

SI streaming instability

iPDF initial probability distribution function in phase space

FFT Fast Fourier Transform

CIC clouds in cells

CMB cosmic microwave background

## INTRODUCTION

---

The formation of the Earth and the other 7 planets in the Solar System has puzzled humans throughout history. By enhancing our capacity to glimpse into the dark night sky, we know from the many detections of extrasolar planets that planetary systems are common in the universe. Apparently, nature finds it easy to form planets out of micrometer-sized cosmic dust. But how nature manages to accomplish this is not yet fully understood. Solving this problem has turned out to be extremely challenging due to the enormous dynamic ranges in space, time and mass scales involved. Planets form in so-called protoplanetary disks, the dusty gaseous disks rotating around newly formed stars. This structure formation process starts from micrometer-sized cosmic dust particles, which coagulate to form ever larger dust aggregates. Small aggregates are held together by cohesive forces, in particular the Van der Waals force. Once these aggregates grow above a kilometer, it is primarily the force of gravity that keeps them together and leads to further agglomeration and growth, eventually forming full-grown planets. This path of growth covers 13 orders of magnitude in size and correspondingly 40 orders of magnitude in mass.

However, as dusty aggregates grow beyond centimeter size, but have not yet reached kilometer scales, they become very fragile and non-cohesive, and it is not clear how growth proceeds in this regime. Such intermediate-size aggregates also tend to rapidly drift towards the star, and thus get lost in the planet-formation process. There are two main scenarios how these problems (together often summarized as the “meter size barrier”) may be overcome. The more popular scenario involves dust particle clustering and/or trapping. This can occur in large-scale pressure maxima or zonal flows as well as in vortices. Dust particles can also be clustered in turbulent flows, see Hogan and Cuzzi [17], such as those triggered by the streaming instability, see Johansen and Youdin [21]. The formation of dense particle clouds can subsequently lead to their gravitational collapse and the formation of  $\gtrsim 100$  km size planetesimals, see Johansen, Klahr, and Henning [20]. The alternative scenario involves fractal/fluffy icy aggregate growth up to sizes of hundreds of meters, followed by gravitational compression, see Kataoka, Akimasa et al. [23], eventually forming  $\sim 10$  km planetesimals. Neither of these scenarios has definitively been proven or disproven yet, because they are extremely hard to model, involving turbulent cascades covering many orders of magnitude in eddy size, and complex-shaped dust aggregates consisting of up to  $\sim 10^{20}$  dust particles.

*Kinetic Field Theory for Structure Formation*

This thesis follows the first path. Given the challenges of the traditional approach, it is worthwhile to explore new analytic means for studying particle clustering. Recently a statistical, kinetic theory for classical particle ensembles in or out of equilibrium called kinetic field theory (**KFT**) is developed, see Bartelmann et al. [4] based on Das and Mazenko [9]. This theory encodes the dynamics of a classical particle ensemble by a generating functional completely specified by the initial probability distribution of particles in phase space and their equation of motion. It describes how the phase-space distribution of the particle ensemble evolves with time. From the evolved generating functional, density and momentum-density power spectra of the particles can be extracted by functional derivatives. This theory has initially been developed for studying the formation and evolution of cosmic structures in the non-linear regime. The power spectrum of cosmic structures even deeply in this regime can be reproduced very well already at low orders in the particle interactions, see Bartelmann et al. [4], Viermann et al. [40], even further, the asymptotic study over the small-scale limit of the free power spectrum in Konrad [25] shows the necessity of the development of a universal  $k^{-3}$  tail below a characteristic scale.

Here we shall adapt **KFT** to the problem of turbulent particle clustering, aiming at bridging the vast dynamical range by analytic methods.

The two problems have several similarities, such as the (initial) collisionlessness and the (eventual) mutual gravitational forces between the particles. There are, however, two essential differences that will require attention. The first difference is that dust particles in a turbulent medium experience friction with the gas. A conventional Hamiltonian system cannot handle dissipative forces. **KFT** does, however, not depend on the equations of motion being Hamiltonian. The loss of their symplectic structure just implies that we will need to include the functional determinant of the phase-space flow of the particles into the generating functional. On the other hand, the friction of the dust particles with the turbulent gas is what drives the particle clustering. This means that we have to provide a description of the turbulent background. To keep this feasible, we will limit ourselves to finding a prescribed turbulent background field that excludes the feedback of the dust onto the gas. The second difference is more technical. To study cosmic structure formation, one of the crucial pieces of evidence is the cosmic microwave background (**CMB**), which can provide the initial matter distribution in the universe. Combining it with the cosmology principle of the universe being isotropic and homogeneous, the initial probability distribution function in phase space (**iPDF**) for particles can be derived analytically by assuming density and momenta fields being Gaussian. However, in planetary formation, for the generality of the protoplanetary disk (**PPD**), the **iPDF** for dust particles in **KFT** needs to come from an evolved 3-dimensional numerical simulation, which does not necessarily have

Gaussian fields in the system. Therefore the development of a new feasible method to extract the mathematical challenging *iPDF* from simulation data is necessary.

### *Outline of the Thesis*

To eventually obtain analytical and numerical results for the planetesimal formation from *KFT*, we pursue three major goals with this work.

(i) The development of a new scheme for computing the *iPDF* of dust particles by Gaussianizing their density and momenta fields in [Chapter 4](#).

(ii) The derivation of the *KFT* density and momentum-density power spectra considering friction and self-gravitational interactions in the system, and the application of novel asymptotic methods to analyze their small-scale behavior in [Chapter 5](#) and [Chapter 6](#).

(iii) The discussion of the criteria for dust particles to overcome the "meter-size barrier" and achieve final gravitational collapse by determining the averaged density growth in [Chapter 5](#).

This thesis is organized as follows.

[Chapter 2](#) first briefly summarizes the gas and dust dynamics within a *PPD*. A shearing box simulation method is introduced next and the equation of motion in its corresponding coordinates for dust particles is derived. Then the Hill stability criteria for self-gravitating particle clouds in *PPDs* is discussed in detail and the corresponding Hill density is given.

[Chapter 3](#) provides the theoretical groundwork for kinetic field theory (*KFT*). Here, the generating functional is derived in the case of  $N$  classical particles, with  $N \gg 1$ . The dust dynamics appropriate for planetary structure formation in *KFT* by considering only friction interaction with an averaged background gas field and gravitational interactions between dust particles is specified. Then the density and momentum-density operators are defined for computing *KFT* power spectra in [Chapter 5](#) and [Chapter 6](#).

[Chapter 4](#) develops the new scheme of modelling the *iPDF* for dust particles after a specific simulation. By Gaussianizing the density field, we obtain the final expression of the *iPDF* using a multivariable Gaussian distribute. Then a pipeline is developed to extract the covariance matrix in the *iPDF* from simulation data. Finally, the momentum covariance matrix is isotropized and rotated to the position and wave vector space for the convenience of [Chapter 5](#) and [Chapter 6](#).

[Chapter 5](#) starts with factorizing the generating functional and introducing the mean-field approach for gravitational interaction to derive the general expression of the *KFT* nonlinear density power spectrum. Next, the linear and nonlinear free, friction, and gravitational density power spectra are analyzed and their large and small asymptotic behaviors are calculated. Then, the universality of a  $k^{-3}$  asymptotic tail for all the nonlinear density power spectra above is concluded, suggesting a scale-invariant structure formation below a characteristic and time-dependent length scale. Furthermore, the analysis of the amplitude for the  $k^{-3}$  small-scale asymptotic behavior shows a

critical particle size  $\tau_s \approx 3.03$  which corresponds to the strongest small-scale structure formation when considering only the friction between dust particles and the constant background gas field. In the end, the averaged density growth is calculated and the criteria for overcoming the "meter-size barrier" is given as  $\tau_s \approx 2.96 \cdot 10^{-5}$ , which is far smaller than the lower limit given by simulations and well possible to achieve by a dust coagulation process.

Chapter 6 starts with the derivation of the general expressions for the three KFT scalar momentum-density power spectra. Next, the linear and nonlinear free, friction, and gravitational momentum-density power spectra are analyzed and their large and small-scale asymptotic behavior is calculated. In the end, the universality of a  $k^{-3}$  tail for all the nonlinear trace momentum-density power spectra and a  $k^{-1}$  tail for all the nonlinear divergence and curl momentum-density power spectra are concluded, suggesting a scale-invariant total kinetic energy accumulation, and momentum-density power accumulation parallel and perpendicular to  $\vec{k}$  space below a characteristic length scale. The further analysis of the amplitude for the  $k^{-3}$  small-scale asymptotic behavior of trace power spectra shows a critical particle size  $\tau_s \approx 3.03$  which corresponds to the maximal small-scale kinetic energy accumulation when considering only the friction between dust particles and the constant background gas field.

Chapter 7 summarizes our results and discusses the outlook for future work.

Part I

FOUNDATIONS



It has just been less than twenty years since the first planet outside our Solar System was detected by Mayor, Michel and Queloz, Didier [29] and confirmed by Marcy et al. [28]. Since then, the study of planet formation has been revolutionized by many observational breakthroughs, which have allowed the detection and characterization of extrasolar planets, the imaging of protoplanetary disks, and the discovery of the Solar System's Kuiper Belt.

Much work has been done to try to understand how extrasolar planets may form. Modern studies of planet formation include comparing exoplanetary systems, the identification of protoplanetary disks around newborn stars, and computer models to trace the creation of planets from their origins in interstellar dust and gas. This Chapter introduces three main parts of this story. In the first part, the main players in the context of planetary formation in PPDs, gas and dust, are introduced. Starting with gas dynamics, one of its distinguishing properties is the internal pressure  $P$  caused by the gas temperature  $T$ , which slightly compensates for the centripetal force and directly provides a change in its Keplerian velocity. In the meantime, this change of gas velocity affects the dust dynamics by slowing down the dust particles via friction and causing their radial drifts toward the central star. The second part of this Chapter introduces one of the particular simulation methods for studying planetary formation and focuses on the derivation of the equation of motion for dust particles in a local frame of reference. This coordinate system is set to orbit with Keplerian velocity around the central star. It is called a shearing box since the Keplerian shear is linearised around the origin of the box. In the third part, the Hill stability criteria for self-gravitating particle clouds in PPDs is discussed in detail and the corresponding Hill density is derived as a key parameter which will be of paramount importance for determining gravitational collapse in Chapter 5. Finally, in the end, we summarize these insights and discuss the need for an alternative analytical approach to planetary structure formation that helps us to understand dust aggregation and the emergence of kilometer-size planetesimals.

## 2.1 GAS DYNAMICS

The gas in a PPD has internal properties that the dust is lacking, such as a pressure  $P$  that caused by the gas temperature  $T$ . Since the internal dust particle density is much larger than the gas density, the resulting force from the gas pressure is negligible. From the inner part, close to the star, the temperature decreases towards the outer part of the disk. Hence, a gradient in pressure is acting in a radially inward direction. The

pressure is supporting the gas radially against stellar gravity, together with the centrifugal force from the circular orbit motion. The structure of this section follows this line of thought. In between, we will define some important parameters (i.e. Keplerian rotation frequency, gas scale height) for later application.

### 2.1.1 Keplerian rotation

In the PPDs, we suppose the mass of the central star is  $M_*$ . Consider a particle on the mid-plane, in the absence of other force. The gravitational pull from the star  $g_*$  on this particle at a distance  $r$  is then:

$$g_* = \frac{GM_*}{r^2} \quad (2.1)$$

From the balance of its centrifugal force, we can get the Keplerian angular frequency([35]):

$$\frac{GM_*}{r^2} = \Omega^2 r \quad \rightarrow \quad \Omega = \sqrt{\frac{GM_*}{r^3}} \quad (2.2)$$

and Keplerian orbital velocity:

$$v_K := v_\phi = \Omega r \quad (2.3)$$

Throughout this thesis, if an object's orbit is referenced to as Keplerian (Kepler [24]), it obeys Equation 2.2 and has an azimuthal velocity of  $v_K$ .

### 2.1.2 Gas disk pressure scale-height

PPDs cool significantly fast via their large surface area. This makes them rather small in their vertical extent (D'Alessio et al. [8]). Still, they are vertically stabilized by a pressure gradient on a pressure scale height  $H$ , which arises from the increasing gas density towards the disk mid-plane. In a steady state, the vertical gravity must then be equal to the vertical pressure gradient. The vertical gravity comes mainly from the central star, as typical PPD models use disk masses of  $m_{\text{disk}} \approx 0.01M_*$ , see Andrews et al. [1] for further reading, as they suggest a typical disk mass to be 0.6% of the stellar mass. So the disk self-gravity contribution is negligible in first-order approximation.

Following the scenario in Section 2.1.1, the gravitational pull in the  $z$  direction from the star on a gas parcel at a distance  $r$  from the star and height  $z$  over the mid-plane, with  $z \ll r$ , then is:

$$g_{*,z} = g_* \sin \theta = \frac{GM_*}{r^2 + z^2} \cdot \frac{z}{\sqrt{r^2 + z^2}} \simeq \frac{GM_* z}{r^3} = \Omega^2 z \quad (2.4)$$

where  $\tan \theta = \frac{z}{r}$ . Now mark the internal gas pressure as  $P$  and the local gas density as  $\rho_g$ . The vertical gas pressure gradient can be decomposed as:

$$\frac{\partial P}{\partial z} = \frac{\partial P}{\partial \rho_g} \frac{\partial \rho_g}{\partial z} \quad (2.5)$$

In this thesis, we focus on local approximations of a **PPD**, thus we can assume the gas to be isothermal locally, meaning the gas has a constant temperature  $T = \text{const.}$  The equation of state is obtained from the ideal gas equation:

$$P = P(\rho_g) = \frac{k_B T}{\mu} \rho_g \quad (2.6)$$

with  $k_B$  being the Boltzmann constant and  $\mu$  being the molecular mass of the gas. Hence the sound speed

$$c_s^2 = \frac{\partial P}{\partial \rho_g} = \frac{k_B T}{\mu} \quad (2.7)$$

is also a constant. By using the ideal gas equation 2.6, we can rewrite the vertical gas pressure gradient as

$$\frac{\partial P}{\partial z} = \frac{P}{\rho_g} \frac{\partial \rho_g}{\partial z} = c_s^2 \frac{\partial \rho_g}{\partial z} \quad (2.8)$$

Now by setting the pressure gradient equal to the vertical gravitational force, we get:

$$\frac{\partial P}{\partial z} = -\rho_g g_{*,z} \quad \rightarrow \quad c_s^2 \frac{\partial \rho_g}{\partial z} = -\rho_g \Omega^2 z \quad (2.9)$$

This can be solved by simple integration to

$$\rho_g(z, r) = \rho_{g,0}(r) \exp\left(-\frac{z^2}{H(r)^2}\right) \quad (2.10)$$

where the vertical gas disk scale height is introduced by defining

$$H(r) := \frac{c_s(r)}{\Omega} \quad (2.11)$$

Furthermore, we can also define the disk aspect ratio  $h$  as

$$h(r) = \frac{H(r)}{r} \quad (2.12)$$

Parametrizing the sound speed via  $c_s \sim r^{-\beta_s}$ , one gets a disk aspect ratio of  $h(r) \sim r^{-\beta_s+1/2}$ . A disk with a constant aspect ratio has  $\beta_s = \frac{1}{2}$ , while a flared disk has a larger outer disk aspect ratio, thus  $\beta_s < \frac{1}{2}$ . Simple PPD models assume no disk flaring, hence a fixed ratio between gas disk scale-height  $H(r)$  and radius  $r$ . Consequently, a disk with a typical aspect ratio of  $h \approx 0.04$  (Hayashi [16]) has a circumference of  $U = \frac{2\pi}{h}H \approx 157H$ , a value that will later be used as a reference, when a local coordinate system for the numerical experiments is introduced.

### 2.1.3 Global pressure gradient

A main feature of a protoplanetary disk now is its high gas content, leading to a different equilibrium state in which the gas is not traveling with Keplerian orbital speed but instead slower. This comes from its intrinsic, radially inward-pointing gradient in the gas density and hence the existing gas pressure gradient. The change in orbital velocity then depends on the strength of this additional pressure-gradient force, as it is stabilizing now the gas together with the orbital centrifugal force.

In a gas-free 1-dimensional case, in the radial direction, the gravitational acceleration  $g_*$  is represented by Equation 2.1. The additional acceleration  $g'$  due to the force from the gas pressure gradient, adds to the gas velocity via:

$$g' = -\frac{1}{\rho_g} \frac{\partial P}{\partial r} \quad (2.13)$$

Consequently, the gas is in hydrostatic equilibrium under the condition of

$$\frac{u(r)^2}{r} = \frac{v_k^2}{r} + g' \cdot r \quad \rightarrow \quad u(r) = v_k \sqrt{1 + \frac{g' \cdot r}{v_k^2}} \approx v_k + \frac{g' \cdot r}{2v_k^2} v_k \quad (2.14)$$

Here  $u(r)$  represents the azimuthal gas velocity and we already use the approximation where  $g' \ll g_*$ . This can be expressed as a deviation from the original Keplerian orbital velocity via

$$\Delta \mathbf{u} = v_k - \mathbf{u} = -\frac{g'}{2g_*} v_k \quad (2.15)$$

Using the conditions for an isothermal disk, of  $P = c_s^2 \rho_g$  and  $H = c_s / \Omega$ , this can be well parametrized in the often used beta-parameter  $\beta_{\ln(\rho)}$  via

$$g' = -\frac{1}{\rho_g} \frac{\partial P}{\partial r} = -\frac{c_s^2}{\rho_g} \frac{\partial \rho_g}{\partial r} = -\frac{H c_s \Omega}{r} \frac{\partial \ln \rho_g}{\partial \ln r} := \beta_{\ln(\rho)} c_s \Omega \quad (2.16)$$

One can also use the disk aspect ratio  $h$  in order to arrive at an even shorter expression for  $\beta_{\ln(\rho)}$

$$\beta_{\ln(\rho)} = -h \frac{\partial \ln \rho_g}{\partial \ln r} \quad (2.17)$$

Now, defining the sub-Keplerianness  $\eta$  of the gas velocity  $\mathbf{u}$  as a factor between Keplerian velocity and its deviation from it, via

$$\mathbf{u}(r) = v_k (1 - \eta) \quad (2.18)$$

Consequently, it can be expressed via the beta-parameter

$$\eta = -\frac{g'}{2g_*} = \frac{1}{2} \frac{H}{r} \beta_{\ln(\rho)} \quad (2.19)$$

or with  $v_k = \Omega r$  and  $c_s = H\Omega$ , we have

$$\eta = \frac{1}{2} \beta_{\ln(\rho)} \frac{c_s}{v_k} \quad (2.20)$$

Typically, the orbital velocity at a distance of  $r = 1\text{AU}$  around a star with mass  $M_* = M_{\text{sun}}$  is about  $32\text{km/s}$ . With a [PPD](#) typical value for  $\eta \approx 10^{-3}$ , the gas orbits at  $1\text{AU}$  with a velocity of

$$\mathbf{u} = (1 - \eta)v_k \approx 31.968\text{km/s} \quad (2.21)$$

This velocity difference might look insignificant, but the resulting radial particle drift due to friction with the gas has challenged the planet formation community now for decades, which also plays a crucial role in the rest of the thesis.

## 2.2 PARTICLE FRICTION AND STOKES NUMBER

In this section, dust is introduced into the coupled system, which changes the dynamics of both components tremendously. Friction couples two systems that have different natural azimuthal velocities. The dust wants to orbit with Keplerian velocity  $v_k$  whereas the pressure-supported gas tries to orbit with  $(1 - \eta)v_k$ . The section introduces the friction timescale  $\tau_s$ , with its canonical representation by the dimensionless Stokes number  $St$ , and briefly discusses the effect of the streaming instability (SI) for planetesimal formation.

### 2.2.1 Friction

Generally describing the interaction between dust particles and an underlying gas flow could be complicated considering the different shapes and properties of dust. Visit Dominik and Tielens [11], Paszun, D. and Dominik, C. [33], Seizinger, A., Speith, R., and Kley, W. [37] and Wada, Koji et al. [41] for further reading. Here we can use the physical description of a particle interacting with a gas flow via a friction force to represent the interaction. In the scope of this thesis, we only consider one kind of simple friction force, which is proportional to the velocity difference of gas and dust particles, times a constant:

$$\vec{f} = -\frac{1}{\tau_s}(\vec{v} - \vec{u}) \quad (2.22)$$

where  $\tau_s$  is called the friction time parametrizing strength of the frictional coupling,  $\vec{v}$  represents the dust-particle velocity, and  $\vec{u}$  represents the velocity of the underlying gas flow. The friction time is often also called stopping time, since it resembles the time a particle needs to adjust to the underlying flow.

A picture to have in mind is throwing a ball while being underwater. If the ball is small, i.e. a tennis ball, the ball will within a few seconds lose its initial velocity due to friction with the water and instead will follow the flow of the water current. If the ball is large, i.e. a bowling ball, the ball will not be affected much by the water current and instead follow its trajectory until gravity takes over and it sinks to the ground. This Gedanken experiment can also be done in PPDs, where tiny dust particles might couple to the sub-Keplerian gas flow within a fraction of an orbital timescale, while a planetesimal will basically never adjust to the gas flow.

For the dust within a PPD the friction time in the two extreme cases of the Gedanken experiment has to be calculated differently. In the first case, the particle with mass  $m$  has a radius  $a$  smaller than the mean-free-path  $\lambda_{\text{free}}$  and the particle is in the Epstein drag regime, which is the regime where particle and gas can both be treated as particles. If the particle size is larger than the mean free path, the particle is in the Stokes

drag regime, which is the fluid regime where a large particle is embedded into the gas, described as a fluid, see Epstein [12] and Okuzumi et al. [32]. The friction times are

$$\tau_s = \begin{cases} \tau_s^{(\text{Ep})} = \frac{3m}{4\rho_g v_{\text{th}} A_p}, & \text{for } a \leq \frac{9}{4}\lambda_{\text{free}} \quad (\text{Epstein}) \\ \tau_s^{(\text{St})} = \frac{4a}{9\lambda_{\text{free}}} \cdot \tau_s^{(\text{Ep})}, & \text{for } a > \frac{9}{4}\lambda_{\text{free}} \quad (\text{Stokes}) \end{cases}$$

where  $A_p$  is the projected particle surface area, and  $v_{\text{th}} = \sqrt{8/\pi}c_s$  is the mean thermal velocity of the gas molecules. The mean-free-path in a PPD can be approximated via

$$\lambda_{\text{free}} \simeq \frac{m_g}{\sigma_{\text{mol}}\rho_g} \quad (2.23)$$

following Okuzumi et al. [32], which is valid as long as the gas particle background is not moving. With the geometrical collisional cross-section of the hydrogen gas molecules of  $\sigma_{\text{mol}} \approx 2 \cdot 10^{-15} \text{cm}^3$ , this leads to a mean-free-path of the order of meters in the mid-plane, and consequently, most of the dust particles will be in the Epstein regime. Further, assuming the particles can be described as being spherical, the stopping time in the Epstein regime can be expressed via

$$\tau_s^{(\text{Ep})} = \frac{\rho_s a}{\rho_g v_{\text{th}}} \quad (2.24)$$

where  $\rho_s$  is the internal density of a dust particle.

Typically, the stopping time is normalized by the characteristic timescale  $\frac{1}{\Omega}$ , i.e. normalized on orbital timescales. The emerging dimensionless quantity is called the Stokes number

$$\text{St} = \tau_s \Omega \quad (2.25)$$

The Stokes number will be used throughout this thesis. Note that it is defined independently of the underlying drag regime, i.e. it is a valid quantity in both, Epstein and Stokes drag regimes, or any other drag regime. Hence the Stokes number is a description of how long a particle takes to couple to the gas, in terms of orbits. The Stokes number actually can be very intuitive, if  $\tau_s \gg \Omega^{-1}$ , then  $\text{St} \gg 1$  and the particle is decoupled from the gas, i.e. not significantly affected by gas drag as its stopping time is much longer than the disk's dynamical timescale. On the other hand, if  $\tau_s \ll \Omega^{-1}$ , then  $\text{St} \ll 1$ , the particle is well coupled to the gas as its motion is strongly affected by the drag force. Particles with  $\text{St} \approx 1$  are called marginally coupled. In Chapter 4, the Stokes number of the simulation we analyzed is given as  $\text{St} = 0.01$ , which means the particles are tightly coupled to the gas.

### 2.2.2 *The streaming instability*

A second consequence of the difference in particle and gas velocities arises once inhomogeneities in the dust-to-gas ratio are considered. Define this ratio as:

$$\varepsilon = \frac{\rho_d}{\rho_g} \quad (2.26)$$

where  $\rho_d$  is the dust density. In the PPDs, the Nakagawa solution for the gas and the dust, see Nakagawa, Sekiya, and Hayashi [31], shows that a patch with a slightly higher dust concentration is less affected by the friction with the background gas, thus will drift more slowly to the central star, and dust from underdense regions can fall into this patch from the radially outward direction. This is then even further enhancing the locally higher dust concentration making this patch even drift less and would be a run-away process if not non-linearities came into play. The linear instability was first endeavored in Youdin and Goodman [44] and a simplified version of the equations can be found in Jacquet, Balbus, and Latter [19]. These authors named it the streaming instability (SI), and found it by solving the dispersion relation for this problem in  $r - z$  direction, i.e. assuming azimuthal symmetry. This instability does not require self-gravity to act. Already in pure hydrodynamical dust-gas calculations, see Youdin and Johansen [43], the instability can act quite strongly. The growth timescales of this instability are found to be faster than the radial drift timescales. Thus, Youdin and Goodman [44] suggested that the SI might be the trigger for planetesimal formation, as it can significantly concentrate dust locally, and maybe even up to values that trigger collapse, however, the latter has never been fully proven, though claims are out there, i.e. from text[39] and Johansen et al. [22]. The open question in their work is whether the collapse comes from SI alone or is assisted by stellar gravity together with extremely high dust-to-gas ratios, in Chapter 5, we will provide our own answer to this question with the new analytical method.

## 2.3 DUST EQUATION OF MOTION IN THE SHEARING SHEET APPROXIMATION

This section starts with describing one of the popular simulation methods, the shearing box coordinate system, to study planetary formation. This local frame of reference is co-moving on a Keplerian orbit, which allows to follow the gas and dust dynamics without taking care of the central star and large scale, i.e. global, disk dynamics. Furthermore, the boundary conditions of this simulation box are discussed, especially the shear periodic boundary condition in the radial direction. In the end, a detailed transformation for the dust dynamical equations to this local coordinate system is provided to help understand the nature of planetesimal formation using this particular simulation method, which also makes up the theoretical foundation for finding the proper dust trajectories in Chapter 3.

### 2.3.1 Shearing Box Approximation

In this thesis, for studying the "meter-size barrier" and the emergence of planetesimals, scales  $L \ll H$  are of interest, where  $H$  is the gas pressure scale height of Equation 2.11. These scales  $L$  are so small that a numerical computation in the form of a global disk, covering the whole PPD is not feasible. Moreover, since we are interested in investigating the local micro-physics of dust, a local approximation is needed. This is done by changing from the global Cartesian coordinate system into a local Cartesian coordinate system at a distance  $R_0$  from the central star that itself orbits around the central star with Keplerian velocity  $v_k(R_0)$ . This type of coordinate system is called shearing sheet, or shearing box coordinate system. See Figure 2.1.

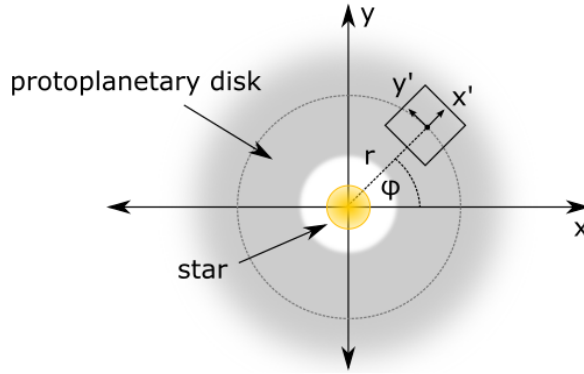


Figure 2.1: In this drawing the shearing box coordinate system is the primed system with coordinates  $x'$  and  $y'$ . It is a coordinate system that orbits around the star with the Keplerian velocity at its origin. Hence, unity vectors in  $\hat{\phi}$  transform into  $\hat{y}$  of the primed system. Consequently, the Keplerian shear has to be linearised in the shearing sheet coordinate system. In order to have the radial boundary condition periodic, we include a shear periodic boundary condition that adjusts the azimuthal velocity when surpassing the radial boundary.

### 2.3.2 Shearing Periodic Condition

In this part, we briefly discuss the boundary conditions of the shearing box simulations. In the  $y$  and  $z$  directions, we have the normal periodical boundary conditions, yet in the  $x$  direction, we adopted the shear periodic boundary condition. Figure 2.2 illustrates how the shear periodic boundary for a shearing sheet domain  $L$  works. At the initial time step  $t = t_0$  (top), the radial periodicity is similar to a classical periodic boundary condition. But, with evolving time, the linear shear moves this periodic

boundary in an azimuthal direction. The azimuthal velocity of the radially next inner domain is given via the linearised Keplerian shear velocity by [Equation 2.33](#) as

$$v_{R-\Delta r} = -\frac{3}{2}\Omega_0(-L) = \frac{3}{2}\Omega_0 L \quad (2.27)$$

In order to correct for this shearing boundary condition, a particle that leaves the radial inner boundary at an azimuthal position of  $y_{p,-L}$ , re-enters the simulation domain on the outer boundary at a position  $y_{p,+L}$ . This new azimuthal position has to be shifted by the shear offset of the radially inner box, i.e.

$$y_{p,+L} = y_{p,-L} + \text{mod}\left(\frac{3}{2}\Omega_0 L \cdot t, L\right) \quad (2.28)$$

The particle azimuthal velocity also has to change by the velocity offset from the inner to the outer boundary, which is also

$$v_{-L} = v_{+L} - \frac{3}{2}\Omega_0 L \quad (2.29)$$

Of course, the same, but with a different sign, happens to a particle that crosses the outer radial boundary.

### 2.3.3 Euler Equations

The dynamics of dust particles in a [PPD](#) are described by the momentum equation, which is an Euler equation with different terms for the individual physical processes that induce momentum:

$$\frac{d\vec{v}}{dt} + (\vec{v} \cdot \vec{\nabla})\vec{v} = -\frac{1}{\tau_s}(\vec{v} - \vec{u}) - \vec{\nabla}\Phi + \text{other forces} \quad (2.30)$$

This equation describes the change over time of the velocity field of a fluid ( $\frac{d\vec{v}}{dt}$ ): It changes due to advection  $((\vec{v} \cdot \vec{\nabla})\vec{v})$ , and other physical processes that are described on the right-hand side. These are friction with gas of velocity  $\vec{u}$  and a friction coefficient of  $\tau_s$ , and gravity  $(-\vec{\nabla}\Phi)$ . But, many other terms could enter this equation.

The goal of this part is to derive the equations of motion for such a shearing sheet coordinate system. The derivation starts from [Equation 2.30](#), but the coordinate transformations will only affect the left-hand side terms, i.e. the time derivative and the advection term. This is only partly true, since also the gravitational potential will change, as shown later in this section, since a [PPD](#) is a rotating system such that the transformation will introduce Coriolis forces.

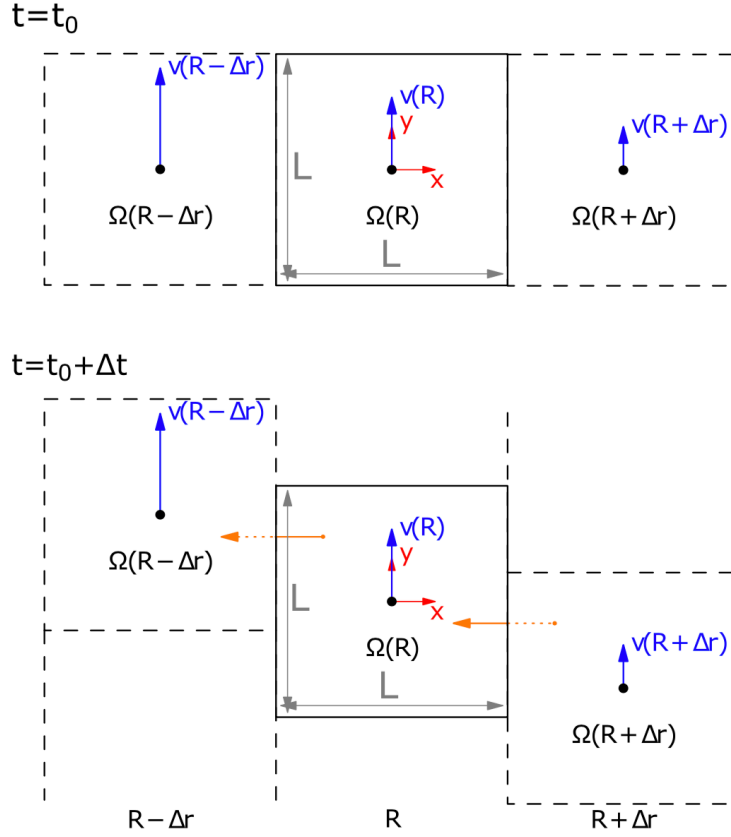


Figure 2.2: Example for the shear periodic boundary condition for a shearing box of size  $L$ . At the initial time step  $t_0$  (top), the radial periodicity is similar to a normal periodic boundary condition. But, with evolving time, the linear shear moves this periodic boundary in azimuthal direction. A particle leaving the radial inner boundary re-enters the simulation domain shifted by the shear-offset, see orange arrow, and its azimuthal velocity is shear corrected.

### *Linearising the Keplerian shear*

First, the Keplerian shear needs to be linearised around  $R_0$ . For this, a Taylor expansion of Equation 2.2 around  $R_0$  at the point  $r = R_0 + \Delta r$  can be done, which leads to

$$\Omega(r) = \Omega_0 \left( 1 - \frac{3}{2} \frac{\Delta r}{R_0} \right) \quad (2.31)$$

where  $\Omega_0 = \Omega(R_0)$ . Using the primed radial coordinate,  $\Delta r$  becomes  $x'$ , and the orbital velocity attains its linearised form:

$$v = \Omega_0 \left(1 - \frac{3}{2} \frac{x'}{R_0}\right) R_0 = \Omega_0 R_0 - \frac{3}{2} \Omega_0 x' \quad (2.32)$$

Thus, the linearised Keplerian shear velocity is approximated in the co-rotation frame as

$$v_{\text{shear}} = -\frac{3}{2} \Omega_0 x' \quad (2.33)$$

*Transforming the advection term into the shearing sheet coordinate system*

Here we start with the advection term as this is easier to transform. In the following the Einstein index notation is used, where there is an unwritten but existing sum over all indices that appear twice. Hence,  $(\vec{v} \cdot \vec{\nabla})\vec{v} = v_i \partial_i v_j$ . This is getting transformed into the primed Cartesian coordinate system via

$$\vec{v} \rightarrow \vec{v}' + \vec{v}_0' = \vec{v}' - \frac{3}{2} \Omega_0 x' \hat{y}' \quad (2.34)$$

where  $\vec{\nabla}' \equiv \vec{\nabla}$  since  $x' \ll R_0$  and  $y' \ll R_0$ . Thus, the advection term becomes

$$v_i \partial_i v_j = [(\vec{v}' + \vec{v}_0') \cdot \vec{\nabla}'](\vec{v}' + \vec{v}_0') = [(\vec{v}' + \vec{v}_0') \cdot \vec{\nabla}']\vec{v}' + [(\vec{v}' + \vec{v}_0') \cdot \vec{\nabla}']\vec{v}_0' \quad (2.35)$$

with

$$[(\vec{v}' + \vec{v}_0') \cdot \vec{\nabla}']\vec{v}' = (v_i + v_{0i}) \partial_i v_j = v_i \partial_i v_j + v_{0i} \partial_i v_j = (\vec{v}' \cdot \vec{\nabla}')\vec{v}' + v'_{0y} \frac{\partial \vec{v}'}{\partial y'} \quad (2.36)$$

$$[(\vec{v}' + \vec{v}_0') \cdot \vec{\nabla}']\vec{v}_0' = (v_i + v_{0i} \delta_{iy}) \partial_i v_{0y} = (-\frac{3}{2} \Omega_0 v'_x) \hat{y}' \quad (2.37)$$

Reassembling both terms, the advection term from [Equation 2.30](#) becomes:

$$(\vec{v} \cdot \vec{\nabla})\vec{v} = (\vec{v}' \cdot \vec{\nabla}')\vec{v}' + v'_{0y} \frac{\partial \vec{v}'}{\partial y'} + (-\frac{3}{2} \Omega_0 v'_x) \hat{y}' \quad (2.38)$$

*Transforming velocity time derivative into the shearing sheet coordinate system*

In order to rewrite the velocity time derivative term of the momentum equation, we need to express  $\frac{d\vec{v}}{dt}$  in cylindrical coordinates. In contrast to the Nabla operator, now the time derivative of the velocity field introduces on one hand the shear advection and on the other hand the Coriolis forces. In cylindrical coordinates, we have:

$$\frac{d\vec{v}}{dt} = \frac{d}{dt}(\dot{r}\hat{r} + r\dot{\phi}\hat{\phi} + \dot{z}\hat{z}) = \ddot{r}\hat{r} + \dot{r}\dot{\phi}\hat{\phi} + \dot{r}\dot{\phi}\hat{\phi} + r\ddot{\phi}\hat{\phi} - r\dot{\phi}^2\hat{r} + \ddot{z}\hat{z} \quad (2.39)$$

Then velocity time derivative term becomes:

$$\begin{aligned} \frac{d\vec{v}}{dt} &= (\ddot{r}\hat{r} + r\ddot{\phi}\hat{\phi} + \ddot{z}\hat{z}) + 2\dot{r}\dot{\phi}\hat{\phi} - r\dot{\phi}^2\hat{r} \\ &= \frac{\partial\vec{v}}{\partial t} + \Delta \end{aligned} \quad (2.40)$$

Where  $\Delta = 2\dot{r}\dot{\phi}\hat{\phi} - r\dot{\phi}^2\hat{r}$ . Now we have to transform  $\Delta$  into the primed coordinate system via

$$x' = r - R_0, \quad y' = R_0(\phi - \phi_0 - \Omega_0 t), \quad z' = z, \quad t' = t. \quad (2.41)$$

Using this transformation, we get the following table that translates the expressions within  $\Delta$ :

$$\begin{array}{ll} \hat{r} = \hat{x}' & \hat{\phi} = \hat{y}' \\ r = R_0 + x' & \phi = \frac{y'}{R_0} + \phi_0 + \Omega_0 t \\ \dot{r} = \dot{x}' = v'_x & \dot{\phi} = \frac{\dot{y}'}{R_0} + \Omega_0 = \frac{1}{R_0}v'_y + \Omega_0 \end{array}$$

Hence the  $\Delta$  term becomes:

$$\begin{aligned} \Delta &= 2v'_x \left( \frac{1}{R_0}v'_y + \Omega_0 \right) \hat{y}' - (R_0 + x') \left( \frac{1}{R_0}v'_y + \Omega_0 \right)^2 \hat{x}' \\ &= 2\Omega_0 v'_x \hat{y}' - \Omega_0^2 R_0 \hat{x}' - 2\Omega_0 v'_y \hat{x}' \end{aligned} \quad (2.42)$$

Here to get the final result in [Equation 2.42](#), we neglect the terms with  $x'$  and  $v'_i v'_j$ .

#### *Transformed momentum equation*

Now we put everything together, and rename the primed system to unprimed. The momentum equation becomes

$$\frac{\partial\vec{v}}{\partial t} + (\vec{v} \cdot \vec{\nabla})\vec{v} + v_{0y} \frac{\partial\vec{v}}{\partial y} - \vec{f}(\vec{v}) - \Omega_0^2 R_0 \hat{x} = -\frac{1}{\tau_s}(\vec{v} - \vec{u}) - \vec{\nabla}\Phi + \dots \quad (2.43)$$

where  $\vec{f}(\vec{v})$  is the Coriolis forces:

$$\vec{f}(\vec{v}) = \begin{pmatrix} 2\Omega_0 v_y \\ -\frac{1}{2}\Omega_0 v_x \\ 0 \end{pmatrix} \quad (2.44)$$

Here we cancel  $\Omega_0^2 R_0$  with part of the gravitation force in  $-\vec{\nabla}\Phi$  and get the final momentum equation of the fluid in the shearing sheet coordinate system as:

$$\frac{\partial \vec{v}}{\partial t} + (\vec{v} \cdot \vec{\nabla})\vec{v} + v_{0y} \frac{\partial \vec{v}}{\partial y} - \vec{f}(\vec{v}) = -\frac{1}{\tau_s}(\vec{v} - \vec{u}) - \vec{\nabla}\Phi + \dots \quad \text{with} \quad v_{0y} = -\frac{3}{2}\Omega_0 x \quad (2.45)$$

where  $\Phi$  now is the change in the gravitational potential from the potential of the central star.

#### 2.4 HILL STABILITY OF A PARTICLE CLOUD

In the following section, the stability of self-gravitating particle clouds in PPDs is analytically investigated. There are two canonically used instability criteria, the Roche stability, and the Hill stability criterion. The first was calculated in the 19th century by Edouard Roche, who investigated the stability of loosely bound material in the vicinity of larger bodies, such as the breakup of comets close to the Sun. Based on his work, George William Hill calculated the dynamical stability of a test mass around a smaller body in a rotating frame. This is typically interpreted as a spherical volume around a minor body, e.g. around Earth, in which a small body, e.g. the Moon, stays bound to it. Being outside of this sphere of influence, the gravitational attraction onto the small body is dominated by a major body, i.e. the Sun. Points on the surface of this sphere show little net acceleration forces. Both criteria state that stability is granted as long as mutual gravitational interaction within a particle cloud is stronger than the gravitational gradient, exerted by a larger mass outside of the body of interest, which is in our case a particle cloud. The Hill stability differs from the Roche criterion by demanding an orbital motion of the particle cloud around a central mass. The additional centrifugal force induced thereby further stabilizes the particle cloud by reducing the gravitational gradient across the cloud. In this thesis, we are more interested in the Hill stability criterion since we will be dealing with simulation data from a local shearing box, thus in the following, we present the derivation of its dynamic equations in detail.

The Hill stability criterion is a dynamical criterion not based on perturbation theory, but on force equilibrium, see Figure 2.3. The Hill sphere is a ‘zero-acceleration’ spherical surface on which a rigidly bound test mass  $\mu$  will not get accelerated. Rigidly bound means the centrifugal forces of  $m$  and  $\mu$  are set to be equal. One can write that centrifugal forces on  $m$  are in equilibrium with the gravitational pull from  $M$ :

$$m\Omega_m^2 D = \frac{G_0 M m}{D^2} \quad \rightarrow \quad \Omega_m = \frac{G_0 M}{D^3} \approx \Omega_\mu \quad (2.46)$$

with  $G_0$  being the gravitational constant. The forces acting on  $\mu$  satisfy

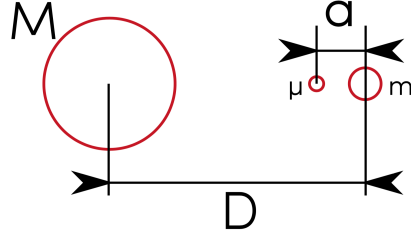


Figure 2.3: The Hill criterion is a criterion for internal stability. It looks for the boundedness of a test mass  $\mu$  to a smaller mass  $m$ , in the vicinity of a larger mass  $M$ . The Hill analysis assumes the smaller mass to orbit around the larger mass. The Hill analysis leads to a Hill sphere, which is the sphere of zero acceleration around the mass  $m$ . Everything inside this sphere is bound, under the assumption of not having escape velocity or other perturbations occurring.

$$\begin{aligned}
 0 &= \sum_i F_i = -F_M + F_m + F_c \\
 &= -\frac{GM\mu}{(D-a)^2} + \frac{Gm\mu}{a^2} + \mu\Omega_\mu^2(D-a) \\
 &= -1 + \frac{(D-a)^2}{a^2} \frac{m}{M} + \frac{(D-a)^3}{D^3}
 \end{aligned} \tag{2.47}$$

In the limit of  $D \gg a$ , the above equation becomes

$$\frac{3a^3}{D^3} = \frac{m}{M} \tag{2.48}$$

Solving for the minimal stable distance of the  $\mu - m$ -system to  $M$  gives

$$D_{\text{crit}} = a \left( \frac{3M}{m} \right)^{\frac{1}{3}} \tag{2.49}$$

For the critical density of a particle cloud, we assume  $m$  to be the center mass of the cloud, i. e. a sphere of particles with  $m = \rho \frac{4}{3} \pi a^3$ . The critical density of the particle cloud  $m$  is then

$$\rho_H = \frac{m}{\frac{4}{3} \pi a^3} = \frac{9}{4\pi} \frac{M}{D^3} \tag{2.50}$$

This density of a particle sphere can now be used as a first approximation for the stability of the system. It is derived in a 1 - d case and clearly some effects are missing, such as friction with the underlying gas disk. But still, we consider this approximation to be sufficient within this work.

## 2.5 SUMMARY AND DISCUSSION

Planetary formation has been puzzling us together with the question of where we are from since day one. In this Chapter, we reviewed the basic gas and dust dynamics in the protoplanetary disk (PPD) related to this work, and realized that the distinguishing feature of gas that dust particles are lacking, i.e. an internal pressure, plays an essential role in initiating the planetesimal formation through the friction interaction and streaming instability (SI) between the two systems. Furthermore, the Hill stability criterion for self-gravitating particle clouds has been investigated in detail. The resulting gravitational instability of a PPD from surpassing the local Hill density provides another important source for planetesimal formation.

One key point to recognize is that the process of planet formation is highly nonlinear. Therefore it is rather difficult to develop any perturbation and linear theories to thoroughly study the problem as in lots of other areas. For example, in cosmology, the cosmological principle of the universe being homogeneous and isotropic allows us to use linear theory to quantify the growth of density perturbations on large scales. This has been very successful and provides some critical insights even until today.

Still, there are considerably different analytical theories have been developed to understand this problem, for example, predicting the behavior of the small-scale grain–grain correlation function using simple models of Gaussian random-field turbulence, see Sigurgeirsson and Stuart [38], and predicting quantities such as the grain density distribution, the density fluctuation power spectrum, maximum grain densities, and correlation functions, as a function of grain stopping/friction time, grain-to-gas volume density ratio, and properties of the turbulence using grain clustering models in turbulence, see Hopkins [18]. However, they either estimate much smaller fluctuations or mostly focus on the inertial-range turbulence, with large Reynolds numbers and Stokes numbers. Rigorous analytical descriptions of how the nonlinear power spectra emerge for different sizes of particles and particularly their small-scale analysis are still missing.

Another more direct and popular approach to this problem has been through different schemes of simulation methods, one of which has been reviewed in this Chapter. Admittedly, there have been plenty of great successes in this area, yet the issues with simulations such as limited resolution, the formation of spurious features, the implementation of initial conditions, or the limited box size, get in the way, let alone the time and energy consumption, especially when one wishes to repeat the simulation for different parameters.

Therefore, in this work, we make use of a recently-developed analytical approach to study planetary structure formation, which circumvents the aforementioned problems: kinetic field theory (KFT) is an analytical approach to structure formation that operates in the particle picture. The dynamics of the particles' phase space trajectories

are governed by their equation of motion in  $6N$ -dimensional phase space. In the next chapter, we review the most important aspects of [KFT](#), relevant to this work.



kinetic field theory (KFT) is a statistical field theory for ensembles of classical particles in or out of equilibrium. The central object in KFT is the generating functional  $Z$ . Similar to the partition function in classical thermodynamics, it contains all information about the probability distribution  $P(\phi)$  of system states  $\phi$

$$Z = \int \mathcal{D}\phi P(\phi). \quad (3.1)$$

In general, the system states  $\phi$  are continuous fields of time, which requires the use of a path integral. In this chapter, we review the foundations of KFT for planetary structure formation. Since KFT became a very diverse theory with various formulations and applications in cosmology, astrophysics and beyond, we restrict this review to those results that are relevant to this work. We recommend the recent review on KFT by Bartelmann et al. [6] to the interested reader.

In the first section, we introduce the tensor notation that is used throughout this work. In the second section, we derive the generating functional  $Z$  for  $N$  particles and compare it with the canonical partition function in equilibrium statistical physics to help understand how classical mechanics can be formulated with path integrals. In the third section, inspired by the equation of motion for dust particles in the shearing box approximation by Equation 2.45, we specify the dust dynamics appropriate for planetary structure formation in KFT by considering only friction interaction with an averaged background gas field and gravitational interactions between dust particles. In the end, we introduce the density and momentum operators which provide the most powerful tools for studying structure formation in Chapter 5 and Chapter 6.

### 3.1 NOTATIONS

We consider a set of  $N$  point particles in the classical  $6N$  dimensional phase space  $\Gamma$ . The trajectory of each particle  $1 \leq j \leq N$  in phase space is the tuple of position  $\vec{q}_j$  and momentum  $\vec{p}_j$  which we denote

$$x_j := \begin{pmatrix} \vec{q}_j \\ \vec{p}_j \end{pmatrix}. \quad (3.2)$$

Note that the following notations are equivalent  $\vec{q}_j \equiv \vec{x}_{q_j}$ ,  $\vec{p}_j \equiv \vec{x}_{p_j}$ .

To compactify notation, we collect the trajectories of all particles in the tensorial object

$$\mathbf{x} := x_j \otimes \mathbf{e}_j, \quad (3.3)$$

where summation over  $j$  is implied, and  $\mathbf{e}_j \in \mathbb{R}^N$  with  $(\mathbf{e}_j)_i = \delta_{ij}$ ,  $1 \leq j \leq N$ . Furthermore, when we consider the collection of all particle positions or momenta separately, we write

$$\begin{aligned} \mathbf{x}_q &:= \vec{q}_j \otimes \mathbf{e}_j \\ \mathbf{x}_p &:= \vec{p}_j \otimes \mathbf{e}_j \end{aligned} \quad (3.4)$$

respectively. Unless otherwise stated, we use bold letters without index (e. g.  $\mathbf{J}$ ,  $\mathbf{x}$ ) to denote  $6N$ -dimensional tensors. We can split these vectors into the  $3N$  dimensional position component (e. g.  $\mathbf{J}_q$ ,  $\mathbf{x}_q$ ) and a  $3N$ -dimensional momentum component (e. g.  $\mathbf{J}_p$ ,  $\mathbf{x}_p$ ). When we use the same letter non-bold with an integer index (e. g.  $J_j$ ,  $x_j$ ), we mean the 6-dimensional phase space tuple of one specific particle. In order to indicate the 3-dimensional position/momentum component of an individual particle, we use non-bold symbols with vector arrow, position/momentum label and integer particle index (e. g.  $\vec{J}_{q_j}$ ,  $\vec{J}_{p_j}$ ,  $\vec{x}_{q_j}$ ,  $\vec{x}_{p_j}$ ).

With these conventions, any bold tensor  $\mathbf{J}$  can be written as

$$\mathbf{J} = \begin{pmatrix} \vec{J}_{q_j} \\ \vec{J}_{p_j} \end{pmatrix} \otimes \mathbf{e}_j. \quad (3.5)$$

We introduce the scalar product

$$\langle \mathbf{J}, \mathbf{x} \rangle := (J_j \otimes \mathbf{e}_j) \cdot (x_i \otimes \mathbf{e}_i) = J_j \cdot x_j \equiv \langle \mathbf{J}_q, \mathbf{x}_q \rangle + \langle \mathbf{J}_p, \mathbf{x}_p \rangle, \quad (3.6)$$

and define the symplectic two-form

$$\mathcal{J} := \begin{pmatrix} 0 & \mathbb{I}_3 \\ -\mathbb{I}_3 & 0 \end{pmatrix} \otimes \mathbb{I}_N. \quad (3.7)$$

We define the gradient with respect to the phase space coordinates of all particles

$$\nabla_{\mathbf{x}} := \begin{pmatrix} \vec{\nabla}_{q_j} \\ \vec{\nabla}_{p_j} \end{pmatrix} \otimes \mathbf{e}_j, \quad (3.8)$$

such that the application to any scalar function  $f$  of the particles' phase space coordinates can be written as

$$\nabla_{\mathbf{x}} f(\mathbf{x}) = \sum_{j=1}^N \begin{pmatrix} \frac{\partial}{\partial q_{j,x}} \\ \frac{\partial}{\partial q_{j,y}} \\ \frac{\partial}{\partial q_{j,z}} \end{pmatrix} f(\mathbf{x}) + \sum_{j=1}^N \begin{pmatrix} \frac{\partial}{\partial p_{j,x}} \\ \frac{\partial}{\partial p_{j,y}} \\ \frac{\partial}{\partial p_{j,z}} \end{pmatrix} f(\mathbf{x}). \quad (3.9)$$

To write equations more compactly, we introduce the following notation for integrals over  $\mathbf{q}$  in real space and over  $\mathbf{k}$  in Fourier space, respectively,

$$\int_{\mathbf{q}} = \int_{\mathbb{R}^3} d^3 \mathbf{q}, \quad \int_{\mathbf{k}} = \int_{\mathbb{R}^3} \frac{d^3 \mathbf{k}}{(2\pi)^3}. \quad (3.10)$$

## 3.2 GENERATING FUNCTIONAL

A path-integral formulation for classical Hamiltonian dynamics of a particle ensemble called kinetic field theory (KFT) was developed and applied to cosmic structure formation in Bartelmann et al. [4], Bartelmann et al. [5] and [6]. In this section, we review the foundations of KFT which are essential to this work, and show that the central object, the generating functional, is completely determined by the equation of motion of particle ensembles and their initial probability distribution function in phase space (iPDF). In the end, a comparison with equilibrium statistical physics is given to help understand the concepts of this theory.

### 3.2.1 The Generating Functional

For classical (canonical) ensembles consisting of  $N$  point particles, the system states  $\phi$  are described by the trajectories  $\mathbf{x}$  in the classical  $6N$ -dimensional phase space  $\Gamma$ , as defined in Equation 3.3. The generating functional defined in Equation 3.1 then turns into

$$Z = \int \mathcal{D}\mathbf{x} P(\mathbf{x}). \quad (3.11)$$

Note that  $P(\mathbf{x})$  is the probability distribution for trajectories in classical phase space, and not the probability distribution to find the system in a specific configuration at a given time. We further split the probability  $P(\mathbf{x})$  for the state  $\mathbf{x}$  to be occupied into a probability  $P(\mathbf{x}^{(i)})$  for the particle ensemble to occupy an initial state  $\mathbf{x}^{(i)}$  (iPDF) at time

$t = 0$ , times the conditional probability  $P(\mathbf{x}|\mathbf{x}^{(i)})$  for the ensemble to move from there to the time-evolved state  $\mathbf{x}$ ,

$$P(\mathbf{x}) = \int d\mathbf{x}^{(i)} P(\mathbf{x}|\mathbf{x}^{(i)}) P(\mathbf{x}^{(i)}) . \quad (3.12)$$

For particles on classical trajectories, the transition probability  $P(\mathbf{x}|\mathbf{x}^{(i)})$  must be a functional delta distribution of the classical particle trajectories,

$$P(\mathbf{x}|\mathbf{x}^{(i)}) = \delta_D[\mathbf{x} - \mathbf{x}_{cl}(\mathbf{x}^{(i)})] , \quad (3.13)$$

where  $\mathbf{x}_{cl}(\mathbf{x}^{(i)})$  denotes the formal solution to the equation of motion of the entire particle ensemble on phase space, with the specified initial phase-space conditions  $\mathbf{x}^{(i)}$ , as illustrated in [Figure 3.1](#).

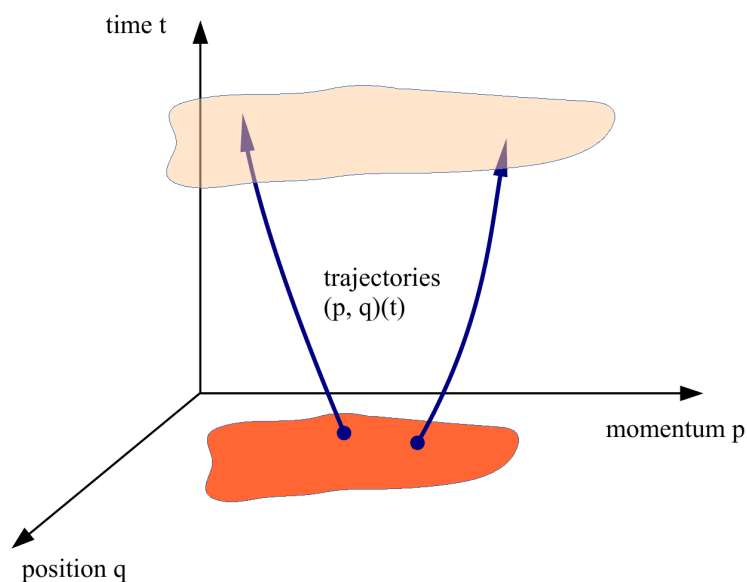


Figure 3.1: Illustration of the main idea of KFT. An initial probability distribution on the phase space is mapped to any later time by classical particle trajectories. Since phase-space trajectories do not cross, this approach avoids the notorious shell-crossing problem by construction.

In classical phase space, trajectories do not cross and are uniquely constrained by the initial conditions because they follow the Hamiltonian flow. Here we write the equation of motion in a more general form as

$$E(\mathbf{x}) = \dot{\mathbf{x}} - \mathbf{f}(\mathbf{x}) = 0 \quad (3.14)$$

where  $\mathbf{f}(\mathbf{x})$  encodes all physical processes that change the particle dynamics in it, which are *not* necessarily Hamiltonian. The functional Dirac delta distribution can be written in terms of the equation of motion as

$$\delta_D [\mathbf{x} - \mathbf{x}_{cl}(\mathbf{x}^{(i)})] = \delta_D [\dot{\mathbf{x}} - \mathbf{f}(\mathbf{x})] \det [\partial_t \delta_b^a - \partial_b f^a] \quad (3.15)$$

where the determinant cannot be taken to be equal to unity as in Liouville's theorem anymore. Thus we preserve the expression for the determinant and write the generating functional in [Equation 3.11](#) in terms of the equation of motion,

$$\begin{aligned} Z &= \int \mathcal{D}\mathbf{x} \int d\mathbf{x}^{(i)} P(\mathbf{x}^{(i)}) \det [\partial_t \delta_b^a - \partial_b f^a] \delta_D [\dot{\mathbf{x}} - \mathbf{f}(\mathbf{x})] \\ &= \int \mathcal{D}\mathbf{x} \int d\mathbf{x}^{(i)} P(\mathbf{x}^{(i)}) \det [\partial_t \delta_b^a - \partial_b f^a] \int \mathcal{D}\chi \exp \left[ i \int_0^\infty dt (\langle \chi, \dot{\mathbf{x}} - \mathbf{f}(\mathbf{x}) \rangle) \right] \end{aligned} \quad (3.16)$$

In the last step, the Dirac delta distribution is expressed as a functional Fourier integral with respect to an auxiliary field  $\chi$ .

In order to generate moments of phase space coordinates from the generating functional, we introduce two source fields, which are conjugate to the phase space trajectories  $\mathbf{x}(t)$  and the auxiliary field  $\chi$ ,

$$\mathbf{J} := \begin{pmatrix} \vec{J}_{q_j} \\ \vec{J}_{p_j} \end{pmatrix} \otimes e_j \quad \text{and} \quad \mathbf{K} := \begin{pmatrix} \vec{K}_{q_j} \\ \vec{K}_{p_j} \end{pmatrix} \otimes e_j \quad (3.17)$$

and turn the generating functional into the expression

$$Z[\mathbf{J}, \mathbf{K}] = \int \mathcal{D}\mathbf{x} \int d\mathbf{x}^{(i)} P(\mathbf{x}^{(i)}) \det [\partial_t \delta_b^a - \partial_b f^a] \int \mathcal{D}\chi \exp \left[ i \int_0^\infty dt (\langle \chi, \dot{\mathbf{x}} - \mathbf{f}(\mathbf{x}) \rangle + \langle \mathbf{J}, \mathbf{x} \rangle + \langle \mathbf{K}, \chi \rangle) \right] \quad (3.18)$$

On the other hand, if we are able to analytically solve the equation of motion for the particle ensemble beginning at  $\mathbf{x}^{(i)}$  and denote the solution as  $\bar{\mathbf{x}}(t)$ , the generating functional in [Equation 3.16](#) becomes

$$Z = \int \mathcal{D}\mathbf{x} \int d\mathbf{x}^{(i)} P(\mathbf{x}^{(i)}) \delta_D [\mathbf{x} - \bar{\mathbf{x}}(t)] \quad (3.19)$$

Now we still introduce the conjugate generator field  $\mathbf{J}$  and get a simpler expression for the generating functional as

$$\begin{aligned}
Z[\mathbf{J}] &= \int \mathcal{D}\mathbf{x} \int d\mathbf{x}^{(i)} \mathcal{P}(\mathbf{x}^{(i)}) \delta_{\mathbb{D}}[\mathbf{x} - \bar{\mathbf{x}}(t)] \exp \left[ i \int_0^\infty dt \langle \mathbf{J}, \mathbf{x} \rangle \right] \\
&= \int d\Gamma \exp \left[ i \int_0^\infty dt \langle \mathbf{J}, \bar{\mathbf{x}}(t) \rangle \right]
\end{aligned} \tag{3.20}$$

where we have introduced the initial phase-space measure

$$d\Gamma := d\mathbf{x}^{(i)} \mathcal{P}(\mathbf{x}^{(i)}) . \tag{3.21}$$

### 3.2.2 Similarities to Equilibrium Statistical Physics

Conceptually, **KFT** is largely different from equilibrium statistical physics, because the former describes a system that may be far from equilibrium.

In equilibrium thermodynamics, the partition sum  $Z$  contains all macroscopic information on a particle ensemble. Taking derivatives of  $Z$ , expectation values for macroscopic state variables can be retrieved. For example, the (negative) derivative of  $Z$  with respect to the inverse temperature  $\beta$  returns the mean internal energy  $U$ , and the derivative of  $Z$  with respect to the chemical potential  $\mu$  returns the mean particle number  $\langle N \rangle$  in a grand-canonical ensemble.

The kinetic field theory (**KFT**) proceeds in an analogous way: it is based on an equivalent to the partition sum for a classical particle ensemble, from which macroscopic, statistical information is retrieved via derivatives. There is one important extension, though: Since **KFT** is a theory for systems possibly out of equilibrium, its equivalent to the partition sum needs to depend on time. It therefore needs to be a functional of ensemble properties, which are themselves functions of time. For this reason,  $Z$  is called a generating functional in **KFT**. Likewise, derivatives need to return functions rather than numbers, and therefore need to be functional derivatives. In **KFT**, time-dependent, macroscopic, statistical information on classical particle ensembles is thus obtained by taking functional derivatives of the generating functional  $Z$ , conceptually similar to thermodynamics.

In equilibrium thermodynamics, the partition sum is an integral over a probability distribution for microstates. In **KFT**, the generating functional is an integral over the probability with which phase-space positions at any time  $t$  will be reached by particles. This probability is determined by the probability for an initial phase-space position to be occupied by a particle, times the conditional transition probability for this particle from its initial to a later phase-space position.

Any initial position in phase space is the starting point of a classical particle trajectory, which solves the equation of motion with the initial phase-space point taken as initial condition. For classical particles, the transition probability from initial to final states takes the form of a (functional) Dirac delta distribution: it vanishes almost

everywhere, except along the actual particle trajectory. This is the main difference to quantum mechanics or quantum field theory, where the transition probability is a path integral over a phase factor containing the action functional.

The canonical partition function  $Z$  and the generating functional  $Z[\mathbf{J}]$  ensure the formal analogy between statistical physics and KFT. Although one describes an equilibrium and the other a non-equilibrium system both contain the initial phase space distribution and the dynamics of the microscopic degrees of freedom. Macroscopic quantities are calculated from partial derivatives of the partition function or the generating functional.

### 3.3 SIMPLIFIED DUST PARTICLE TRAJECTORIES

In the last section, we reviewed how classical mechanics can generally be formulated in the path integral formalism, and come to understand that the equation of motion for particle ensembles plays an essential role in the generating functional. In this section, first we show the difficulties of finding the generating functional  $Z[\mathbf{J}, \mathbf{K}]$  in Equation 3.18 using the full equation of motion for dust particles in the shearing box approximation by Equation 2.45, then review how simplified and more ideal dust particle trajectories are specified by reducing the interactions considered strictly to only friction and gravity.

#### 3.3.1 Complications with the Full Equation of Motion

For one dust particle, if we set its mass to unity, we can describe its dynamics by borrowing the equation of motion from Equation 2.45 and rewrite it in phase space as

$$\begin{aligned} \partial_t \vec{q} &= \vec{p} \\ \partial_t \vec{p} &= -\frac{1}{\tau_s} \vec{p} + f(\vec{p}) + \frac{3}{2} \Omega_0 q_x \frac{\partial \vec{p}}{\partial q_y} - (\vec{p} \cdot \vec{\nabla}_q) \vec{p} + \left( \frac{\vec{u}}{\tau_s} - \vec{\nabla}_q \Phi \right), \end{aligned} \quad (3.22)$$

thus its trajectory  $x$  in phase space satisfies

$$\partial_t x - J^1 x - \frac{1}{2} (x^T J^2) x - K_1 = 0 \quad (3.23)$$

where

$$J^1 = \begin{pmatrix} 0 & & & \\ & \mathbb{I}_3 & & \\ 0 & \left(-\frac{1}{\tau_s} + \frac{3}{2} \Omega_0 q_x \frac{\partial}{\partial q_y}\right) \mathbb{I}_3 & + J_4^1 & \end{pmatrix} \quad \text{with} \quad J_4^1 = \begin{pmatrix} 0 & 2\Omega_0 & 0 \\ -\frac{1}{2}\Omega_0 & 0 & 0 \\ 0 & 0 & 0 \end{pmatrix}, \quad (3.24)$$

$$J^2 = \begin{pmatrix} 0 \\ -2\vec{\nabla}_q \end{pmatrix}, \quad \text{and} \quad K_1 = \begin{pmatrix} 0 \\ \frac{\vec{u}}{\tau_s} - \vec{\nabla}_q \Phi \end{pmatrix}. \quad (3.25)$$

Note that here <sup>1</sup> and <sup>2</sup> are superscripts, not exponents. There are various difficulties when plugging [Equation 3.23](#) in the generating functional  $Z[\mathbf{J}, \mathbf{K}]$  in [Equation 3.18](#), one of which lies in finding the determinant of matrix  $[\partial_t \delta_b^a - \partial_b f^a]$  where in this case  $f^a = J^{1ac} \chi_c + \frac{1}{2} \chi_c J^{2c} \chi^a + K_1^a$ . Furthermore, [Equation 3.23](#) shows non-linearly dependence of particle trajectory  $\chi$ , meaning that the determinant will be a function of  $\chi$  and its derivatives, instead of unity or any other constants. This extra function would make the integral in the generating function too difficult to proceed with. More fundamentally, it could cause the resulting phase space trajectories to intersect. Therefore, it's more feasible and appropriate to modify the equation of motion for dust particles slightly and preserve the most essential interactions and plug it in [KFT](#).

### 3.3.2 Dust Particles Trajectory

To simplify the equation of motion for dust particles, first, we omit the advection term  $(\vec{p} \cdot \vec{\nabla}_q) \vec{p}$  in [Equation 3.22](#) which brings the nonlinearity  $-\frac{1}{2} (\chi^T J)^2 \chi$  to [Equation 3.23](#), then to retain the overall isotropic feature of the system, we leave out both the Coriolis force  $f(\vec{p})$  and the Keplerian shear term  $\frac{3}{2} \Omega_0 q_x \frac{\partial \vec{p}}{\partial q_y}$ , which is caused by the coordinate transformation. In the end, for one dust particle, keeping the friction interaction with the gas and the gravitational interaction with each other, we can write its equation of motion in phase space as

$$\partial_t \chi - \mathcal{J}^1 \chi - K_1 = 0 \quad (3.26)$$

with the new  $\mathcal{J}^1$  being

$$\mathcal{J}^1 = \begin{pmatrix} 0 & \mathbb{I}_3 \\ 0 & -\frac{1}{\tau_s} \mathbb{I}_3 \end{pmatrix} \quad (3.27)$$

and  $K_1$  stays the same as in [Equation 3.25](#).

Since  $\mathcal{J}^1$  now becomes a constant matrix, we realize the analytical expression for dust particle trajectory can be easily calculated and we can plug the N-particle result into the simpler expression of generating functional  $Z[\mathbf{J}]$  in [Equation 3.20](#). In order to solve [Equation 3.26](#), first we have to find its homogeneous solution,

$$\partial_t \chi - \mathcal{J}^1 \chi = 0 \quad (3.28)$$

The solution of Equation 3.28 is:

$$x = \exp\left(\int_0^t \mathcal{J}^1 d\bar{t}\right) x_0 \quad (3.29)$$

where  $x_0$  is the integral constant. When we add the inhomogeneous term on the right hand of the equation, we need the variation of constants to get the solution, setting:

$$x = \exp\left(\int_0^t \mathcal{J}^1 d\bar{t}\right) x_0(t) \quad (3.30)$$

We insert this into Equation 3.26,

$$\exp\left(\int_0^t \mathcal{J}^1 d\bar{t}\right) \partial_t x_0 + \mathcal{J}^1 x_0 \exp\left(\int_0^t \mathcal{J}^1 d\bar{t}\right) - \mathcal{J}^1 x = K_1(t) \quad (3.31)$$

which leads to:

$$x_0(t) = x^{(i)} + \int_0^t \exp\left(-\int_0^{t'} \mathcal{J}^1 d\bar{t}\right) K_1(t') dt' \quad (3.32)$$

where  $x^{(i)}$  is an integral constant representing the initial dust particle coordinates in phase space. Combining Equation 3.29 and Equation 3.32, we have the solution for one dust particle trajectory in phase space  $x$  as:

$$x(t) = \exp\left(\int_0^t \mathcal{J}^1 dt'\right) x^{(i)} + \int_0^t \exp\left(\int_{t'}^t \mathcal{J}^1 d\bar{t}\right) K_1(t') dt' \quad (t > t') \quad (3.33)$$

By the definition of the Green's function, we can read off the Green's function  $G$  of the differential Equation 3.26 as:

$$G(t, t') = \exp\left(\int_{t'}^t \mathcal{J}^1 d\bar{t}\right) = \exp(\mathcal{J}^1(t - t')), \quad (3.34)$$

then we perform a Taylor expansion in order to obtain the Green's function in matrix form,

$$\exp(\mathcal{J}^1(t - t')) = \sum_{i=0}^{\infty} \frac{(\mathcal{J}^1(t - t'))^i}{i!}, \quad (3.35)$$

for matrix  $\mathcal{J}^1$ , we find that  $i$ -th power is related to itself by:

$$(\mathcal{J}^1)^i = \mathcal{J}^1 \cdot \left(-\frac{1}{\tau_s}\right)^{i-1}, \quad (3.36)$$

thus the power series in [Equation 3.35](#) becomes:

$$\begin{aligned} \sum_{i=0}^{\infty} \frac{(\mathcal{J}^1(t-t'))^i}{i!} &= \mathbb{I}_6 + \sum_{i=1}^{\infty} \frac{\mathcal{J}^1 \left(-\frac{1}{\tau_s}\right)^{i-1} (t-t')^i}{i!} \\ &= \mathbb{I}_6 - \mathcal{J}^1 \tau_s \left( \sum_{i=0}^{\infty} \frac{\left(-\frac{t-t'}{\tau_s}\right)^i}{i!} - 1 \right) \\ &= \mathbb{I}_6 + \mathcal{J}^1 \tau_s \left( 1 - \exp\left(-\frac{t-t'}{\tau_s}\right) \right). \end{aligned} \quad (3.37)$$

This result leads to the final expression of the Green's function in matrix form as:

$$\mathbf{G}(t, t') = \begin{pmatrix} \mathbb{I}_3 & \tau_s \left(1 - e^{-\frac{t-t'}{\tau_s}}\right) \mathbb{I}_3 \\ 0 & e^{-\frac{t-t'}{\tau_s}} \mathbb{I}_3 \end{pmatrix} \quad (3.38)$$

With component functions

$$\begin{aligned} g_{qq}(t, t') &= 1, \\ g_{qp}(t, t') &= \tau_s \left(1 - e^{-\frac{t-t'}{\tau_s}}\right), \\ g_{pp}(t, t') &= e^{-\frac{t-t'}{\tau_s}}. \end{aligned} \quad (3.39)$$

For simplicity, we abbreviate  $g_{qp}(t, 0) := g_{qp}(t)$  and  $g_{pp}(t, 0) := g_{pp}(t)$ . Now that we have the Green's function, we can immediately write down the phase space trajectories  $\bar{\mathbf{x}}$  for an  $N$  point dust ensemble as:

$$\bar{\mathbf{x}} = \mathcal{G}(t, 0) \mathbf{x}^{(i)} + \int_0^t dt' \mathcal{G}(t, t') \mathbf{K}_1(t') \quad (3.40)$$

with the  $6N \times 6N$  dimensional Green's function

$$\mathcal{G}(t, t') = \mathbf{G}(t, t') \otimes \mathbb{I}_N \quad (3.41)$$

and the  $6N$  dimensional vector being

$$\mathbf{K}_1 = \left( \begin{array}{c} 0 \\ \frac{\vec{u}}{\tau_s} - \vec{\nabla}_{\mathbf{q}_j} \Phi_j \end{array} \right) \otimes \mathbf{e}_j. \quad (3.42)$$

$\mathbf{K}_1$  represents all the external forces and interactions with dust particles, in this case specifically friction with the gas and gravity sourced by the fluctuations of the local matter density  $\rho$  around its time-dependent mean density  $\bar{\rho}$  via the Poisson equation

$$\nabla^2 \Phi = 4\pi G_0 (\rho - \bar{\rho}). \quad (3.43)$$

Now concerning the friction term, we can further simplify the trajectories of the dust ensemble in phase space by remembering that after a short time evolution, small-size dust particles tend to flow with the background gas field with a slower than Keplerian azimuthal velocity due to the friction between the two systems. If we neglect the feedback of the dust onto the gas and assume the lower azimuthal velocity of the gas due to its internal pressure gradient is locally stable, then we can limit ourselves to a prescribed constant background gas velocity field  $\vec{u} \equiv \vec{u}_0$ , instead of a more challenging functional form.

### 3.4 OPERATORS

So far we only considered the microscopic degrees of freedom of the particle ensemble, since those are the dynamical fields of **KFT**. For our discussion of structure formation, the standard application of **KFT** in this thesis will concern the calculation of density and momentum power spectra. We shall thus proceed to define different operators and study their action on the generating functional in [Equation 3.20](#).

Generally, by applying differential operators to the generating functional and setting the source fields to zero afterwards, functions of the phase space trajectories can be generated. In the simplest case, applying a functional derivative with respect to the component  $J_j(t)$  of the generator field generates the average phase space trajectories of particle  $j$  at time  $t$ ,

$$-i \frac{\delta}{\delta J_j(t)} Z[\mathbf{J}] \Big|_{\mathbf{J}=0} = \langle \bar{x}_j(t) \rangle \quad (3.44)$$

More generally, we apply operators in form of functional derivatives with respect to the field components, to generate functions of the phase space trajectories.

$$f(x_j) = f \left( -i \frac{\delta}{\delta J_j(t)} \right) Z[\mathbf{J}] \Big|_{\mathbf{J}=0} \quad (3.45)$$

### 3.4.1 Density Operator

One important operator is the particle density operator in Fourier space. The number density of the particles at any time  $t_1$  is

$$\rho(\vec{q}, t_1) = \sum_{j=1}^N \rho_j(\vec{q}, t_1) = \sum_{j=1}^N \delta_D(\vec{q} - \vec{q}_j(t_1)) \quad (3.46)$$

In a Fourier representation, the density mode with the wave number  $\vec{k}_1$  becomes

$$\tilde{\rho}(\vec{k}_1, t_1) =: \tilde{\rho}(1) = \sum_{j=1}^N e^{-i\vec{k}_1 \cdot \vec{q}_j(t_1)} \quad (3.47)$$

where we have introduced the conventional short-hand notation  $(\vec{k}_j, t_j) =: (j)$ . Replacing the particle position  $\vec{q}_j(t_1)$  by a functional derivative with respect to the generator-field component  $\vec{J}_{q_j}(t_1)$ , we find the density operator

$$\hat{\rho}(1) = \sum_{j=1}^N \hat{\rho}_j(1) \quad (3.48)$$

composed of the one-particle density operators

$$\hat{\rho}_j(1) := \exp\left(-\vec{k}_1 \cdot \frac{\delta}{\delta \vec{J}_{q_j}(t_1)}\right) \quad (3.49)$$

For indistinguishable particles, which we shall henceforth assume, we can set the particle index  $j$  to an arbitrary value without loss of generality. Since the operator in [Equation 3.49](#) is an exponential of a derivative with respect to the generator field, it corresponds to a finite translation of the generator field. After applying  $r \geq 1$  of these operators, the generator field is translated by

$$\mathbf{J} \rightarrow \mathbf{J} - \sum_{j=1}^r \delta(t' - t_j) \vec{k}_j \cdot \begin{pmatrix} 1 \\ 0 \end{pmatrix} \otimes \vec{e}_j \quad (3.50)$$

Setting the generator field  $\mathbf{J}$  to zero after application of the density operator turns the generating functional  $Z[\mathbf{J}]$  by [Equation 3.20](#) into

$$Z^d[\mathbf{L}] = \int d\Gamma e^{i\langle \mathbf{L}_q, \mathbf{q} \rangle + i\langle \mathbf{L}_p, \mathbf{p} \rangle + iS_1} \quad (3.51)$$

with the components

$$\mathbf{L}_q = - \sum_{j=1}^r \vec{k}_j \otimes \vec{e}_j \quad (3.52)$$

$$\mathbf{L}_p = - \sum_{j=1}^r g_{qp}(t_j) \vec{k}_j \otimes \vec{e}_j \quad (3.53)$$

of the translations and the interaction term

$$S_I = - \sum_{j=1}^r \vec{k}_j \int_0^{t_j} dt' g_{qp}(t_j, t') \left( \frac{\vec{u}_0}{\tau_s} - \vec{\nabla}_{q_j} \Phi \right) \quad (3.54)$$

In [Equation 3.51](#),  $\mathbf{q}$  and  $\mathbf{p}$  are the  $3N$  vectors representing the initial positions and momenta of the particle ensemble in phase space,

$$\begin{pmatrix} \mathbf{q} \\ \mathbf{p} \end{pmatrix} := \mathbf{x}^{(i)} \quad (3.55)$$

### 3.4.2 Momentum-Density Operator

Another important and conceptually straightforward application of [KFT](#) is to calculate the momentum power spectra, see [Littek \[27\]](#), which is related to the definition of a momentum operator. The momentum field could naively be constructed as

$$\vec{p}(t_1) = \sum_{j=1}^N \vec{p}_j(t_1) \quad (3.56)$$

with  $\vec{p}_j(t_1)$  being the momentum of particles  $j$ . Notice this momentum field lacks any spatial dependence since has no information on the position of the particle. In order to retain any spatial information, we have to impose that each particle can contribute to the momentum at a position  $\vec{q}$  if and only if it is at this position,

$$\begin{aligned} \Pi(\vec{q}, t_1) &= \sum_{j=1}^N \vec{p}_j(t_1) \delta_D(\vec{q} - \vec{q}_j(t_1)) \\ &= \sum_{j=1}^N \vec{p}_j(t_1) \rho_j(\vec{q}, t_1) \end{aligned} \quad (3.57)$$

In the last step, we have identified the Dirac delta distribution with the density of the  $j$ th particle at position  $\vec{q}$  and time  $t_1$ . Thus, the new field  $\Pi(\vec{q}, t)$  is a momentum-density field.

Fourier-transforming  $\Pi(\vec{q}, t_1)$  and replacing the phase-space coordinates of particle  $j$  by functional derivatives with respect to the corresponding source fields, we find the momentum-density operator

$$\hat{\Pi}(1) = \sum_{j=1}^N \hat{\Pi}_j(1) \quad (3.58)$$

composed of the one-particle momentum-density operators

$$\hat{\Pi}_j(1) = \frac{\delta}{i\delta\vec{J}_{p_j}(t_1)} \hat{\rho}_j(1) \quad (3.59)$$

with  $\hat{\rho}_j(1)$  being the one-particle density operator from Equation 3.49. And the components of the momentum-density field are available by specifying the operator to

$$\hat{\Pi}_j^\alpha(1) := \frac{\delta}{i\delta J_{p_j}^\alpha(t_1)} \hat{\rho}_j(1) \quad (3.60)$$

where  $\alpha = (1, 2, 3)$  enumerates the Cartesian vector components. The application of  $r \geq 1$  momentum-density operators by Equation 3.59 to the generating functional  $Z[\mathbf{J}]$  translates the generator field  $\mathbf{J}$ , as shown in Equation 3.50, and pulls down the momentum trajectories from the phase factor in Equation 3.40. Having applied these operators and setting the generator field  $\mathbf{J}$  to zero afterwards, we arrive at the final expression of the generating functional

$$Z^m[\mathbf{L}] = \int d\Gamma \prod_{j=1}^r \left[ g_{pp}(t_j) \vec{p}_j + \int_0^{t_j} dt' g_{pp}(t_j, t') \left( \frac{\vec{u}_0}{\tau_s} - \vec{\nabla}_{q_j} \Phi \right) \right] \cdot e^{i\langle L_q, q \rangle + i\langle L_p, p \rangle + iS_I} \quad (3.61)$$

where the momentum propagator  $g_{pp}(t, t')$  is defined in Equation 3.39.

### 3.5 SUMMARY AND DISCUSSION

In this chapter, we summarized the basic foundations of KFT that apply to planetary structure formation. We started with a review on how classical mechanics can be formulated in the framework of path integrals, and showed that this theory encodes the

dynamics of a classical particle ensemble by a central object, the generating functional  $Z[\mathbf{J}, \mathbf{K}]$  or  $Z[\mathbf{J}]$ , which is completely specified by the equation of motion for particle ensembles and their initial probability distribution function in phase space.

Building on that, we reviewed the difficulties of plugging the exact dust dynamics into the generating functional, and managed to find a simpler and more feasible dust particle trajectory by retaining only the friction interaction with a constant background gas distribution and the gravitational interaction among dust particles themselves. It's worth mentioning that if we want to go beyond the scope of this thesis and study a more complicated form of protoplanetary disk (PPD), KFT could still be a rather useful tool once we come up with a solution for the functional determinant introduced to the generating functional. And this question itself would be of great interest to the development of KFT since this solution could vastly expand its applications to many more areas.

In the end, considering the standard application of KFT in this thesis will concern the analysis of density and momentum-density power spectra in Chapter 5 and Chapter 6, we reviewed how functions of the phase space coordinates at arbitrary times can be generated by applying operators to the generating functional. More specifically, we introduced the density and momentum-density operators, and studied their actions on the generating functional.

At this moment, if we stay close to the story of KFT, we immediately realize there is still one more essential element in the generating functional remains unknown, and we will need to deal with that before diving right into applying KFT to planetary formation. The initial probability distribution function in phase space (iPDF) describes the particle ensemble's initial state in phase space. It was beautifully derived analytically in Bartelmann et al. [4] by assuming the density and momentum fields are all Gaussian random fields, which is a perfectly valid assumption concerning the application to cosmology. While it is a little more complicated when it comes to planetary formation. First of all, there is no "cosmological principle" in planetary formation, the vast dynamic ranges in space, time and mass scales and the continuous structure formation make it extremely difficult to find a distribution function for dust particles. Even though it is the initial state that we are interested in, we still wish to choose a relatively well-evolved state to represent the protoplanetary disk (PPD) in general, which can currently be best achieved by using simulation data. Therefore, in Chapter 4, we will derive the iPDF by constructing a suitable model from one specific simulation snapshot, after that, we will finally apply KFT to studying planetary formation in Chapter 5 and Chapter 6.



Part II

RESULTS



## INITIAL PROBABILITY DISTRIBUTION FUNCTION IN PHASE SPACE

---

Having introduced the basics of kinetic field theory (KFT), in this Chapter, without losing the generality of the protoplanetary disk (PPD), we derive the other essential element for the generating functional, the initial probability distribution function in phase space (iPDF)  $P(\mathbf{x}^{(i)})$  for particle ensembles, from a 3-dimensional local streaming instability (SI) simulation. For the sake of readability, we omit the upper index (i) and understand that we construct the probability distribution for the initial phase-space coordinates.

Mathematically speaking, the probability distribution function we are looking for is a multivariate probability density function whose variants describe particle positions and momenta in phase space. Generally, for different variants following their respective probability distributions, there is no universal method to obtain the combined probability density function easily. Inspired by Regős and Szalay [34] and Bartelmann et al. [4], in this Chapter, we develop an effective and rather simple method to calculate the iPDF for dust particles as long as certain criteria are satisfied.

This Chapter is constructed as follows: in the first section, we specify the key parameters of the simulation snapshot that is used throughout this entire thesis. In the second section, to derive the expression of the iPDF, first, we calculate the individual density and momentum probability distribution functions of the dust ensemble, then by Gaussianizing their density field, we obtain the final expression of the iPDF using the multivariate Gaussian distribute. In the end, we extract from the simulation the crucial component of the iPDF, the covariance matrix, by analyzing the initial spatial power spectra and correlation functions of the dust ensemble from a pipeline we developed. Furthermore, the momentum covariance matrix is isotropized and rotated to the position and wavenumber space for the convenience of Chapter 5 and Chapter 6.

### 4.1 SIMULATION SPECIFICATION

The three-dimensional streaming instability (SI) simulation by the Pencil code is performed in the shearing-sheet approximation. The is a Cartesian coordinate system co-rotating with the Keplerian orbital frequency  $\Omega$ , at an arbitrary distance  $R_0$  from the central star, see Section 2.3.1. Arbitrary means that the simulation results are valid independent of the distance from the star, and thus the simulation time and length scales are set in PPD units of  $H$  and  $\Omega$ . In the following, all derived quantities, e.g. distance and friction coefficients, are thus given in disk units as well. The coordinate

system  $(x, y, z)$  of the shearing box can be identified as  $(r, \phi, z)$  for small  $r$  and  $\phi$ , see [Figure 2.1](#) and [Figure 4.1](#). The boundary conditions of the shearing sheet are periodic in the  $y$ - and  $z$ -directions, and shear-periodic in the  $x$ -direction. The latter means that the velocities and positions have to be readjusted for a quantity or particle that is transported over the radial boundary condition, see [Section 2.3.2](#). For further detail on the simulation method, we refer to the original code papers by Brandenburg and Dobler [7] and code implementation paper by Youdin and Johansen [43].

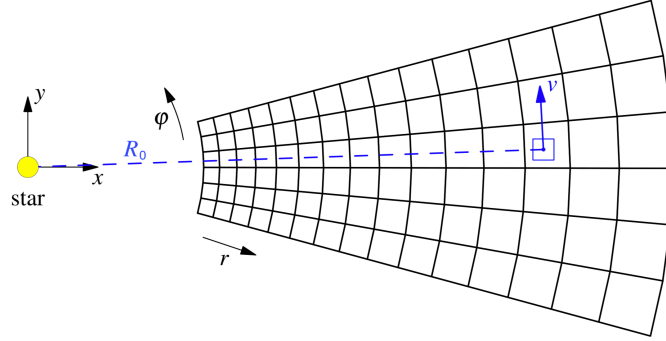


Figure 4.1: The shearing sheet approximation allows to simulate a patch (blue box) out of a protoplanetary disk (black grid). The center of the shearing box has a distance  $R_0$  from the star and moves with Keplerian velocity  $v_K = \Omega R_0$  around it. This motion is translated by the coordinate transformation and shear linearisation into a linear shearing motion, see [Section 2.3](#). In this shearing box coordinate system, the center of the domain is at rest. Everything closer to the star ( $x < 0$ ) moves forward in an azimuthal direction, and everything towards the outside of the domain ( $x > 0$ ) moves backward.

The snapshot of the [SI](#) simulation has been provided to us by Andreas Schreiber from his doctoral work in the Max Planck Institute for Astronomy (MPIA), see Schreiber [36]. This snapshot, deliberately taken at  $t_{\text{snap}} \neq 0$ , will already contain some structure caused by streaming instability ([SI](#)), which gives us a more accurate description of the initial state for dust particles in a general [PPD](#). We aim at studying what [KFT](#) predicts for the further evolution of the power spectrum of these structures. The main parameters are listed below:

1. The friction coefficient between dust particles and gas,  $\tau_s$ , as represented by the Stokes number  $St = \tau_s \Omega = 0.01$ ;
2. The domain size  $L_x = L_y = L_z = L = 0.1$  of the simulation in terms of the disk scale height  $H = c_s \Omega^{-1}$ , where the isothermal sound speed  $c_s$  is taken to be constant. Note that  $L$  is chosen large enough for assuming that the structures studied later are statistically homogeneous and isotropic in the simulation domain, see [Figure 4.2](#);

3. The initial dust-to-gas mass ratio,  $\epsilon_0 = \rho_d/\rho_g = 1.0$ , where the initial mean gas density  $\bar{\rho}_g$  is set to 1.0 for simplicity. This sets the total dust mass to  $M_d = \bar{\rho}_g L^3 = 10^{-3}$ ;
4. The particle number is  $N \approx 2.1 \cdot 10^7$ , thus the mass of each particle is given by  $m_d = M_d/N$ ;
5. The time of the snapshot is  $t_{\text{snap}} = 4.25$ , which means that this snapshot is taken after the simulation box has orbited the central star  $\frac{4.25}{2\pi}$  times and has already well developed over time.

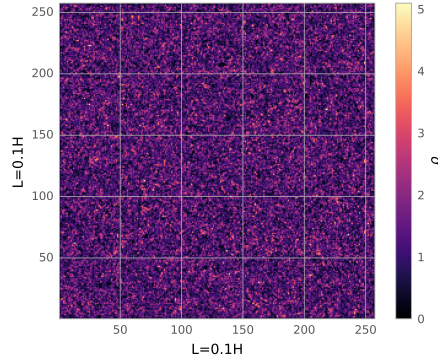


Figure 4.2: This plot shows the dust particles' density distribution  $\rho$  in an  $x - y$  slice of the simulation snapshot discussed in this paper. The overall density distribution throughout the whole plot is more or less equal, suggesting a nearly homogeneous and isotropic simulation domain.

## 4.2 INITIAL PROBABILITY DISTRIBUTION FUNCTION

Calculating the *iPDF* from simulation data for dust particles is one of the major and most difficult tasks when applying *KFT* to planetary formation. As mentioned before, the *iPDF* we are looking for is a joint probability density function for three position and three momentum components. From the simulation data, it is straightforward to estimate the probability density function for each component, but it is quite unfeasible to accurately determine the complete *iPDF* for all the components. Therefore, We rather choose a different approach: we determine the second-order moments of the distributions and transform the variables such that we can model their joint distribution by a multivariate Gaussian distribution.

The joint probability density function for a  $k$ -dimensional multivariate Gaussian distribution with average  $\boldsymbol{\mu}$  and covariance  $\boldsymbol{\Sigma}$  can be written as

$$P(\mathbf{x}) = \frac{\exp\left(-\frac{1}{2}(\mathbf{x} - \boldsymbol{\mu})^\top \boldsymbol{\Sigma}^{-1}(\mathbf{x} - \boldsymbol{\mu})\right)}{\sqrt{(2\pi)^k \det \boldsymbol{\Sigma}}}, \quad (4.1)$$

where  $\mathbf{x}$  and  $\boldsymbol{\mu}$  are real,  $k$ -dimensional column vectors.

Since we assume the particles to be sampled from the density field, we can reduce the number of variants from six to four, viz. one for the density and three for the momentum components. If the density and momentum components had themselves Gaussian distributions, we could immediately write down their joint probability distribution as above.

#### 4.2.1 Density and Momentum Distribution

In this section, we present an examination of the probability distribution of each variant. By adapting suitable fitting functions, we can then decide if they are Gaussian distributions.

The results for all three momentum components are shown in [Figure 4.3](#). Their distributions can individually be fit by Gaussians with amplitudes  $A_i$ , mean values  $p_{ic}$ , and standard deviations  $\sigma_i$ ,

$$f_p(p_i) = A_i \exp\left(-\frac{1}{2}\left(\frac{p_i - p_{ic}}{\sigma_i}\right)^2\right) \quad i = 1, 2, 3. \quad (4.2)$$

Here we use the subscript  $i = 1, 2, 3$  to represent the  $x, y, z$  directions. The values of the fit parameters for all momentum components are listed in [Table 4.1](#).

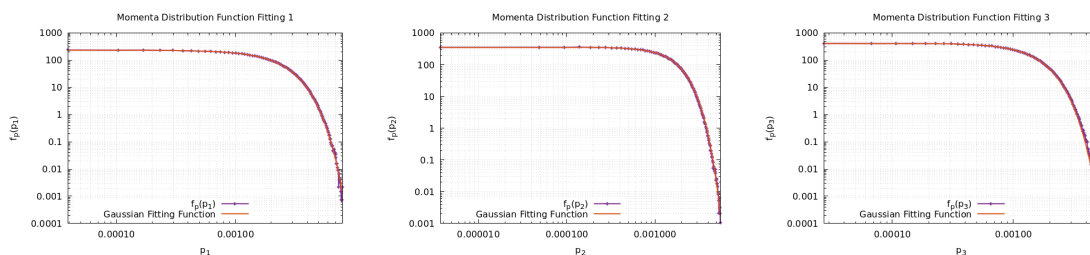


Figure 4.3: Momentum distributions in the  $x, y, z$  directions with double-logarithmic scaling. The purple dotted lines represent actual data, the red lines are the curves of the Gaussian fitting functions described by [Equation 4.2](#). The curves show that the momentum distributions can individually be well described by Gaussians. Notice that the mean values  $p_{1c}$  and  $p_{2c}$  are set to zero here.

Notice that the mean values  $p_{ic}$  for momentum in  $x$  and  $y$  direction are nonzero. This is the exact reflection of the azimuthal drag and the radial drift in [Section 2.1](#) and

	$A_i$	$p_{ic}$	$\sigma_i$
1	238.44	$-2.359 \times 10^{-4}$	0.00167
2	355.40	-0.0249	0.00112
3	413.54	0.0	$9.61 \times 10^{-4}$

Table 4.1: Best-fitting parameters of the momentum distributions in all spatial directions. Notice that the mean values for the momenta in the  $x$  and  $y$  directions do not vanish due to drift motion. We set them to zero for the calculations later.

[Section 5.3](#). The friction force between gas and dust is slowing down the velocity of dust particles in the  $y'$  direction, this directly leads to the drift of dust particles in the  $-x'$  direction, see [Figure 2.1](#). Since in *KFT*, we are exclusively interested in the statistical behavior of the system, in the following calculations of this Chapter, we neglect any bulk motion and set them back to zero.

However, there is still one important usage for the mean velocity  $p_{2c}$  in  $y$  direction. At the end of [Section 3.3](#), we concluded that for small-size dust particles that are well coupled to the gas field, we can ignore the feedback effect from the dust, and assume the background gas is locally stable and can be approximated by a constant velocity field. Since the simulation snapshot represents a well-evolved system and it contains very small dust particles ( $St = 0.01$ ), we can set the averaged constant background gas velocity field as

$$\vec{u}_0 = -0.0249\hat{y}, \quad (4.3)$$

and this information will be particularly important in [Chapter 6](#).

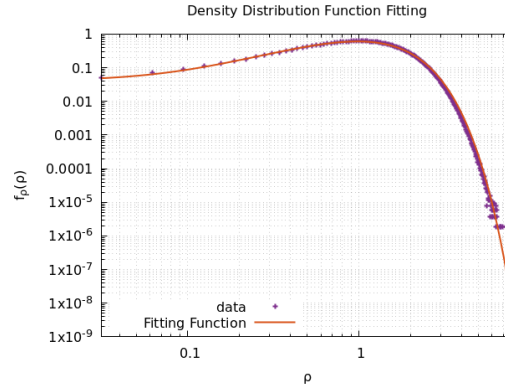


Figure 4.4: Density distribution function in double-logarithm scaling. The data points in the plot are represented by the purple dots, and the orange curve shows the fit function by [Equation 4.4](#).

Now we move on to the density distribution, which is unfortunately not a Gaussian, see [Figure 4.4](#). Rather, it can be approximated by

$$f_{\rho}(\rho) = \frac{3}{2} \frac{(b + \rho^{3/2}) \exp(-\rho^{3/2})}{b\Gamma(2/3) + \Gamma(5/3)} \quad (4.4)$$

with  $b = 0.025$ , which is normalized to unity in  $[0, \infty]$ . This result reflects some structure formation in the simulation as expected.

#### 4.2.2 Gaussianization of the Density Field

Since all momentum components have Gaussian distributions, while the density has not, we transform to a new density variable  $\bar{\rho}$  which is also distributed in a Gaussian way. Let  $\bar{\rho}$  satisfy the mathematical criteria of variable transformation and be a strictly monotonic, real-valued function of  $\rho$ ,  $\bar{\rho} = h(\rho)$ , then the probability densities  $f_{\rho}$  of  $\rho$  and  $f_{\bar{\rho}}$  of  $\bar{\rho}$  are related by

$$f_{\rho}(\rho) = f_{\bar{\rho}}(h(\rho))h'(\rho) , \quad (4.5)$$

where the prime denotes the derivative of  $h$  with respect to  $\rho$ , while their cumulative probability distributions (CDF) must be related by

$$F_{\rho}(\rho) = F_{\bar{\rho}}(\bar{\rho}) . \quad (4.6)$$

Since  $f_{\bar{\rho}}$  is supposed to be a Gaussian with mean value  $\mu$  and standard deviation  $\sigma$ , its CDF is the error function

$$F_{\bar{\rho}}(\bar{\rho}) = \frac{1}{2} \left[ 1 + \operatorname{erf} \left( \frac{\bar{\rho} - \mu}{\sigma} \right) \right] \quad (4.7)$$

The centred and normalized density variable  $\tilde{\rho} = (\bar{\rho} - \mu)/\sigma$  is related to the density  $\rho$  by

$$\tilde{\rho} = \operatorname{erf}^{-1} [2F_{\rho}(\rho) - 1] , \quad (4.8)$$

with the CDF of  $\rho$ , see [Figure 4.5](#), given by

$$F_{\rho}(\rho) = \int_0^{\rho} f_{\rho}(\rho) d\rho = \frac{b\gamma(2/3, \rho^{3/2}) + \gamma(5/3, \rho^{3/2})}{b\Gamma(2/3) + \Gamma(5/3)} \quad (4.9)$$

Here,  $\operatorname{erf}^{-1}$  is the inverse error function and  $\gamma(a, x)$  the incomplete Gamma function.

Since  $F_{\rho}(\rho)$  and the inverse error function are both monotonically increasing, we can verify that  $\tilde{\rho}$  is a real-valued, strictly monotonic function of  $\rho$ . To illustrate that the new density variable  $\tilde{\rho}$  does indeed follow a Gaussian distribution, its probability distribution function and the fitting result are given in [Figure 4.6](#).

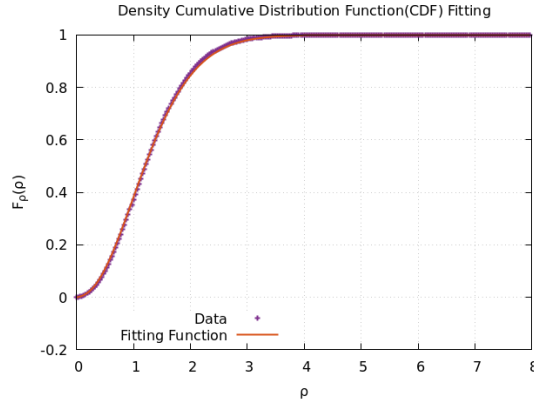


Figure 4.5: This figure shows how the cumulative distribution function (CDF) of the original density variable  $F_\rho(\rho)$  changes from 0 to 1. The purple dots come from the numerical counts for particle number density in phase space, while the orange line represents the curve of Equation 4.9 which is the analytical integration of the original density distribution by Equation 4.4.

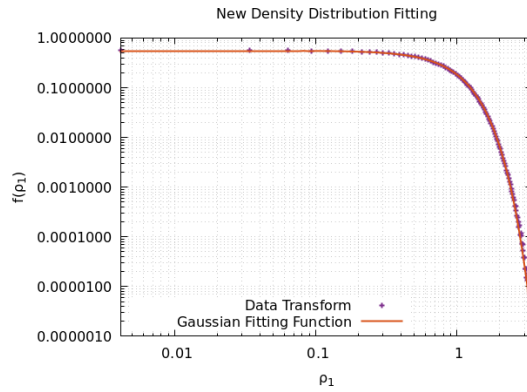


Figure 4.6: Probability distribution of the centred and normalized density variable  $\tilde{\rho}$  in double-logarithmic scaling. The purple dots show the data points transformed as in Equation 4.8. The orange curve shows a Gaussian fit to these points. Their agreement illustrates that  $\tilde{\rho}$  does indeed follow a Gaussian distribution.

### 4.2.3 Inverse Density Transformation

Now that we have successfully acquired the relation  $\tilde{\rho}(\rho)$  in Equation 4.8, for the convenience of future calculations, we are also interested in its inverse function  $\rho(\tilde{\rho})$ . Due to the complicated form of  $F_\rho(\rho)$  in Equation 4.9, it is quite difficult to derive the inverse function  $\rho = h_1^{-1}(\tilde{\rho}) = g(\tilde{\rho})$  analytically. Even we could, it would enormously complicate the further computations in KFT. Therefore, we decide to find this inverse function numerically through polynomial fittings.

It turns out that even a simple quadratic function can already represent the inverse density function  $\rho = g(\tilde{\rho})$  due to the rather narrow domain of the function to be inverted. [Figure 4.7](#) shows the result of the quadratic polynomial fitting function where

$$\rho = a_1(\tilde{\rho} + a_2)^2, \quad (4.10)$$

with  $a_1 = 0.1823 \pm 0.0005$  and  $a_2 = 2.569 \pm 0.006$ . We can see the fitting function matches the actual inverse density data very well, especially in the range  $\tilde{\rho} \geq \tilde{\rho}_0 = -a_2$ . In the case of  $\tilde{\rho} < \tilde{\rho}_0$ , the fitting function no longer satisfies the only mathematical criteria of being monotonically increasing, however, since their corresponding values of  $\rho$  and  $F_\rho(\rho)$  are both very small, it is justified to neglect such insignificant values of  $\tilde{\rho}$  altogether.

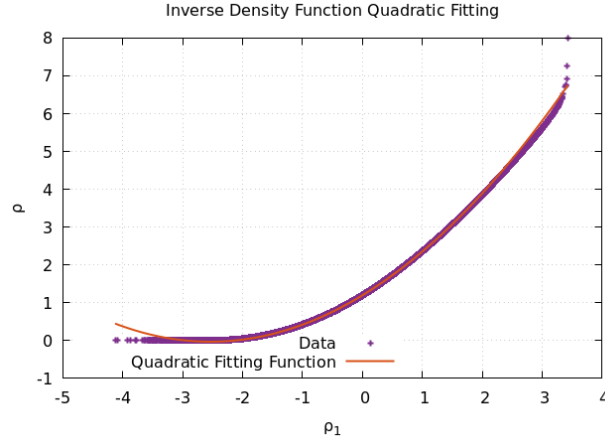


Figure 4.7: This plot shows the quadratic polynomial fitting result of the inverse density relation  $\rho = g(\tilde{\rho})$ . The purple dots are obtained by switching the axis of [Equation 4.8](#). The orange line represents the quadratic fitting function by [Equation 4.10](#).

We can thus choose

$$\sigma = \sqrt{a_1}, \quad \mu = \sqrt{a_1} a_2 \quad (4.11)$$

in [Equation 4.7](#) to relate the density  $\rho$  to the density variable  $\tilde{\rho}$  simply by

$$\rho = \tilde{\rho}^2. \quad (4.12)$$

with

$$\tilde{\rho} = \sqrt{a_1} \left( \text{erf}^{-1} [2F_\rho(\rho) - 1] + a_2 \right) \quad (4.13)$$

representing the inverse of the original relation. Thus, the density variable  $\bar{\rho}$ , which follows by the construction of a Gaussian distribution with mean  $\mu$  and standard deviation  $\sigma$ , is well approximated by the square root of the density  $\rho$ .

To further confirm the approximation we introduced above, [Figure 4.8](#) shows the relative difference between the original density variable  $\rho_{\text{data}}$  and the density variable  $\rho_{\text{aprx}}$  obtained by numerical approximation [Equation 4.12](#). Notice that its values lie mostly within the  $\pm 2\%$  range except at very small  $\rho_{\text{data}}$ , which further supports our approximation. In the meantime, since we will be working with a more ideal dust particle model adapted from the simulation data from [Section 4.3.5](#), this small relative difference seems even more harmless for our further calculation.

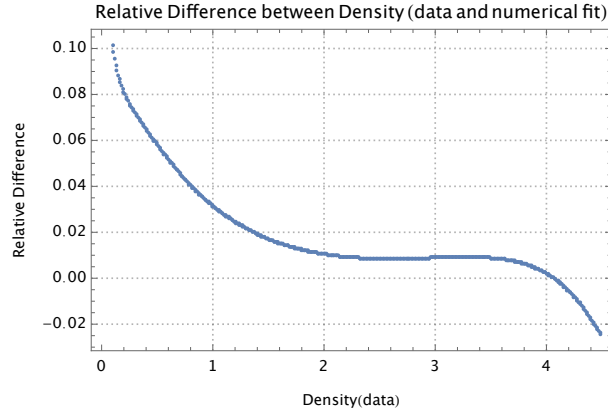


Figure 4.8: This is the relative difference plot between original density field  $\rho_{\text{data}}$  and the approximate original density field  $\rho_{\text{aprx}}$  obtained by [Equation 4.12](#).

#### 4.2.4 The Final Expression

Having assured that the momentum components and the density variable  $\bar{\rho}$  are Gaussian variates to sufficient approximation, we adopt the same method as in Appendix A of Bartelmann et al. [4] to find the initial probability distribution function in phase space for dust particles. First, we introduce a data tensor  $\mathbf{d}$  composed of all variables as,

$$\mathbf{d} := \begin{pmatrix} \bar{\rho} \\ \bar{\mathbf{p}}_j \end{pmatrix} \otimes \mathbf{e}_j \quad (4.14)$$

and its Fourier-conjugate  $\mathbf{t}$  can be expressed as

$$\mathbf{t} := \begin{pmatrix} t_{\bar{\rho}} \\ \vec{t}_{\bar{\mathbf{p}}} \end{pmatrix}_j \otimes \mathbf{e}_j \quad (4.15)$$

where  $(t_{\bar{\rho}}, \vec{t}_{\bar{\mathbf{p}}})_j$  is Fourier-conjugate to  $(\bar{\rho}, \vec{\mathbf{p}})_j$  of particle  $j$ . The joint probability distribution function thus can be written as

$$P(\mathbf{d}) = \frac{1}{\sqrt{(2\pi)^{4N} \det \bar{\mathbf{C}}}} \exp\left(-\frac{1}{2}(\mathbf{d} - \boldsymbol{\mu})^T \bar{\mathbf{C}}^{-1}(\mathbf{d} - \boldsymbol{\mu})\right) \quad (4.16)$$

where  $\boldsymbol{\mu}$  holds the mean values of the Gaussian random variables,  $\bar{\mathbf{C}}^{-1}$  is the inverse of the covariance matrix  $\bar{\mathbf{C}}$  of  $N$  particles which can be decomposed as

$$\bar{\mathbf{C}} = \langle \mathbf{d} \otimes \mathbf{d} \rangle = \begin{pmatrix} \langle \bar{\rho}_j \bar{\rho}_k \rangle & \langle \bar{\rho}_j \vec{\mathbf{p}}_k \rangle^T \\ \langle \vec{\mathbf{p}}_j \bar{\rho}_k \rangle & \langle \vec{\mathbf{p}}_j \vec{\mathbf{p}}_k \rangle \end{pmatrix} \otimes E_{jk} \quad (4.17)$$

with  $E_{jk} = \mathbf{e}_j \otimes \mathbf{e}_k$ .

Since the positions  $\vec{q}_j$  of the  $N$  particles in configuration space are required to sample the density distribution, we have

$$P(\vec{q}_j | \bar{\rho}_j) = \int d\rho_j P(\vec{q}_j | \rho_j) P(\rho_j | \bar{\rho}_j) \quad (4.18)$$

assuming Poisson sampling. Since the new density field is nothing but a point-to-point transformation from the old density field, the conditional probability  $P(\rho_j | \bar{\rho}_j)$  can be expressed by a Dirac delta distribution, thus the conditional probability  $P(\vec{q}_j | \bar{\rho}_j)$  can be written as

$$P(\vec{q}_j | \bar{\rho}_j) = \int d\rho_j P(\vec{q}_j | \rho_j) P(\rho_j | \bar{\rho}_j) = \int d\rho_j \frac{\rho_j}{N} \delta(\rho_j - \rho_j(\bar{\rho}_j)) = \frac{\rho_j(\bar{\rho}_j)}{N} \quad (4.19)$$

The probability for finding a particle at position  $\vec{q}_j$  with momentum  $\vec{\mathbf{p}}_j$  can thus be expressed by

$$P(\vec{q}_j, \vec{\mathbf{p}}_j) = \int d\bar{\rho}_j P(\vec{q}_j | \bar{\rho}_j) P(\bar{\rho}_j, \vec{\mathbf{p}}_j) = \frac{1}{N} \int d\bar{\rho}_j \rho_j(\bar{\rho}_j) P(\bar{\rho}_j, \vec{\mathbf{p}}_j) \quad (4.20)$$

and the probability distribution for the complete set  $\{\vec{q}_j, \vec{\mathbf{p}}_j\}$  of  $N$  phase-space coordinates is

$$P(\{\vec{q}_j, \vec{p}_j\}) = N^{-N} \int d^N \bar{\rho} \prod_{j=1}^{j=N} \rho_j(\bar{\rho}_j) P(\{\bar{\rho}_j, \vec{p}_j\}) = N^{-N} \int d^N \bar{\rho} \prod_{j=1}^{j=N} \bar{\rho}_j^2 P(\mathbf{d}), \quad (4.21)$$

with  $P(\mathbf{d})$  defined in equation 4.16. Here we already used the relation  $\rho(\bar{\rho})$  of Equation 4.12. For evaluating  $P(\mathbf{d})$ , we turn to its characteristic function,

$$\phi(\mathbf{t}) = \exp\left(-\frac{1}{2} \mathbf{t}^\top \bar{\mathbf{C}} \mathbf{t} + i \mathbf{t}^\top \boldsymbol{\mu}\right) \quad (4.22)$$

The probability distribution for the data tensor is then given by the inverse Fourier transformation of the characteristic function

$$P(\mathbf{d}) = \int \frac{d\mathbf{t}_p}{(2\pi)^{3N}} \exp\left(-\frac{1}{2} \mathbf{t}_p^\top \bar{\mathbf{C}}_{pp} \mathbf{t}_p + i \mathbf{t}_p^\top \boldsymbol{\mu}_p + i \langle \mathbf{t}_p, \mathbf{p} \rangle\right) \cdot \int \frac{d\mathbf{t}_{\bar{\rho}}}{(2\pi)^N} \exp\left(-\frac{1}{2} \mathbf{t}_{\bar{\rho}}^\top \bar{\mathbf{C}}_{\bar{\rho}\bar{\rho}} \mathbf{t}_{\bar{\rho}} - \mathbf{t}_{\bar{\rho}}^\top \bar{\mathbf{C}}_{\bar{\rho}p} \mathbf{t}_p + i \mathbf{t}_{\bar{\rho}}^\top \boldsymbol{\mu}_{\bar{\rho}} + i \langle \mathbf{t}_{\bar{\rho}}, \bar{\boldsymbol{\rho}} \rangle\right) \quad (4.23)$$

where we have defined the tensors

$$\mathbf{t}_{\bar{\rho}} := \mathbf{t}_{\bar{\rho}_j} \otimes \mathbf{e}_j, \quad \mathbf{t}_p := \vec{\mathbf{t}}_{p_j} \otimes \mathbf{e}_j, \quad \bar{\boldsymbol{\rho}} := \bar{\rho}_j \otimes \mathbf{e}_j, \quad \mathbf{p} := \vec{\mathbf{p}}_j \otimes \mathbf{e}_j \quad (4.24)$$

and the covariance matrices

$$\bar{\mathbf{C}}_{pp} := \bar{\mathbf{C}}_{p_j p_k} \otimes \mathbf{E}_{jk}, \quad \bar{\mathbf{C}}_{\bar{\rho}\bar{\rho}} := \bar{\mathbf{C}}_{\bar{\rho}_j \bar{\rho}_k} \otimes \mathbf{E}_{jk}, \quad \bar{\mathbf{C}}_{\bar{\rho}p} := \bar{\mathbf{C}}_{\bar{\rho}_j p_k} \otimes \mathbf{E}_{jk} \quad (4.25)$$

Therefore the full probability distribution for  $N$  particles in phase space will be given by

$$P(\mathbf{q}, \mathbf{p}) = P(\{\vec{q}_j, \vec{p}_j\}) = N^{-N} \int d\bar{\boldsymbol{\rho}} \prod_{j=1}^N \bar{\rho}_j^2 \int \frac{d\mathbf{t}_p}{(2\pi)^{3N}} \exp\left(-\frac{1}{2} \mathbf{t}_p^\top \bar{\mathbf{C}}_{pp} \mathbf{t}_p + i \mathbf{t}_p^\top \boldsymbol{\mu}_p + i \langle \mathbf{t}_p, \mathbf{p} \rangle\right) \cdot \int \frac{d\mathbf{t}_{\bar{\rho}}}{(2\pi)^N} \exp\left(-\frac{1}{2} \mathbf{t}_{\bar{\rho}}^\top \bar{\mathbf{C}}_{\bar{\rho}\bar{\rho}} \mathbf{t}_{\bar{\rho}} - \mathbf{t}_{\bar{\rho}}^\top \bar{\mathbf{C}}_{\bar{\rho}p} \mathbf{t}_p + i \mathbf{t}_{\bar{\rho}}^\top \boldsymbol{\mu}_{\bar{\rho}} + i \langle \mathbf{t}_{\bar{\rho}}, \bar{\boldsymbol{\rho}} \rangle\right) \quad (4.26)$$

Now to calculate the above expression, we first integrate over  $\bar{\boldsymbol{\rho}}$  and evaluate

$$I_1(\mathbf{t}_{\bar{\rho}}) := \int d\bar{\boldsymbol{\rho}} \prod_{j=1}^N \bar{\rho}_j^2 \exp(i \langle \mathbf{t}_{\bar{\rho}}, \bar{\boldsymbol{\rho}} \rangle) = \prod_{j=1}^N \left( \int d\bar{\rho}_j \bar{\rho}_j^2 \exp(i \mathbf{t}_{\bar{\rho}_j} \bar{\rho}_j) \right) \quad (4.27)$$

The factors under the product are

$$\int d\bar{\rho}_j \bar{\rho}_j^2 \exp(it_{\bar{\rho}_j} \bar{\rho}_j) = -\frac{\partial^2}{\partial t_{\bar{\rho}_j}^2} \int d\bar{\rho}_j \exp(it_{\bar{\rho}_j} \bar{\rho}_j) = -2\pi \frac{\partial^2}{\partial t_{\bar{\rho}_j}^2} \delta_D(t_{\bar{\rho}_j}) \quad (4.28)$$

where  $\delta_D$  is the Dirac delta distribution. This leads us to

$$I_1(\mathbf{t}_{\bar{\rho}}) = (-2\pi)^N \prod_{j=1}^N \frac{\partial^2}{\partial t_{\bar{\rho}_j}^2} \delta_D(\mathbf{t}_{\bar{\rho}}) = (-2\pi)^N \left( \prod_{j=1}^N \frac{\partial}{\partial t_{\bar{\rho}_j}} \right)^2 \delta_D(\mathbf{t}_{\bar{\rho}}) \quad (4.29)$$

Notice that the validation of the integral  $I_{1j}(t_{\bar{\rho}_j}) = \int d\bar{\rho}_j \exp(it_{\bar{\rho}_j} \bar{\rho}_j) = 2\pi \delta_D(t_{\bar{\rho}_j})$  requires the integration range to extend to infinity. While this is not the case for the density variable  $\bar{\rho}$  from the simulation data, however, since it follows Gaussian distribution in general, considering the entire [PPD](#) area, the integration range is wide enough compared to  $\frac{1}{t_{\bar{\rho}_j}}$  for the integral to approximate the delta distribution well, see [Figure 4.9](#).

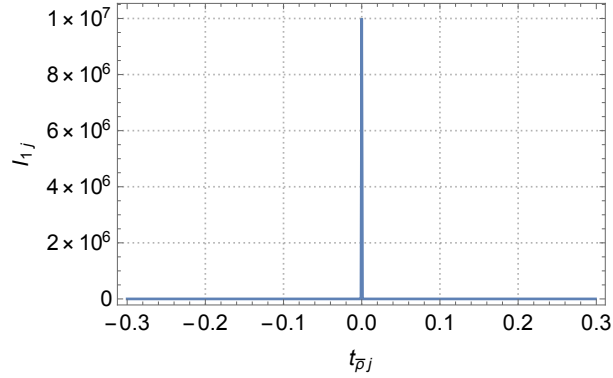


Figure 4.9: This plot shows the numerical results of the integration  $I_{1j}(t_{\bar{\rho}_j}) = \int_{\bar{\rho}_{\min}}^{\bar{\rho}_{\max}} d\bar{\rho}_j \exp(it_{\bar{\rho}_j} \bar{\rho}_j)$  within the range  $-0.3 < t_{\bar{\rho}_j} < 0.3$ , where  $\bar{\rho}_{\min} \approx 0$ , we choose  $\bar{\rho}_{\max} \approx 10^7$  according to the initial particle number  $N$ . The fact that the nonzero values of this curve are all occur near  $t_{\bar{\rho}} \approx 0$  satisfies the definition of a Dirac Delta distribution, which validates our integration result in [Equation 4.28](#).

Next, we integrate over  $\mathbf{t}_{\bar{\rho}}$ , applying two partial integrations and we have

$$\begin{aligned}
 I_2(\mathbf{t}_p) &:= \int \frac{d\mathbf{t}_{\bar{\rho}}}{(2\pi)^N} \exp\left(-\frac{1}{2}\mathbf{t}_{\bar{\rho}}^\top \bar{\mathbf{C}}_{\bar{\rho}\bar{\rho}} \mathbf{t}_{\bar{\rho}} - \mathbf{t}_{\bar{\rho}}^\top \bar{\mathbf{C}}_{\bar{\rho}p} \mathbf{t}_p + i\mathbf{t}_{\bar{\rho}}^\top \boldsymbol{\mu}_{\bar{\rho}}\right) I_1(\mathbf{t}_{\bar{\rho}}) \\
 &= -(-1)^N \int d\mathbf{t}_{\bar{\rho}} \left( \prod_{j=1}^N \frac{\partial}{\partial t_{\bar{\rho}_j}} \exp\left(-\frac{1}{2}\mathbf{t}_{\bar{\rho}}^\top \bar{\mathbf{C}}_{\bar{\rho}\bar{\rho}} \mathbf{t}_{\bar{\rho}} - \mathbf{t}_{\bar{\rho}}^\top \bar{\mathbf{C}}_{\bar{\rho}p} \mathbf{t}_p + i\mathbf{t}_{\bar{\rho}}^\top \boldsymbol{\mu}_{\bar{\rho}}\right) \right) \left( \prod_{j=1}^N \frac{\partial}{\partial t_{\bar{\rho}_j}} \delta_D(\mathbf{t}_{\bar{\rho}}) \right) \\
 &= (-1)^N \int d\mathbf{t}_{\bar{\rho}} \left( \prod_{j=1}^N \frac{\partial^2}{\partial t_{\bar{\rho}_j}^2} \exp\left(-\frac{1}{2}\mathbf{t}_{\bar{\rho}}^\top \bar{\mathbf{C}}_{\bar{\rho}\bar{\rho}} \mathbf{t}_{\bar{\rho}} - \mathbf{t}_{\bar{\rho}}^\top \bar{\mathbf{C}}_{\bar{\rho}p} \mathbf{t}_p + i\mathbf{t}_{\bar{\rho}}^\top \boldsymbol{\mu}_{\bar{\rho}}\right) \right) \delta_D(\mathbf{t}_{\bar{\rho}}) \\
 &= (-1)^N \left( \prod_{j=1}^N \frac{\partial^2}{\partial t_{\bar{\rho}_j}^2} \right) \exp\left(-\frac{1}{2}\mathbf{t}_{\bar{\rho}}^\top \bar{\mathbf{C}}_{\bar{\rho}\bar{\rho}} \mathbf{t}_{\bar{\rho}} - \mathbf{t}_{\bar{\rho}}^\top \bar{\mathbf{C}}_{\bar{\rho}p} \mathbf{t}_p + i\mathbf{t}_{\bar{\rho}}^\top \boldsymbol{\mu}_{\bar{\rho}}\right) \Big|_{\mathbf{t}_{\bar{\rho}}=0} \\
 &= \mathcal{C}(\mathbf{t}_p)
 \end{aligned} \tag{4.30}$$

where  $\mathcal{C}(\mathbf{t}_p)$  is a correlation operator to be evaluated. Notice that to get to the final result in Equation 4.30, we have used the fact that an integration of a complete derivative is zero except for boundary terms. To evaluate the operator  $\mathcal{C}(\mathbf{t}_p)$ , first, we apply the second derivative operator  $\frac{\partial^2}{\partial t_{\bar{\rho}_j}^2}$  to the exponential expression in  $\mathcal{C}(\mathbf{t}_p)$ ,

$$\begin{aligned}
 \mathcal{C}_j(\mathbf{t}_p) &= \frac{\partial^2}{\partial t_{\bar{\rho}_j}^2} \left( \exp\left(-\frac{1}{2}\mathbf{t}_{\bar{\rho}}^\top \bar{\mathbf{C}}_{\bar{\rho}\bar{\rho}} \mathbf{t}_{\bar{\rho}} - \mathbf{t}_{\bar{\rho}}^\top \bar{\mathbf{C}}_{\bar{\rho}p} \mathbf{t}_p + i\mathbf{t}_{\bar{\rho}}^\top \boldsymbol{\mu}_{\bar{\rho}}\right) \right) \Big|_{\mathbf{t}_{\bar{\rho}}=0} \\
 &= \left( -\bar{\mathbf{C}}_{\bar{\rho}_j\bar{\rho}_j} + (-\bar{\mathbf{C}}_{\bar{\rho}_j\bar{\rho}} \mathbf{t}_{\bar{\rho}} - \bar{\mathbf{C}}_{\bar{\rho}_j p} \mathbf{t}_p + i\boldsymbol{\mu}_{\bar{\rho}_j})^2 \right) \exp\left(-\frac{1}{2}\mathbf{t}_{\bar{\rho}}^\top \bar{\mathbf{C}}_{\bar{\rho}\bar{\rho}} \mathbf{t}_{\bar{\rho}} - \mathbf{t}_{\bar{\rho}}^\top \bar{\mathbf{C}}_{\bar{\rho}p} \mathbf{t}_p + i\mathbf{t}_{\bar{\rho}}^\top \boldsymbol{\mu}_{\bar{\rho}}\right) \Big|_{\mathbf{t}_{\bar{\rho}}=0} \\
 &= -\bar{\mathbf{C}}_{\bar{\rho}_j\bar{\rho}_j} + (-\bar{\mathbf{C}}_{\bar{\rho}_j p} \mathbf{t}_p + i\boldsymbol{\mu}_{\bar{\rho}_j})^2
 \end{aligned} \tag{4.31}$$

Then we apply the second derivative operator  $\frac{\partial^2}{\partial t_{\bar{\rho}_k}^2} \frac{\partial^2}{\partial t_{\bar{\rho}_j}^2}$  twice to the same exponential expression,

$$\begin{aligned}
 \mathcal{C}_{jk}(\mathbf{t}_p) &= \frac{\partial^2}{\partial t_{\bar{\rho}_k}^2} \frac{\partial^2}{\partial t_{\bar{\rho}_j}^2} \left( \exp\left(-\frac{1}{2}\mathbf{t}_{\bar{\rho}}^\top \bar{\mathbf{C}}_{\bar{\rho}\bar{\rho}} \mathbf{t}_{\bar{\rho}} - \mathbf{t}_{\bar{\rho}}^\top \bar{\mathbf{C}}_{\bar{\rho}p} \mathbf{t}_p + i\mathbf{t}_{\bar{\rho}}^\top \boldsymbol{\mu}_{\bar{\rho}}\right) \right) \Big|_{\mathbf{t}_{\bar{\rho}}=0} \\
 &= \left( -\bar{\mathbf{C}}_{\bar{\rho}_j\bar{\rho}_j} + (-\bar{\mathbf{C}}_{\bar{\rho}_j p} \mathbf{t}_p + i\boldsymbol{\mu}_{\bar{\rho}_j})^2 \right) \left( -\bar{\mathbf{C}}_{\bar{\rho}_k\bar{\rho}_k} + (-\bar{\mathbf{C}}_{\bar{\rho}_k p} \mathbf{t}_p + i\boldsymbol{\mu}_{\bar{\rho}_k})^2 \right) + 2\bar{\mathbf{C}}_{\bar{\rho}_j\bar{\rho}_k}^2 \\
 &\quad - 4\bar{\mathbf{C}}_{\bar{\rho}_j\bar{\rho}_k} \left( -\bar{\mathbf{C}}_{\bar{\rho}_j p} \mathbf{t}_p + i\boldsymbol{\mu}_{\bar{\rho}_j} \right) \left( -\bar{\mathbf{C}}_{\bar{\rho}_k p} \mathbf{t}_p + i\boldsymbol{\mu}_{\bar{\rho}_k} \right)
 \end{aligned} \tag{4.32}$$

After applying the second derivative operator  $\frac{\partial^2}{\partial t_{\bar{\rho}_k}^2} \frac{\partial^2}{\partial t_{\bar{\rho}_j}^2} \frac{\partial^2}{\partial t_{\bar{\rho}_i}^2}$  three times to the exponential expression in  $\mathcal{C}(\mathbf{t}_p)$ ,

$$\begin{aligned}
\mathcal{C}_{ijk}(\mathbf{t}_p) &= \frac{\partial^2}{\partial t_{\rho_k}^2} \frac{\partial^2}{\partial t_{\rho_j}^2} \frac{\partial^2}{\partial t_{\rho_i}^2} \left( \exp \left( -\frac{1}{2} \mathbf{t}_\rho^\top \bar{\mathbf{C}}_{\rho\rho} \mathbf{t}_\rho - \mathbf{t}_\rho^\top \bar{\mathbf{C}}_{\rho p} \mathbf{t}_p + i \mathbf{t}_\rho^\top \boldsymbol{\mu}_\rho \right) \right) \Big|_{\mathbf{t}_\rho=0} \\
&= \left( -\bar{\mathbf{C}}_{\rho_i \rho_i} + (-\bar{\mathbf{C}}_{\rho_i p} \mathbf{t}_p + i \boldsymbol{\mu}_{\rho_i})^2 \right) \left( -\bar{\mathbf{C}}_{\rho_j \rho_j} + (-\bar{\mathbf{C}}_{\rho_j p} \mathbf{t}_p + i \boldsymbol{\mu}_{\rho_j})^2 \right) \\
&\quad \cdot \left( -\bar{\mathbf{C}}_{\rho_k \rho_k} + (-\bar{\mathbf{C}}_{\rho_k p} \mathbf{t}_p + i \boldsymbol{\mu}_{\rho_k})^2 \right) + 2 \bar{\mathbf{C}}_{\rho_j \rho_k}^2 \left( -\bar{\mathbf{C}}_{\rho_i \rho_i} + (-\bar{\mathbf{C}}_{\rho_i p} \mathbf{t}_p + i \boldsymbol{\mu}_{\rho_i})^2 \right) \\
&\quad + 2 \bar{\mathbf{C}}_{\rho_k \rho_i}^2 \left( -\bar{\mathbf{C}}_{\rho_j \rho_j} + (-\bar{\mathbf{C}}_{\rho_j p} \mathbf{t}_p + i \boldsymbol{\mu}_{\rho_j})^2 \right) + 2 \bar{\mathbf{C}}_{\rho_i \rho_j}^2 \left( -\bar{\mathbf{C}}_{\rho_k \rho_k} + (-\bar{\mathbf{C}}_{\rho_k p} \mathbf{t}_p + i \boldsymbol{\mu}_{\rho_k})^2 \right) \\
&\quad - 4 \bar{\mathbf{C}}_{\rho_j \rho_i} \left( -\bar{\mathbf{C}}_{\rho_j p} \mathbf{t}_p + i \boldsymbol{\mu}_{\rho_j} \right) \left( -\bar{\mathbf{C}}_{\rho_i p} \mathbf{t}_p + i \boldsymbol{\mu}_{\rho_i} \right) \left( -\bar{\mathbf{C}}_{\rho_k \rho_k} + (-\bar{\mathbf{C}}_{\rho_k p} \mathbf{t}_p + i \boldsymbol{\mu}_{\rho_k})^2 \right) \\
&\quad - 4 \bar{\mathbf{C}}_{\rho_k \rho_i} \left( -\bar{\mathbf{C}}_{\rho_k p} \mathbf{t}_p + i \boldsymbol{\mu}_{\rho_k} \right) \left( -\bar{\mathbf{C}}_{\rho_i p} \mathbf{t}_p + i \boldsymbol{\mu}_{\rho_i} \right) \left( -\bar{\mathbf{C}}_{\rho_j \rho_j} + (-\bar{\mathbf{C}}_{\rho_j p} \mathbf{t}_p + i \boldsymbol{\mu}_{\rho_j})^2 \right) \\
&\quad - 4 \bar{\mathbf{C}}_{\rho_j \rho_k} \left( -\bar{\mathbf{C}}_{\rho_j p} \mathbf{t}_p + i \boldsymbol{\mu}_{\rho_j} \right) \left( -\bar{\mathbf{C}}_{\rho_k p} \mathbf{t}_p + i \boldsymbol{\mu}_{\rho_k} \right) \left( -\bar{\mathbf{C}}_{\rho_i \rho_i} + (-\bar{\mathbf{C}}_{\rho_i p} \mathbf{t}_p + i \boldsymbol{\mu}_{\rho_i})^2 \right) \\
&\quad + 8 \bar{\mathbf{C}}_{\rho_j \rho_i} \bar{\mathbf{C}}_{\rho_k \rho_i} \left( -\bar{\mathbf{C}}_{\rho_j p} \mathbf{t}_p + i \boldsymbol{\mu}_{\rho_j} \right) \left( -\bar{\mathbf{C}}_{\rho_k p} \mathbf{t}_p + i \boldsymbol{\mu}_{\rho_k} \right) \\
&\quad + 8 \bar{\mathbf{C}}_{\rho_j \rho_k} \bar{\mathbf{C}}_{\rho_k \rho_i} \left( -\bar{\mathbf{C}}_{\rho_j p} \mathbf{t}_p + i \boldsymbol{\mu}_{\rho_j} \right) \left( -\bar{\mathbf{C}}_{\rho_i p} \mathbf{t}_p + i \boldsymbol{\mu}_{\rho_i} \right) \\
&\quad + 8 \bar{\mathbf{C}}_{\rho_j \rho_k} \bar{\mathbf{C}}_{\rho_j \rho_i} \left( -\bar{\mathbf{C}}_{\rho_k p} \mathbf{t}_p + i \boldsymbol{\mu}_{\rho_k} \right) \left( -\bar{\mathbf{C}}_{\rho_i p} \mathbf{t}_p + i \boldsymbol{\mu}_{\rho_i} \right) - 8 \bar{\mathbf{C}}_{\rho_j \rho_i} \bar{\mathbf{C}}_{\rho_k \rho_i} \bar{\mathbf{C}}_{\rho_j \rho_k}
\end{aligned} \tag{4.33}$$

We can obtain the hierarchy

$$\begin{aligned}
 \frac{\mathcal{C}(\mathbf{t}_p)}{(-1)^N} &= \prod_{j=1}^N \left( -\bar{C}_{\bar{\rho}_j \bar{\rho}_j} + (-\bar{C}_{\bar{\rho}_j p} \mathbf{t}_p + i\mu_{\bar{\rho}_j})^2 \right) \\
 &+ \sum_{(j,k)} 2\bar{C}_{\bar{\rho}_j \bar{\rho}_k} \left( \bar{C}_{\bar{\rho}_j \bar{\rho}_k} - 2(-\bar{C}_{\bar{\rho}_j p} \mathbf{t}_p + i\mu_{\bar{\rho}_j})(-\bar{C}_{\bar{\rho}_k p} \mathbf{t}_p + i\mu_{\bar{\rho}_k}) \right) \cdot \\
 &\prod_{\{l\}} \left( -\bar{C}_{\bar{\rho}_l \bar{\rho}_l} + (-\bar{C}_{\bar{\rho}_l p} \mathbf{t}_p + i\mu_{\bar{\rho}_l})^2 \right) \\
 &+ \sum_{(j,k)} 2\bar{C}_{\bar{\rho}_j \bar{\rho}_k} \left( \bar{C}_{\bar{\rho}_j \bar{\rho}_k} - 2(-\bar{C}_{\bar{\rho}_j p} \mathbf{t}_p + i\mu_{\bar{\rho}_j})(-\bar{C}_{\bar{\rho}_k p} \mathbf{t}_p + i\mu_{\bar{\rho}_k}) \right) \cdot \\
 &\sum_{(a,b)'} 2\bar{C}_{\bar{\rho}_a \bar{\rho}_b} \left( \bar{C}_{\bar{\rho}_a \bar{\rho}_b} - 2(-\bar{C}_{\bar{\rho}_a p} \mathbf{t}_p + i\mu_{\bar{\rho}_a})(-\bar{C}_{\bar{\rho}_b p} \mathbf{t}_p + i\mu_{\bar{\rho}_b}) \right) \cdot \tag{4.34} \\
 &\prod_{\{l\}} \left( -\bar{C}_{\bar{\rho}_l \bar{\rho}_l} + (-\bar{C}_{\bar{\rho}_l p} \mathbf{t}_p + i\mu_{\bar{\rho}_l})^2 \right) \\
 &+ \sum_{(i,j,k)} 2\bar{C}_{\bar{\rho}_j \bar{\rho}_k} \bar{C}_{\bar{\rho}_j \bar{\rho}_i} \left( 4(-\bar{C}_{\bar{\rho}_k p} \mathbf{t}_p + i\mu_{\bar{\rho}_k})(-\bar{C}_{\bar{\rho}_i p} \mathbf{t}_p + i\mu_{\bar{\rho}_i}) - \bar{C}_{\bar{\rho}_k \bar{\rho}_i} \right) \cdot \\
 &\prod_{\{l\}} \left( -\bar{C}_{\bar{\rho}_l \bar{\rho}_l} + (-\bar{C}_{\bar{\rho}_l p} \mathbf{t}_p + i\mu_{\bar{\rho}_l})^2 \right) \\
 &+ \dots
 \end{aligned}$$

being the expression for the correlation operator. In the second line, the sum extends over all pairs  $(j, k \neq j)$ , and the product includes all indices  $l$  except  $(j, k)$ . In the fourth line, the sum extends over products of pairs  $(j, k \neq j)$  and  $(a, b \neq a)$ , where  $(a, b)'$  excludes the indices  $j$  and  $k$ , and the product includes all indices  $l$  except  $(j, k, a, b)$ . Analogous terms with products over three, four and more pairs have to be added. The last two lines give the sum over products of three particles  $(i, j, k | i \neq j \neq k)$ , and analogous terms with products over two, three and more triaparticles have to be added.

Having evaluated the correlation operator  $\mathcal{C}(\mathbf{t}_p)$ , we insert  $I_2(\mathbf{t}_p) = \mathcal{C}(\mathbf{t}_p)$  in the last integration

$$I_3(\mathbf{p}) := \int \frac{d\mathbf{t}_p}{(2\pi)^{3N}} \mathcal{C}(\mathbf{t}_p) \exp \left( -\frac{1}{2} \mathbf{t}_p^\top \bar{C}_{pp} \mathbf{t}_p + i \langle \mathbf{t}_p, \mathbf{p} \rangle \right) \tag{4.35}$$

Notice that except for the correlation operator  $\mathcal{C}(\mathbf{t}_p)$ , the rest of the above integral is a general Fourier transformation of a Gaussian. We can thus convert  $\mathcal{C}(\mathbf{t}_p)$  into an operator of the momentum  $\mathbf{p}$  by replacing  $\mathbf{t}_p \rightarrow -i\partial_p$ , pull it out of the integral

by Equation 4.35 and carry out the final Gaussian integration to arrive at the final expression for the *iPDF* for  $N$  particles

$$P(\mathbf{q}, \mathbf{p}) = \frac{N^{-N} \mathcal{C}(-i\partial_{\mathbf{p}})}{\sqrt{(2\pi)^{3N} \det \bar{C}_{pp}}} \exp\left(-\frac{1}{2} \mathbf{p}^T \bar{C}_{pp}^{-1} \mathbf{p}\right) \quad (4.36)$$

### 4.3 COVARIANCE MATRIX

At the end of the last section, the final expression of the *iPDF* is derived, yet there is one more item in Equation 4.36 that remains unknown. In this section, we thus summarize how we estimate the covariance matrix from simulation data. Notice not only the momenta covariance matrix  $\bar{C}_{pp}$  is of interest, hidden in the correlation operator  $\mathcal{C}(-i\partial_{\mathbf{p}})$ , we also need the density covariance matrix  $\bar{C}_{\bar{\rho}\bar{\rho}}$  and the cross covariance matrix between density and momenta  $\bar{C}_{\bar{\rho}p}$ . Naturally, we wish to compute the covariance matrices by directly calculating their spatial correlation functions, which, unfortunately, is not efficiently achievable due to the enormous number of particles. Therefore, in the following, we develop a different and more efficient scheme to first calculate the spatial power spectra of particles and further compute their corresponding correlation functions and covariance matrices from the *SI* simulation data. In the end, for the convenience of Chapter 5 and Chapter 6, we isotropize the momentum covariance matrix and rotate it to the position and wavenumber space.

#### 4.3.1 Initial Power Spectra and Correlation Functions

We will begin with a comprehensible definition of the spatial correlation functions. Corresponding to the three types of covariance matrices  $\bar{C}_{pp}$ ,  $\bar{C}_{\bar{\rho}\bar{\rho}}$  and  $\bar{C}_{\bar{\rho}p}$ , there are three types of spatial correlation functions, which respectively are density, momentum and density-momentum correlation functions. Denoting density as  $\bar{\rho}$  and momentum as  $p_i$  for  $i = \{1, 2, 3\}$ , the density correlation function is defined as

$$\zeta_{00}(\vec{r}) = \langle \bar{\rho}(\vec{q}) \bar{\rho}(\vec{q} + \vec{r}) \rangle = \frac{\int_{\mathbf{q}} \bar{\rho}(\vec{q}) \bar{\rho}(\vec{q} + \vec{r})}{\int d^3 \vec{q}} = \frac{1}{L^3} \int_{\mathbf{q}} \bar{\rho}(\vec{q}) \bar{\rho}(\vec{q} + \vec{r}) \quad (4.37)$$

Where  $L$  in the  $N$ -body simulation is the size of the simulation box. The spatial correlation functions of the momenta follow the identical concept, but the momenta are three-dimensional. We define

$$\zeta_{ij}(\vec{r}) = \langle \vec{p}_i(\vec{q}) \vec{p}_j(\vec{q} + \vec{r}) \rangle = \frac{\int_{\mathbf{q}} \vec{p}_i(\vec{q}) \vec{p}_j(\vec{q} + \vec{r})}{\int d^3 \vec{q}} = \frac{1}{L^3} \int_{\mathbf{q}} \vec{p}_i(\vec{q}) \vec{p}_j(\vec{q} + \vec{r}) \quad i, j = 1, 2, 3$$

(4.38)

They describe how each of the momentum components relates to each other at different positions. Since covariance matrices are all symmetrical, then in three dimensions, there are  $n_{pp} = 6$  spatial momentum correlation functions. The spatial cross-correlation functions between density and momentum components are similarly defined by

$$\zeta_{0i}(\vec{r}) = \langle \bar{\rho}(\vec{q}) \vec{p}_i(\vec{q} + \vec{r}) \rangle = \frac{\int_{\mathbf{q}} \bar{\rho}(\vec{q}) \vec{p}_i(\vec{q} + \vec{r})}{\int d^3 \vec{q}} = \frac{1}{L^3} \int_{\mathbf{q}} \bar{\rho}(\vec{q}) \vec{p}_i(\vec{q} + \vec{r}) \quad i = 1, 2, 3 \quad (4.39)$$

They describe how the density relates to each of the momentum components at different positions. In three dimensions, there are  $n_{\bar{\rho}p} = 3$  spatial density-momentum cross correlation functions.

Thus we have defined  $n_{\bar{\rho}} + n_{pp} + n_{\bar{\rho}p} = 1 + 6 + 3 = 10$  spatial correlation functions for a symmetrical covariance matrix, for  $N$  particles, it can be generated by

$$\bar{C} = C_{ij} \otimes E_{ij} = \begin{pmatrix} \zeta_{00}(\vec{r}_{ij}) & \zeta_{01}(\vec{r}_{ij}) & \zeta_{02}(\vec{r}_{ij}) & \zeta_{03}(\vec{r}_{ij}) \\ \zeta_{10}(\vec{r}_{ij}) & \zeta_{11}(\vec{r}_{ij}) & \zeta_{12}(\vec{r}_{ij}) & \zeta_{13}(\vec{r}_{ij}) \\ \zeta_{20}(\vec{r}_{ij}) & \zeta_{21}(\vec{r}_{ij}) & \zeta_{22}(\vec{r}_{ij}) & \zeta_{23}(\vec{r}_{ij}) \\ \zeta_{30}(\vec{r}_{ij}) & \zeta_{31}(\vec{r}_{ij}) & \zeta_{32}(\vec{r}_{ij}) & \zeta_{33}(\vec{r}_{ij}) \end{pmatrix} \otimes E_{ij} \quad (4.40)$$

with  $\vec{r}_{ij} = \vec{q}_i - \vec{q}_j$  measuring the relative position of particle  $i$  and  $j$ .

The spatial power spectrum is merely the Fourier transform of the spatial correlation functions defined as  $P(\vec{r}) = \int_{\mathbf{r}} \zeta(\vec{r}) e^{-i\vec{k} \cdot \vec{r}}$ . Thus the spatial power spectra respectively for [Equation 4.37-4.39](#) are

$$\begin{aligned} P_{00}(\vec{k}) &= \int_{\mathbf{r}} \zeta_{00}(\vec{r}) e^{-i\vec{k} \cdot \vec{r}} = \frac{1}{L^3} \bar{\rho}_k(\vec{k}) \bar{\rho}_k(-\vec{k}) \\ P_{ij}(\vec{k}) &= \int_{\mathbf{r}} \zeta_{ij}(\vec{r}) e^{-i\vec{k} \cdot \vec{r}} = \frac{1}{L^3} p_{kj}(\vec{k}) p_{ki}(-\vec{k}) \\ P_{0i}(\vec{k}) &= \int_{\mathbf{r}} \zeta_{0i}(\vec{r}) e^{-i\vec{k} \cdot \vec{r}} = \frac{1}{L^3} p_{ki}(\vec{k}) \bar{\rho}_k(-\vec{k}) \end{aligned} \quad (4.41)$$

### 4.3.2 The Pipeline

Due to the enormous number of dust particles, instead of computing the spatial correlation functions directly, we have chosen a different path. The essential concept is that by transforming the density and momentum fields into Fourier space, we will initially

calculate their spatial power spectra defined in Equation 4.41, then by looking for fitting functions for the numerical power spectra, we can obtain our spatial correlation functions and thus the components of the covariance matrices by performing simple analytical integrations.

#### 4.3.2.1 Fast Fourier Transform

To implement this method, the first step is to transform the density and momentum fields into Fourier space. Here we employ the Fast Fourier Transform (FFT) by adapting the FFTW code to the algorithm. Suppose we have a sequence of  $N$  complex numbers  $\{x_k\} := x_0, x_1, \dots, x_{N-1}$ , the discrete Fourier transform  $\{X_k\} := X_0, X_1, \dots, X_{N-1}$  is:

$$X_k = \sum_{n=0}^{N-1} x_n e^{-i \frac{2\pi kn}{N}} = \sum_{n=0}^{N-1} x_n \left[ \cos \frac{2\pi kn}{N} - i \sin \frac{2\pi kn}{N} \right] \quad (4.42)$$

For more details on the algorithm underlying, we refer to the tutorial paper by Frigo and Johnson [13].

#### 4.3.2.2 Clouds in Cells

Implied by Equation 4.42, in order to exploit FFT to our density and momentum fields, it is essential to first place the particle positions on a grid. Taking both computation time and accuracy into account, we introduce the clouds in cells (CIC) method to our algorithm, the basic idea of which is to assign the mass of each particle in the simulation box to the masses of all the grid cells next to it (in the three-dimensional case, the number of neighboring cells is  $2^3 = 8$ ). The illustration of the CIC method in two-dimensional space is shown in Figure 4.10.

In the following, we will demonstrate in the simplest case how to allocate the mass of particles to the grids in three-dimensional space by the CIC method. Suppose we have a three-dimensional grid, where each cell has unit length. Now we consider the density assignment for a particle with coordinates  $\{x_p, y_p, z_p\}$ . The smallest indices of the cells related to this particle are given as:

$$i = [x_p]; \quad j = [y_p]; \quad k = [z_p] \quad (4.43)$$

where  $[x]$  is the integer floor function. For convenience, we can assume the cell's center is at  $\{x_c, y_c, z_c\} = \{i, j, k\}$ . In three dimensions, a particle at  $\{x_p, y_p, z_p\}$  may contribute to densities in the parent cell  $\{i, j, k\}$  and seven neighboring cells. We define:

$$d_x = x_p - x_c; \quad d_y = y_p - y_c; \quad dz = z_p - z_c \quad (4.44)$$

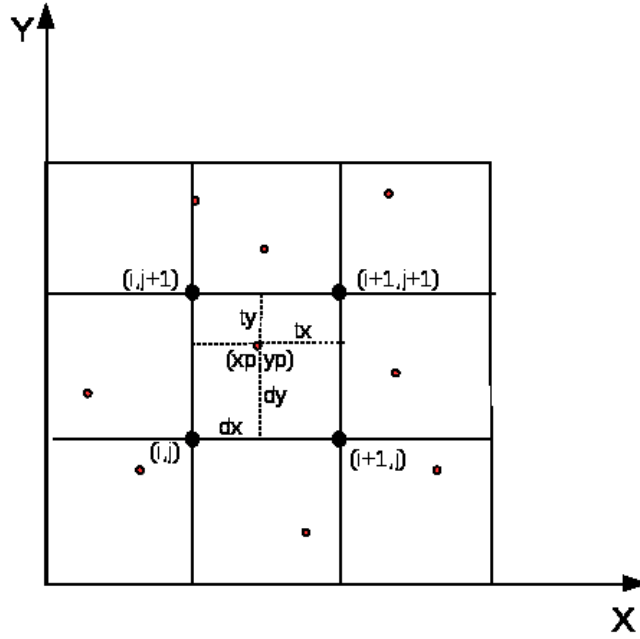


Figure 4.10: This picture is given to illustrate the concept of the CIC code. Suppose we have a two-dimensional grid, the black grid points represent the center of cells and the small red dots mimic particles, the side length of each cell is set to be unity, the mass of each particle is one unit mass, for a particle at  $p = (x_p, y_p)$ , we can assign its mass to the four grid points next to it, which are the points  $(i, j)$ ,  $(i + 1, j)$ ,  $(i, j + 1)$ ,  $(i + 1, j + 1)$ . The weight assigned to each point depends only on its relative position to this particle. For example, for grid point  $(i, j)$ , the mass it gains from particle  $p$  is:  $\Delta m_{i,j} = t_x t_y$ .

$$t_x = 1 - d_x; \quad t_y = 1 - d_y; \quad t_z = 1 - d_z \quad (4.45)$$

The contributions to the eight cells are then linear interpolations in 3 dimensions as:

$$\rho_{i,j,k} = \rho_{i,j,k} + m_p t_x t_y t_z; \quad \rho_{i+1,j,k} = \rho_{i+1,j,k} + m_p d_x t_y t_z; \quad (4.46)$$

$$\rho_{i,j+1,k} = \rho_{i,j+1,k} + m_p t_x d_y t_z; \quad \rho_{i,j,k+1} = \rho_{i,j,k+1} + m_p t_x t_y d_z; \quad (4.47)$$

$$\rho_{i+1,j+1,k} = \rho_{i+1,j+1,k} + m_p d_x d_y t_z; \quad (4.48)$$

$$\rho_{i+1,j,k+1} = \rho_{i+1,j,k+1} + m_p d_x t_y d_z; \quad (4.49)$$

$$\rho_{i,j+1,k+1} = \rho_{i,j+1,k+1} + m_p t_x d_y d_z; \quad (4.50)$$

$$\rho_{i+1,j+1,k+1} = \rho_{i+1,j+1,k+1} + m_p d_x d_y d_z; \quad (4.51)$$

Now to transform momentum fields to Fourier space, it is also essential to acquire the momentum information for each grid cell. Here we decide to approximate the momentum of each cell by adopting the momentum of the particle closest to the center of that cell. With this approximation, a side effect could appear when the number of particles in each cell is too large. In such case we could lose too much information.

Since the particle number in the simulation is relatively large, considering both the algorithm's efficiency and the resolution of the simulation, the grid size for each dimension is set to be 256, so on average, there is  $\frac{N}{256^3} = 1.25 \approx 1$  particle in each cell. For this reason, we consider our method of extracting momenta information to be reliable.

#### 4.3.2.3 Initial Power Spectra

Now that the density and momentum fields are transformed to Fourier space, we could already calculate their spatial power spectra based on Equation 4.41. To further simplify the algorithm, if we assume that the size of the simulation box is significantly larger than the correlation scales, then the short-time SI simulation (see Section 4.1) will not alter the isotropic property of the system. Thus the spatial power spectra we are looking for will no longer depend on the direction of the wave vector  $\vec{k}$ , only the absolute length of it, for that we can rewrite the density spatial power spectrum as:

$$\bar{P}_{00}(k) = P_{00}(\vec{k}) = \frac{1}{L^3} \bar{\rho}_k(\vec{k}) \bar{\rho}_k(-\vec{k}) = \frac{1}{L^3} |\bar{\rho}_k(\vec{k})|^2 \quad (4.52)$$

With regard to the spatial momentum power spectra  $P_{ij}(\vec{k})$ , since the covariance matrices is symmetric, we define

$$\bar{P}_{ij}(k) = \frac{1}{2} \left( P_{ij}(\vec{k}) + P_{ji}(\vec{k}) \right) = \frac{1}{L^3} \left| \Re \left( p_{kj}(\vec{k}) \right) \Re \left( p_{ki}(\vec{k}) \right) + \Im \left( p_{kj}(\vec{k}) \right) \Im \left( p_{ki}(\vec{k}) \right) \right| \quad (4.53)$$

Where  $\Re(z)$  and  $\Im(z)$  respectively give the real and imaginary part of a complex number  $z$ . In analogy to the above calculation, we can immediately find the expression for the new density-momenta spatial power spectra as

$$\bar{P}_{0i}(k) = \frac{1}{2} \left( P_{0i}(\vec{k}) + P_{i0}(\vec{k}) \right) = \frac{1}{L^3} \left| \Re \left( p_{ki}(\vec{k}) \right) \Re \left( \bar{\rho}_k(\vec{k}) \right) + \Im \left( p_{ki}(\vec{k}) \right) \Im \left( \bar{\rho}_k(\vec{k}) \right) \right| \quad (4.54)$$

Thus the combined spatial correlation functions  $\zeta_{\mu\nu}(r)$  of density, momenta and density-momenta are then obtained by Fourier transform as

$$\zeta_{\mu\nu}(r) = \int_{\mathbf{k}} \bar{P}_{\mu\nu}(k) e^{2\pi i \vec{k} \cdot \vec{r}} = \int_0^\infty \frac{dk}{2\pi^2} k^2 \bar{P}_{\mu\nu}(k) j_0(2\pi k r) \quad (4.55)$$

where  $j_0(2\pi kr) = \frac{\sin(2\pi kr)}{2\pi kr}$  is the first order of spherical Bessel function, and  $\mu, \nu = 0, 1, 2, 3$ .

In summary, the pipeline for obtaining the covariance matrices has 5 important steps:

1. Place particles on grids, using the clouds in cells (CIC) algorithm;
2. Obtain density and momentum fields in Fourier space, using Fast Fourier Transform (FFT);
3. Calculate spatial power spectra  $\bar{P}_{\mu\nu}(k)$  in Equation 4.52-4.54 and find appropriate fitting functions;
4. Obtain spatial correlation functions  $\zeta_{\mu\nu}(r)$  in Equation 4.55 by reverse Fourier transforms;
5. Generate covariance matrix  $\bar{C}$  in Equation 4.40 by calculating  $\zeta_{\mu\nu}(r)$  of each pair of particles.

#### 4.3.3 The Final Results

We start with the momentum power spectra  $P_{ij}(k)$  shown in Figure 4.11. Note that all the  $k$  axis from here now on are scaled by  $\frac{2\pi}{L}$ .

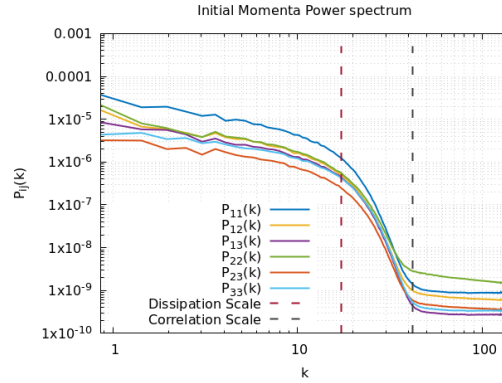


Figure 4.11: The six independent components of the momentum power spectrum are shown here. The red vertical line at  $k = 17.5$  represents the dissipation scale  $l_d$  and the grey vertical line at  $k = 42$  represents the correlation scale  $l_c$ .

They are all of similar shapes, characterized by a first (larger) scale at  $k \approx 17.5$  and a second (smaller) scale at  $k \approx 42$ . These two scales represent respectively the dissipation scale  $l_d$  and the correlation scale  $l_c$ . On scales smaller than  $l_c$ , the particles are significantly less correlated due to their random thermal motion. Moreover, since

the simulated density field is resolved into a finite number of particles, shot noise becomes visible at small scales, preventing the power spectra from falling to zero. On scales larger than  $l_d$ , the curves approach power laws reflecting the turbulence. In between these two scales, the dissipation process becomes visible, where the turbulent kinetic energy is converted to heat.

The shape of the momentum power spectra are well described by the function

$$P_{ij}(k) = c_{1ij} + \frac{c_{2ij}}{k^{\alpha_{ij}}} \exp\left(-\frac{k^2}{2\sigma_{ij}^2}\right) \quad (4.56)$$

with  $c_{1ij}$ ,  $c_{2ij}$  and  $\sigma_{ij}$  being used as fit parameters. The exponents  $\alpha_{ij}$  are close enough to  $2/3$  for keeping them fixed at this value. Best-fitting values for the remaining coefficients are listed in [Table 4.2](#), and the individual fits are shown in [Figure 4.12](#).

	$c_{1ij} \cdot 10^{-10}$	$c_{2ij} \cdot 10^{-6}$	$\sigma_{ij}$
$P_{11}$	9.12	33.8	9.74
$P_{12}$	6.62	12.3	10.12
$P_{13}$	2.72	9.98	10.37
$P_{22}$	18.3	12.2	10.56
$P_{23}$	3.93	5.18	10.49
$P_{33}$	3.42	8.51	10.37

Table 4.2: Best-fitting parameters for all six independent momentum power spectra. The small but nonzero first value for all curves reflects the shot noise.

Even though the data become noisier towards small wave numbers, the fit function follows the data accurately, and the common exponent  $\alpha_{ij} = 2/3$  well describes the slope of the power spectra at large scales.

The density power spectrum  $P_{00}(k)$  shown in [Figure 4.13](#) suggests a fit function of the form

$$P_{00}(k) = \frac{c_{200}}{k} \exp\left(-\frac{k^2}{2\sigma_{00}^2}\right), \quad (4.57)$$

with best-fitting values for the parameters  $c_{100}$ ,  $c_{200}$  and  $\sigma_{00}$  shown in [Table 4.3](#).

	$c_{200}$	$\sigma_{00}$
$P_{00}$	$8.70 \times 10^{-2}$	65.64

Table 4.3: This table shows the fitting coefficient for the density spatial power spectrum  $P_{00}(k)$ .

Unlike the momentum power spectra shown in [Figure 4.11](#), the density power spectrum keeps decreasing for increasing wave numbers  $k$ . At small wave numbers, the

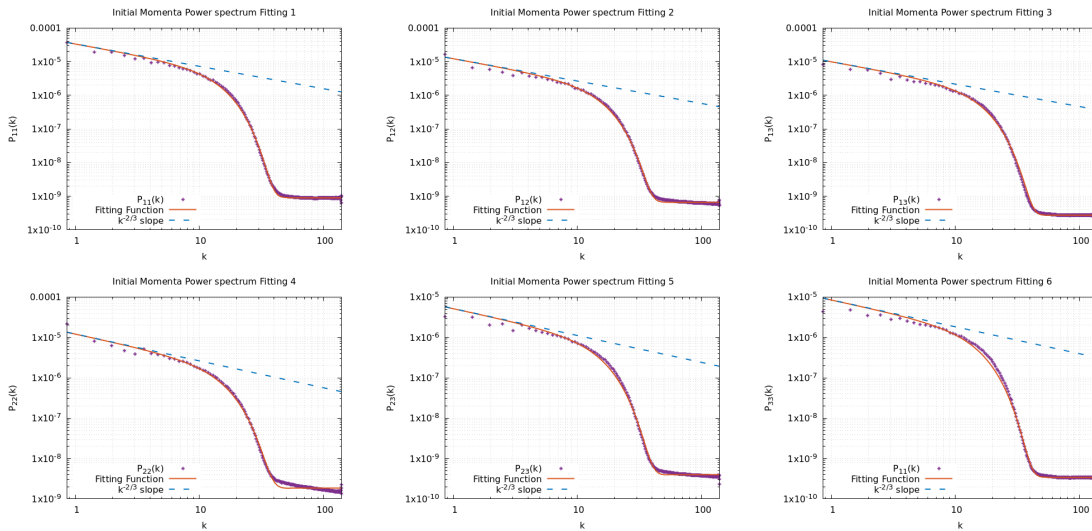


Figure 4.12: Momentum power spectra measured from the simulation (purple dots) together with the individual fit functions of the form of Equation 4.56 (orange lines). The blue dashed lines illustrate the  $k^{-2/3}$  slope for reference.

data becomes noisy, but the fit function still follows the data points reasonably well. Since we do not want to model one simulation precisely, but to extract appropriate model functions from it, we believe that our fit function of Equation 4.57 is acceptable.

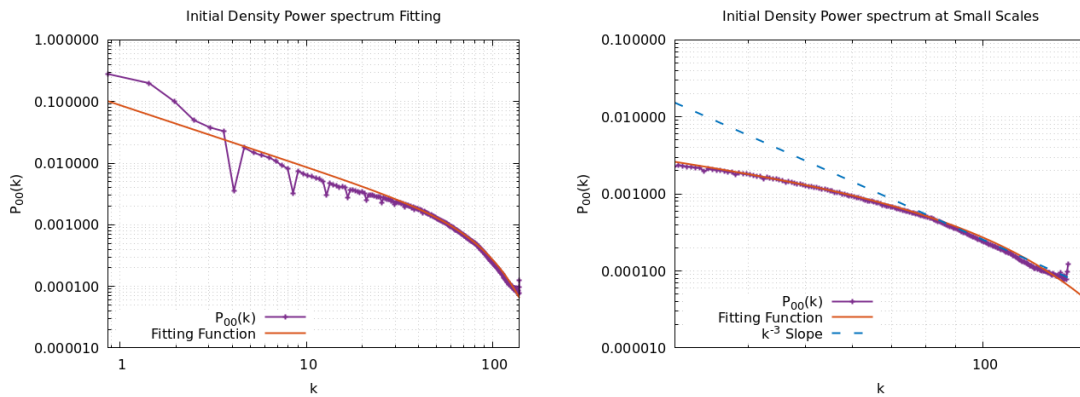


Figure 4.13: Density power spectra extracted from the simulation (purple points) and modeled by the fit function Equation 4.57 (orange line). Left: complete  $k$  range allowed by the simulation data; right: small scales, i. e. large wave numbers. The blue dashed line represents the  $k^{-3}$  slope.

The right panel of Figure 4.13 enlarges the density power spectrum at smaller scales. Notice that the power spectrum changes shape at around  $k \approx 85$ . At smaller scales, i.e.

larger wave numbers, the power spectrum turns into a  $k^{-3}$  slope, indicating structure formation at small scales.

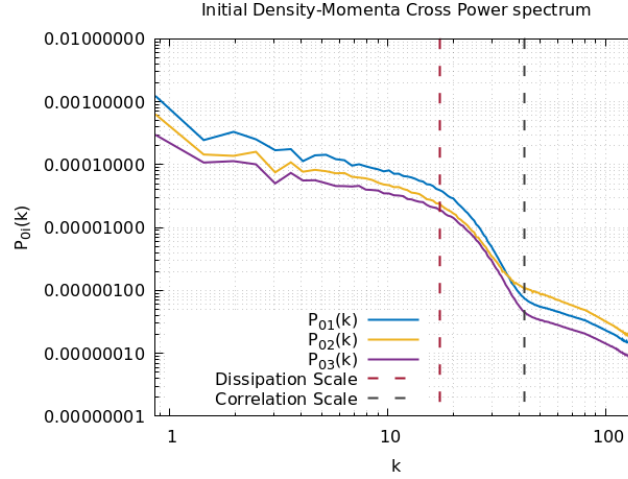


Figure 4.14: Cross power spectra between the density and the momentum components. Similar to the momentum power spectra shown in Figure 4.11, the orange vertical line at  $k = 17.5$  represents the dissipation scale  $l_d$ , and the yellow vertical line at  $k = 42$  the correlation scale  $l_c$ .

Finally, we turn to the cross power spectra between density and momenta, illustrated in Figure 4.14. The shape of these three cross power spectra closely resembles that of the individual momentum and density spectra shown in Figure 4.11 and Figure 4.13, with similar parameter values. A suitable fit function is

$$P_{0i}(k) = \frac{c_{10i}}{k^{\beta_{0i}}} + \frac{c_{20i}}{k^{\alpha_{0i}}} \exp\left(-\frac{k^2}{2\sigma_{0i}^2}\right). \quad (4.58)$$

The extra exponent  $\beta_{0i}$  is introduced to follow the small-scale tails in Figure 4.14. Fitting this function to the simulation data, we find universal exponents  $\alpha_{0i} = 1/3$  and  $\beta_{0i} = 4/3$ . The remaining fit parameters are listed in Table 4.4. As Figure 4.15 shows, the fit function follows the data points very closely.

	$c_{10i} \cdot 10^{-4}$	$c_{20i} \cdot 10^{-4}$	$\sigma_{0i}$
$P_{01}$	1.04	2.58	11.93
$P_{02}$	1.47	1.28	12.28
$P_{03}$	0.61	1.03	12.73

Table 4.4: Fit parameters for all density-momentum cross power spectra.

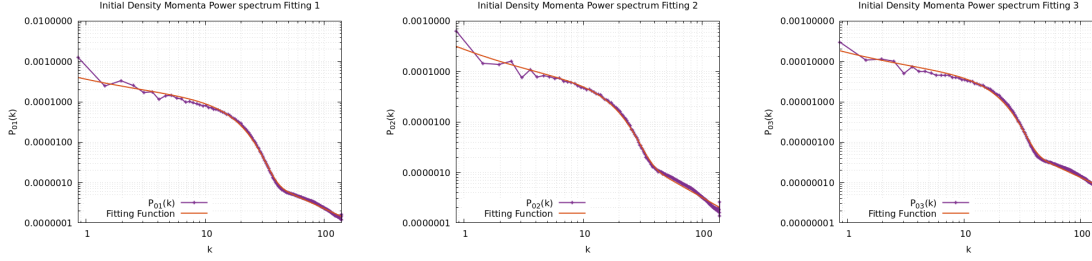


Figure 4.15: Density-momentum cross power spectra overlaid with the fit function Equation 4.58, with exponents  $\beta_{0i} = 4/3$  and  $\alpha_{0i} = 1/3$ . The purple dots are the data points, the green lines show the fits with parameters listed in Table 4.4.

From the density, momentum, and density-momentum power spectra deduced and modeled above, we can now calculate the correlation functions  $\zeta_{\mu\nu}(r)$  via the Fourier transform in Equation 4.55, thereby dropping delta distributions originating from shot-noise terms. The results are

$$\zeta_{\mu\nu}(r) = \begin{cases} \frac{1}{\sqrt{2}\pi^2} \frac{c_{200}\sigma_{00}}{r} F\left(\frac{\sigma_{00}}{\sqrt{2}}r\right) & \text{for } \mu, \nu = 0 \\ \frac{1}{2^{5/6}\pi^2} c_{2ij}\sigma_{ij}^{7/3}\Gamma\left(\frac{7}{6}\right) {}_1F_1\left(\frac{7}{6}, \frac{3}{2}, -\frac{1}{2}\sigma_{ij}^2 r^2\right) & \text{for } \mu, \nu = 1, 2, 3 \\ \frac{\sqrt{3}c_{10i}}{4\pi^2 r^{5/3}} \Gamma\left(\frac{2}{3}\right) + \frac{1}{2^{2/3}\pi^2} c_{20i}\sigma_{0i}^{8/3}\Gamma\left(\frac{4}{3}\right) {}_1F_1\left(\frac{4}{3}, \frac{3}{2}, -\frac{1}{2}\sigma_{0i}^2 r^2\right) & \text{for } \mu = 0, \nu = 1, 2, 3 \end{cases} \quad (4.59)$$

Here,  $F$  is the Dawson integral,  $\Gamma$  the Gamma function, and  ${}_1F_1[z]$  the Kummer confluent hypergeometric function. These correlation functions are shown in Figure 4.16. We note the similarity of the curves in the three panels of this Figure. In particular, they all change shape at a relatively small scale  $r_d$ , above which they fall off more steeply.

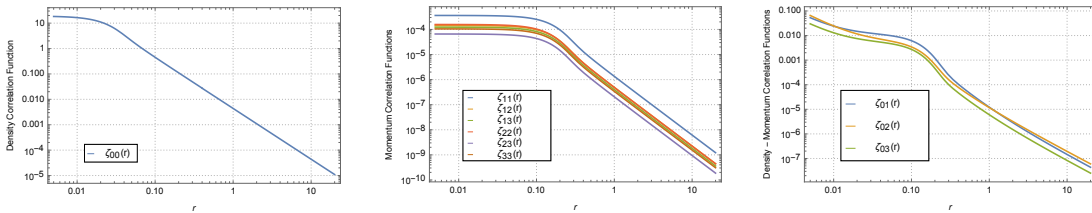


Figure 4.16: The density, momentum, and density-momentum correlation functions of Equation 4.59 are shown here in the left, center, and right panels, respectively. The horizontal axes are scaled in  $L = 0.1H$ , i.e. with the same length scale as the simulation boxes.

For any pair  $(i, j)$  or particles, the complete correlation matrix can now be written in the form

$$\bar{C}_{ij}(r_{ij}) = \begin{pmatrix} \zeta_{00}(r_{ij}) & \zeta_{0k}^\top(r_{ij}) \\ \zeta_{0k}(r_{ij}) & \zeta_{kl}(r_{ij}) \end{pmatrix} \quad (4.60)$$

with  $k, l \in 1, 2, 3$  and  $r_{ij} = |\vec{q}_i - \vec{q}_j|$ . The covariance matrix for the entire particle ensemble defined in Equation 4.17 is then  $\bar{C} = \bar{C}_{ij} \otimes E_{ij}$ .

#### 4.3.4 Approximating The Correlation Operator

Now that the density covariance matrix  $\bar{C}_{\bar{\rho}\bar{\rho}}$  and the cross covariance matrix between density and momenta  $\bar{C}_{\bar{\rho}\mathbf{p}}$  are generated from simulation data, we make use of their amplitude difference and try to simplify the correlation operator  $\mathcal{C}(-i\partial_{\mathbf{p}}) = \mathcal{C}(\mathbf{p})$ .

The values and coefficients of the spatial correlation functions shown in Figure 4.16 and Table 4.3, Table 4.4 imply the following relations where

$$\bar{C}_{\bar{\rho}_j\bar{\rho}_j} > \bar{C}_{\bar{\rho}_j\mathbf{p}_k} \gg \bar{C}_{\bar{\rho}_j\mathbf{p}_k}^2, \quad \bar{C}_{\bar{\rho}_j\bar{\rho}_j} = \zeta_{00}(0) > \bar{C}_{\bar{\rho}_j\bar{\rho}_k} = \zeta_{00}(r_{jk}) > 0 \quad (4.61)$$

with the indices  $j$  and  $k$  indicating an arbitrary pair of distinct particles and  $\zeta_{00}(r)$  is given in Equation 4.59. In the meantime, the initial momentum power spectra shown in Figure 4.11 and their coefficients given in Table 4.2 further indicate that the value of  $t_{\mathbf{p}}$  satisfies

$$|t_{\mathbf{p}_k}| \leq 5.81 \cdot 10^{-3}. \quad (4.62)$$

Given the above relations, since the correlation operator  $\mathcal{C}(\mathbf{p})$  has the hierarchical structure given in Equation 4.34, we can ignore the terms including  $\bar{C}_{\bar{\rho}_j\mathbf{p}_k} t_{\mathbf{p}_k}$  and  $\bar{C}_{\bar{\rho}_j\bar{\rho}_k}$  in Equation 4.34 and approximate the correlation operator  $\mathcal{C}(\mathbf{p})$  by the constant only involving the density auto-correlations

$$\mathcal{C}(\mathbf{p}) = \mathcal{C} = (\zeta_{00}(0) + \mu_{\bar{\rho}}^2)^N. \quad (4.63)$$

with the mean value of the density field  $\bar{\rho}$  as  $\mu_{\bar{\rho}} = \sqrt{a_1} a_2$  given in Equation 4.11.

Therefore we can write down the much simpler, but accurately approximated iPDF for the ensemble of  $N$  dust particles as

$$P(\mathbf{q}, \mathbf{p}) = \frac{\mathcal{C}^{N-N}}{\sqrt{(2\pi)^{3N} \det \bar{C}_{\mathbf{p}\mathbf{p}}}} \exp\left(-\frac{1}{2} \mathbf{p}^\top \bar{C}_{\mathbf{p}\mathbf{p}}^{-1} \mathbf{p}\right) \quad (4.64)$$

### 4.3.5 Rotate Momentum Covariance Matrix

To this point, employing the pipeline we developed in Section 4.3.2, the full initial covariance matrix  $\bar{C}$  has been recovered from a 3-dimensional N-particle SI simulation for the iPDF we derived in Equation 4.36 and simplified in Equation 4.64. Due to the significance of the momentum covariance matrix, in this section, we isotropize it for the convenience of further calculations in Chapter 5 and Chapter 6.

Since all momenta correlation functions  $\zeta_{ij}(r)$  share the same format, see Equation 4.55, and the fitting coefficients  $\sigma_{ij}$  shown in Table 4.2 have very similar values, we can take the average of the  $\sigma_{ij}$  and define a new universal fitting coefficient  $\bar{\sigma}$  as,

$$\bar{\sigma} = \frac{1}{6} \sum_{i,j=1, i \leq j}^{i,j=3} \sigma_{ij}, \quad (4.65)$$

then a new universal correlation function  $\zeta_{pp}(r)$  can be specified as

$$\zeta_{pp}(r) = \frac{1}{2^{\frac{7}{6}} \pi^2} \bar{\sigma}^{\frac{7}{3}} \Gamma\left(\frac{7}{6}\right) {}_1F_1\left(\frac{7}{6}, \frac{3}{2}, -\frac{1}{2} \bar{\sigma}^2 r^2\right). \quad (4.66)$$

with its Fourier transform defined as the averaged initial momentum power spectrum  $P_0(k)$

$$P_0(k) = \int_r \zeta_{pp}(r) e^{-i\vec{k} \cdot \vec{r}} = \frac{1}{k^{2/3}} \exp\left(-\frac{k^2}{2\bar{\sigma}^2}\right). \quad (4.67)$$

The only difference between each of the momentum correlation functions now lies in the fitting coefficient  $c_{2ij}$ . As shown in Figure 4.2, since the spatial scales we are considering are small compared to the scale height  $H$  of the protoplanetary disk, the density distribution of the particles in the simulation box should be rather homogeneous and isotropic, which implies the same for the momentum distribution. By calculating the eigenvalues and eigenvectors of the sampled momentum covariance matrices  $\bar{C}_{p_i p_j}$ , it appears that all eigenvectors of them are very close to be aligned with the coordinate axis and all eigenvalues are quite similar or at least have the same order of magnitude, which indicate that the three axes could easily be treated equally, or we can say that the system is indeed very close to being isotropic. Thus we can average the modified momentum covariance matrix  $\bar{C}_{p_i p_j}$  to read

$$\bar{C}_{p_i p_j} = \begin{pmatrix} b_0 & b_1 & b_1 \\ b_1 & b_0 & b_1 \\ b_1 & b_1 & b_0 \end{pmatrix} \zeta_{pp}(r_{ij}) \quad (4.68)$$

with prefactors

$$b_0 = \frac{1}{3}(c_{211} + c_{222} + c_{233}); \quad b_1 = \frac{1}{3}(c_{212} + c_{213} + c_{223}) \quad (4.69)$$

For calculating future [KFT](#) nonlinear density power spectra, we now rotate from the coordinate frame of the simulation box into a coordinate frame in which the relative position vector  $\vec{r}_{ij} = \vec{q}_i - \vec{q}_j$  between the particles is the polar axis. We first define the projectors

$$\pi_{\parallel} = \hat{q} \otimes \hat{q} \quad \pi_{\perp} = \mathbb{1}_3 - \pi_{\parallel} \quad (4.70)$$

parallel and perpendicular to  $\hat{q} = \vec{r}_{ij}/|\vec{r}_{ij}|$ . There,  $\bar{C}_{p_i p_j}$  is of the form

$$\bar{C}_{p_i p_j} = -m_1 \mathbb{1}_3 - m_2 \hat{q} \otimes \hat{q} = -(m_1 + m_2) \pi_{\parallel} - m_1 \pi_{\perp} \quad (4.71)$$

Since matrix rotations do not change their trace and determinant, we first calculate the eigenvalues of the matrix in [Equation 4.68](#) being

$$\lambda_{1,2} = (b_0 - b_1) \zeta_{pp}(r_{ij}), \quad \lambda_3 = (b_0 + 2b_1) \zeta_{pp}(r_{ij}), \quad (4.72)$$

thus its trace and determinant are

$$\text{tr} \bar{C}_{p_i p_j} = 3b_0 \zeta_{pp}(r_{ij}), \quad \det \bar{C}_{p_i p_j} = (b_0 - b_1)^2 (b_0 + 2b_1) \zeta_{pp}^3(r_{ij}). \quad (4.73)$$

On the other hand, the eigenvalues of the momenta covariance matrix in [Equation 4.71](#) are

$$l_{1,2} = -m_1, \quad l_3 = -(m_1 + m_2). \quad (4.74)$$

Identifying these with the eigenvalues in [Equation 4.72](#), we have

$$m_1(r_{ij}) = (b_1 - b_0) \zeta_{pp}(r_{ij}), \quad m_2(r_{ij}) = -3b_1 \zeta_{pp}(r_{ij}), \quad (4.75)$$

which ensures that the trace and determinant of the matrix to remain unchanged. Therefore, by setting  $m_1$  and  $m_2$  as above, we are able to rotate the momentum covariance matrix  $\bar{C}_{p_i p_j}$  in the  $\hat{q}$  space.

Due to the complicated analytic form of  $\zeta_{pp}(r)$ , a simpler approximation will help better understand its asymptotic behavior and further help with the [KFT](#) power spectra analysis in [Chapter 5](#) and [Chapter 6](#). Define  $\zeta(r)$  as

$$\zeta_{pp}(r) \sim \zeta(r) = \frac{0.04}{(0.0075 + r^2)^{7/6}}. \quad (4.76)$$

Further define  $a_1(r)$  and  $a_2(r)$  as

$$|m_1(r)| = -m_1(r) \sim a_1(r) = (b_0 - b_1)\zeta(r) = \frac{3.5 \times 10^{-7}}{(0.0075 + r^2)^{7/6}} \quad (4.77)$$

$$|m_2(r)| = -m_2(r) \sim a_2(r) = 3b_1\zeta(r) = \frac{1.1 \times 10^{-6}}{(0.0075 + r^2)^{7/6}} \quad (4.78)$$

They are compared with the original functions  $\zeta_{pp}(r)$ ,  $|m_1(r)|$  and  $|m_2(r)|$  in [Figure 4.17](#). Notice at both small and large  $r$ , the asymptotic behavior of the approximate functions match the original ones very well.

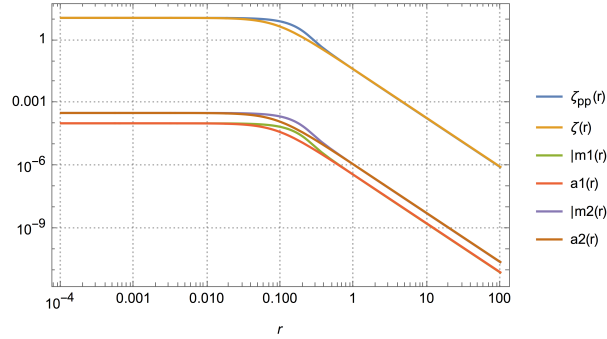


Figure 4.17: The function of  $\zeta_{pp}(r)$  (blue line),  $|m_1(r)|$  (green line) and  $|m_2(r)|$  (purple line) are shown together with their approximations  $\zeta(r)$  (yellow line),  $a_1(r)$  (red line) and  $a_2(r)$  (orange line) given by [Equation 4.76-4.78](#).

Furthermore, [Figure 4.18](#) also shows the shape of the averaged initial momenta power spectrum  $P_0(k)$  and its asymptotic behavior  $k^{-\frac{2}{3}}$  at large scales.

Now for calculating future KFT nonlinear momentum power spectra, we need to rotate to the wavenumber  $\hat{k}$  space, in which the relative wavenumber vector  $\vec{k}_{ij} = \vec{k}_i - \vec{k}_j$  between the particles is the polar axis. Define projectors

$$\tilde{\pi}_{\parallel} = \hat{k} \otimes \hat{k} \quad \tilde{\pi}_{\perp} = \mathbb{1}_3 - \tilde{\pi}_{\parallel} \quad (4.79)$$

parallel and perpendicular to  $\hat{k} = \vec{k}_{ij}/|\vec{k}_{ij}|$  and wave number  $\vec{k}_i$  is the fourier conjugate of particle position  $\vec{q}_i$ .  $\tilde{C}_{p_i p_j}$  has the same form in this space as

$$\tilde{C}_{p_i p_j} = -m_3 \mathbb{1}_3 - m_4 \hat{k} \otimes \hat{k} = -(m_3 + m_4) \tilde{\pi}_{\parallel} - m_3 \tilde{\pi}_{\perp} \quad (4.80)$$

Comparing [Equation 4.71](#) with [Equation 4.80](#), we have

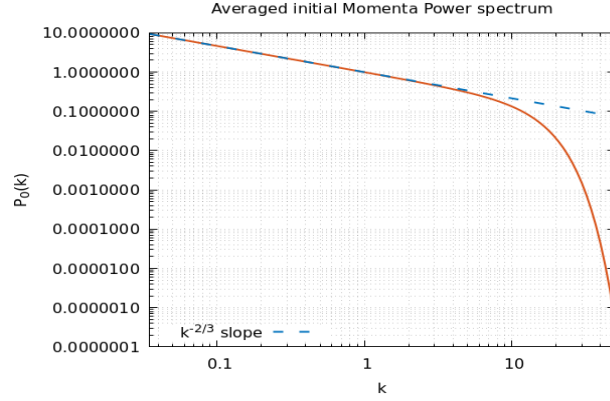


Figure 4.18: The function of  $P_0(k)$  (orange line) given by Equation 4.67 is shown together with its asymptotic behavior  $k^{-\frac{2}{3}}$  (blue dashed line).

$$(m_1 + m_2)\pi_{\parallel} + m_1\pi_{\perp} = (m_3 + m_4)\tilde{\pi}_{\parallel} + m_3\tilde{\pi}_{\perp} \quad (4.81)$$

respectively. Multiply this equation by  $\tilde{\pi}_{\parallel}$  and  $\tilde{\pi}_{\perp}$  and take the trace of the resulting two equations to find

$$m_3 + m_4 = \mu^2(m_1 + m_2) + (1 - \mu^2)m_1 \quad (4.82)$$

$$2m_3 = (1 - \mu^2)(m_1 + m_2) + (1 + \mu^2)m_1 \quad (4.83)$$

We introduce the cosine  $\mu := \hat{k} \cdot \hat{q}$  of the angle between  $\vec{k}_{ij}$  and  $\vec{r}_{ij}$ , and apply the following matrix trace equations

$$\text{tr}(\tilde{\pi}_{\parallel}\tilde{\pi}_{\parallel}) = 1, \quad \text{tr}(\tilde{\pi}_{\parallel}\tilde{\pi}_{\perp}) = 0, \quad \text{tr}(\tilde{\pi}_{\parallel}\pi_{\parallel}) = \mu^2, \quad \text{tr}(\tilde{\pi}_{\parallel}\pi_{\perp}) = 1 - \mu^2, \quad (4.84)$$

$$\text{tr}(\tilde{\pi}_{\perp}\tilde{\pi}_{\perp}) = 2, \quad \text{tr}(\tilde{\pi}_{\perp}\pi_{\parallel}) = 1 - \mu^2, \quad \text{tr}(\tilde{\pi}_{\perp}\pi_{\perp}) = 1 + \mu^2 \quad (4.85)$$

Thus by setting  $m_3$  and  $m_4$  as

$$m_3(r_{ij}) = m_1(r_{ij}) + \frac{1}{2}(1 - \mu^2)m_2(r_{ij}) = \left(\frac{3\mu^2 - 1}{2}b_1 - b_0\right)\zeta_{pp}(r_{ij}), \quad (4.86)$$

$$m_4(r_{ij}) = \frac{3\mu^2 - 1}{2}m_2(r_{ij}) = \frac{3}{2}(1 - 3\mu^2)b_1\zeta_{pp}(r_{ij}), \quad (4.87)$$

we can rotate the momenta covariance matrix to the wave number  $\hat{k}$  space.

## 4.4 SUMMARY AND DISCUSSION

In this chapter, we provided the last piece of the puzzle of applying KFT to planetary formation and derived the initial probability distribution function in phase space (iPDF) for N-point dust particles from a 3-dimensional streaming instability (SI) local shearing sheet simulation. We started with listing the key parameters of the simulation and realized two important points, one of which is that the time of the snapshot is chosen to be nonzero which leads to potential structure formation in the system, the other one is that the size of the simulation box is large enough for us to assume homogeneity and isotropy yet small enough compared to the scale height of the protoplanetary disk (PPD) to be able to represent anywhere of the disk.

Next, we related the particle positions with their density field and found out that the momentum fields of dust particles are all Gaussian while the density field is not. By Gaussianizing the density field and numerically approximating the inverse density function, we made use of the multivariate Gaussian distribution in Equation 4.1 and derived the final expression for the iPDF in Equation 4.36. It is worth mentioning here that although in this thesis the data only shows the necessity of Gaussianizing the density field, for other types of simulation data that show non-gaussian momentum distributions, we can still employ the same method and Gaussianize them in a similar manner as long as the new Gaussianized fields relate with the original ones by monotonically increasing functions. And even better, since there will only be extra delta function distribution, the final expression of the iPDF in Equation 4.36 stays in the very same form.

We then reviewed the numerical method developed to extract the missing element, the covariance matrices in the iPDF, from simulation data. Due to the enormous number of dust particles, we chose to recover the covariance matrices from their corresponding spatial correlation functions, which were calculated from the inverse Fourier transformation of their spatial power spectra. A total five-step pipeline was developed in Section 4.3.2 to achieve this goal, among which, the most crucial was to find fitting functions for the initial spatial power spectra of the dust particles. The final fitting and inverse Fourier transform results were shown in Section 4.3.3. For momentum and density-momentum power spectra, we saw two characteristic scales which represent the correlation and dissipation scales of the system. And for the density power spectrum, it is interesting to see a  $k^{-3}$  slope showing up at small scales. Building on these results, we further made use of the value difference between the density covariance matrix  $\bar{C}_{\rho\rho}$  and the momentum density cross covariance matrix  $\bar{C}_{\rho p}$ , and managed to simplify the complicated correlation operator  $\mathcal{C}(\mathbf{p})$  to a constant  $\mathcal{C}$  in Equation 4.63 by only preserving the density auto correlations.

In the end, we discussed the near-isotropic nature of the momentum distribution in the system and isotropized the momentum covariance matrix for the convenience of further computations. Furthermore, using the fact that matrix rotations do not change

their trace and determinant, we managed to rotate the momentum covariance matrix into the relative position and wave number space in the form of [Equation 4.71](#) and [Equation 4.80](#) for calculating future KFT nonlinear density and momentum power spectra in [Chapter 5](#) and [Chapter 6](#). Moreover, a simpler approximation of the universal correlation function  $\zeta_{pp}(\mathbf{r})$  in [Equation 4.76](#) is given for a better understanding of its asymptotic behavior at large and small scales, which will come in handy for the later KFT power spectra analysis.

## DUST DENSITY POWER SPECTRUM BY KFT

In this Chapter, we focus on extracting the planetary structure formation information by analyzing the **KFT** density power spectrum for dust particles derived from the generating functional in [Equation 3.51](#),

$$Z^d[\mathbf{L}] = \int d\mathbf{q}d\mathbf{p}P(\mathbf{q}, \mathbf{p})e^{i\langle \mathbf{L}_q, \mathbf{q} \rangle + i\langle \mathbf{L}_p, \mathbf{p} \rangle + iS_I} \quad (5.1)$$

which is obtained by applying two density operators to [Equation 3.20](#) and setting the generator field  $\mathbf{J}$  to zero afterwards, with

$$P(\mathbf{q}, \mathbf{p}) = \frac{cN^{-N}}{\sqrt{(2\pi)^{3N} \det \bar{C}_{pp}}} \exp\left(-\frac{1}{2}\mathbf{p}^T \bar{C}_{pp}^{-1} \mathbf{p}\right), \quad (5.2)$$

$$\mathbf{L}_q = -\sum_{j=1}^2 \vec{k}_j \otimes \vec{e}_j, \quad \mathbf{L}_p = -\sum_{j=1}^2 g_{qp}(t_j) \vec{k}_j \otimes \vec{e}_j, \quad (5.3)$$

$$S_I = -\sum_{j=1}^2 \vec{k}_j \int_0^{t_j} dt' g_{qp}(t_j, t') \left( \frac{\vec{u}_0}{\tau_s} - \vec{\nabla}_{q_j} \Phi \right). \quad (5.4)$$

This chapter is structured as follows. In the first section, we factorize the generating functional and introduce the mean field approach for gravitational interaction to derive the general expression of the **KFT** nonlinear density power spectrum. In the second section, we first ignore the friction and gravitational interactions. In the limit of  $\tau_s \rightarrow \infty$ , the freely streaming particles' linear and nonlinear density power spectra are derived and their small-scale asymptotic behavior is analyzed. In the third section, we add friction interaction back to the picture. For different values of  $\tau_s$ , we calculate the linear and nonlinear density power spectra and analyze their asymptotic behavior at small scales. In the fourth section, we welcome the gravitational interaction back into the play. For different values of  $\tau_s$ , we compute the gravitational density power spectrum and further determine the possibility of gravitational collapse and planetesimal formation. In the end, the universality of a  $k^{-3}$  tail for all the density power spectra calculated above is concluded, suggesting scale-invariant structure formation below a characteristic and time-dependent length scale, which is typically way below the resolution limit of numerical simulations at early times.

On a side note, since the **KFT** calculations are based on the simulation results derived in [Chapter 4](#), whose time and lengths are scaled in the unit of  $H$  and  $\Omega$ , we would like

to specify the dimensionless quantities will be used in [Chapter 5](#) and [Chapter 6](#) up front. In the following, the length scale is set in the unit of  $L = 0.1H$ , the wavenumber scale is set by  $\frac{2\pi}{L}$ , the time scale is set in the unit of  $\Omega^{-1}$ , which immediately means that the friction coefficient  $\tau_s$  in [Equation 5.2-5.4](#) is actually the dimensionless quantity Stokes number  $St = \tau_s \Omega$  in [Equation 2.25](#). Furthermore, since the gas density  $\rho_g$  and the speed of sound  $c_s$  remain constants in our simulation and further calculations, the Stokes number actually measures the size of dust particles. To keep its physical meaning clearer, we will keep the mark  $\tau_s$  for the actual meaning of the Stokes number  $St$  throughout all calculations in this thesis.

## 5.1 ANALYTICAL DERIVATION OF DENSITY POWER SPECTRUM

In this section, we start with the factorized generating functional in [Equation 5.1](#), to perform the integration. Notice if we ignore the interaction term  $S_I$ , the rest of the integral becomes a complete Fourier transformation of the [iPDF](#). Therefore, in the following, we aim to average the interaction term over the phase space coordinates and pull it in front of the integral. Eventually, we wish to write the density factorized generating functional as

$$Z^d[\mathbf{L}] = e^{i\langle S_I \rangle} \int d\mathbf{q} d\mathbf{p} P(\mathbf{q}, \mathbf{p}) e^{i\langle \mathbf{L}_q, \mathbf{q} \rangle + i\langle \mathbf{L}_p, \mathbf{p} \rangle} \approx e^{i\langle S_I \rangle} Z_0^d[\mathbf{L}], \quad (5.5)$$

with the gravity-free generating function  $Z_0^d[\mathbf{L}]$  defined above. By performing the integration in  $Z_0^d[\mathbf{L}]$  and combing the averaged interaction results, we derive the final expression for the [KFT](#) nonlinear density power spectrum.

Since the power spectrum only involves 2 particles, without losing generality, in the following, for any two indistinguishable particles, we mark them with subscripts  $_1$  and  $_2$ , while we mark the rest  $N - 2$  particles with subscripts  $_3, \dots, N$ .

### 5.1.1 KFT Nonlinear Density Power Spectrum

First, we focus on solving the gravity-free generating functional  $Z_0^d[\mathbf{L}]$  in [Equation 5.5](#). Integrating it over  $\mathbf{p}$  gives

$$\begin{aligned} Z_0^d[\mathbf{L}] &= \mathcal{C}N^{-N} \int d\mathbf{q} e^{i\langle \mathbf{L}_q, \mathbf{q} \rangle} \int d\mathbf{p} \frac{1}{\sqrt{(2\pi)^{3N} \det \bar{\mathbf{C}}_{pp}}} \exp\left(-\frac{1}{2} \mathbf{p}^T \bar{\mathbf{C}}_{pp}^{-1} \mathbf{p} + i\langle \mathbf{L}_p, \mathbf{p} \rangle\right) \\ &= \mathcal{C}N^{-N} \int d\mathbf{q} \exp(i\langle \mathbf{L}_q, \mathbf{q} \rangle) \exp\left(-\frac{1}{2} \mathbf{L}_p^T \bar{\mathbf{C}}_{pp} \mathbf{L}_p\right). \end{aligned} \quad (5.6)$$

Since the translation components  $\mathbf{L}_q, \mathbf{L}_p$  given in [Equation 5.3](#) only involve particles  $_1$  and  $_2$ , We can split the integral above by particle index as

$$Z_0^d[\mathbf{L}] = \mathcal{C}N^{-N}Q(\vec{k}_1, \vec{k}_2, t) \int dq_3 \dots dq_N \quad (5.7)$$

with the integration over all other particle positions  $\vec{q}_i$  with  $i = 3, \dots, N$  being

$$\int dq_3 \dots dq_N = V^{N-2} \quad (5.8)$$

where the factor  $V \equiv \int_{q_i}$  is the volume of the 3-dimensional space. The integral over  $\vec{q}_1$  and  $\vec{q}_2$  becomes

$$Q(\vec{k}_1, \vec{k}_2, t) = \int_{q_1} \int_{q_2} \exp\left(-i\left(\vec{k}_1 \cdot \vec{q}_1 + \vec{k}_2 \cdot \vec{q}_2\right)\right) \cdot \exp\left(-\frac{1}{2}\vec{L}_{p_1}\bar{C}_{p_1p_1}\vec{L}_{p_1} - \frac{1}{2}\vec{L}_{p_2}\bar{C}_{p_2p_2}\vec{L}_{p_2} - \vec{L}_{p_1}\bar{C}_{p_1p_2}\vec{L}_{p_2}\right) \quad (5.9)$$

Since the momentum covariance matrix  $\bar{C}_{pp}$  is generated from momenta correlation functions in terms of the absolute distance between two particles, we further define the relative position  $\vec{r} = \vec{q}_1 - \vec{q}_2$  and its absolute value  $r = |\vec{r}|$ , then rewrite

$$Q(\vec{k}_1, \vec{k}_2, t) = \int_{q_1} \exp\left(-i\left(\vec{k}_1 + \vec{k}_2\right) \cdot \vec{q}_1\right) \cdot \int_r \exp\left(-\frac{1}{2}\vec{L}_{p_1}\bar{C}_{p_1p_1}(0)\vec{L}_{p_1} - \frac{1}{2}\vec{L}_{p_2}\bar{C}_{p_2p_2}(0)\vec{L}_{p_2} - \vec{L}_{p_1}\bar{C}_{p_1p_2}(r)\vec{L}_{p_2} + i\vec{k}_2 \cdot \vec{r}\right) = (2\pi)^3\delta(\vec{k}_1 + \vec{k}_2)\mathcal{P}(k_1, t), \quad (5.10)$$

which leads to the final expression of the gravity-free generating functional

$$Z_0^d[\mathbf{L}] = \mathcal{C}N^{-N}V^{N-2}(2\pi)^3\delta(\vec{k}_1 + \vec{k}_2)\mathcal{P}(k_1, t), \quad (5.11)$$

with the gravity-free **KFT** nonlinear density power spectrum being

$$\mathcal{P}(k_1, t) = \int_r e^{-g_{4p}^2(t)k_1^2((m_1(r)-m_1(0))+\mu^2(m_2(r)-m_2(0)))} e^{-ik_1 r \mu}, \quad (5.12)$$

where  $\mu$  is the cosine of the angle enclosed by  $\vec{k}$  and  $\vec{r}$ .  $m_1(r)$  and  $m_2(r)$  are given in [Equation 4.75](#). Here we have applied the expression of  $\bar{C}_{pp}$  in position space given

in Equation 4.71 and Equation 4.75 to the result, and we have also used here that  $\vec{k}_1 + \vec{k}_2 = 0$  as required by the delta distribution in Equation 5.10.

Before moving on, we would like to discuss more about the gravity-free density power spectrum  $\mathcal{P}(k_1, t)$ . Denote its integrand as

$$I_c(k_1, r) = \exp(-g_{qp}^2(t)k_1^2((m_1(r) - m_1(0)) + \mu^2(m_2(r) - m_2(0)))) , \quad (5.13)$$

given the shape of  $m_1(r)$  and  $m_2(r)$  in Figure 4.17, we realize at the limit of  $r \rightarrow \infty$ , the integrand satisfies

$$\lim_{r \rightarrow \infty} I_c(k_1, r) = \exp(g_{qp}^2(t)k_1^2(m_1(0) + \mu^2 m_2(0))) \neq 0 \quad (5.14)$$

suggesting the result of the integral in Equation 5.12 is divergent. To guarantee a convergent density power spectrum, we split  $\mathcal{P}(k_1, t)$  from Equation 5.12 into

$$\mathcal{P}(k_1, t) = \int_r \left( e^{-g_{qp}^2(t)k_1^2(m_1(r) + \mu^2 m_2(r))} - 1 \right) e^{y - ik_1 r \mu} + \int_r e^{y - ik_1 r \mu} \quad (5.15)$$

with

$$y(t, \mu) = g_{qp}^2(t)k_1^2(m_1(0) + \mu^2 m_2(0)) \quad (5.16)$$

denoting the first term on the right-hand side of Equation 5.15 as  $\mathcal{P}_f(k_1, t)$ , we have

$$\begin{aligned} \mathcal{P}_f(k_1, t) &= 2\pi \int_0^\infty dr r^2 l(r) = 2\pi \int_0^\infty dr r^2 \cdot \\ &\int_{-1}^1 d\mu \left( e^{-g_{qp}^2(t)k_1^2(m_1(r) + \mu^2 m_2(r))} - 1 \right) e^{y - ik_1 r \mu} . \end{aligned} \quad (5.17)$$

At finite time  $t$  and wave number  $k_1$ , using the asymptotic approximations of  $m_1(r)$  and  $m_2(r)$  in Equation 4.77 and Equation 4.78, the expression in parentheses satisfies

$$\lim_{r \rightarrow \infty} \left( e^{-g_{qp}^2(t)k_1^2(m_1(r) + \mu^2 m_2(r))} - 1 \right) = \lim_{r \rightarrow \infty} g_{qp}^2(t)k_1^2(b_0 - b_1 + 3b_1\mu^2) \frac{0.04}{r^{7/3}} = 0 , \quad (5.18)$$

In the limit of  $r \rightarrow \infty$ , the integrand  $r^2 l(r)$  of Equation 5.17 becomes

$$\begin{aligned} \lim_{r \rightarrow \infty} r^2 l(r) &= \lim_{r \rightarrow \infty} 0.04 g_{qp}^2(t)k_1^2 \frac{r^2}{r^{7/3}} \int_{-1}^1 d\mu (b_0 - b_1 + 3b_1\mu^2) e^{y(t, \mu)k_1^2} \cos(k_1 r \mu) \\ &< 0.08 g_{qp}^2(t)k_1^2 (b_0 + 2b_1) e^{y(t, 0)k_1^2} \lim_{r \rightarrow \infty} \frac{1}{r^{1/3}} \frac{\sin(k_1 r)}{k_1 r} = 0 , \end{aligned} \quad (5.19)$$

which guarantees that  $\mathcal{P}_f(k_1, t)$  converges at large  $r$ . We have used here that  $y(t, \mu)$  is a negative, monotonically decreasing function of  $\mu^2$  with a maximum at  $y(t, 0)$ . The more detailed discussion in [Section A.2](#) shows that we can safely ignore the second integral on the right hand side of [Equation 5.15](#) and write down the final expression for the non-linearly evolved density power spectrum

$$\mathcal{P}_f(k_1, t) = \int_r \left( e^{-g_{qp}^2(t) k_1^2 (m_1(r) + \mu^2 m_2(r))} - 1 \right) e^{y - ik_1 r \mu} . \quad (5.20)$$

### 5.1.2 Average The Gravitational Interaction

Now that the gravity-free [KFT](#) nonlinear density power spectrum is found in [Equation 5.20](#), we analyze in this section the interaction term  $S_I$  in [Equation 5.4](#) and present the mean field approach for averaging the gravitational interactions between dust particles, which is a great simplification compared to other perturbation approaches and will be massively used throughout [Chapter 5](#) and [Chapter 6](#).

Notice the interaction term  $S_I$  has two important parts. One marked as  $S_{I1}$  in [Equation 5.21](#) comes from the friction between dust and a constant background gas field, the other one marked as  $S_{I2}$  represents the self gravitational interaction among dust particles,

$$\begin{aligned} S_{I1} &= - \sum_{j=1}^2 \vec{k}_j \int_0^{t_j} dt' g_{qp}(t_j, t') \frac{\vec{u}_0}{\tau_s} = \frac{\vec{k}_1 \cdot \vec{u}_0}{\tau_s} \left( \int_0^{t_2} dt' g_{qp}(t_2, t') - \int_0^{t_1} dt' g_{qp}(t_1, t') \right), \\ S_{I2} &= \sum_{j=1}^2 \vec{k}_j \int_0^{t_j} dt' g_{qp}(t_j, t') \vec{\nabla}_{q_j} \Phi = \vec{k}_1 \cdot \left( \int_0^{t_1} dt' g_{qp}(t_1, t') \vec{\nabla}_{q_1} \Phi - \int_0^{t_2} dt' g_{qp}(t_2, t') \vec{\nabla}_{q_2} \Phi \right). \end{aligned} \quad (5.21)$$

Here we have used the relation  $\vec{k}_1 + \vec{k}_2 = 0$  given by the Dirac delta function in [Equation 5.10](#). Since we are interested in the density power spectrum of two different particles at the same evolution time  $t_1 = t_2 = t$ , the above expressions instantly simplify to

$$\begin{aligned} S_{I1} &= 0, \\ S_{I2} &= \vec{k}_1 \cdot \int_0^t dt' g_{qp}(t, t') \left( \vec{\nabla}_{q_1} \Phi - \vec{\nabla}_{q_2} \Phi \right), \end{aligned} \quad (5.22)$$

which means the friction with the constant background gas field only contributes to the nonlinear density power spectrum through its propagator  $g_{qp}(t)$  in [Equation 3.39](#).

Therefore, the only expression left in the interaction term  $S_I$  is the gravitational interaction, thus we can rewrite

$$S_I = S_{I2} = \vec{k}_1 \cdot \int_0^t dt' g_{qp}(t, t') \left( \vec{\nabla}_{q_1} \Phi - \vec{\nabla}_{q_2} \Phi \right). \quad (5.23)$$

To investigate the effect of the interaction term on the density power spectrum, more generally, we set the initial time of switching on the self-gravity of dust particles as  $t_0$ , thus the expression of the interaction term  $S_I$  in [Equation 5.23](#) becomes

$$S_I = -\vec{k}_1 \cdot \int_{t_0}^t dt' g_{qp}(t, t') (\vec{f}_1(t') - \vec{f}_2(t')) \quad \text{with} \quad \vec{f}_i(t') = -\vec{\nabla}_{q_i} \Phi, \quad (5.24)$$

where  $\vec{f}_i(t)$  is the gravitational force acting on particle  $i$ . Dropping the time argument for brevity, we bring the force terms into the form

$$\vec{f}_1 - \vec{f}_2 = 2\vec{f}_{12} + \sum_{j=3}^N (\vec{f}_{1j} - \vec{f}_{2j}) \quad (5.25)$$

where  $\vec{f}_{ij}$  is the force on particle  $i$  due to particle  $j$ , and we have used  $\vec{f}_{12} - \vec{f}_{21} = 2\vec{f}_{12}$  by Newton's third law. If we can neglect three-point correlations for now, the second term on the right-hand side of [Equation 5.25](#) can be neglected in an isotropic random field since the forces exerted by particles  $j$  with  $j \geq 3$  on particles 1 and 2 will vanish on average because there is no preferred direction they could point to. We can then simplify the interaction term to

$$S_I = 2\vec{k}_1 \cdot \int_{t_0}^t dt' g_{qp}(t, t') \vec{\nabla}_1 \Phi_2(t') \quad (5.26)$$

containing the projection of the force  $\vec{f}_{12}$  between particles 1 and 2 on the wave vector  $\vec{k}_1$ .

To average the force term  $\vec{\nabla}_1 \Phi_2$ , first consider the Poisson equation

$$\nabla^2 \Phi = 4\pi G_0 \rho, \quad (5.27)$$

Where  $\rho(\vec{q}, t_1)$  is the particles' number density at position  $\vec{q}$  and time  $t_1$  given in [Equation 3.46](#). Now we write the gravitational potential  $\Phi(\vec{q})$  in the Fourier mode as

$$\Phi(\vec{q}) = \sum_{j=1}^N \int_{\mathbf{k}} \tilde{\Phi}_j e^{i\vec{k} \cdot (\vec{q} - \vec{q}_j)} \quad (5.28)$$

with  $\tilde{\Phi}_j$  being the Fourier mode of the gravitational potential of particle  $j$ . The Fourier transformation of Equation 5.27 on particle  $j$  thus becomes

$$-k^2 \tilde{\Phi}_j = 4\pi G_0, \quad (5.29)$$

and the gradient of the potential of particle 2 at the position of particle 1 is

$$\vec{\nabla}_1 \Phi_2(t) = -i4\pi G_0 \int_{\vec{k}} \frac{\vec{k}}{k^2} e^{i\vec{k} \cdot (\vec{q}_1(t) - \vec{q}_2(t))} \quad (5.30)$$

A seemingly radical approximation of the interaction term Equation 5.26 consists in replacing the potential gradient  $\vec{\nabla}_1 \Phi_2$  between the particles 1 and 2 by a suitable average. Simply averaging  $\vec{\nabla}_1 \Phi_2$  over all particle pairs would return zero because of the statistical isotropy of the particle distribution. It is thus important to realize that the interaction term in Equation 5.26 contains the projection of the potential gradient on the wave vector  $\vec{k}_1$  of the density mode considered. We thus need to calculate the projection  $\hat{k}_1 \cdot \vec{\nabla}_1 \Phi_2$  in a suitable average which does not vanish for particles correlated with the density mode  $\vec{k}_1$ .

For uncorrelated particles in a homogeneous random field, the direction of  $\vec{\nabla}_1 \Phi_2$  is random with respect to  $\vec{k}_1$ , thus its contribution to the average must vanish, while the correlated part remains. We thus weigh the potential gradient  $\vec{\nabla}_1 \Phi_2$  with the density correlation function  $\xi_\rho(|\vec{q}_1 - \vec{q}_2|)$  at time  $t$  and take the Fourier transform of the result to obtain the average Fourier component of the potential gradient at wave number  $\vec{k}_1$ ,

$$\langle \vec{\nabla}_1 \Phi_2 \rangle(k_1, t) = \int_{q_{12}} \xi_\rho(q_{12}, t) \vec{\nabla}_1 \Phi_2 e^{-i\vec{k}_1 \cdot \vec{q}_{12}} \quad (5.31)$$

with  $\vec{q}_{12} = \vec{q}_1 - \vec{q}_2$  and  $q_{12} = |\vec{q}_{12}|$ . Let us further write the Fourier representations of  $\xi_\rho(q_{12}, t)$  and  $\vec{\nabla}_1 \Phi_2$  as

$$\xi_\rho(q_{12}, t) = \int_{\vec{k}} P(\vec{k}, t) e^{i\vec{k} \cdot \vec{q}_{12}}, \quad \vec{\nabla}_1 \Phi_2 = -i4\pi G_0 \int_{\vec{k}_2} \frac{\vec{k}_2}{k_2^2} e^{i\vec{k}_2 \cdot \vec{q}_{12}}, \quad (5.32)$$

where  $P(\vec{k})$  represents the dust density power spectrum at evolution time  $t$ . Plugging them into Equation 5.31 we obtain

$$\begin{aligned} \langle \vec{\nabla}_1 \Phi_2 \rangle(k_1, t) &= -i4\pi G_0 \int_{\vec{k}} \int_{\vec{k}_2} P(\vec{k}, t) \frac{\vec{k}_2}{k_2^2} \int_{q_{12}} e^{i(\vec{k} + \vec{k}_2 - \vec{k}_1) \cdot \vec{q}_{12}} \\ &= -i4\pi G_0 \int_{\vec{k}} \frac{\vec{k}_1 - \vec{k}}{(\vec{k}_1 - \vec{k})^2} P(\vec{k}, t). \end{aligned} \quad (5.33)$$

The mean interaction term then can be written as

$$\langle S_I \rangle(\vec{k}_1, t) = 2\vec{k}_1 \cdot \int_{t_0}^t dt' g_{qp}(t, t') \langle \vec{\nabla}_1 \Phi_2 \rangle(k_1, t'), \quad (5.34)$$

with the averaged potential gradient in the direction of the wave vector  $\vec{k}_1$  as

$$\hat{k}_1 \cdot \langle \vec{\nabla}_1 \Phi_2 \rangle(k_1, t') = -\frac{iG_0}{\pi k_1} \int_0^\infty dk k^2 P(k, t') J\left(\frac{k}{k_1}\right), \quad (5.35)$$

where

$$J(y) = 1 + \frac{1-y^2}{2y} \ln \frac{1+y}{|1-y|}. \quad (5.36)$$

Thus we have averaged the gravitational interaction term over the phase space coordinates and left it a function of wavenumber  $k_1$  and evolution time  $t$ . Pulling it out of the factorized generating functional in [Equation 5.1](#) and combining with the results in [Section 5.1.1](#) gives the final expression of  $Z^d[\mathbf{L}]$  as

$$Z^d[\mathbf{L}] = \mathcal{C} N^{-N} V^{N-2} (2\pi)^3 \delta(\vec{k}_1 + \vec{k}_2) e^{i\langle S_I \rangle} \mathcal{P}_f(k_1, t) \quad (5.37)$$

with the full [KFT](#) nonlinearly evolved density power spectrum being

$$\mathcal{P}_g(k_1, t) = e^{i\langle S_I \rangle} \mathcal{P}_f(k_1, t). \quad (5.38)$$

Due to the complicated form of  $\mathcal{P}_g(k_1, t)$ , in the following sections, we will analyze the full [KFT](#) nonlinear density power spectrum step by step. In [Section 5.2](#), we calculate the linear and nonlinear free density power spectrum for freely streaming dust particles and introduce the new asymptotic method to analyze its small-scale asymptotic behavior. In [Section 5.3](#), we further consider adding the friction with the constant background gas field to the system and compute the friction density power spectrum using the same method developed in the last section. In [Section 5.4](#), we finally present the analysis of the full [KFT](#) density power spectrum considering both friction and gravitational interactions and extract the information on gravitational collapse for different strengths of friction in the system.

## 5.2 FREELY STREAMING PARTICLES

We start with the propagator  $g_{qp}(t, t')$  defined in Equation 3.39. Since the friction coefficient  $\tau_s$  measures the time a particle needs to adjust to the underlying flow, in the limit of  $\tau_s \rightarrow \infty$ , a particle needs forever to adjust to the underlying flow. The friction force in Equation 2.22 thus becomes

$$\lim_{\tau_s \rightarrow \infty} \vec{f} = \lim_{\tau_s \rightarrow \infty} -\frac{\vec{p} - \vec{u}_0}{\tau_s} = 0, \quad (5.39)$$

meaning there is then no friction between dust particles and the background gas. The corresponding free propagator becomes

$$\lim_{\tau_s \rightarrow \infty} g_{qp}(t, t') = g_0(t, t') = \lim_{\tau_s \rightarrow \infty} \tau_s \left( 1 - \exp\left(-\frac{t-t'}{\tau_s}\right) \right) = \lim_{\tau_s \rightarrow \infty} \tau_s \frac{t-t'}{\tau_s} = t-t' \quad (5.40)$$

Now if we further ignore the gravitational interaction embedded in the interaction term  $S_I$  and require

$$S_{I\text{free}} = 0, \quad (5.41)$$

then we get the exact dynamic setup of freely streaming particles. Their KFT nonlinear density power spectrum becomes

$$\mathcal{P}_{\text{free}}(k_1, t) = \int_{\mathbf{r}} \left( e^{-g_0^2(t)k_1^2(m_1(\mathbf{r})+\mu^2 m_2(\mathbf{r}))} - 1 \right) e^{g_0^2(t)k_1^2(m_1(0)+\mu^2 m_2(0)) - ik_1 \mathbf{r} \cdot \boldsymbol{\mu}}. \quad (5.42)$$

In this section, we first derive the expression of the linear free density power spectrum  $\mathcal{P}_{\text{lin}}(k_1, t)$  for the freely streaming particles at a very early evolution time and analyze its  $k^{-1}$  small-scale asymptotic behavior. Then we return to the nonlinear free density power spectrum  $\mathcal{P}_{\text{free}}(k_1, t)$  by employing a new analytical asymptotic method developed by Dr. Sara Konrad in Konrad [25]. Furthermore, for the nonlinear density power spectrum, we analyze the time dependence of its  $k^{-3}$  small-scale asymptotic behavior and conclude that the structure in a system filled by freely streaming particles first accumulates until it reaches its maximum and then dissipates at small scales.

## 5.2.1 Linear Density Power Spectrum

At very early times, the free propagator satisfies  $g_0(t) = t \rightarrow 0$ . The exponential in Equation 5.42 can thus be Taylor approximated to first order,

$$\mathcal{P}_{\text{free}}(k_1, t) \approx \mathcal{P}_{\text{lin}}(k_1, t) = -g_0^2(t)k_1^2 \int_r (m_1(r) + \mu^2 m_2(r)) e^{-ik_1 r \mu}. \quad (5.43)$$

Integrating it over the spherical coordinates  $\mu$  and  $\varphi$  gives

$$\mathcal{P}_{\text{lin}}(k_1, t) = -4\pi g_0^2(t) \int_0^\infty dr \left[ \left( \frac{6b_1 \sin(k_1 r)}{k_1 r} - 6b_1 \cos(k_1 r) \right) \zeta_{\text{pp}}(r) \right. \\ \left. \underbrace{-(b_0 + 2b_1)k_1 r \sin(k_1 r) \zeta_{\text{pp}}(r)}_{(1)} \right]. \quad (5.44)$$

The integral over (1) can be carried out to give

$$4\pi g_0^2(t) \int_0^\infty dr (b_0 + 2b_1)k_1 r \sin(k_1 r) \zeta_{\text{pp}}(r) = g_0^2 k_1^2 (b_0 + 2b_1) P_0(k_1) \quad (5.45)$$

with the averaged initial momentum power spectrum  $P_0(k_1)$  defined in [Equation 4.67](#).

Since  $P_0(k_1) \propto k^{-2/3}$  at small wave numbers, i.e. at large scales, the integral (1) is proportional to  $k_1^{4/3}$  when  $k_1$  is small. On the other hand, substituting  $r \rightarrow r_1/k_1$  in [Equation 5.44](#) gives

$$\mathcal{P}_{\text{lin}}(k_1, t) = -\frac{4\pi g_0^2(t)}{k_1} \int_0^\infty dr_1 \zeta_{\text{pp}} \left( \frac{r_1}{k_1} \right) \cdot \\ \left( \frac{6b_1 \sin(r_1)}{r_1} - 6b_1 \cos(r_1) - (b_0 + 2b_1)r_1 \sin(r_1) \right). \quad (5.46)$$

When  $k_1 \rightarrow 0$ , according to [Equation 4.76](#), we have  $\zeta_{\text{pp}}(r_1/k_1) \propto (k_1/r_1)^{7/3}$ , thus the linear density power spectrum satisfies  $\mathcal{P}_{\text{lin}}(k_1, t) \propto k_1^{4/3}$ , which coincides with the conclusion on the integral over (1). For  $k_1 \rightarrow \infty$ , the result of the integral in [Equation 5.46](#) can be shown to be independent of  $k_1$  in [Section A.1.1](#), thus the density power spectrum satisfies  $\mathcal{P}_{\text{lin}}(k_1, t) \propto k_1^{-1}$  for small scales.

[Figure 5.1](#) shows the linear free density power spectrum  $\mathcal{P}_{\text{lin}}(k_1, t)$  defined in [Equation 5.44](#) at  $t = 0.4\pi$  together with its asymptotic behavior at both small and large  $k_1$ , which verifies our asymptotic analysis for both small and large scales. Note that the radical change of the curve around scale  $k_1 \approx 10$  is due to a sign shift of computing [Equation 5.44](#). Though the power spectrum is expected to be positive, the integral over the linear Taylor expansion of the modified density power spectrum in [Equation 5.20](#) could as well become negative.

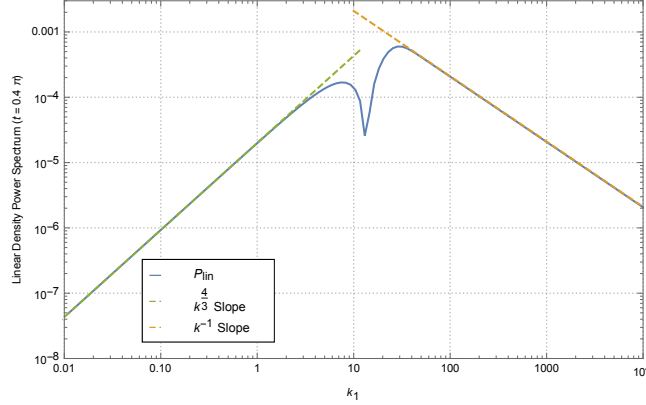


Figure 5.1: Illustration of the shape of the linear density power spectrum  $\mathcal{P}_{\text{lin}}(k_1, t)$  (blue line) and its asymptotic behavior at small (yellow dashed line) and large scales (green dashed line).

### 5.2.2 Free Density Power Spectrum

We now return to the non-linear free density power spectrum in Equation 5.42 and integrate over the angular coordinates  $\varphi$  and  $\mu$  to write

$$\mathcal{P}_{\text{free}}(k_1, t) = 2\pi \int_0^\infty dr r^2 l(r) \quad (5.47)$$

as in Equation 5.17 with the function  $l(r)$  being

$$\begin{aligned} l(r) = & \frac{\sqrt{\pi}}{2} \frac{\exp\left(g_0^2(t)k_1^2(m_1(r) - m_1(0)) + \frac{k_1^2 r^2}{4g_0^2(t)k_1^2(m_2(0) - m_2(r))}\right)}{\sqrt{g_0^2(t)k_1^2(m_2(0) - m_2(r))}} \\ & \left[ -\text{erf}\left(\frac{k_1 r - 2ig_0^2(t)k_1^2(m_2(0) - m_2(r))}{2\sqrt{g_0^2(t)k_1^2(m_2(0) - m_2(r))}}\right) + \text{erf}\left(\frac{k_1 r + 2ig_0^2(t)k_1^2(m_2(0) - m_2(r))}{2\sqrt{g_0^2(t)k_1^2(m_2(0) - m_2(r))}}\right) \right] + \\ & \frac{\sqrt{\pi}}{2} \frac{\exp\left(g_0^2(t)k_1^2 m_1(0) + \frac{k_1^2 r^2}{4g_0^2(t)k_1^2 m_2(0)}\right)}{\sqrt{g_0^2(t)k_1^2 m_2(0)}} \\ & \left[ \text{erf}\left(\frac{k_1 r - 2ig_0^2(t)k_1^2 m_2(0)}{2\sqrt{g_0^2(t)k_1^2 m_2(0)}}\right) - \text{erf}\left(\frac{k_1 r + 2ig_0^2(t)k_1^2 m_2(0)}{2\sqrt{g_0^2(t)k_1^2 m_2(0)}}\right) \right], \end{aligned} \quad (5.48)$$

where  $\text{erf}(z)$  represents the error function. Figure 5.2 shows the function  $r^2 l(r)$  and its large-scale asymptotic behavior at three different scales at time  $t = 4\pi$ . With in-

creasing wave number,  $r^2 l(r)$  more and more resembles a delta distribution. In all the plots, the function decreases to negligibly small values with an envelope proportional to  $r^{-4/3}$ , confirming that our results for the non-linear density power spectrum  $\mathcal{P}_{\text{free}}(k_1, t)$  as shown in Equation 5.19 converge.

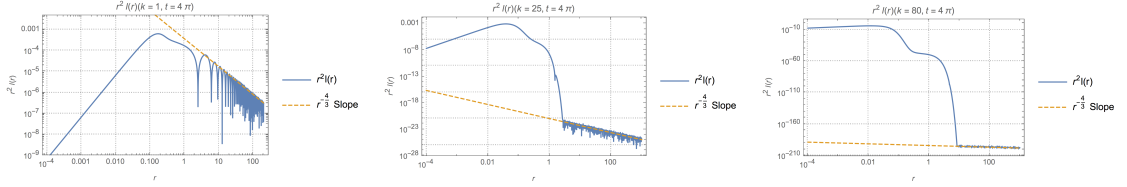


Figure 5.2: The radial integrand of the free power spectrum,  $r^2 l(r)$ , is shown here for  $k_1 = 1.0$ ,  $k_1 = 25.0$  and  $k_1 = 80.0$  (blue lines) at time  $t = 4\pi$ . The yellow dashed lines indicate the  $r^{-4/3}$  slope.

Figure 5.3 shows the directly integrated function  $\mathcal{P}_{\text{free}}(k_1, t)$  and compares it to the density power spectrum  $\mathcal{P}_{\text{lin}}(k_1, t)$  linearly evolved to  $t = 4\pi$ . At large scales, it reproduces the  $k^{4/3}$  slope of  $\mathcal{P}_{\text{lin}}(k_1, t)$ . At small scales, however, nonlinear evolution causes the spectrum to fall off like  $k^{-3}$ . This asymptotic slope sets in near  $k \approx 25$ , which coincides with the scale where  $r^2 l(r)$  in Figure 5.2 changes shape.

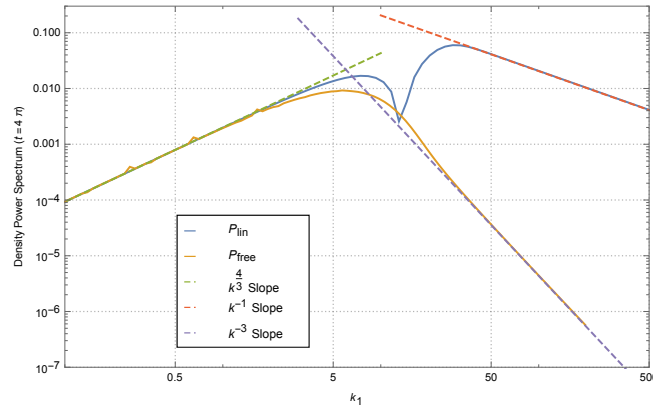


Figure 5.3: The linearly evolved density power spectrum  $\mathcal{P}_{\text{lin}}(k_1, t)$  (blue line) compared to the free non-linear density power spectrum  $\mathcal{P}_{\text{free}}(k_1, t)$  (yellow line). The asymptotic behaviour at large (green dashed line) and small scales is also indicated. At small scales, the linear power spectrum falls off like  $k^{-1}$  (red dashed line), while the free non-linear power spectrum develops a  $k^{-3}$  slope (purple dashed line).

To better understand the  $k^{-3}$  behaviour at small scales, we adopt an asymptotic analysis developed by Konrad [25]. Consider integrals of the form

$$P(k) = \int_{\mathcal{D}} e^{-|k|^s f(x)} g(x) e^{i\vec{k} \cdot \vec{x}} dx, \quad s \geq 2 \quad (5.49)$$

over a possibly unbounded domain  $D \subset \mathbb{R}^3$ . Following Konrad [25], if the function  $f(x)$  satisfies the three criteria that

1.  $f(x)$  has an isolated global minimum at  $\vec{x} = 0$ ;
2.  $f(x)$  is quadratically integrable on  $\mathbb{R}^3$ ; and
3. the Hessian matrix  $A = \partial_i \partial_j f(x)$  exists at the origin and is positive definite,

then its asymptotic expansion in the limit  $k \rightarrow \infty$  can be expressed by

$$P(k) \sim g(0)e^{-|k|^s f(0)} \sqrt{\frac{(2\pi)^3}{|k|^{3s} \det A}} \exp\left(-\frac{k^T A^{-1} k}{2|k|^s}\right) \quad \text{as } |k| \rightarrow \infty. \quad (5.50)$$

We rewrite the non-linear density power spectrum in equation 5.42 as

$$\begin{aligned} \mathcal{P}_{\text{free}}(k_1, t) = & \int_r e^{-g_0^2(t) k_1^2 ((m_1(r) - m_1(0)) + \mu^2 (m_2(r) - m_2(0)))} e^{-ik_1 r \mu} \\ & - \int_r e^{g_0^2(t) k_1^2 (m_1(0) + \mu^2 m_2(0))} e^{-ik_1 r \mu}. \end{aligned} \quad (5.51)$$

As will be shown in Equation A.24, the second term drops to zero exponentially for  $k_1 \rightarrow \infty$ , allowing us to restrict the asymptotic analysis to the first of these integrals. The functions  $f(x)$  and  $g(x)$  from Equation 5.49 become

$$f(r) = g_0^2(t) ((m_1(r) - m_1(0)) + (m_2(r) - m_2(0)) \mu^2), \quad g(r) = 1. \quad (5.52)$$

Requirements 1 and 2 are obviously satisfied based on the analysis of  $m_1(r)$  and  $m_2(r)$  in Equation 4.77, Equation 4.78 and Figure 4.17. To examine requirement 3, we expand  $f(r)$  into a Taylor series around  $r = 0$ ,

$$f(r) = (b_1 - b_0 - 3\mu^2 b_1) \frac{g_0^2(t)}{2^{5/6} \pi^2} \bar{\sigma}^{7/3} \Gamma\left(\frac{3}{2}\right) \sum_{n=1}^{\infty} \frac{\Gamma\left(\frac{7}{6} + n\right)}{\Gamma\left(\frac{3}{2} + n\right)} \frac{\left(-\frac{\bar{\sigma}^2 r^2}{2}\right)^n}{n!}, \quad (5.53)$$

where we have used the Taylor series of a hypergeometric function as

$${}_1F_1(a, b, z) = \sum_{n=0}^{\infty} \frac{a(a+1) \cdots (a+n-1)}{b(b+1) \cdots (b+n-1)} \frac{z^n}{n!} = \frac{\Gamma\left(\frac{3}{2}\right)}{\Gamma\left(\frac{7}{6}\right)} \sum_{n=0}^{\infty} \frac{\Gamma\left(\frac{7}{6} + n\right)}{\Gamma\left(\frac{3}{2} + n\right)} \frac{z^n}{n!}. \quad (5.54)$$

Thus the Hessian  $A$  at the origin reduces to the matrix

$$A = \partial_i \partial_j f(r)|_{r=0} = g_0^2 \sigma_1^2 [(b_0 - b_1) \mathbb{1}_3 + 3b_1 \hat{k}_1 \otimes \hat{k}_1], \quad \sigma_1^2 = \frac{\bar{\sigma}^{13/3}}{2^{5/6} \pi^2} \frac{\Gamma\left(\frac{3}{2}\right) \Gamma\left(\frac{13}{6}\right)}{\Gamma\left(\frac{5}{2}\right)},$$

(5.55)

with  $b_0 > b_1 > 0$ . This shows that requirement 3 is fulfilled.

The nonlinear free density power spectrum  $\mathcal{P}_{\text{free}}(k_1, t)$  in Equation 5.42 thus meets all three requirements. Since  $f(0) = 0$  and  $g(0) = 1$ , its asymptotic expansion for  $k_1 \rightarrow \infty$  reads

$$\mathcal{P}_{\text{free}}(k_1) \sim \frac{1}{|k_1|^3} \sqrt{\frac{(2\pi)^3}{\det A}} \exp\left(-\frac{k_1^\top A^{-1} k_1}{2|k_1|^2}\right) = \frac{\mathcal{P}^{(0)}(t)}{|k_1|^3}. \quad (5.56)$$

This  $k^{-3}$  asymptotic behavior only depends on the number of spatial dimensions ( $d = 3$ ) and the shape of the function  $f(r)$ . Since  $f(r)$  solely depends on the initial momentum correlation functions of dust particles, the small-scale tail proportional to  $k^{-3}$  is entirely fixed by the initial conditions of the particle ensemble. As time passes, the non-linear free density power spectrum will thus always approach the  $k^{-3}$  asymptotic behavior. Let us now explore its time dependence.

### 5.2.3 Time Dependence of Small Scale Behaviours

Figure 5.11 shows the non-linear density power spectrum  $\mathcal{P}_{\text{free}}(k_1, t)$  at four different times. All these spectra develop the universal  $k^{-3}$  slope at small scales. At larger scales, the spectrum grows with time, while it first increases then decreases at small scales. This reflects that structures form by correlated, freely streaming particles. Their collective streaming builds up structures at all scales first, but then destroys them later on scales small enough for particle streams to cross.

To better understand how the amplitude of the  $k^{-3}$  asymptotic tail depends on time, the left panel of Figure 5.5 shows the power  $k_1^3 \mathcal{P}_{\text{free}}(k_1, t)$  with the wave numbers  $k_0$  marked by points where the  $k^{-3}$  asymptotic slope is reached. As time proceeds,  $k_0$  moves towards larger scales (smaller  $k$ ), while the amplitude of the  $k^{-3}$  tail first increases, then decreases. The relation between  $k_0$  and time  $t$  is given in the right panel of Figure 5.5. Its decreasing slope shows that structure formation rapidly proceeds towards small scales first and then slows down. Additionally, we mention that since the free propagator has the form  $g_0(t) = t$ , the right panel of Figure 5.5 furthermore represents the relation between the starting scale  $k_0$  and the general propagator. Therefore, in the following sections, if we replace  $g_0(t)$  by  $g_{\text{qp}}(t)$ , the relation between  $k_0$  and  $g_{\text{qp}}(t)$  remains the same as shown in this plot.

We further evaluate the amplitude  $\mathcal{P}^{(0)}$  of the asymptotic tail defined in Equation 5.56. The Hessian  $A$  in Equation 5.55 has the determinant

$$\det A = (b_0 - b_1)^2 (b_0 + 2b_1) g_0^6(t) \sigma_1^6 \quad (5.57)$$

and the inverse

$$A^{-1} = \frac{1}{g_0^2(t) \sigma_1^2} \frac{1}{b_0 - b_1} \left( \mathbb{1}_3 - \frac{3b_1}{(b_0 + 2b_1)} \hat{k}_1 \otimes \hat{k}_1 \right), \quad (5.58)$$

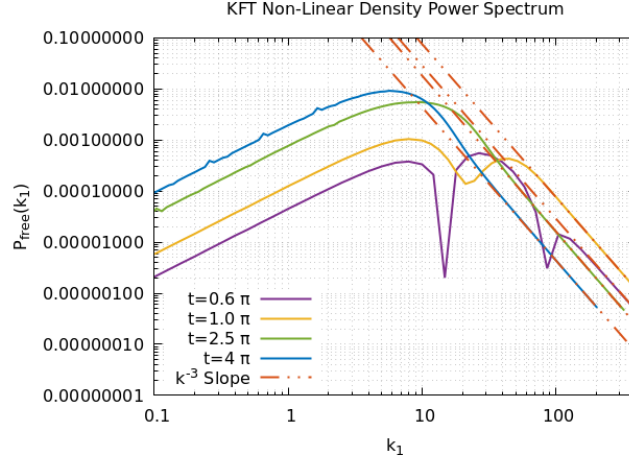


Figure 5.4: Non-linear density power spectra  $\mathcal{P}_{\text{free}}(k_1, t)$  together with their small scale asymptotic behavior (orange dash-dotted lines) at the four different times  $t = 0.6\pi$  (purple line),  $t = 1\pi$  (yellow line),  $t = 2.5\pi$  (green line) and  $t = 4\pi$  (blue line).

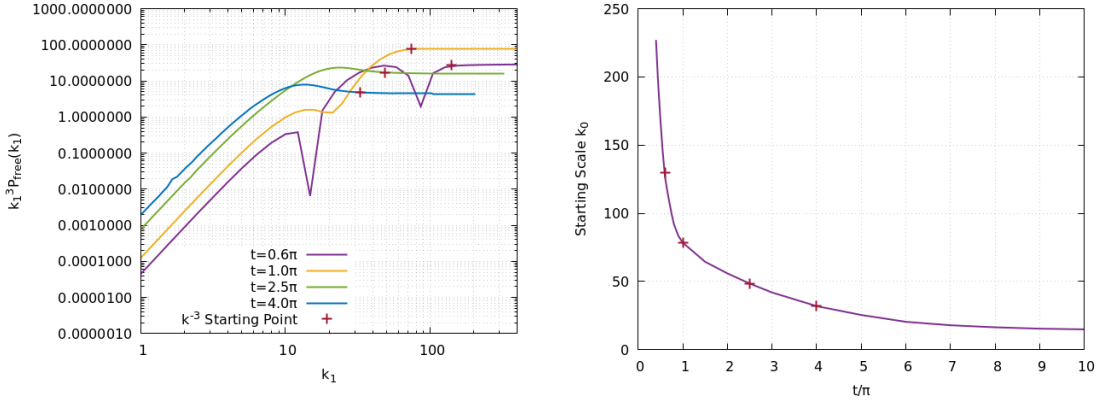


Figure 5.5: Left: Power  $k_1^3 \mathcal{P}_{\text{free}}(k_1, t)$  as a function of  $k_1$  at the four different times  $t = 0.6\pi$  (purple line),  $t = 1\pi$  (yellow line),  $t = 2.5\pi$  (green line) and  $t = 4\pi$  (blue line). The red dots mark the wave number  $k_0$  where the  $k^{-3}$  slope is reached. Dependence of  $k_0$  on time, with the points indicating  $k_0$  for the four different times given.

thus the amplitude  $\mathcal{P}^{(0)}(t)$  becomes

$$\mathcal{P}^{(0)}(t) = \frac{1}{g_0^3(t)\sigma_1^3(b_0 - b_1)} \sqrt{\frac{(2\pi)^3}{b_0 + 2b_1}} \exp\left(-\frac{1}{2g_0^2(t)\sigma_1^2(b_0 + 2b_1)}\right). \quad (5.59)$$

It reaches a maximum with height

$$\mathcal{P}_{\text{max}}^{(0)} = \left(\frac{6\pi}{e}\right)^{3/2} \frac{b_0 + 2b_1}{b_0 - b_1} \approx 75.53 \quad \text{at} \quad t_{\text{max}} = \sigma_1^{-1} \sqrt{\frac{1}{3(b_0 + 2b_1)}} \approx 0.97\pi. \quad (5.60)$$

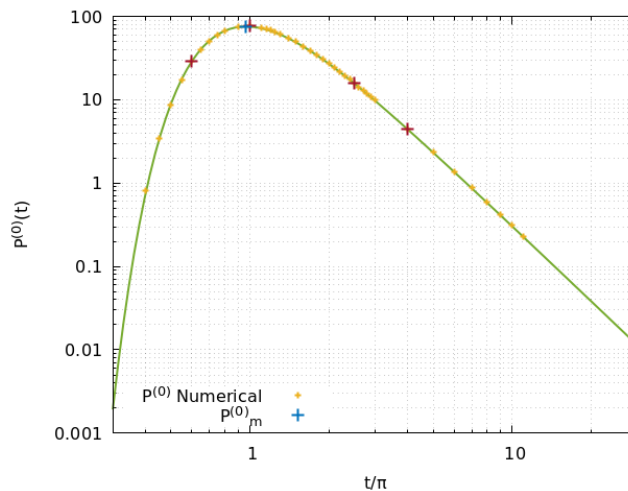


Figure 5.6: Amplitude  $\mathcal{P}^{(0)}(t)$  for the asymptotic  $k^{-3}$  tail of the free, non-linear power spectrum as a function of time  $t$ . The blue point indicates its maximum  $\mathcal{P}_{\max}^{(0)}$  at time  $t_{\max}$  according to Equation 5.60. The yellow points are obtained by direct integration of Equation 5.20. The four red points mark the amplitudes at the times  $t = 0.6\pi$ ,  $t = 1.0\pi$ ,  $t = 2.5\pi$ , and  $t = 4.0\pi$ .

Figure 5.16 shows the amplitude  $\mathcal{P}^{(0)}(t)$  for the  $k^{-3}$  asymptotic tail as a function of time, calculated analytically by Equation 5.59 and numerically by direct integration of Equation 5.42. Their perfect match confirms the asymptotic result. The rapid increase at early times shows that small-scale structures form rapidly. After  $t_{\max}$ , the amplitude of the  $k^{-3}$  slope decreases, showing that small-scale structures are destroyed after formerly convergent particle streams cross and begin diverging.

### 5.3 FRICTION DENSITY POWER SPECTRUM

In Section 5.1.2, we conclude that the effect of the friction interaction to the density power spectrum only shows up in the propagator  $g_{qp}(t, t')$  by Equation 3.39. Thus to evaluate  $\mathcal{P}_f(k_1, t)$  in Equation 5.20, we first study the value of the friction coefficient  $\tau_s$  in  $g_{qp}(t)$ .

Figure 5.7 shows the shape of  $g_{qp}(t)$  with five different friction coefficients  $\tau_s = 0.25, \tau_s = 0.5, \tau_s = 1.0, \tau_s = 5.0, \tau_s = 10.0$  and the shape of the free propagator  $g_0(t) = t$ . Compared to the free propagator, the friction coefficient  $\tau_s$  sets an upper limit for  $g_{qp}(t)$ . The larger  $\tau_s$  becomes, the more similar  $g_{qp}(t)$  and  $g_0(t)$  become. This result makes perfect sense since  $\tau_s$  defined in Equation 2.23 and Equation 2.25 directly relates to the size of the particles. The larger the particles become, the less coupled they are to the gas and the weaker friction drag they feel. At the limit of  $\tau_s \rightarrow \infty$ , the friction disappears and it recovers the free propagator  $g_0(t)$ .

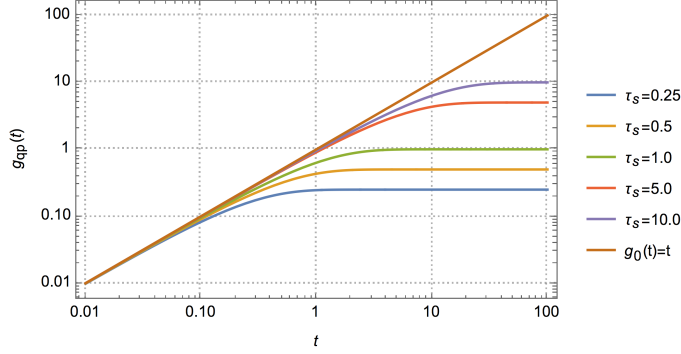


Figure 5.7: This plot compares the propagator  $g_{qp}(t)$  in Equation 3.39 respectively at  $\tau_s = 0.25$  (blue line),  $\tau_s = 0.5$  (yellow line),  $\tau_s = 1.0$  (green line),  $\tau_s = 5.0$  (red line) and  $\tau_s = 10.0$  (purple line) together with the freely streaming propagator  $g_0(t) = t$  (brown line).

In this section, we still ignore the gravitational interaction among dust particles, yet return to the full expression of the propagator  $g_{qp}(t, t')$  in Equation 3.39 and the nonlinear density power spectrum  $\mathcal{P}_f(k_1, t)$  in Equation 5.20 to reconsider the friction interaction between dust and the constant background gas field in the system. We start with deriving the expression of the linear density power spectrum  $\mathcal{P}_{\text{lin}}(k_1, t)$  for very small dust particles and conclude the development of the  $k^{-1}$  tail at small scales. Next, for larger dust particles at finite evolution time, we compute the nonlinear density power spectrum  $\mathcal{P}_f(k_1, t)$  by employing the same asymptotic analysis shown in Section 5.2.2. In the end, we analyze the time and particle-size dependence for the small-scale  $k^{-3}$  asymptotic behaviors of  $\mathcal{P}_f(k_1, t)$  and find a critical particle size  $\tau_s^c$  pure mathematically which corresponds to the maximum small scale structure formation.

### 5.3.1 Linear Power Spectrum At Small $\tau_s$

We start with very small particles, since the propagator always satisfies  $g_{qp}(t, t') \leq \tau_s$ , at the limit of  $\tau_s \rightarrow 0$ , the exponential in Equation 5.20 can be Taylor approximated to the first order,

$$\mathcal{P}_f(k_1, t) \approx \mathcal{P}_{\text{lin}}(k_1, t) = -g_{qp}^2(t) k_1^2 \int_r (m_1(r) + \mu^2 m_2(r)) e^{-ik_1 r \mu} \quad (5.61)$$

after integrating over the spherical coordinates  $\mu$  and  $\phi$ , it becomes

$$\mathcal{P}_{\text{flin}}(k_1, t) = -4\pi g_{\text{qp}}^2(t) \int_0^\infty dr \left[ \left( \frac{6b_1 \sin(k_1 r)}{k_1 r} - 6b_1 \cos(k_1 r) \right) \zeta_{\text{pp}}(r) - (b_0 + 2b_1)k_1 r \sin(k_1 r) \zeta_{\text{pp}}(r) \right], \quad (5.62)$$

which has the identical expression as Equation 5.44 just with a different propagator  $g_{\text{qp}}(t)$ . Thus we conclude that the linear density power spectrum also satisfies  $\mathcal{P}_{\text{flin}}(k_1, t) \propto k_1^{\frac{4}{3}}$  at large scales, and at small scales, it follows  $\mathcal{P}_{\text{flin}}(k_1, t) \propto k_1^{-1}$ .

Figure 5.8 shows the linear density power spectrum  $\mathcal{P}_{\text{flin}}(k_1, t)$  defined in Equation 5.62 with parameter  $\tau_s = 0.01$  at  $t = 0.001$  and  $t = 10.0$  together with their asymptotic behaviors at both small and large  $k_1$ , which verifies our previous conclusions at both small and large scales. The fact that the value of  $\mathcal{P}_{\text{flin}}(k_1, t)$  becomes larger at later times implies that there is continuous structure formation at all scales as time proceeds, while the shape of the propagator  $g_{\text{qp}}(t)$  in Figure 5.7 further indicates that the structure formation for small size particles already rapidly occurs at a very early stage of evolution.

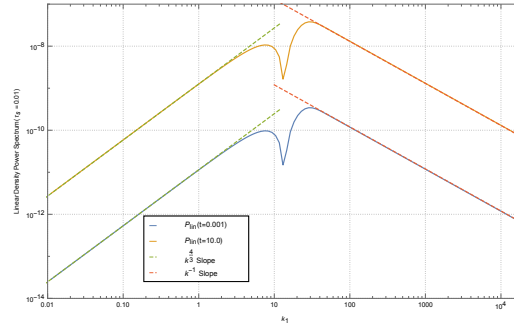


Figure 5.8: This plot illustrates the shape of linear density power spectrum  $\mathcal{P}_{\text{flin}}(k_1, t)$  with  $\tau_s = 0.01$  at evolution time  $t = 0.001$  (blue line) and  $t = 10.0$  (yellow line). Their asymptotic behavior at small and large scales are represented by the green and red dashed lines.

Figure 5.9 shows the shape of the linear density power spectrum  $\mathcal{P}_{\text{flin}}(k_1, t)$  at evolution time  $t = 10.0$  with friction coefficients  $\tau_s = 0.1$ ,  $\tau_s = 0.01$  and  $\tau_s = 0.001$  together with their asymptotic behaviour at small and large  $k_1$ . For all three values of  $\tau_s$  we consider here, the propagator satisfies  $g_{\text{qp}}(t = 10.0) \approx \tau_s$ . The comparison of the three curves suggests that at the range of small  $\tau_s$ , relatively larger dust particles that experience weaker friction actually bring more power to the KFT linear density power spectrum, meaning it stimulates more structure formation when the dust particles have more time to evolve and interact with the background gas.

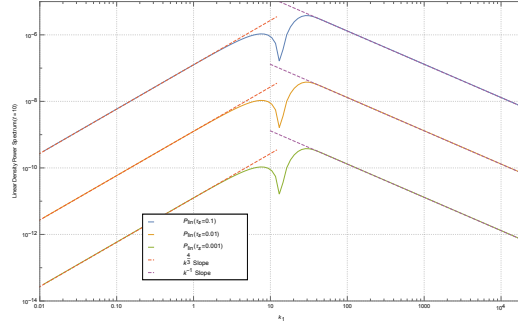


Figure 5.9: This plot illustrates the shape of linear density power spectrum  $\mathcal{P}_{\text{lin}}(k_1, t)$  at evolution time  $t = 10.0$  with friction coefficient  $\tau_s = 0.1$  (blue line),  $\tau_s = 0.01$  (yellow line) and  $\tau_s = 0.001$  (green line). Their asymptotic behavior at small and large scales are represented by the red and purple dashed lines.

### 5.3.2 Non Linear Power Spectrum At Large $\tau_s$

When the friction coefficient  $\tau_s$  gets larger, the linear approximation of the density power spectrum  $\mathcal{P}_f(k_1, t)$  only remains true at a very early stage of evolution. In the limit of  $t \rightarrow 0$ , the propagator satisfies

$$\lim_{t \rightarrow 0} g_{\text{qp}}(t) = g_0(t) = t \rightarrow 0, \tag{5.63}$$

thus we return to the linear free density power spectrum  $\mathcal{P}_{\text{lin}}(k_1, t)$  in Equation 5.61. All analyses and asymptotic behavior we deduced in Section 5.2.1 remain true in this case.

While when the evolution time  $t$  gets larger, the linear approximation no longer holds, we need to return to the nonlinear density power spectrum  $\mathcal{P}_f(k_1, t)$  given in Equation 5.20. Integrating it over spherical coordinates  $\varphi$  and  $\mu$  to write

$$\mathcal{P}_f(k_1, t) = 2\pi \int_0^\infty dr r^2 l(r) \tag{5.64}$$

as in Equation 5.17 where  $l(r)$  has the same expression with Equation 5.48 with a different propagator  $g_{\text{qp}}(t)$ .

Figure 5.10 shows the direct integration of function  $\mathcal{P}_f(k_1, t)$  with friction coefficient  $\tau_s = 5.0$  and compares it to the linear density power spectrum  $\mathcal{P}_{\text{flin}}(k_1, t)$  in Equation 5.62 at evolution time  $t = 10.0$ . At large scales, it develops a  $k^{\frac{4}{3}}$  slope same as  $\mathcal{P}_{\text{flin}}(k_1, t)$ , while at smaller scales, the nonlinear growth becomes more important and the power spectrum develops a  $k^{-3}$  slope just as the nonlinear free power spectrum in Figure 5.3.

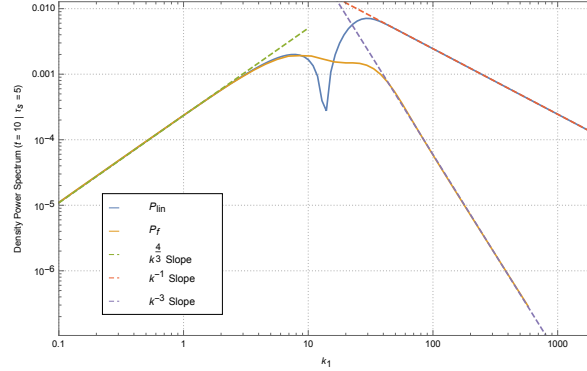


Figure 5.10: This plot compares the linear density power spectrum  $\mathcal{P}_{\text{lin}}(k_1, t)$  (blue line) with the nonlinear density power spectrum  $\mathcal{P}_f(k_1, t)$  (yellow line) together with their asymptotic behavior at large (green dashed line) and small scales. At small scales, the asymptotic behavior of the linear power spectrum is proportional to  $k^{-1}$  (red dashed line), while the nonlinear power spectrum develops a different  $k^{-3}$  slope (purple dashed line).

We can employ the same asymptotic analysis shown in [Section 5.2.2](#) to explain the  $k^{-3}$  behavior at small scales. Given that the only difference between  $\mathcal{P}_{\text{free}}(k_1, t)$  and  $\mathcal{P}_f(k_1, t)$  lies in the propagator  $g_{\text{qp}}(t)$ , we can immediately write down its asymptotic expansion for  $k_1 \rightarrow \infty$  as

$$\mathcal{P}_f(k_1) \sim \frac{1}{|k_1|^3} \sqrt{\frac{(2\pi)^3}{\det A_f}} \exp\left(-\frac{k_1^\top A_f^{-1} k_1}{2|k_1|^2}\right) = \frac{\mathcal{P}_f^{(0)}(t)}{|k_1|^3}, \quad (5.65)$$

where the new Hessian matrix  $A_f$  at the origin reads

$$A_f = g_{\text{qp}}^2(t) \sigma_1^2 [(b_0 - b_1)\mathbb{1}_3 + 3b_1 \hat{k}_1 \otimes \hat{k}_1], \quad (5.66)$$

and the new amplitude for the  $k^{-3}$  slope becomes

$$\mathcal{P}_f^{(0)}(t) = \frac{1}{g_{\text{qp}}^3(t) \sigma_1^3 (b_0 - b_1)} \sqrt{\frac{(2\pi)^3}{b_0 + 2b_1}} \exp\left(-\frac{1}{2g_{\text{qp}}^2(t) \sigma_1^2 (b_0 + 2b_1)}\right). \quad (5.67)$$

### 5.3.3 Time and Particle-Size Dependence At Small Scales

To investigate the time dependence of the nonlinear density power spectrum, [Figure 5.11](#) shows the direct integration of function  $\mathcal{P}_f(k_1, t)$  with friction coefficient  $\tau_s = 5.0$  at different evolution time  $t = 2.0$ ,  $t = 10.0$  and  $t = 100.0$ . We can see once

more that the  $k^{-3}$  asymptotic behavior at small scales is universal. The comparison of the three curves at different times shows that at larger scales, the power of the density field grows over time, while at smaller scales, the amplitude of the  $k^{-3}$  slope first increases then decreases, which indicates that structures formed by correlated particles interacting by friction build up at all scales during an earlier periods of evolution, yet as time proceeds, structures at small scales start being destroyed.

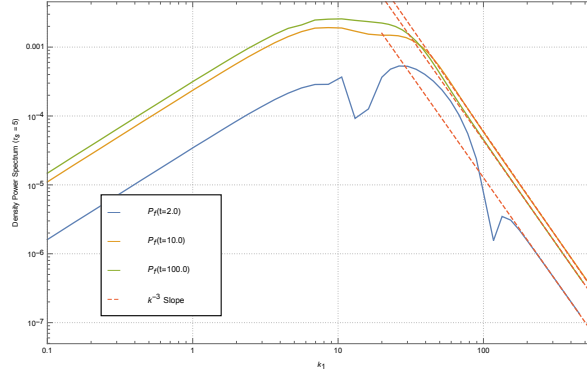


Figure 5.11: This plot shows the density power spectrum  $\mathcal{P}_f(k_1, t)$  with friction at evolution times  $t = 2.0$  (blue line),  $t = 10.0$  (yellow line) and  $t = 100.0$  (green line) with the friction coefficient  $\tau_s = 5.0$ . At small scales, they all develop  $k^{-3}$  slopes (red dashed lines).

To investigate how the size of particles affects the shape of the nonlinear density power spectrum, Figure 5.12 shows  $\mathcal{P}_f(k_1, t)$  at evolution times  $t = 2.0$  (left panel) and  $t = 10.0$  (right panel) with friction coefficients  $\tau_s = 5.0$ ,  $\tau_s = 10.0$  and  $\tau_s = 20.0$ . In the left panel, the power of the density field grows with the friction coefficient  $\tau_s$  for almost all the  $k_1$  concerned, which suggests that with the size of the particles becoming large and the corresponding friction between dust particles and the background gas becoming less effective, more structure formation occurs at all scales during a relatively earlier period of evolution. However, in the right panel, that is no longer the case. The nonlinear density power spectrum still becomes stronger with larger  $\tau_s$  on large scales, however, at small scales, the amplitude of the  $k^{-3}$  slope decreases with  $\tau_s$  getting larger, indicating more structure is being destroyed at small scales during a relatively later period of evolution for larger size particles that experience less friction drag from the background gas.

Notice in Figure 5.10, Figure 5.11 and Figure 5.12, the nonlinear density power spectrum  $\mathcal{P}_f(k_1, t)$  always gets stronger at large scales with larger friction coefficient  $\tau_s$  and longer evolution time  $t$ , while at small scales, it behaves in a more complicated manner.

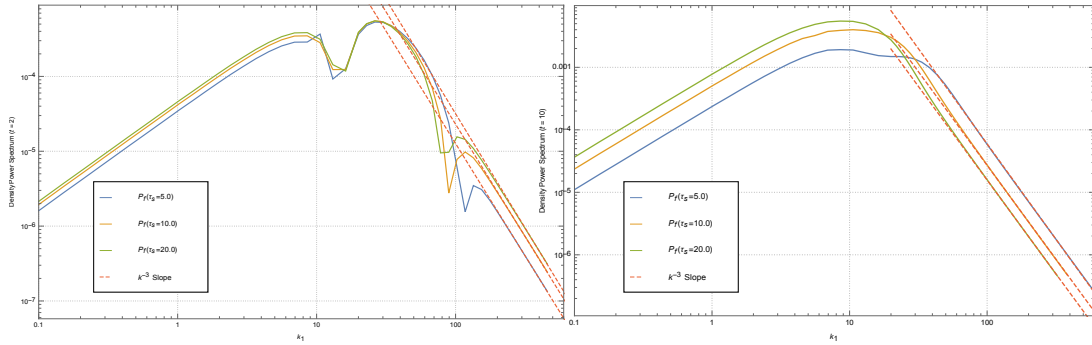


Figure 5.12: These two plots show the shape of the nonlinear density power spectrum  $\mathcal{P}_f(k_1, t)$  at evolution times  $t = 2.0$  (left panel) and  $t = 10.0$  (right panel) with the friction coefficients  $\tau_s = 5.0$  (blue line),  $\tau_s = 10.0$  (yellow line) and  $\tau_s = 20.0$  (green line) together with their small scale  $k^{-3}$  asymptotic behavior (red dashed lines).

To quantify the time and particle-size dependency of the small-scale asymptotic behaviors, we first require the amplitude of the  $k^{-3}$  slope satisfies  $\frac{d\mathcal{P}_f^{(0)}(t)}{dt} = \frac{d\mathcal{P}_f^{(0)}}{dg_{qp}} \frac{dg_{qp}}{dt} = 0$ , its maximal  $\mathcal{P}_{fm}^{(0)}$  at time  $t_m$  can be obtained as follows

$$\mathcal{P}_{fm}^{(0)} = \mathcal{P}_{max}^{(0)} = \left(\frac{6\pi}{e}\right)^{3/2} \frac{b_0 + 2b_1}{b_0 - b_1}, \quad t_m = -\tau_s \ln\left(1 - \frac{g_{qpm}}{\tau_s}\right) \quad (5.68)$$

where

$$g_{qpm} = t_{max} = \sqrt{\frac{1}{3\sigma_1^2 (b_0 + 2b_1)}} \approx 3.04 \quad (5.69)$$

In Equation 5.60, notice that the maximal value of the amplitude  $\mathcal{P}_f^{(0)}(t)$  remains the same constant for all friction coefficients  $\tau_s$  even in the case of  $\tau_s \rightarrow \infty$  ( $\mathcal{P}_{max}^{(0)}$ ). While the expression for time  $t_m$  sets a limit for  $\tau_s$ . In the case of  $\tau_s > g_{qpm}$ ,  $t_m$  exists and monotonously decreases with  $\tau_s$  getting larger, see Figure 5.13, meaning that the starting time of structure being destroyed at small scales becomes earlier as particles are getting larger, which would result in less small-scale and more large-scale structure formation to occur in systems with larger particles at the end stage of evolution with friction, which agrees with the simulation results in Johansen and Youdin [21]. In the limit of  $\tau_s \rightarrow \infty$ ,

$$\lim_{\tau_s \rightarrow \infty} t_m = \tau_s \frac{g_{qpm}}{\tau_s} = g_{qpm} \quad (5.70)$$

sets a lower limit for  $t_m$ , suggesting that in the case of relatively large  $\tau_s$ , the maximal amplitude  $\mathcal{P}_{\text{fm}}^{(0)}$  will not show up at least after evolution time  $t = g_{\text{qpm}} = t_{\text{max}}$ . While in the case of  $\tau_s < g_{\text{qpm}}$ ,  $t_m$  does not exist, meaning that the amplitude  $\mathcal{P}_f^{(0)}(t)$  of the  $k^{-3}$  slope will monotonously increase until the propagator  $g_{\text{qp}}(t)$  reaches its maximum.

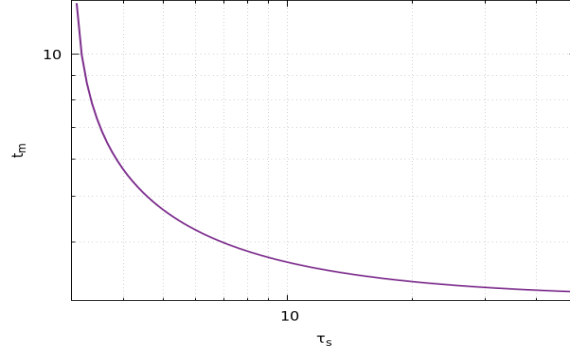


Figure 5.13: This plot shows the value of  $t_m$  as a function of the friction coefficient  $\tau_s$ .

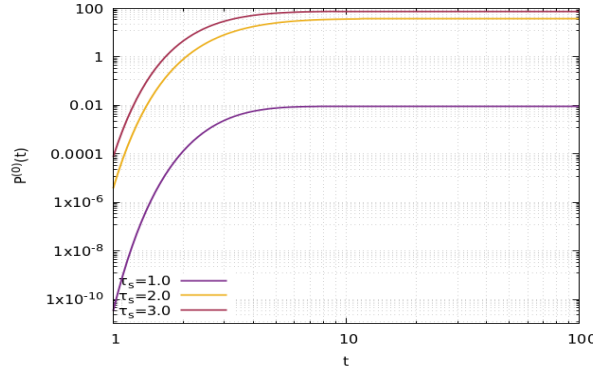


Figure 5.14: This plot illustrates the evolution of the amplitude  $\mathcal{P}_f^{(0)}(t)$  for the  $k^{-3}$  slope as a function of time  $t$  with friction coefficients  $\tau_s = 1.0$  (purple line),  $\tau_s = 2.0$  (yellow line) and  $\tau_s = 3.0$  (burgundy line).

Figure 5.14 shows the shape of  $\mathcal{P}_f^{(0)}(t)$  with relatively small friction coefficients  $\tau_s = 1.0$ ,  $\tau_s = 2.0$  and  $\tau_s = 3.0$ . They all indeed share the same monotonously increasing pattern, which suggests the structure in the system continuously builds up at small scales until the velocity of the dust particles becomes the same as that of the background gas. On the other hand, since the power of the density field always increases at large scales for larger  $\tau_s$  and longer  $t$ , we can say that for smaller-size particles experiencing relatively stronger dust-gas friction, there is continuous structure formation at all scales until the system reaches its stable state, see Figure 5.15. Also

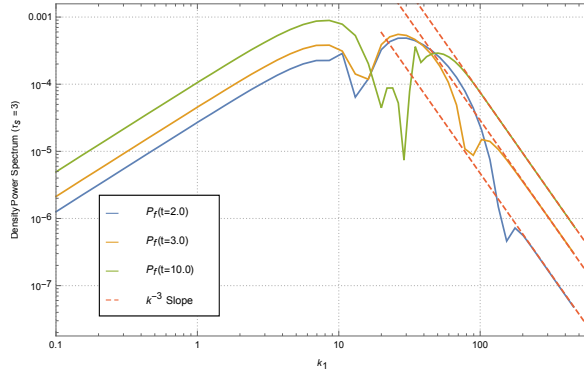


Figure 5.15: This plot shows the density power spectrum  $\mathcal{P}_f(k_1, t)$  with friction at evolution times  $t = 2.0$  (blue line),  $t = 3.0$  (yellow line) and  $t = 10.0$  (green line) with the friction coefficient  $\tau_s = 3.0$ . At small scales, they all develop  $k^{-3}$  slopes (red dashed lines). As time proceeds, the power spectrum grows at both large and small scales.

notice with  $\tau_s$  growing while still in the range of  $\tau_s < g_{\text{qpm}}$ , the value of the amplitude  $\mathcal{P}_f^{(0)}(t)$  increases significantly, indicating that more power and more structure formation occurs when the dust particles are larger and have more time to evolve and interact with the background gas, which coincides with our conclusions of [Figure 5.9](#).

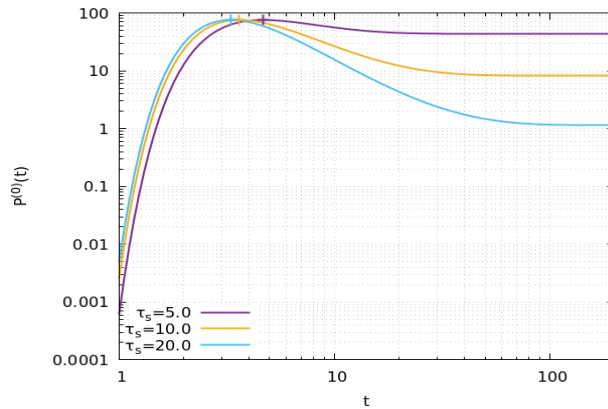


Figure 5.16: This plot illustrates the shape of the amplitude  $\mathcal{P}_f^{(0)}(t)$  for the  $k^{-3}$  slope as a function of time  $t$  with friction coefficient  $\tau_s = 5.0$  (purple line),  $\tau_s = 10.0$  (yellow line) and  $\tau_s = 20.0$  (light blue line). The crosses of the same color on each curve represent their maximum value  $\mathcal{P}_{\text{fm}}^{(0)}$  at time  $t_m$  by [Equation 5.60](#).

[Figure 5.16](#) shows how the amplitude  $\mathcal{P}_f^{(0)}(t)$  for the  $k^{-3}$  slope changes over time with relatively large friction coefficients  $\tau_s = 5.0$ ,  $\tau_s = 10.0$  and  $\tau_s = 20.0$ . They all show the same maximal amplitude  $\mathcal{P}_{\text{fm}}^{(0)}$  as expected. With  $\tau_s$  getting larger,  $t_m$  be-

comes smaller, as shown in [Figure 5.13](#). The fast-increasing value for the amplitudes at the earlier time suggests rapid structure formation occurs at small scales during the very early stage of the evolution, while as time proceeds, the amplitude for the  $k^{-3}$  slope starts decreasing, meaning the structure will continuously be destroyed at smaller scales during the later stage of evolution until the propagator  $g_{qp}(t)$  reaches its maximum, then the dust particles freeze in. This change of behavior for the amplitude  $\mathcal{P}_f^{(0)}(t)$  at small scales compared to the continuous power increase at large scales suggests that there exists a special particle size  $\tau_s^c = g_{qp m}$  corresponding to the strongest small scale structure formation in the system due to the friction.

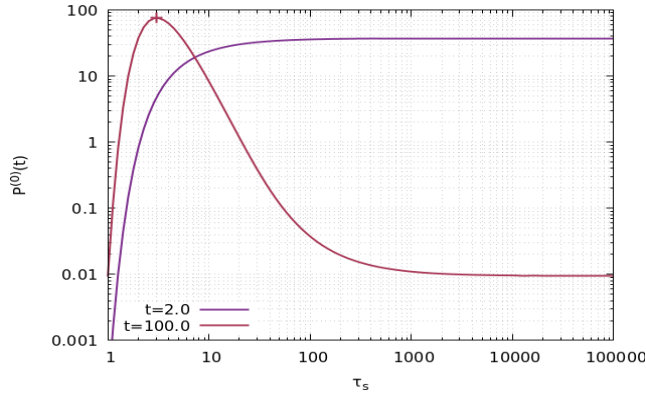


Figure 5.17: This plot illustrates the shape of the amplitude  $\mathcal{P}_f^{(0)}(t)$  for the  $k^{-3}$  slope as a function of friction coefficient  $\tau_s$  at two different time  $t = 2.0$  (purple line) and  $t = 100.0$  (burgundy line). The same color dot on the burgundy curve represents its maximal  $\mathcal{P}_{fm}^{(0)}$  at friction coefficient  $\tau_{sm}$  calculated by [Equation 5.71](#).

Further, we want to determine the relation between the small-scale asymptotic behavior and particle size  $\tau_s$ . By requiring  $\frac{d\mathcal{P}_f^{(0)}(t)}{d\tau_s} = \frac{d\mathcal{P}_f^{(0)}}{dg_{qp}} \frac{dg_{qp}}{d\tau_s} = 0$ , we get the same maximal amplitude  $\mathcal{P}_{fm}^{(0)}$  as in [Equation 5.68](#), while the corresponding  $\tau_{sm}$  satisfies

$$\tau_{sm} \left( 1 - e^{-\frac{t}{\tau_{sm}}} \right) = g_{qp m}. \quad (5.71)$$

[Figure 5.17](#) shows the shape of the amplitude  $\mathcal{P}_f^{(0)}(t)$  for the  $k^{-3}$  slope as a function of the friction coefficient  $\tau_s$  at times  $t = 2.0$  and  $t = 100.0$ . At relatively earlier evolution time  $t = 2.0$ , the amplitude for  $k^{-3}$  slope monotonously increases with  $\tau_s$  getting larger, meaning that at earlier times, there is always more structure formation at small scales for larger size particles, however, the amplitude never reaches its maximum value  $\mathcal{P}_m^{(0)}$  at  $t = 2.0 < g_{qp m}$ , which agrees with the conclusion in [Equation 5.70](#). At later evolution time  $t = 100.0$ , the amplitude rapidly increases until reaches its maximum at  $\tau_{sm}$  before it starts decreasing, indicating that at a later time, there is

structure formation at small scales for small size particles, while for larger size particles, the structures at small scales are being destroyed. Notice with  $\tau_s$  getting larger, at a given evolution time  $t$ , due to the asymptotic behavior of the propagator  $g_{qp}(t)$  in Equation 5.40, the amplitude always reaches a constant, which indicates that when the particle size is large enough, the small scale structures in the system are always destroyed in a similar manner at given evolution time  $t$ .

#### 5.4 GRAVITATIONAL DENSITY POWER SPECTRUM

With the gravity-free KFT nonlinear density power spectrum  $\mathcal{P}_f(k_1, t)$  in Equation 5.20 and its linear form  $\mathcal{P}_{\text{lin}}(k_1, t)$  in Equation 5.62 obtained, we successfully include friction between the dust particles and the constant background gas field to the KFT framework. In this section, we further switch on the self-gravity among dust particles in the system at time  $t_0$  and compute the full nonlinear KFT density power spectrum  $\mathcal{P}_g(k_1, t)$  in Equation 5.38 by calculating the averaged interaction term  $i\langle S_I \rangle$  in Equation 5.34 where

$$i\langle S_I \rangle = \frac{2\hat{G}}{\pi} \int_{t_0}^t dt' g_{qp}(t, t') \int_0^\infty dk k^2 P(k, t') J\left(\frac{k}{k_1}\right), \quad (5.72)$$

with  $J(y)$  defined in Equation 5.36 and the notation  $\hat{G}$  adopted to represent the gravitational constant in the dimensionless code units. Since the density of a particle cloud has to be larger than the critical Hill density  $\rho_H$  in Equation 2.50 to allow the cloud to withstand the tidal shear while in orbit around a star of mass  $M$  at distance  $D$ , we therefore wish to alter the dimensionless gravitational constant  $\hat{G}_0$  in order for it to represent a value that sets the total system density in relation to its Hill density.

By looking at the Poisson equation in code units

$$\frac{\nabla^2 \Phi}{\Omega^2} = \frac{4\pi G_0 \rho_d}{\Omega^2} = \frac{4\pi G_0 \bar{\rho}_g}{\Omega^2} \frac{\rho_d}{\bar{\rho}_g}, \quad (5.73)$$

we can read off the gravitational constant and the dust density in code units as

$$\hat{G} = \frac{G_0 \bar{\rho}_g}{\Omega^2}, \quad \hat{\rho} = \frac{\rho_d}{\bar{\rho}_g}, \quad (5.74)$$

with the mean gas density in the simulation satisfying  $\bar{\rho}_g = 1.0$ . Now introduce a scaling parameter  $f$  and we can express the dust density in terms of Hill density by

$$\rho_d = f \cdot \rho_H = \frac{9f M}{4\pi D^3}, \quad (5.75)$$

Using  $G_0 M = \Omega^2 D^3$ , we obtain the final expression for the dimensionless gravitational constant as

$$\hat{G} = \frac{9f}{4\pi\varepsilon} = f \cdot \hat{G}_0, \quad (5.76)$$

which now expresses densities in terms of the Hill density, with  $\varepsilon$  being the dust-to-gas ratio defined in Equation 2.26 and  $\hat{G}_0 = 0.71$  is just the condition for a 3-dimensional simulation to be at Hill density.

The following section is structured as follows. With  $\hat{G}_0$  solved for the interaction term  $S_I$ , we start with looking for a proper approximation for  $P(k, t')$  in Equation 5.72 to simplify the integrations. Next, we calculate the full linear KFT density power spectrum  $\mathcal{P}_{\text{glin}}(k_1, t)$  for small-size dust particles by calculating the corresponding averaged interaction term  $i\langle S_I \rangle$  and combing it with the gravity-free linear KFT density power spectrum  $\mathcal{P}_{\text{flin}}(k_1, t)$  in Equation 5.62. We then calculate  $i\langle S_I \rangle$  for large-size particles and combine it with the gravity-free nonlinear KFT density power spectrum  $\mathcal{P}_f(k_1, t)$  to compute the full nonlinear KFT density power spectrum  $\mathcal{P}_g(k_1, t)$ . We further discuss the relation between  $i\langle S_I \rangle$  and the particle size  $\tau_s$ , and study how the gravitational interaction affects the critical particle size  $\tau_s^c$  discovered in Section 5.3.3. In the end, by calculating the averaged dust density growth for the small-size-particle system and comparing it to reasonable collapse criteria, we find the minimum particle size  $\tau_s^g$  that assures a final gravitational collapse, which also turns out small enough for successfully overcome the "meter-size barrier".

#### 5.4.1 Proper Approximation for $P(k, t)$

Due to the difficulties to acquire and further integrate the density power spectrum  $P(k, t')$  at evolution time  $t'$ , we therefore look for some sort of approximation in this section. In Section 5.3, various figures have shown that the value of the gravity-free density power spectrum  $\mathcal{P}_f(k_1, t)$  is far smaller than unity, which leads to a negligible mean interaction term  $i\langle S_I \rangle$  at early times  $t \gtrsim t_0$ . Thus we assume it is reasonable to approximate  $P(k, t')$  by its initial power spectrum  $P(k, t' = t_0) = P_{\text{ini}}(k, t_0)$ , where  $t_0$  represents the time of switching on the self-gravity among dust particles. we can thus adopt the gravity-free density power spectrum  $\mathcal{P}_f(k, t_0)$  as  $P_{\text{ini}}(k, t_0)$  and carry out the integral in Equation 5.72 without the time element. Furthermore, to avoid the complicated form of Equation 5.20, we exploit the asymptotic behavior of  $\mathcal{P}_f(k, t_0)$  at both large and small scales and apply the numerical fitting method to find the proper approximation for  $P_{\text{ini}}(k, t_0)$ .

In view of the small friction coefficient  $\tau_s$ , we employ the linear density power spectrum  $\mathcal{P}_{\text{flin}}(k, t)$  in Equation 5.62 which is proportional to  $g_{\text{qp}}^2(t)$ , define

$$P_{\text{inis}}(k, t_0) = c_0 g_{\text{qp}}^2(t_0) k^{\frac{4}{3}} \left( 1 - \exp\left(-\frac{c_1}{k^{\frac{7}{3}}}\right) \right) \quad (5.77)$$

so that it satisfies  $P_{\text{inis}}(k, t_0) \propto k^{\frac{4}{3}}$  at the limit of  $k \rightarrow 0$  and  $P_{\text{inis}}(k, t_0) \propto k^{-1}$  at the limit of  $k \rightarrow \infty$  as  $\mathcal{P}_{\text{flin}}(k, t)$ . The fitting coefficient  $c_0$  can be calculated by

$$c_0 = \frac{\mathcal{P}_{\text{flin}}(k_1, t)}{g_{\text{qp}}^2(t) k_1^{\frac{4}{3}}} = 1.29 \times 10^{-5} \quad (5.78)$$

at wave number  $k_1 = 0.1$ , and the fitting coefficient  $c_1$  can be calculated by

$$c_1 = \frac{k_1 \mathcal{P}_{\text{flin}}(k_1, t)}{g_{\text{qp}}^2(t)} = 1015.5 \quad (5.79)$$

at wave number  $k_1 = 1000.0$ . For very large time  $t_0 \geq 10.0$ , the propagator  $g_{\text{qp}}(t_0)$  can be approximated as  $\tau_s$ , thus we have

$$P_{\text{inis}}(k, t_0) = c_0 \tau_s^2 k^{\frac{4}{3}} \left( 1 - \exp\left(-\frac{c_1}{k^{\frac{7}{3}}}\right) \right), \quad \text{for } t_0 \geq 10.0 \quad (5.80)$$

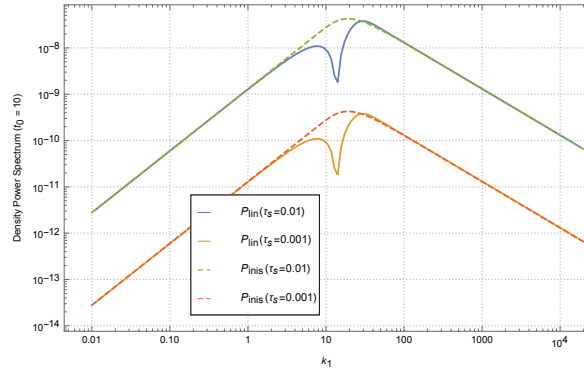


Figure 5.18: This plot compares the linear friction density power spectrum  $\mathcal{P}_{\text{lin}}(k, t_0)$  (solid lines) and the initial density power spectrum  $P_{\text{inis}}(k, t_0)$  (dashed lines) at evolution time  $t_0 = 10.0$  with two different friction coefficient  $\tau_s = 0.01$  (blue, green) and  $\tau_s = 0.001$  (yellow, red).

Figure 5.18 compares the shape of  $\mathcal{P}_{\text{flin}}(k, t_0)$  and  $P_{\text{inis}}(k, t_0)$  at initial time  $t_0 = 10.0$  with two different friction coefficients  $\tau_s = 0.01$  and  $\tau_s = 0.001$ . Here the extremely small friction coefficients are chosen to help study the "meter-size barrier". Note that except for some small difference at intermediate wave numbers  $k$ , the overall shape of

two sets of curves matches each other very well, especially the asymptotic behavior at the small and large scales, suggesting that the function  $P_{\text{inis}}(k, t_0)$  is a good approximation to  $\mathcal{P}_{\text{flin}}(k, t)$ . Notice though that the asymptotic study on the nonlinear density power spectrum  $\mathcal{P}_f(k, t)$  in [Section 5.3.2](#) states that there exists a  $k^{-3}$  tail instead of  $k^{-1}$  at very small scales for density power spectrum, due to the extremely small value of  $g_{\text{qp}}(t_0)$ , its starting scales  $k_0$  becomes exceedingly large which we can easily ignore for the small-size-particle system.

However, with a relatively larger friction coefficient  $\tau_s$ , define

$$P_{\text{ini}}(k, t_0) = c_0 g_{\text{qp}}^2(t_0) k^{\frac{4}{3}} \left( 1 - \exp\left(-\frac{c_2}{k^{\frac{13}{3}}}\right) \right) \quad (5.81)$$

so that it satisfies  $P_{\text{ini}}(k, t_0) \propto k^{\frac{4}{3}}$  at the limit of  $k \rightarrow 0$  and  $P_{\text{ini}}(k, t_0) \propto k^{-3}$  at the limit of  $k \rightarrow \infty$  as the nonlinear density power spectrum  $\mathcal{P}_f(k, t)$ , here we already use the fact that at large scales the nonlinear density power spectrum  $\mathcal{P}_f(k_1, t)$  is identical with the linear one  $\mathcal{P}_{\text{flin}}(k_1, t)$ , see [Figure 5.10](#). The fitting coefficient  $c_2$  can be calculated by comparing the small-scale asymptotic behavior of [Equation 5.81](#) and [Equation 5.65](#). By setting  $P_{\text{ini}}(k, t_0) = \mathcal{P}_f(k, t_0)$  in the limit of  $k \rightarrow \infty$ , we have

$$c_2 = \frac{\mathcal{P}_f^{(0)}(t_0)}{c_0 g_{\text{qp}}^2(t_0)} \quad (5.82)$$

with  $\mathcal{P}_f^{(0)}(t)$  being the analytic expression of the amplitude for the  $k^{-3}$  tail in [Equation 5.67](#).

[Table 5.1](#) gives the fitting coefficients  $c_0 g_{\text{qp}}^2(t_0)$  and  $c_2$  for  $\tau_s = 3.0$  respectively at the initial time  $t_0 = 2.0$  and at  $t_0 = 10.0$ . Note that the friction coefficient is chosen to be compliant with the condition of  $\tau_s < \tau_s^c$ , where the structure of the system is stably building up at all scales due to the friction between gas and dust.

	$t_0 = 2.0$	$t_0 = 10.0$
$c_0 g_{\text{qp}}^2(t_0)$	$2.75 \times 10^{-5}$	$1.08 \times 10^{-4}$
$c_2$	$1.69 \times 10^5$	$6.83 \times 10^5$

Table 5.1: This table gives the values for the fitting coefficients  $c_0 g_{\text{qp}}^2(t_0)$  and  $c_2$  in [Equation 5.81](#) for  $\tau_s = 3.0$  at the initial time  $t_0 = 2.0$  and at  $t_0 = 10.0$ .

[Figure 5.19](#) compares the shape of  $\mathcal{P}_f(k, t_0)$  and  $P_{\text{ini}}(k, t_0)$  at initial time  $t_0 = 2.0$  and at  $t = 10.0$  with the friction coefficient  $\tau_s = 3.0$ . Though there are some offsets at the middle range of wave number  $k$ , note that the overall shape of two sets of curves matches each other pretty well, especially at the small and large scales, which validates our choice of the function  $P_{\text{ini}}(k, t_0)$ .

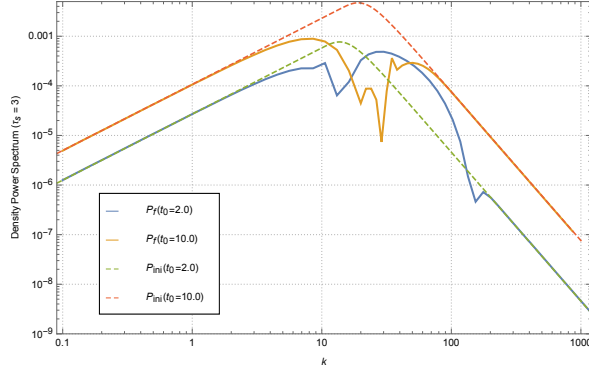


Figure 5.19: This plot compares the density power spectrum  $\mathcal{P}_f(k, t_0)$  with friction (solid lines) and the initial density power spectrum  $\mathcal{P}_{ini}(k, t_0)$  (dashed lines) at evolution time  $t_0 = 2.0$  (blue, green) and at  $t_0 = 10.0$  (yellow, red) with the friction coefficient  $\tau_s = 3.0$ .

Concluding, it is worth mentioning that the numerical functions we find above to approximate  $\mathcal{P}_{flin}(k_1, t_0)$  and  $\mathcal{P}_f(k_1, t_0)$  are suitable for any time arguments, therefore, we can also use these expressions to replace the density power spectrum  $\mathcal{P}_f(k_1, t)$  in Equation 5.38 when computing the full KFT density power spectrum  $\mathcal{P}_g(k_1, t)$  to further simplify our calculations.

#### 5.4.2 Linear Power Spectrum at Small $\tau_s$

In this section, we first study the full linear KFT density power spectrum  $\mathcal{P}_{glin}(k_1, t)$  for small size particles with small friction coefficients  $\tau_s$ . Since we will only consider the initial time  $t_0 = 10.0 \gg \tau_s$  in the following, we can directly plug Equation 5.80 into Equation 5.72 and obtain the final expression for the mean interaction term as

$$i\langle S_I \rangle(k_1, t) = \frac{2c_0 \hat{G}}{\pi} \left( \tau_s^3 (t - t_0) + \tau_s^4 \left( e^{-\frac{t-t_0}{\tau_s}} - 1 \right) \right) \int_0^\infty dk k^{\frac{10}{3}} \left( 1 + \frac{k_1^2 - k^2}{2kk_1} \ln \frac{k + k_1}{|k - k_1|} \right) \left( 1 - \exp \left( -\frac{c_1}{k^{\frac{7}{3}}} \right) \right). \quad (5.83)$$

For large arguments, the integrand of the mean interaction term becomes

$$\lim_{k \rightarrow \infty} k^{\frac{10}{3}} \left( 1 + \frac{k_1^2 - k^2}{2kk_1} \ln \frac{k + k_1}{|k - k_1|} \right) \left( 1 - \exp \left( -\frac{c_1}{k^{\frac{7}{3}}} \right) \right) = \lim_{k \rightarrow \infty} c_1 k J \left( \frac{k}{k_1} \right) \quad (5.84)$$

To determine whether this integrand is convergent, first we have to determine the asymptotic behavior of  $J \left( \frac{k}{k_1} \right)$ , see Figure 5.20. In the limit of  $k \rightarrow 0$  we have

$$\lim_{k \rightarrow 0} J\left(\frac{k}{k_1}\right) = J(0) = \lim_{k_1 \rightarrow \infty} 2 - \frac{2}{3} \frac{k^2}{k_1^2} = 2 \quad (5.85)$$

as a constant, while in the limit of  $k \rightarrow \infty$ , its asymptotic behavior becomes

$$\lim_{k \rightarrow \infty} J\left(\frac{k}{k_1}\right) = \lim_{k \rightarrow \infty} \frac{2k_1^2}{3k^2} \quad (5.86)$$

which increase proportionally to  $k_1^2$  and decreases proportionally to  $k^2$ .

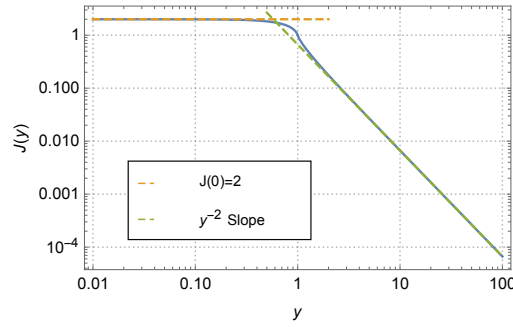


Figure 5.20: This plot shows the shape of  $J(y)$  in Equation 5.36 together with its asymptotic constant  $J(0) = 2$  at small  $y$  from Equation 5.85 and the  $y^{-2}$  slope at larger  $y$  from Equation 5.86.

Returning to the integrand in Equation 5.84, it is obviously not converging when integrating to infinity. Thus a cutoff for the integral in Equation 5.83 needs to be introduced. The analysis of the dust initial power spectrum from simulation data in Section 4.3.3 shows that the wave number corresponding to the minimal inter dust particle distance has the magnitude of  $k_{m_0} \sim 10^2$ , since each dust particle in the simulation is composed by about  $10^{11}$  pebbles on average, thus it is reasonable to set an upper limit for the wave number as

$$k_m = 10^{2 + \frac{11}{3}} = 10^{17/3} \quad (5.87)$$

to suppress modes on scales smaller than the minimal distance between pebbles.

Figure 5.21 shows the shape of the mean interaction term  $i\langle S_I \rangle$  in Equation 5.83 with cutoff scale  $k_m$  as a function of wave number  $k_1$  with the initial time  $t_0 = 10.0$  and the friction coefficients  $\tau_s = 0.01$  and  $\tau_s = 0.001$  respectively at evolution times  $t = 11.0$ ,  $t = 20.0$  and  $t = 100.0$  when the gravitational parameter is set to  $f = 1$ . At large and small scales, their  $k_1^2$  asymptotic slope and the asymptotic constants also are given in the plot. The comparison of curves at different evolution time  $t$  with the same friction

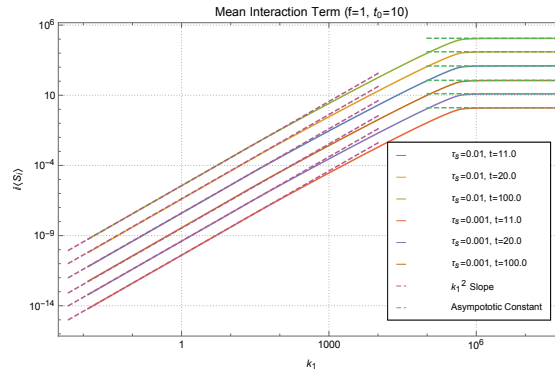


Figure 5.21: This plot illustrates the shape of the mean interaction term  $i\langle S_I \rangle(k_1, t)$  as a function of wave number  $k_1$  (solid lines) with gravitational parameter  $f = 1$  at initial time  $t_0 = 10.0$  and evolution time  $t = 11.0$  (blue, red),  $t = 20.0$  (yellow, purple) and  $t = 100.0$  (green, brown) with two different friction coefficients  $\tau_s = 0.01$  (blue, yellow, green) and  $\tau_s = 0.001$  (red, purple, brown). Their  $k^2$  asymptotic behaviors at large scales are represented by the purple dashed lines. The asymptotic constants at small scales are illustrated in green dashed lines.

coefficient  $\tau_s$  shows that the value of the mean interaction term grows large over time, which means that as time proceeds, its contribution to the nonlinear density power spectrum will become more and more important. While the difference between the curves have the same evolution time  $t$  with different friction coefficient  $\tau_s$  suggests that the effect of the self-gravity interaction will become significantly stronger with larger size dust particles, meaning that larger dust particles are much easier to aggregate to even larger particles due to their much stronger gravitational interaction with each other, which agrees with our intuition. On the other hand, for smaller particles, their stronger friction with the background gas slows down the gravitational collapse, yet potentially provides more time for further planetesimal evolution.

Furthermore, we explore how the evolution time  $t$  and the friction coefficient  $\tau_s$  affect the value of  $i\langle S_I \rangle(k_1, t)$ . First consider the limit of  $t \rightarrow \infty$ ,

$$\lim_{t \rightarrow \infty} i\langle S_I \rangle(k_1, t) \propto \lim_{t \rightarrow \infty} \left( \tau_s^3(t - t_0) + \tau_s^4 \left( e^{-\frac{t-t_0}{\tau_s}} - 1 \right) \right) = \tau_s^3(t - t_0) \rightarrow \infty \quad (5.88)$$

thus as time proceeds, the value of the mean interaction term will continually increase proportional to the evolution time  $t$ , see the left panel of [Figure 5.22](#), suggesting more power and more structure would build up in the system if the gravitational interaction persists, which eventually would lead to collapse, then, however, the mean-field approximation is likely to break down.

On the other hand, since we are interested in small values of  $\tau_s$ , in the limit of  $\tau_s \rightarrow 0$ , we have

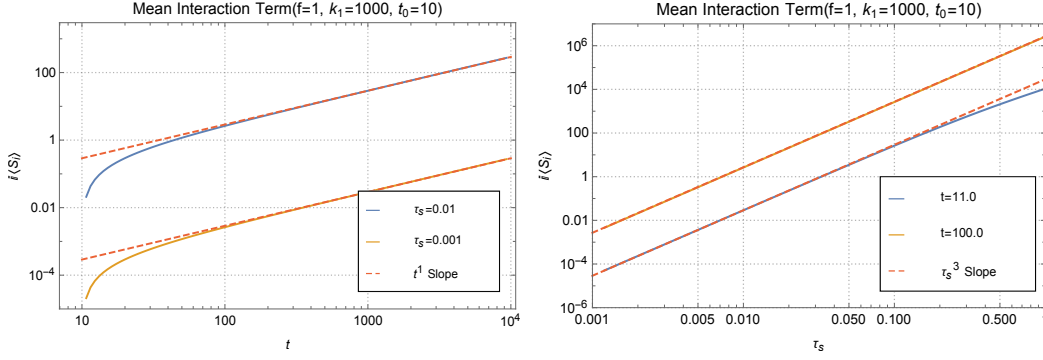


Figure 5.22: These two plots show the shape of the mean interaction term  $i\langle S_I \rangle(k_1, t)$  in Equation 5.83 as a function of evolution time  $t$  (left panel) and small valued friction coefficient  $\tau_s$  (right panel). The red dashed line in the left panel represents the  $t^1$  asymptotic slope from Equation 5.88. The red dashed line in the right panel represents the  $\tau_s^3$  asymptotic slope from Equation 5.89. The upper limit for  $\tau_s$  in the right panel plot is roughly chosen to be 1 for studying small valued  $\tau_s$ .

$$\lim_{\tau_s \rightarrow 0} i\langle S_I \rangle(k_1, t) \propto \lim_{\tau_s \rightarrow 0} \tau_s^4 \left( e^{-\frac{t-t_0}{\tau_s}} - 1 + \frac{t}{\tau_s} - \frac{t_0}{\tau_s} \right) = \tau_s^3 (t - t_0), \quad (5.89)$$

thus when the friction between dust and gas is relatively strong where the particle size is correspondingly small, the value of the mean interaction term would increase proportional to  $\tau_s^3$ , see the right panel of Figure 5.22, meaning that when particles are relatively small, with increasing particle size, the gravitational interaction between particles gets much stronger, which would effectively speed up the gravitational collapse.

Now we evaluate how the mean interaction term contributes to the full linear density power spectrum  $\mathcal{P}_{\text{glin}}(k_1, t) = e^{i\langle S_I \rangle} \mathcal{P}_{\text{flin}}(k_1, t)$ .

Figure 5.23 shows the shape of  $\mathcal{P}_{\text{glin}}(k_1, t)$  at three different evolution times  $t = 11.0$ ,  $t = 20.0$  and  $t = 100.0$  with the initial time  $t_0 = 10.0$  and two different friction coefficients  $\tau_s = 0.01$  and  $\tau_s = 0.001$  while the density of the dust particles is set to be Hill density ( $f = 1$ ). In the left panel, notice the value of the density power spectrum already shows a great increase even at the very early stage of gravitational evolution, and the increase become much more significant from small to intermediate scales over time. While in the right panel, the power of the density field increases much more slowly over time, as time proceeds, structure starts building up much faster at small scales, which potentially could still lead to gravitational collapse. The comparison of the two plots suggests that if dust particles are relatively larger, then the gravitational interaction will increase the power of the density field significantly, which leads to a much faster gravitational collapse.

In both Figure 5.23 and Figure 5.24, notice no matter how significant the density power spectrum  $\mathcal{P}_{\text{glin}}(k_1, t)$  changes, at very small scales, it always develops the same

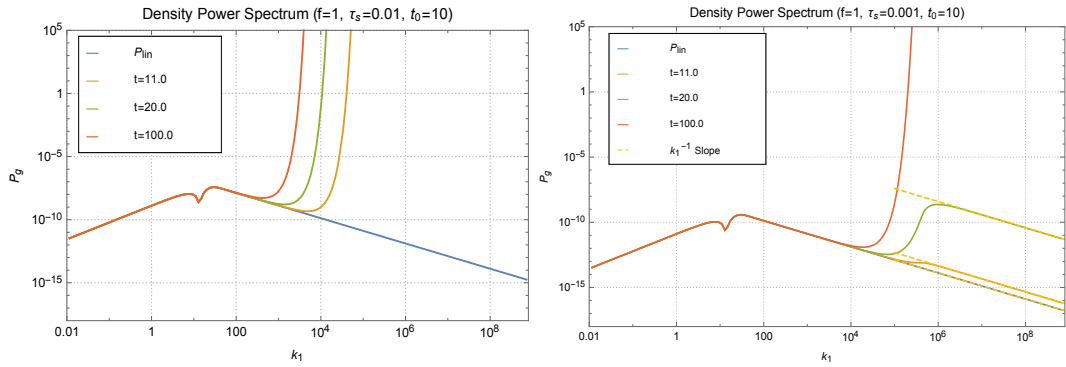


Figure 5.23: These two plots illustrate the shape of the full linear density power spectrum  $\mathcal{P}_{\text{glin}}(k_1, t)$  as a function of wave number  $k_1$  with the initial time  $t_0 = 10.0$  and the friction coefficients  $\tau_s = 0.01$  (left panel) and  $\tau_s = 0.001$  (right panel) at three evolution time  $t = 11.0$  (orange),  $t = 20.0$  (green) and  $t = 100.0$  (red) with the parameter  $f = 1$ . The blue lines represent the corresponding initial linear friction density power spectrum  $\mathcal{P}_{\text{lin}}(k_1, t_0)$  in both plots. And the yellow dashed lines illustrate the small scale  $k^{-1}$  asymptotic behavior.

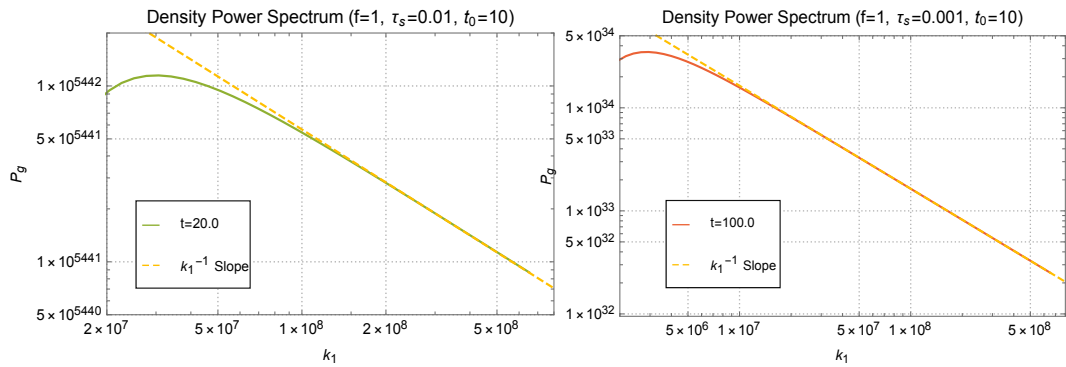


Figure 5.24: These plots zoom in to the very small scales of [Figure 5.23](#) and illustrate their small scale  $k^{-1}$  asymptotic behaviors (yellow dashed line). The linear density power spectrum  $\mathcal{P}_{\text{glin}}(k_1, t)$  at evolution time  $t = 20.0$  with  $\tau_s = 0.01$  (green line) is given in the left panel,  $\mathcal{P}_{\text{g}}(k_1, t)$  at evolution time  $t = 100.0$  with  $\tau_s = 0.001$  (red line) is given in the right panel.

$k^{-1}$  tail as the initial linear friction power spectrum [Equation 5.44](#) due to the asymptotic constant of  $i\langle S_I \rangle(k_1, t)$ , suggesting that the gravitational interaction among dust particles does not alter the small scale structure hierarchy of the system.

Now to investigate how the value of dust density affects the shape of the density power spectrum, [Figure 5.25](#) shows the shape of  $\mathcal{P}_{\text{glin}}(k_1, t)$  as a function of wave number  $k_1$  with friction coefficient  $\tau_s = 0.001$  at the initial time  $t_0 = 10.0$  and three evolution times  $t = 11.0$ ,  $t = 20.0$  and  $t = 100.0$  respectively with  $f = 1$  and  $f = 8$ . The large increase of the density power spectrum at small scales with larger gravi-

tational parameter  $f$  suggests that the self-gravity among smaller size dust particles becomes much stronger with larger dust density. Despite their stronger friction with the background gas, it still leads to faster gravitational collapse.

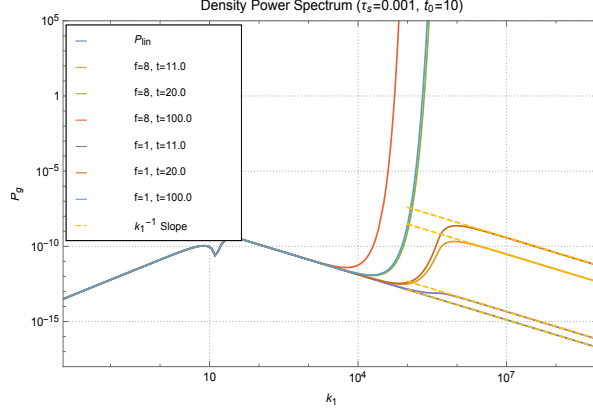


Figure 5.25: This plot illustrates the shape of the full nonlinear density power spectrum  $\mathcal{P}_{\text{glin}}(k_1, t)$  as a function of wave number  $k_1$  with the friction coefficients  $\tau_s = 0.001$  and initial time  $t_0 = 10.0$  at three different evolution times  $t = 11.0$  (yellow, purple lines),  $t = 20.0$  (green, brown lines) and  $t = 100$  (red, light blue lines) with two different gravitational parameters  $f = 8$  (yellow, green, red lines) and  $f = 1$  (purple, brown, light blue lines). The initial friction power spectrum  $\mathcal{P}_{\text{flin}}(k_1, t)$  is represented by the blue line.

In both [Figure 5.23](#) and [Figure 5.25](#), notice the difference between  $\mathcal{P}_{\text{glin}}(k_1, t)$  and  $\mathcal{P}_{\text{flin}}(k_1, t)$  becomes significantly larger at small scales over time, which suggests that the approximation of  $P(k, t') \approx P_{\text{ini}}(k, t_0)$  in [Section 5.4.1](#) to be quite inappropriate. However, the results we obtain are still considered valuable for providing a useful lower limit for the mean interaction term and further an upper limit for the time scale for gravitational collapse.

To further illustrate how the evolution time  $t$ , the friction coefficient  $\tau_s$ , and the value of dust density affect the full density power spectrum, [Figure 5.26](#) shows the shape of  $\frac{\mathcal{P}_{\text{glin}}(k_1, t)}{\mathcal{P}_{\text{flin}}(k_1, t)}$  as a function of evolution time  $t$  at small scale  $k_1 = 1000$  and initial time  $t_0 = 10.0$  with different friction coefficients  $\tau_s = 0.01$  and  $\tau_s = 0.001$ , and different gravitational parameters  $f = 1$  and  $f = 8$ . We can see that as time proceeds while still within the averaged lifetime  $10^6$  of a PPD, at scales that are typically smaller than the simulation resolution, the value of the density power spectrum increases significantly, meaning that the gravitational interaction indeed accelerates the dust aggregation process at least at small scales even for extremely small particles. The comparison between different curves further confirms that larger and denser particle ensembles experience much stronger gravitational interaction, which would lead to faster gravitational collapse.

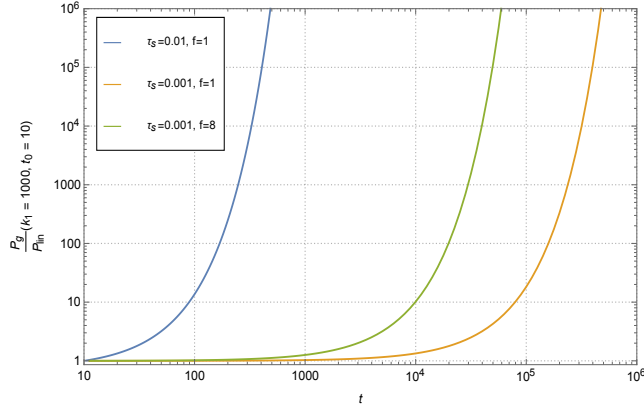


Figure 5.26: This plot illustrates the ratio between the full linear density power spectrum  $\mathcal{P}_{\text{glin}}(k_1, t)$  and the initial linear density power spectrum  $\mathcal{P}_{\text{flin}}(k_1, t)$  as a function of evolution time  $t$  with initial time  $t_0 = 10.0$  and the friction coefficients  $\tau_s = 0.01$  (blue) and  $\tau_s = 0.001$  (yellow, green) at two different gravitational parameters  $f = 1$  (blue, yellow) and  $f = 8$  (green). The upper limit of the  $t$  axis  $t_{\text{max}} = 10^6$  is chosen according to the dynamic lifetime of an average PPD.

#### 5.4.3 Non Linear Power Spectrum at Large $\tau_s$

Now we proceed with the nonlinear KFT density power spectrum with larger  $\tau_s$ . Plugging Equation 5.81 and Equation 5.82 into Equation 5.72 and Equation 5.34, the final expression for the mean interaction term with larger  $\tau_s$  is given by

$$i\langle S_I \rangle(k_1, t) = \frac{2c_0 g_{\text{qp}}^2(t_0) f \hat{G}_0}{\pi} \left( \tau_s(t - t_0) + \tau_s^2 \left( e^{-\frac{t-t_0}{\tau_s}} - 1 \right) \right) \int_0^\infty dk k^{\frac{10}{3}} \left( 1 + \frac{k_1^2 - k^2}{2kk_1} \ln \frac{k + k_1}{|k - k_1|} \right) \left( 1 - \exp \left( -\frac{\mathcal{P}^{(0)}(t_0)}{c_0 g_{\text{qp}}^2(t_0) k^{\frac{13}{3}}} \right) \right). \quad (5.90)$$

For large arguments, the integrand of the mean interaction term becomes

$$\lim_{k \rightarrow \infty} k^{\frac{10}{3}} \left( 1 + \frac{k_1^2 - k^2}{2kk_1} \ln \frac{k + k_1}{|k - k_1|} \right) \left( 1 - \exp \left( -\frac{\mathcal{P}^{(0)}(t_0)}{c_0 g_{\text{qp}}^2(t_0) k^{\frac{13}{3}}} \right) \right) = \frac{\mathcal{P}^{(0)}(t_0) J \left( \frac{k}{k_1} \right)}{c_0 g_{\text{qp}}^2(t_0) k}, \quad (5.91)$$

this integral only converges at large  $k$  if we set the value of  $\frac{k}{k_1}$  to be large enough so that  $J \left( \frac{k}{k_1} \right)$  follows its asymptotic behavior in Equation 5.85. Figure 5.20 shows that the minimal value for  $\frac{k}{k_1}$  to satisfy this condition is  $\frac{k}{k_1} = 1$ , thus we need to ensure the integral's upper limit satisfies  $k > k_1$  for it to be convergent. However, to preserve all

small-scale contributions to the density power spectrum, especially at smaller  $k_1$  and leave out the extremely small scale fluctuations at very large  $k_1$ , we still implement the cutoff scale  $k_m$  in Equation 5.87 for the above integral.

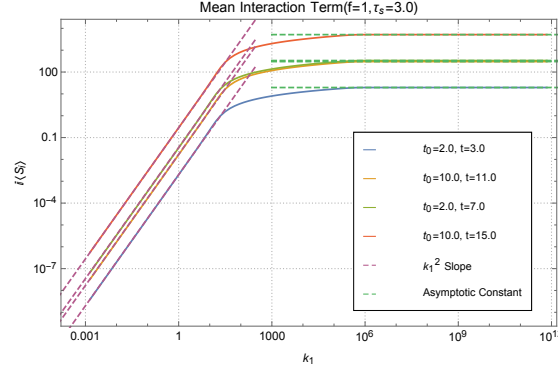


Figure 5.27: This plot illustrates the shape of the mean interaction term  $i\langle S_I \rangle(k_1, t)$  as a function of wave number  $k_1$  (solid lines) with the friction coefficient  $\tau_s = 3.0$  at four sets of initial times  $t_0$  and evolution times  $t$ , which respectively are:  $t_0 = 2.0, t = 3.0$  (blue);  $t_0 = 10.0, t = 11.0$  (yellow);  $t_0 = 2.0, t = 7.0$  (green);  $t_0 = 10.0, t = 15.0$  (red). Their  $k^2$  asymptotic behavior at large scales is represented by the purple dashed lines. Their asymptotic constant at small scales is represented by the green dashed lines.

Figure 5.27 shows the shape of the mean interaction term  $i\langle S_I \rangle(k_1, t)$  in Equation 5.90 as a function of wave number  $k_1$  with the friction coefficient  $\tau_s = 3.0$  respectively at evolution times  $t - t_0 = 1.0$  and  $t - t_0 = 5.0$  with two different initial times  $t_0 = 2.0$  and  $t_0 = 10.0$ . At large and small scales, their  $k^2$  and  $k^0$  asymptotic behavior is also given in the plot. The comparison of curves at different evolution times  $t$  with the same initial time  $t_0$  shows the value of  $i\langle S_I \rangle(k_1, t)$  grows larger over time, which means that as time proceeds, the contribution of the gravitational interaction should get more and more important to the nonlinear density power spectrum. While the difference between the curves for the same evolution time difference  $t - t_0$  with different initial time  $t_0$  suggests that the effect of the self-gravity interaction among dust particles will become significantly stronger at the end stage of the friction evolution where the dust particles more or less flow with the background gas and the friction becomes much weaker.

To explore further how the evolution time  $t$  and the friction coefficient  $\tau_s$  affect the value of  $i\langle S_I \rangle(k_1, t)$ , first consider the limit of  $t \rightarrow \infty$ , since the  $t$  dependence of Equation 5.90 remains the same as Equation 5.83, the mean interaction term continually increases proportionally to the evolution time  $t$  as Equation 5.88. On the other hand, at the limit of  $\tau_s \rightarrow \infty$ , the dust particles are so large that they no longer feel the friction of the background gas, and the mean interaction term

$$\lim_{\tau_s \rightarrow \infty} i\langle S_I \rangle(k_1, t) \propto \lim_{\tau_s \rightarrow \infty} g_{qp}^2(t_0) \tau_s^2 \left( e^{-\frac{t-t_0}{\tau_s}} - 1 + \frac{t}{\tau_s} - \frac{t_0}{\tau_s} \right) = \frac{(t-t_0)^2 t_0^2}{2} \quad (5.92)$$

becomes a constant consisting of time  $t$  and  $t_0$ . Here we already use the asymptotic behavior of  $g_{qp}(t)$  and  $\mathcal{P}_f^{(0)}(t)$  in Equation 5.67 and Figure 5.17 at the limit of  $\tau_s \rightarrow \infty$ . This behavior suggests that when the particles' size gets much larger, the gravitational attraction dominates the system, then the intensity of the gravitational interaction reduces to a function of time only, since no system would collapse instantly even without friction slowing down the gravitational attraction between the particles. This asymptotic result makes perfect sense.

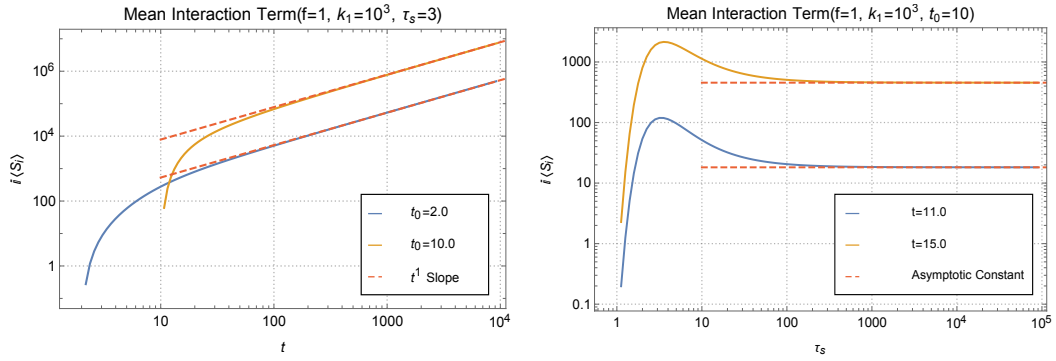


Figure 5.28: These two plots show the shape of the mean interaction term  $i\langle S_I \rangle(k_1, t)$  in Equation 5.90 as a function of evolution time  $t$  (left panel) and large valued friction coefficient  $\tau_s$  (right panel). The red dashed line in the left panel represents the  $t^1$  asymptotic slope from Equation 5.88. The red dashed line in the right panel represents the asymptotic constant from Equation 5.92.

Notice the right panel in Figure 5.28 shows a maximal value of the mean interaction term  $i\langle S_I \rangle(k_1, t)$  in term of the friction coefficient  $\tau_s$ , suggesting a most-effective particle size  $\tau_{se}$  corresponding to the gravitational interaction.

To study this behavior further, Figure 5.29 shows the mean interaction term  $i\langle S_I \rangle(k_1, t)$  in Equation 5.90 as a function of  $\tau_s$  with parameter  $f = 1$  and initial time  $t_0 = 10.0$  and evolution time  $t = 11.0$  at six different scales. Notice each of the curves has a different peak point, and with decreasing scale (larger  $k_1$ ), the value of  $\tau_{se}$  decreases until it reaches a certain constant roughly at  $\tau_{se} \approx 3.31$ , while in the meantime the maximal  $i\langle S_I \rangle(k_1, t)$  grows larger, meaning that at larger scales, the most effective particle size is larger than at small scales, however, the gravitational interaction gets much stronger overall at smaller scales. At very small scales, the most effective particle size stays the same suggesting that there exists one particle size that contributes to the strongest small-scale structure formation due to the gravitational interaction at earlier evolution time. This behavior corresponds to the very similar behavior of  $\tau_s^c$  in Section 5.3.3,

though the original limit is  $\tau_s^c = 3.04$  in Equation 5.69, the self-gravity among dust particles traps larger size dust particles at small scales, which shifts the separation point to the new  $\tau_{se} \approx 3.31$ .

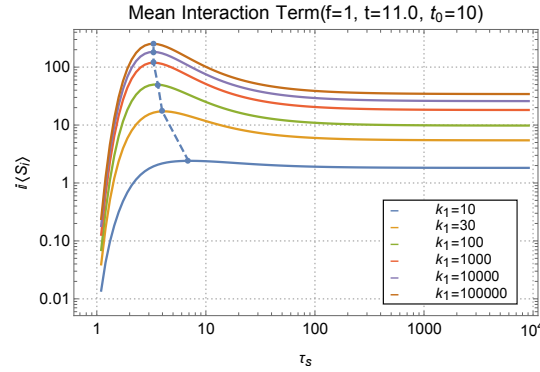


Figure 5.29: This plot shows the mean interaction term  $i\langle S_I \rangle(k_1, t)$  in Equation 5.90 as a function of  $\tau_s$  with gravitational parameter  $f = 1$  and initial time  $t_0 = 10.0$  and evolution time  $t = 11.0$  at six different scales respectively are  $k_1 = 10.0$  (blue line),  $k_1 = 30.0$  (orange line),  $k_1 = 100.0$  (green line),  $k_1 = 1000.0$  (red line),  $k_1 = 10000.0$  (purple line) and  $k_1 = 100000.0$  (brown line).

Furthermore, Figure 5.30 shows the mean interaction term  $i\langle S_I \rangle(k_1, t)$  in Equation 5.90 as a function of  $\tau_s$  at scale  $k_1 = 1000.0$  with parameter  $f = 1$  and initial time  $t_0 = 10.0$  at five different evolution time. As time proceeds, the most effective particle size and the maximal gravitational effect both increase, meaning that gravitational interaction grows stronger with time and therefore traps larger size dust particles at small scales which eventually leads to gravitational collapse starting from small scales.

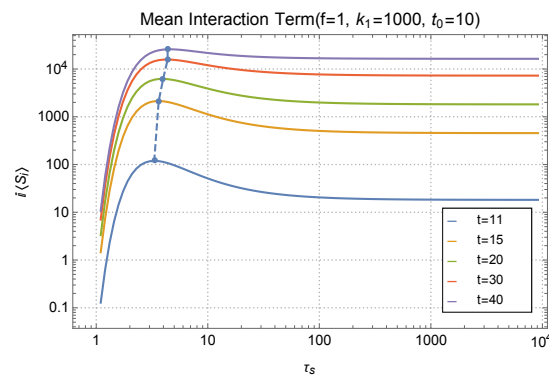


Figure 5.30: This plot shows the mean interaction term  $i\langle S_I \rangle(k_1, t)$  in Equation 5.90 as a function of  $\tau_s$  at scale  $k_1 = 1000.0$  with parameter  $f = 1$  and initial time  $t_0 = 10.0$  at five different evolution time respectively are  $t = 11$ ,  $t = 15$ ,  $t = 20$ ,  $t = 30$  and  $t = 40$ .

Now we evaluate how the mean interaction term contributes to the final nonlinear density power spectrum  $\mathcal{P}_g(k_1, t)$  in Equation 5.38. Since we are more interested in the scenario where the self-gravitational interaction sets in as soon as possible, we will limit ourselves to the initial time  $t_0 = 2.0$  in the following discussions.

Figure 5.31 shows the shape of  $\mathcal{P}_g(k_1, t)$  at two different evolution times  $t = 3.0$  and  $t = 7.0$  with the initial time  $t_0 = 2.0$  and the friction coefficient  $\tau_s = 3.0$  while the density of the dust particles is set to be the Hill density ( $f = 1$ ). Their small-scale  $k^{-3}$  asymptotic behavior is also marked in the plot. The comparison of the three curves suggests that if the self-gravity among dust particles is switched on at the early stage of friction evolution ( $t_0 = 2.0$ ), where the friction between dust and gas is still relatively strong, the density power spectrum increases relatively little at small scales when the evolution time  $t$  is small, while as time proceeds, the gravitational interaction starts to affect the nonlinear density power spectrum much more from small to intermediate scales which leads to gravitational collapse at a later time.

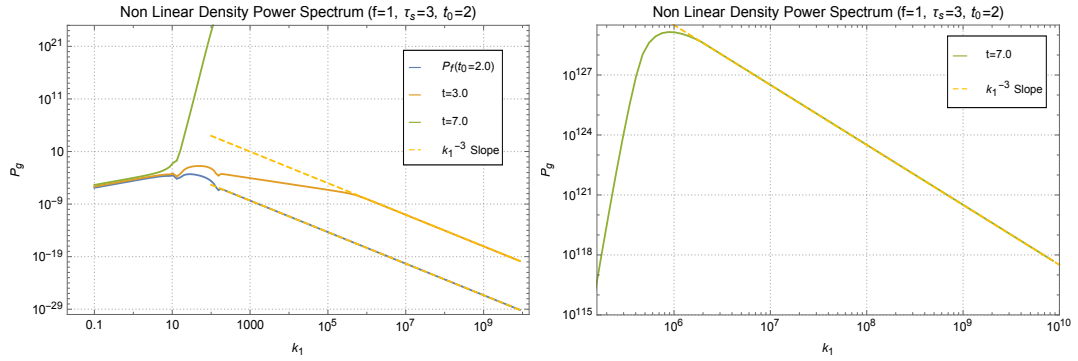


Figure 5.31: These two plots show the shape of  $\mathcal{P}_g(k_1, t)$  as a function of  $k_1$  at two different evolution times  $t = 3.0$  (orange line) and  $t = 7.0$  (green lines) with the initial time  $t_0 = 2.0$  (blue line) and the friction coefficient  $\tau_s = 3.0$  while the density of the dust particles is set to be the Hill density ( $f = 1$ ). Their small-scale  $k^{-3}$  asymptotic behavior is illustrated by the yellow dashed lines. The right panel zoom-in plot shows the small scale  $k^{-3}$  tail of  $\mathcal{P}_g(k_1, t)$  at  $t = 7.0$ .

Notice that in Figure 5.31, the nonlinear density power spectrum  $\mathcal{P}_g(k_1, t)$  always develops a  $k^{-3}$  tail at small scales like the density power spectrum  $\mathcal{P}_f(k_1, t)$  with friction due to the asymptotically constant  $i\langle S_I \rangle(k_1, t)$  at small scales, meaning that the gravitational interaction among dust particles does not change the small scale structure hierarchy of the system, which agrees with our previous conclusions. However, it is worth mentioning that the universal  $k^{-3}$  slope is solely decided by the cutoff scale  $k_m$ , if we choose  $k_m$  to be proportional to  $k_1$  instead of a constant, then this  $k^{-3}$  slope will likely not preserve, which will lead to a stronger and faster gravitational collapse.

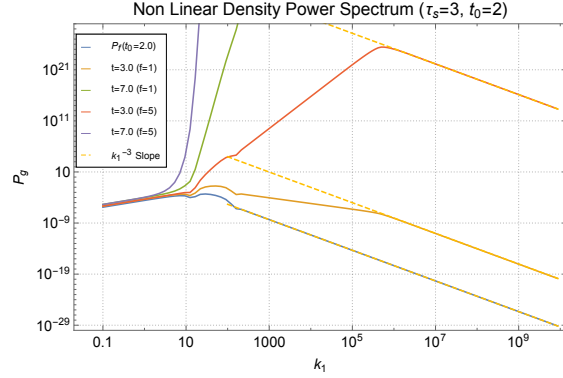


Figure 5.32: This plot illustrates the shape of the full nonlinear density power spectrum  $\mathcal{P}_g(k_1, t)$  as a function of wave number  $k_1$  with the friction coefficients  $\tau_s = 3.0$  and initial time  $t_0 = 2.0$  at two different evolution times  $t = 3.0$  (yellow, red lines) and  $t = 7.0$  (green, purple lines) with two different gravitational parameters  $f = 1$  (yellow, green lines) and  $f = 5$  (red, purple lines). The initial friction power spectrum  $\mathcal{P}_f(k_1, t)$  is represented by the blue line. The  $k^{-3}$  tail at small scales is illustrated by the yellow dashed lines.

While to illustrate how the weaker friction/stronger gravitational interaction affects the shape of the density power spectrum, we increase the value of the gravitational parameter by setting the density of the dust particles to be five times the Hill density ( $f = 5$ ). Figure 5.32 shows the shape of  $\mathcal{P}_g(k_1, t)$  as a function of wave number  $k_1$  with the initial time  $t_0 = 2.0$  and the friction coefficient  $\tau_s = 3.0$  at two evolution times  $t = 3.0$  and  $t = 7.0$  and two different gravitational constants  $f = 1$  and  $f = 5$ . The different shapes of the curves with different gravitational parameters  $f$  suggest that when the friction between dust particles and the background gas becomes weaker compared to the self-gravity among dust particles, the value of the nonlinear density power spectrum increases much stronger given the same evolution time  $t$ , which further supports our conclusion above that weaker friction between dust and gas could speed up the gravitational collapse.

#### 5.4.4 Determine Gravitational Collapse at Small $\tau_s$

As the dust particles start aggregating due to the self-gravitational interaction, at the end of this section, to determine the gravitational collapse conditions for small particles and further study the "meter-size barrier", we adopt a more feasible however rather adventurous method based on the mean field approach to directly calculate the averaged value of the density field.

Define the averaged density field for a system of small particles as

$$\begin{aligned}\bar{\rho}^2 &= \int_{k_1} \mathcal{P}_{\text{glin}}(k_1, t) e^{i\vec{k}_1 \cdot \vec{q}} \Big|_{\vec{q}=0} = \frac{1}{2\pi^2} \int_0^{k_m} k_1^2 \mathcal{P}_{\text{glin}}(k_1, t) dk_1 \\ &= \frac{1}{2\pi^2} \int_0^{k_m} k_1^2 e^{i\langle S_I(k_1, t) \rangle} \mathcal{P}_{\text{flin}}(k_1, t) dk_1. \quad (5.93)\end{aligned}$$

To determine the gravitational collapse, rather than the absolute values, we are more interested in its ratio with the initial averaged density field, thus define

$$\delta^2 = \frac{\bar{\rho}^2}{\bar{\rho}_0^2} \quad \text{with} \quad (5.94)$$

$$\bar{\rho}_0^2 = \int_{k_1} \mathcal{P}_{\text{flin}}(k_1, t_0) e^{i\vec{k}_1 \cdot \vec{q}} \Big|_{\vec{q}=0} = \frac{1}{2\pi^2} \int_0^{k_m} k_1^2 \mathcal{P}_{\text{flin}}(k_1, t_0) dk_1 \quad (5.95)$$

Due to the complicated form of  $\mathcal{P}_{\text{flin}}(k, t)$  in Equation 5.62, here we adopt the numerical fitting function  $P_{\text{inis}}(k, t)$  for large time arguments in Equation 5.80 as a proper approximation.

However, the rather lengthy expression for the mean interaction term  $i\langle S_I(k_1, t) \rangle$  in Equation 5.83 still implies difficulties with the numerical implementation, thus we exploit the asymptotic behavior of  $i\langle S_I(k_1, t) \rangle$  at large and small scales, further combine with Equation 5.88, Equation 5.89 to retain its time and friction coefficient dependence, and define the numerical fitting function for the mean interaction term as

$$i\langle S_I(k_1, t) \rangle \approx S_{\text{fit}}(k_1, t) = f\beta k_1^2 \left( 1 - \exp\left(-\frac{\alpha}{k_1^2}\right) \right) \tau_s^3(t - t_0), \quad (5.96)$$

The fitting coefficient  $\beta$  can be calculated directly by comparing the small-scale asymptotic behavior of Equation 5.83 at large evolution time  $t$  and Equation 5.96 as

$$\lim_{k_1 \rightarrow 0} i\langle S_I(k_1, t) \rangle = \lim_{k_1 \rightarrow 0} S_{\text{fit}}(k_1, t) \quad \rightarrow \quad (5.97)$$

$$\frac{2c_0 f \hat{G}_0}{\pi} \tau_s^3(t - t_0) \int_0^{k_m} k^{\frac{10}{3}} \frac{2k_1^2}{3k^2} \left( 1 - \exp\left(-\frac{c_1}{k^{\frac{7}{3}}}\right) \right) = f\beta k_1^2 \tau_s^3(t - t_0) \quad (5.98)$$

here we already use the asymptotic behavior of  $J\left(\frac{k}{k_1}\right)$  in Equation 5.86, thus the final value for  $\beta$  becomes

$$\beta = \frac{4c_0 \hat{G}_0}{3\pi} \int_0^{k_m} k^{\frac{4}{3}} \left( 1 - \exp\left(-\frac{c_1}{k^{\frac{7}{3}}}\right) \right) = 4.05 \times 10^{-2} \quad (5.99)$$

In a similar manner, the fitting coefficient  $\alpha$  can be calculated by comparing the large scales asymptotic behavior of Equation 5.83 at large evolution time  $t$  and Equation 5.96 as

$$\lim_{k_1 \rightarrow \infty} i\langle S_I(k_1, t) \rangle = \lim_{k_1 \rightarrow \infty} S_{\text{fit}}(k_1, t) \rightarrow \tag{5.100}$$

$$\frac{4c_0 f \hat{G}_0}{\pi} \tau_s^3 (t - t_0) \int_0^{k_m} k^{\frac{10}{3}} \left( 1 - \exp\left(-\frac{c_1}{k^{\frac{7}{3}}}\right) \right) = f\beta\alpha\tau_s^3 (t - t_0) \tag{5.101}$$

here we also use the asymptotic behaviour of  $J\left(\frac{k}{k_1}\right)$  in Equation 5.85. The final value for  $\alpha$  becomes

$$\alpha = \frac{4c_0 \hat{G}_0}{\beta\pi} \int_0^{k_m} k^{\frac{10}{3}} \left( 1 - \exp\left(-\frac{c_1}{k^{\frac{7}{3}}}\right) \right) = 3.15 \times 10^{10} \tag{5.102}$$

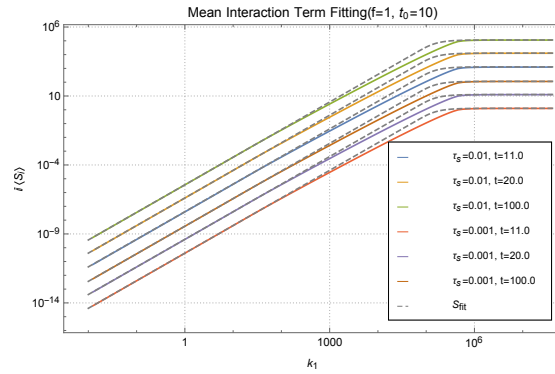


Figure 5.33: This plot compares the mean interaction term  $i\langle S_I(\vec{k}_1, t) \rangle$  in Equation 5.83 with its numerical fitting function  $S_{\text{fit}}(k_1, t)$  in Equation 5.96 (gray dashed lines) as a function of wave number  $k_1$  (solid lines) with gravitational parameter  $f = 1$  at initial time  $t_0 = 10.0$  and evolution times  $t = 11.0$  (blue, red),  $t = 20.0$  (yellow, purple) and  $t = 100.0$  (green, brown) with two different friction coefficients  $\tau_s = 0.01$  (blue, yellow, green) and  $\tau_s = 0.001$  (red, purple, brown).

Figure 5.33 compares the mean interaction term  $i\langle S_I(\vec{k}_1, t) \rangle$  in Equation 5.83 with its numerical fitting function  $S_{\text{fit}}(k_1, t)$  in Equation 5.96 as a function of wave number  $k_1$  with gravitational parameter  $f = 1$  at initial time  $t_0 = 10.0$  and evolution times  $t = 11.0$ ,  $t = 20.0$  and  $t = 100.0$  with two different friction coefficients  $\tau_s = 0.01$  and  $\tau_s = 0.001$ . At both large and small scales, notice their asymptotic behavior matches very well with each other. To be precise, we calculate the relative difference  $\frac{|i\langle S_I(\vec{k}_1, t) \rangle - S_{\text{fit}}(k_1, t)|}{i\langle S_I(\vec{k}_1, t) \rangle}$  for each set of curves, at large scales, the relative difference is always smaller than 2.5%,

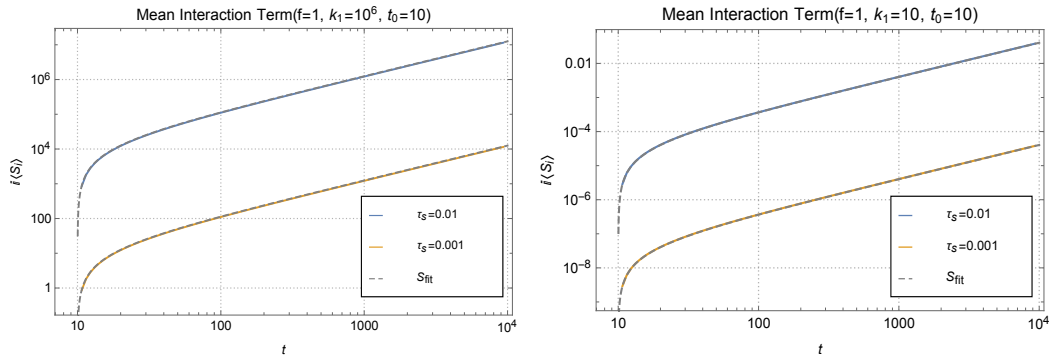


Figure 5.34: These two plots show the shape of the mean interaction term  $i\langle S_I \rangle(k_1, t)$  in Equation 5.83 and its fitting function  $S_{\text{fit}}(k_1, t)$  (gray dashed lines) in Equation 5.96 as a function of evolution time  $t$  at small (left panel) and large (right panel) scales with gravitational parameter  $f = 1$  and initial time  $t_0 = 10.0$  and two different friction coefficients  $\tau_s = 0.01$  (blue lines) and  $\tau_s = 0.001$  (yellow lines).

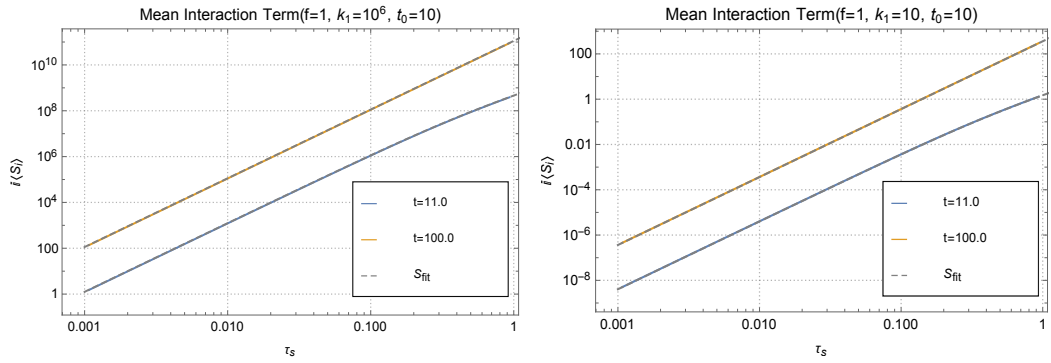


Figure 5.35: These two plots show the shape of the mean interaction term  $i\langle S_I \rangle(k_1, t)$  in Equation 5.83 and its fitting function  $S_{\text{fit}}(k_1, t)$  (gray dashed lines) in Equation 5.96 as a function of friction coefficient  $\tau_s$  at small (left panel) and large (right panel) scales with gravitational parameter  $f = 1$  and initial time  $t_0 = 10.0$  and two different evolution times  $t = 11.0$  (blue lines) and  $t = 100.0$  (red lines).

while the small scale behavior is more precise with a relative difference not exceeding 0.1%.

Furthermore, Figure 5.34 shows the comparison of  $i\langle S_I \rangle(k_1, t)$  and  $S_{\text{fit}}(k_1, t)$  as a function of evolution time  $t$  at both small ( $k_1 = 10^6$ ) and large ( $k_1 = 10$ ) scales with  $f = 1$  and  $t_0 = 10.0$  at two different friction coefficients  $\tau_s = 0.01$  and  $\tau_s = 0.001$ . Figure 5.35 show the comparison of  $i\langle S_I \rangle(k_1, t)$  and  $S_{\text{fit}}(k_1, t)$  as a function of friction coefficient  $\tau_s$  at the same small and large scales with  $f = 1$  and  $t_0 = 10.0$  at two different evolution time  $t = 11.0$  and  $t = 100.0$ . Notice the eight sets of curves in the

four plots all agree with each other extremely well, which further justifies our choice of the fitting function  $S_{\text{fit}}(k_1, t)$ .

Now plugging the expression of Equation 5.96 and Equation 5.80 into Equation 5.94, we have

$$\delta^2(t, \tau_s, f) = \frac{\int_0^{k_m} c_0 \tau_s^2 k_1^{\frac{10}{3}} \exp(S_{\text{fit}}(k_1, t)) \left(1 - \exp\left(-\frac{c_1}{k_1^{\frac{7}{3}}}\right)\right)}{\int_0^{k_m} c_0 \tau_s^2 k_1^{\frac{10}{3}} \left(1 - \exp\left(-\frac{c_1}{k_1^{\frac{7}{3}}}\right)\right)}. \quad (5.103)$$

To determine if the system is experiencing gravitational collapse, according to the initial particle number  $N \approx 2.1 \cdot 10^7$  in the simulation, we roughly set a lower limit for the density ratio as

$$\delta_-^2 = 10^{14}, \quad (5.104)$$

as long as  $\delta^2(t, \tau_s, f) > \delta_-^2$ , we say that the dust particles in the system are collapsing due to their self-gravitational interactions.

Figure 5.36 shows the shape of the density ratio  $\delta^2(t, \tau_s, f)$  in Equation 5.103 as a function of the evolution time  $t$ , together with its numerical fitting function  $\delta^2(t, \tau_s, f) \approx x_0^{t-t_0}$  at parameters  $f = 1$ ,  $\tau_s = 0.01$  and  $t_0 = 10.0$ . The zoom-in plot in the right panel at a smaller evolution time is provided for locating the crossing point  $\delta^2(t_c, \tau_s, f) = \delta_-^2$  more easily. In both plots, the two sets of curves match pretty well with each other, suggesting despite the complicated integral in Equation 5.103, we can roughly claim the relation between the density ratio and the evolution time to be as simple as

$$\delta^2(t, \tau_s, f) \approx x_0^{t-t_0}, \quad (5.105)$$

thus the crossing point  $t_c$  can be approximated as

$$t_c - t_0 = \frac{\ln \delta_-^2}{\ln x_0} = 2.58 \times 10^{-2} \quad (5.106)$$

Figure 5.37 similarly shows the shape of the density ratio  $\delta^2(t, \tau_s, f)$  in Equation 5.103 as a function of the friction coefficient  $\tau_s$ , together with its numerical fitting function  $\delta^2(t, \tau_s, f) \approx x_1^{\tau_s^3}$  at parameters  $f = 1$ ,  $t_0 = 10.0$  and  $t = 20.0$ . The zoom-in plot in the right panel at a smaller friction coefficient is provided for the same reason. In both plots, the two sets of curves also match very well with each other, meaning that we also can use a much simpler equation to represent the relation between the density ratio and the friction coefficient as

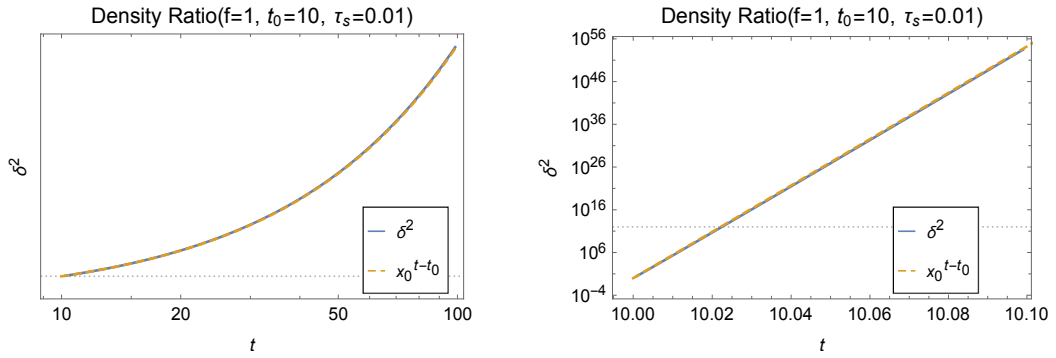


Figure 5.36: These two plots show the shape of the density ration  $\delta^2(t, \tau_s, f)$  in Equation 5.103 as a function of evolution time  $t$  at parameters  $f = 1$ ,  $\tau_s = 0.01$  and  $t_0 = 10.0$  (blue line), together with its numerical fitting function  $\delta^2 \approx x_0^{t-t_0}$  (yellow dashed line). The gray dashed lines in both plots represent the lower limit  $\delta^2_-$  in Equation 5.104.

$$\delta^2(t, \tau_s, f) \approx x_1^{\tau_s^3}, \quad (5.107)$$

with the crossing point  $\tau_{s_c}$  being approximated as

$$\tau_{s_c} = \left( \frac{\ln \delta^2_-}{\ln x_1} \right)^{\frac{1}{3}} = 1.38 \times 10^{-3} \quad (5.108)$$

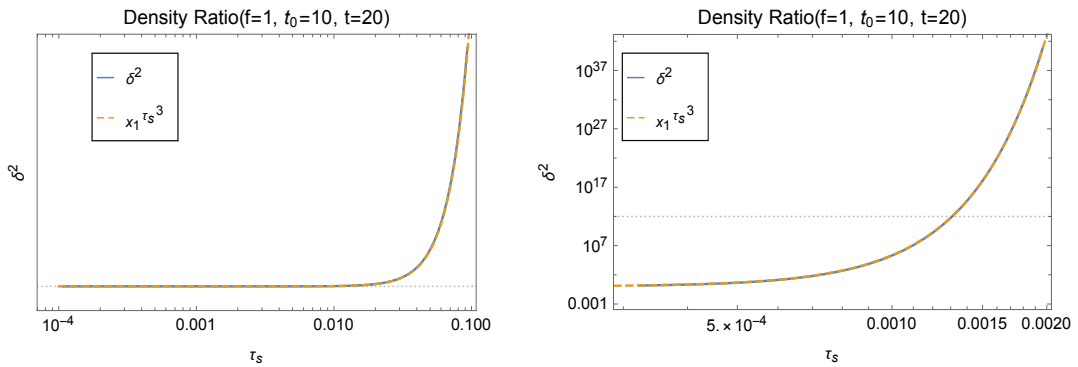


Figure 5.37: These two plots show the shape of the density ration  $\delta^2(t, \tau_s, f)$  in Equation 5.103 as a function of friction coefficient  $\tau_s$  at parameters  $f = 1$ ,  $t_0 = 10.0$  and  $t = 20.0$  (blue line), together with its numerical fitting function  $\delta^2 \approx x_1^{\tau_s^3}$  (yellow dashed line). The gray dashed lines in both plots represent the lower limit  $\delta^2_-$  in Equation 5.104.

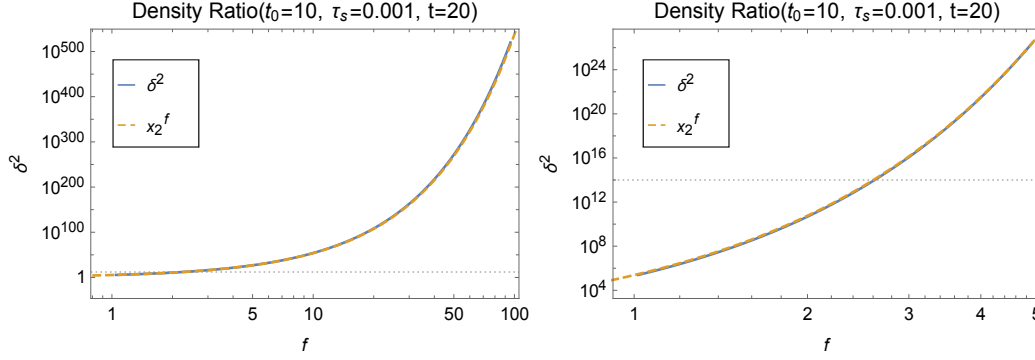


Figure 5.38: These two plots show the shape of the density ratio  $\delta^2(t, \tau_s, f)$  in Equation 5.103 as a function of gravitational parameter  $f$  at parameters  $t_0 = 10.0$ ,  $\tau_s = 0.001$  and  $t = 20.0$  (blue line), together with its numerical fitting function  $\delta^2 \approx x_2^f$  (yellow dashed line). The gray dashed lines in both plots represent the lower limit  $\delta_-^2$  in Equation 5.104.

In the end, Figure 5.38 shows the shape of the density ratio  $\delta^2(t, \tau_s, f)$  in Equation 5.103 as a function of the gravitational parameter  $f$ , together with its numerical fitting function  $\delta^2(t, \tau_s, f) \approx x_2^f$  at parameters  $t_0 = 10.0$ ,  $\tau_s = 0.001$  and  $t = 20.0$ . The right panel plot is also zoomed in to the curve with smaller gravitational parameters to show the crossing point  $f_c$  more clearly. In both plots, the fact that the two sets of curves match pretty well with each other means that the relation between the density ratio and the gravitational parameter can be represented by the simple function

$$\delta^2(t, \tau_s, f) \approx x_2^f, \quad (5.109)$$

and the crossing point  $f_c$  can be approximated as

$$f_c = \frac{\ln \delta_-^2}{\ln x_2} = 2.60. \quad (5.110)$$

Furthermore, combining the conclusions in Equation 5.105, Equation 5.107 and Equation 5.109 gives us the final fitting function for the density ratio as

$$\delta^2(t, \tau_s, f) \approx y_0^{(t-t_0)\tau_s^3 f} \quad (5.111)$$

here  $y_0$  is the fitting coefficient determined by the  $k$  integration in Equation 5.103. This approximation can also be seen roughly from the original expression of the density ratio in Equation 5.103, if we write  $S_{\text{fit}}(k_1, t) = (t - t_0)\tau_s^3 f s(k_1)$ , then we have

$$\delta^2(t, \tau, f) = \frac{\int_0^{k_m} c_0 \tau_s^2 k_1^{\frac{10}{3}} \overbrace{\left(1 - \exp\left(-\frac{c_1}{k_1^{\frac{7}{3}}}\right)\right)}^{(1)} \overbrace{\exp(s(k_1))}^{(2)} (t-t_0)\tau_s^3 f}{\int_0^{k_m} c_0 \tau_s^2 k_1^{\frac{10}{3}} \left(1 - \exp\left(-\frac{c_1}{k_1^{\frac{7}{3}}}\right)\right)}. \quad (5.112)$$

If the value of (2) exceeds the value of (1), then the  $t$ ,  $\tau_s$  and  $f$  dependence of the density ratio should stay more or less the same with (2), which is exactly the same with our fitting function [Equation 5.111](#). To further confirm this relation, we compute the value of  $(t-t_0)\tau_s^3 f$  for  $\delta^2(t, \tau_s, f) = \delta_-^2$  using the three crossing points in [Equation 5.106](#), [Equation 5.108](#) and [Equation 5.110](#),

$$\begin{aligned} (t_c - t_0)\tau_s^3 f &= 2.58 \times 10^{-8} \\ (t - t_0)\tau_{s_c}^3 f &= 2.61 \times 10^{-8} \\ (t - t_0)\tau_{s_c}^3 f_c &= 2.60 \times 10^{-8} \end{aligned} \quad (5.113)$$

The fact that the three values are very similar to each other further verifies our fitting function in [Equation 5.111](#), now if we take the average and define the index value  $l_- = (t-t_0)\tau_s^3 f$  for  $\delta^2(t, \tau_s, f) = \delta_-^2$ , we have the condition for gravitational collapse as

$$l_- = (t-t_0)\tau_s^3 f = 2.60 \times 10^{-8} \quad (5.114)$$

For the averaged lifetime of a protoplanetary disk, we have  $t-t_0 \approx t = 10^6$ , thus for a last-minute gravitational collapse, we have the minimal value

$$(\tau_s^3 f)_{\min} = 2.60 \times 10^{-14} \quad (5.115)$$

for a stable particle cloud with a minimal density being the Hill density  $f = 1$ , the corresponding friction coefficient  $\tau_s^g = 2.96 \times 10^{-5}$  gives the minimal particle size to assure a final gravitational collapse. Notice the value of  $l_- = 2.60 \times 10^{-8}$  sensitively depends on the initial simulation setup. With different values of the initial momentum covariance matrix in [Section 4.3.5](#), this number could be very different. Nevertheless, this is still a very interesting and important result that comes from a general simulation setup, the value of  $\tau_s^g$  significantly lowers the limit for the size of dust particles that can lead to a gravitational collapse compared to the limit  $10^{-3}$  given by streaming instability (SI) simulations, which is much closer to the lower end of the "meter-size barrier" and proves that accumulated self-gravitational interaction among particles over a long term is strong enough for smaller particles to successfully "jump the barrier".

5.5 FURTHER DISCUSSION OF  $k^{-3}$  BEHAVIOUR

At the end of this Chapter, we would like to further discuss the universal  $k^{-3}$  small-scale asymptotic behavior shown in all the [KFT](#) nonlinear density power spectra.

In [Section 5.2.2](#) and [Section 5.3.2](#), we employ the recently developed asymptotic analysis method in Konrad [25] and conclude that the gravity-free nonlinear [KFT](#) density power spectrum has the asymptotic expansion at the limit of  $k_1 \rightarrow \infty$  as

$$\mathcal{P}_f(k_1) \sim \frac{1}{|k_1|^3} \sqrt{\frac{(2\pi)^3}{\det A_f}} \exp\left(-\frac{k_1^\top A_f^{-1} k_1}{2|k_1|^2}\right) = \frac{\mathcal{P}_f^{(0)}(t)}{|k_1|^3}, \quad \text{with} \quad \lim_{\tau_s \rightarrow \infty} \mathcal{P}_f^{(0)}(t) = \mathcal{P}^{(0)}(t), \quad (5.116)$$

where  $\mathcal{P}_f^{(0)}(t)$  is given in [Equation 5.67](#) and  $\mathcal{P}^{(0)}(t)$  is given in [Equation 5.59](#). Furthermore, in [Section 5.4.3](#), by introducing a constant cutoff scale  $k_m$  which corresponds to the minimal distance between pebbles, we find the asymptotic constant for the mean interaction term  $i\langle S_I \rangle(k_1, t)$  at very small scales which further leads to the same  $k^{-3}$  tail for the full nonlinear density power spectrum as

$$\lim_{k_1 \rightarrow \infty} \mathcal{P}_g(k_1, t) = \lim_{k_1 \rightarrow \infty} \exp(i\langle S_I \rangle) \frac{\mathcal{P}_f^{(0)}(t)}{|k_1|^3} = \text{Constant} \cdot \frac{\mathcal{P}_f^{(0)}(t)}{|k_1|^3}. \quad (5.117)$$

These two equations suggest that the universal  $k^{-3}$  tail at small scales of the nonlinear density power spectrum always persists in a system with both friction and self-gravitational interactions, and its very presence is solely decided by the number of dimensions of the system of interests and the mathematical constraints set by criteria [1-3](#) for the form of its initial correlation functions. This conclusion is particularly significant for implying a scale-invariant density power increase at small scales by  $k^3 \mathcal{P} = \text{constant}$  even in a system considering friction and self-gravity. Though we discussed in [Section 5.4.3](#) that changing the form of the cutoff scale  $k_m$  will alter this slope for the gravitational case, however, these results still provide a lower limit for the gravitational aggregation and suggest that the total density power caused by the self-gravitational interaction will always increase at smaller scales.

## 5.6 SUMMARY AND DISCUSSION

In this Chapter, building on the simplified dust trajectory in [Chapter 3](#) and their initial probability distribution function in phase space ([iPDF](#)) in [Chapter 4](#), we finally apply the [KFT](#) method to planetary structure formation and give a full analysis of the dust particles' density power spectrum.

In the first section, we reviewed the derivation of the full nonlinear **KFT** density power spectrum for dust particles considering both the friction with the constant background gas field and their self-gravitational interaction with each other. We started with the factorized generating functional  $Z^d[\mathbf{L}]$  in Equation 5.1, by adopting the mean-field approach and averaging the self-gravitational interaction over the phase space coordinates with their density correlation functions, we pulled the interaction term in front of the integral and wrote the factorized generating functional as Equation 5.5. With the newly defined gravity-free generating functional  $Z_0^d[\mathbf{L}]$  being a complete Fourier transform of the **iPDF**, we completed the analytical integral and obtained the full **KFT** density power spectrum by combining the averaged interaction results. In the end, we modified the gravity-free **KFT** density power spectrum from  $\mathcal{P}(k_1, t)$  to  $\mathcal{P}_f(k_1, t)$  to guarantee its convergence.

In the second section, we ignored the friction ( $\tau_s \rightarrow \infty$ ) and the self-gravitational interaction in the system and reviewed the linear and nonlinear free **KFT** density power spectra for dust particles. First, we derived the expression of the linear free density power spectrum  $\mathcal{P}_{\text{lin}}(k_1, t)$  for the freely streaming particles at a very early evolution time ( $t \rightarrow 0$ ) and analyzed its  $k^{-1}$  small-scale asymptotic behavior. Then we introduced the new analytical asymptotic method developed by Konrad [25] to analyze the nonlinear free density power spectrum  $\mathcal{P}_{\text{free}}(k_1, t)$  and concluded that the nonlinear structure in the system changed the  $k^{-1}$  small scale asymptotic behavior to a  $k^{-3}$  tail. Furthermore, the constant power  $k_1^3 \mathcal{P}_{\text{free}}(k_1, t)$  indicated that for freely streaming particles, there is scale-invariant structure formation below a characteristic length scale, which is typically way below the resolution limit of numerical simulations at early times. This is a significant and mathematically rigorous conclusion that depends on the number of spatial dimensions and the form of the initial correlation functions. In the end, we analyzed the time-dependence of the small-scale  $k^{-3}$  asymptotic behavior and found an evolution time  $t_{\text{max}}$  corresponding to the maximal small-scale structure formation. The wave number  $k_0$  where the asymptotic behavior sets in decreases with time, first rapidly, then slowly, showing that small-scale structure formation proceeds quickly initially and then slows down. Furthermore, we discussed the relation between  $k_0$  and evolution time actually representing its relation with the general propagator  $g_{\text{qp}}(t)$ , due to the special form of the propagator  $g_0(t) = t$ .

In the third section, we still ignored the self-gravitational interaction among dust particles and reviewed the linear and nonlinear **KFT** density power spectra for dust particles undergoing friction with the constant background gas field. First, we derived the expression of the linear density power spectrum  $\mathcal{P}_{\text{lin}}(k_1, t)$  for very small dust particles  $\tau_s \rightarrow 0$  and concluded on the development of the  $k^{-1}$  tail at small scales. Then the analysis of how this small-scale behavior depends on time and particle size further suggests that more small-scale structure formation occurs for very small particles as the evolution time gets longer and the particle size gets larger. Next, we computed the nonlinear density power spectrum  $\mathcal{P}_f(k_1, t)$  for larger dust particles at finite evolution

time by employing the same asymptotic analysis as in Section 5.2.2 and found the same  $k^{-3}$  small-scale nonlinear asymptotic behavior, which implies the same scale-invariant structure formation at very small scales. In the end, we analyzed the time and particle-size dependence for the small-scale  $k^{-3}$  asymptotic behavior of  $\mathcal{P}_f(k_1, t)$ , and found a minimal evolution time  $g_{qp,m}$ , before which the small scale structure never reaches to its maximum, and a critical particle size  $\tau_s^c$ , at which the system shows the maximal small scale structure formation. More specifically, when the particle size  $\tau_s < \tau_s^c$ , the small-scale structure continuously forms yet is always smaller than its maximum until the propagator  $g_{qp}(t)$  reaches its maximum and the system freezes, while if the particle size  $\tau_s > \tau_s^c$ , then the small-scale structure initially grows until it reaches its maximum, then dissipates over time until the system freezes.

In the fourth section, we further considered both friction and gravitational interactions in the system to calculate the full linear and nonlinear KFT density power spectra and determine the conditions for gravitational collapses. We started with specifying the dimensionless gravitational constant  $\hat{G} = f\hat{G}_0$  in which the dust density is scaled by the critical Hill density that can withstand the tidal shear in the particle cloud. Next, we found the fitting functions for the gravity-free density power spectra  $\mathcal{P}_{\text{flin}}(k_1, t_0)$  and  $\mathcal{P}_f(k_1, t_0)$  at evolution time  $t_0$  to approximate the density power spectrum  $P(k, t')$  at time  $t'$  occurring in the mean interaction term  $i\langle S_I \rangle(k_1, t)$ , which provided the gravitational growth to the full density power spectrum. Then, for smaller particles, we calculated their corresponding mean interaction term by setting the cutoff scale  $k_m$  to the minimal pebble separation and computed the linear full density power spectrum  $\mathcal{P}_{\text{glin}}(k_1, t)$ . The results further concluded that larger particle sizes and denser particle clouds would lead to faster gravitational aggregation and potentially faster gravitational collapse in the system. We then calculate  $i\langle S_I \rangle(k_1, t)$  and the full nonlinear KFT density power spectrum  $\mathcal{P}_g(k_1, t)$  for large-size particles by employing the same constant cutoff scale  $k_m$ . The analysis showed that increasing the density of the dust particles leads to stronger gravitational interaction/weaker friction interaction, which speeds up the gravitational evolution and collapses significantly. Moreover, due to the attractive nature of gravity, we found the presence of self-gravitational interaction in the system helps trap larger dust particles at small scales and changed the particle size  $\tau_s^c = 3.04$  that corresponds to the strongest small-scale structure formation to larger values as evolution time proceeds. Lastly, we replaced  $i\langle S_I \rangle(k_1, t)$  by its fitting function  $S_{\text{fit}}(k_1, t, \tau_s, f)$  to calculate the averaged density growth  $\delta^2$  from initial time  $t_0$  to later evolution time  $t$ . By setting the collapse criteria to  $\delta^2 = 10^{14}$ , we found the relation  $\tau_s^3(t - t_0)f = 2.60 \times 10^{-8}$  for smaller particles to determine the collapse moment in a PPD with the initial setup as the simulation. Furthermore, by setting the dust density as the critical Hill density ( $f = 1$ ) and the evolution time as the averaged lifetime of a PPD ( $t = 10^6$ ), we found the minimal particle size  $\tau_s^g = 2.96 \times 10^{-5}$  to ensure a final gravitational collapse in the system, which greatly lowered the limit  $10^{-3}$  set by simulations and provided evidence that accumulated self-gravitational interaction over a

long evolution time could be sufficient for smaller particles to successfully "jump the barrier" and achieve gravitational collapse.

In the end, we summarized the universal  $k^{-3}$  asymptotic behavior at small scales for all nonlinear KFT density power spectra and concluded its necessary development for a 3-dimensional system considering both friction and self-gravity with its initial correlation functions satisfying the mathematical criteria 1-3. Though the small-scale  $k^{-3}$  asymptotic behavior for  $\mathcal{P}_g(k_1, t)$  highly depended on the choice of the constant cutoff scale  $k_m$ , these results still provided a lower limit for the gravitational aggregation and evidence that the total density structure bought by the self-gravitational interaction will always increase at the scale getting smaller.

## DUST MOMENTUM-DENSITY POWER SPECTRA BY KFT

In this Chapter, we focus on extracting the kinetic information of a general proto-planetary disk (PPD) with the initial setup as the simulation by analyzing the 2-point KFT momentum-density power spectra for dust particles derived from the momentum factorized generating functional in Equation 3.61 where we've rewritten as

$$\begin{aligned} Z^m[\mathbf{L}] &= \int d\Gamma \prod_{j=1}^2 \left[ g_{pp}(t_j) \vec{p}_j + \int_0^{t_j} dt' g_{pp}(t_j, t') \left( \frac{\vec{u}_0}{\tau_s} - \vec{\nabla}_{\mathbf{q}_j} \Phi \right) \right] \cdot e^{i\langle \mathbf{L}_q, \mathbf{q} \rangle + i\langle \mathbf{L}_p, \mathbf{p} \rangle + iS_I} \\ &= \prod_{j=1}^2 \left[ -ig_{pp}(t_j) \frac{\partial}{\partial \vec{L}_{p_j}} + \int_0^{t_j} dt' g_{pp}(t_j, t') \left( \frac{\vec{u}_0}{\tau_s} - \vec{f}_j(t') \right) \right] Z^d[\mathbf{L}], \end{aligned} \quad (6.1)$$

with the momentum propagator  $g_{pp}(t)$  given in Equation 3.39, the averaged force term  $\vec{f}_j(t') = \langle \vec{\nabla}_{\mathbf{q}_j} \Phi \rangle(\mathbf{k}_1, t)$  given in Equation 5.33, and the density factorized generating functional  $Z^d[\mathbf{L}]$  given in Equation 5.5. Here we've applied the mean field approach to average all gravitational terms over the phase space coordinates to pull the momentum density operators in the front.

There are three scalar momentum-density power spectra will be calculated in this Chapter that are derived from the following quantities

$$\text{tr} \left( \hat{\Pi}_1(1) \hat{\Pi}_2(2) Z[\mathbf{J}] \Big|_{\mathbf{J}=0} \right) = \text{tr} (Z^m[\mathbf{L}]), \quad (6.2)$$

$$\left( \vec{\nabla}_{\mathbf{q}} \cdot \hat{\Pi}_1(1) \right) \left( \vec{\nabla}_{\mathbf{q}} \cdot \hat{\Pi}_2(2) \right) Z[\mathbf{J}] \Big|_{\mathbf{J}=0} = \vec{k}_1 \cdot Z^m[\mathbf{L}] \vec{k}_1, \quad (6.3)$$

$$\left( \vec{\nabla}_{\mathbf{q}} \times \hat{\Pi}_1(1) \right) \cdot \left( \vec{\nabla}_{\mathbf{q}} \times \hat{\Pi}_2(2) \right) Z[\mathbf{J}] \Big|_{\mathbf{J}=0} = k_1^2 \text{tr} (Z^m[\mathbf{L}]) - \vec{k}_1 \cdot Z^m[\mathbf{L}] \vec{k}_1, \quad (6.4)$$

with the momentum-density operator  $\hat{\Pi}_j(1)$  defined in Equation 3.59, and we've used the condition  $\vec{k}_1 + \vec{k}_2 = 0$  in Equation 5.10 ensured by the statistical homogeneity in the system.

This chapter is structured as follows. In the first section, we derive the general expressions for the three KFT scalar momentum-density power spectra by calculating in detail the factorized generating functional  $Z^m[\mathbf{L}]$  and the quantities defined in Equation 6.2-6.4. In the second section, we introduce a new asymptotic method to help analyze certain types of integrals shown in the three momentum-density power spectra. In the third section, we ignore the friction and self-gravitational interaction in the

system. For freely streaming particles at different evolution times, their linear and nonlinear momentum-density power spectra are derived and their small-scale kinetic information is analyzed. In the fourth section, we add friction interaction back to the system. For different sizes of particles with different values of  $\tau_s$ , we calculate the corresponding linear and nonlinear momentum-density power spectra and analyze their asymptotic behaviors at small scales. In the end, we welcome the self-gravitational interaction among dust particles back into the play, for different values of  $\tau_s$ , we compute the gravitational momentum-density power spectra and further discuss their effects on the kinetic information.

### 6.1 ANALYTICAL DERIVATION OF MOMENTUM-DENSITY POWER SPECTRA

In this section, we start with the factorized generating functional in [Equation 6.1](#), since the averaged interaction term  $i\langle S_I \rangle(k_1, t)$  hidden in  $Z^d[\mathbf{L}]$  only relies on the evolution time and the wavenumber  $k_1$ , the momentum-density operator doesn't apply to them, we can thus pull them in the front and rewrite

$$Z^m[\mathbf{L}] = e^{i\langle S_I \rangle} \bar{Z}_{12}[\mathbf{L}], \quad (6.5)$$

with the definition of a new "free" generating functional  $\bar{Z}_{12}[\mathbf{L}]$  as

$$\bar{Z}_{12}[\mathbf{L}] = \prod_{j=1}^2 \left[ -ig_{pp}(t_j) \frac{\partial}{\partial \bar{L}_{p_j}} + \int_0^{t_j} dt' g_{pp}(t_j, t') \left( \frac{\vec{u}_0}{\tau_s} - \vec{f}_j(t') \right) \right] Z_0^d[\mathbf{L}]. \quad (6.6)$$

By analyzing the matrix components of  $\bar{Z}_{12}[\mathbf{L}]$  and calculating the quantities in [Equation 6.2-6.4](#), we derive the final expressions for the three KFT scalar momentum-density power spectra. Here "free" is in quotes for the reason that though we split the interaction term from the new generating functional, the friction and self-gravitational interactions are still embedded in the momentum-density operators.

#### 6.1.1 Factorize Generating Functional

First, we focus on solving the "free" generating functional in [Equation 6.6](#), at the evolution time  $t = t_1 = t_2$ , write its matrix components as

$$\begin{aligned} \bar{Z}_{12}^{\eta\rho}[\mathbf{L}] &= \bar{Z}_{12}^{\eta\rho(1)}[\mathbf{L}] + \bar{Z}_{12}^{\eta\rho(2)}[\mathbf{L}] + \bar{Z}_{12}^{\eta\rho(3)}[\mathbf{L}] = \left[ -ig_{pp}(t) \frac{\partial}{\partial \bar{L}_{p_1}^\eta} + u_0^\eta (1 - g_{pp}(t)) - F_1^\eta(t) \right] \\ &\quad \cdot \left[ -ig_{pp}(t) \frac{\partial}{\partial \bar{L}_{p_2}^\rho} + u_0^\rho (1 - g_{pp}(t)) - F_2^\rho(t) \right] Z_0^d[\mathbf{L}], \quad (6.7) \end{aligned}$$

with

$$\bar{Z}_{12}^{\eta\rho(1)}[\mathbf{L}] = -g_{pp}^2(t) \frac{\partial^2}{\partial L_{p_1}^\eta \partial L_{p_2}^\rho} Z_0^d[\mathbf{L}], \quad (6.8)$$

$$\begin{aligned} \bar{Z}_{12}^{\eta\rho(2)}[\mathbf{L}] = & \left[ (F_2^\rho(t) - u_0^\rho(1 - g_{pp}(t))) \frac{\partial}{\partial L_{p_1}^\eta} + (F_1^\eta(t) - u_0^\eta(1 - g_{pp}(t))) \frac{\partial}{\partial L_{p_2}^\rho} \right] \\ & \cdot ig_{pp}(t) Z_0^d[\mathbf{L}], \end{aligned} \quad (6.9)$$

$$\bar{Z}_{12}^{\eta\rho(3)}[\mathbf{L}] = [u_0^\eta(1 - g_{pp}(t)) - F_1^\eta(t)] [u_0^\rho(1 - g_{pp}(t)) - F_2^\rho(t)] Z_0^d[\mathbf{L}], \quad (6.10)$$

where we've performed the integral  $\int_0^t dt' g_{pp}(t, t') = g_{qp}(t) = \tau_s(1 - g_{pp}(t))$  and defined time-averaged force  $\vec{F}_j(t)$  as

$$\vec{F}_j(t) = \int_{t_0}^t dt' g_{pp}(t, t') \vec{f}_j(t'), \quad (6.11)$$

with Newton's third law assures  $\vec{f}_1(t') + \vec{f}_2(t') = 0$  and further  $\vec{F}_1(t) + \vec{F}_2(t) = 0$ .

For the convenience of calculations in this Chapter, we rewrite the gravity-free generating functional  $Z_0^d[\mathbf{L}]$  in [Equation 5.11](#) as

$$Z_0^d[\mathbf{L}] = \mathcal{C} N^{-N} V^{N-2} (2\pi)^3 \delta(\vec{k}_1 + \vec{k}_2) \bar{D} \quad (6.12)$$

where the new integral  $\bar{D}$  is defined as

$$\begin{aligned} \bar{D} = & \int_{\mathbf{r}} \exp \left( -\frac{1}{2} \vec{L}_{p_1} \bar{C}_{p_1 p_1}(0) \vec{L}_{p_1} - \frac{1}{2} \vec{L}_{p_2} \bar{C}_{p_2 p_2}(0) \vec{L}_{p_2} - \vec{L}_{p_1} \bar{C}_{p_1 p_2}(r) \vec{L}_{p_2} + i\vec{k}_2 \cdot \vec{r} \right) \\ = & \bar{D}_1 \int_{\mathbf{r}} \bar{D}_2, \end{aligned} \quad (6.13)$$

with components

$$\bar{D}_1 = \exp \left( \frac{1}{2} m_3(0) (L_{p_1}^2 + L_{p_2}^2) \right), \quad (6.14)$$

$$\bar{D}_2 = \exp \left( \frac{1}{2} m_4(0) (\vec{L}_{p_1} \tilde{\pi}_{\parallel} \vec{L}_{p_1} + \vec{L}_{p_2} \tilde{\pi}_{\parallel} \vec{L}_{p_2}) + m_3(r) \vec{L}_{p_1} \cdot \vec{L}_{p_2} + m_4(r) \vec{L}_{p_1} \tilde{\pi}_{\parallel} \vec{L}_{p_2} + i\vec{k}_2 \cdot \vec{r} \right). \quad (6.15)$$

Here the momentum covariance matrix  $\bar{C}_{pp}$  is rotated to the wavenumber  $\hat{k}$  space by [Equation 4.80](#) instead of the  $\hat{q}$  space in [Section 5.1.1](#), and  $m_3(r)$  and  $m_4(r)$  are given in [Equation 4.86](#) and [Equation 4.87](#).

We start solving Equation 6.7 by looking into the derivatives of integral  $\bar{D}$  in the equation Equation 6.13. First apply one momentum density operator  $\frac{\partial}{\partial L_{p_j}^\rho}$  in front of  $\bar{D}$  to obtain

$$\frac{\partial}{\partial L_{p_j}^\rho} \bar{D} = \frac{\partial \bar{D}_1}{\partial L_{p_j}^\rho} \int_r \bar{D}_2 + \bar{D}_1 \int_r \frac{\partial \bar{D}_2}{\partial L_{p_j}^\rho}, \quad (6.16)$$

with the first derivatives of  $\bar{D}_1$  and  $\bar{D}_2$  being

$$\frac{\partial \bar{D}_1}{\partial L_{p_j}^\rho} = m_3(0) (\delta_{1j} L_{p_1}^\rho + \delta_{2j} L_{p_2}^\rho) \bar{D}_1, \quad (6.17)$$

$$\begin{aligned} \frac{\partial \bar{D}_2}{\partial L_{p_j}^\rho} = & \bar{D}_2 \left( \frac{1}{2} m_4(0) \left( (\tilde{\pi}_{\parallel} \vec{L}_{p_1} + \vec{L}_{p_1} \tilde{\pi}_{\parallel})^\rho \delta_{1j} + (\tilde{\pi}_{\parallel} \vec{L}_{p_2} + \vec{L}_{p_2} \tilde{\pi}_{\parallel})^\rho \delta_{2j} \right) \right. \\ & \left. + m_3(r) \left( L_{p_1}^\rho \delta_{2j} + L_{p_2}^\rho \delta_{1j} \right) + m_4(r) \left( (\tilde{\pi}_{\parallel} \vec{L}_{p_2})^\rho \delta_{1j} + (\vec{L}_{p_1} \tilde{\pi}_{\parallel})^\rho \delta_{2j} \right) \right). \end{aligned} \quad (6.18)$$

Then apply another momentum density operator  $\frac{\partial}{\partial L_{p_k}^\eta}$  in front of  $\bar{D}$  to obtain

$$\frac{\partial}{\partial L_{p_k}^\eta} \frac{\partial}{\partial L_{p_j}^\rho} \bar{D} = \frac{\partial^2 \bar{D}_1}{\partial L_{p_k}^\eta \partial L_{p_j}^\rho} \int_r \bar{D}_2 + \frac{\partial \bar{D}_1}{\partial L_{p_j}^\rho} \int_r \frac{\partial \bar{D}_2}{\partial L_{p_k}^\eta} + \frac{\partial \bar{D}_1}{\partial L_{p_k}^\eta} \int_r \frac{\partial \bar{D}_2}{\partial L_{p_j}^\rho} + \bar{D}_1 \int_r \frac{\partial^2 \bar{D}_2}{\partial L_{p_k}^\eta \partial L_{p_j}^\rho}, \quad (6.19)$$

with the second derivatives of  $\bar{D}_1$  and  $\bar{D}_2$  being

$$\begin{aligned} \frac{\partial^2 \bar{D}_1}{\partial L_{p_k}^\eta \partial L_{p_j}^\rho} = & m_3^2(0) (\delta_{1j} L_{p_1}^\rho + \delta_{2j} L_{p_2}^\rho) (\delta_{1k} L_{p_1}^\eta + \delta_{2k} L_{p_2}^\eta) \bar{D}_1 + \\ & m_3(0) (\delta_{1j} \delta_{1k} \delta^{\eta\rho} + \delta_{2j} \delta_{2k} \delta^{\eta\rho}) \bar{D}_1 \end{aligned} \quad (6.20)$$

$$\begin{aligned} & \stackrel{\text{if } j \neq k}{=} m_3^2(0) (\delta_{1j} L_{p_1}^\rho + \delta_{2j} L_{p_2}^\rho) (\delta_{1k} L_{p_1}^\eta + \delta_{2k} L_{p_2}^\eta) \bar{D}_1, \\ \frac{\partial^2 \bar{D}_2}{\partial L_{p_k}^\eta \partial L_{p_j}^\rho} = & \underbrace{\left( m_4(0) \tilde{\pi}_{\parallel}^{\eta\rho} (\delta_{1j} \delta_{1k} + \delta_{2j} \delta_{2k}) + (m_3(r) \delta^{\eta\rho} + m_4(r) \tilde{\pi}_{\parallel}^{\eta\rho}) (\delta_{1k} \delta_{2j} + \delta_{2k} \delta_{1j}) \right)}_{\text{part-1}} \\ & \cdot \bar{D}_2 + \frac{\partial \bar{D}_2}{\partial L_{p_k}^\eta} \left( \frac{1}{2} m_4(0) \left( (\tilde{\pi}_{\parallel} \vec{L}_{p_1} + \vec{L}_{p_1} \tilde{\pi}_{\parallel})^\rho \delta_{1j} + (\tilde{\pi}_{\parallel} \vec{L}_{p_2} + \vec{L}_{p_2} \tilde{\pi}_{\parallel})^\rho \delta_{2j} \right) \right. \\ & \left. + m_3(r) \left( L_{p_1}^\rho \delta_{2j} + L_{p_2}^\rho \delta_{1j} \right) + m_4(r) \left( (\tilde{\pi}_{\parallel} \vec{L}_{p_2})^\rho \delta_{1j} + (\vec{L}_{p_1} \tilde{\pi}_{\parallel})^\rho \delta_{2j} \right) \right). \end{aligned} \quad (6.21)$$

We can thus write the expression for  $\bar{Z}_{12}^{\eta\rho(1)}[\mathbf{L}]$  as

$$\begin{aligned}
 \bar{Z}_{12}^{\eta\rho(1)}[\mathbf{L}] = & -\mathcal{C}N^{-N}V^{N-2}(2\pi)^3\delta(\vec{k}_1 + \vec{k}_2)g_{pp}^2(t) \left[ \underbrace{\frac{m_3^2(0)L_{p_2}^\rho L_{p_1}^\eta \bar{D}}{\frac{\partial^2 \bar{D}_1}{\partial L_{p_1}^\eta \partial L_{p_2}^\rho} \int_r \bar{D}_2}}_{\frac{\partial^2 \bar{D}_1}{\partial L_{p_1}^\eta \partial L_{p_2}^\rho} \int_r \bar{D}_2} + \int_r \left( \underbrace{m_3(0)L_{p_2}^\rho \bar{D}_1}_{\frac{\partial \bar{D}_1}{\partial L_{p_2}^\rho}} \right. \right. \\
 & \cdot \underbrace{\bar{D}_2 \left( \frac{1}{2}m_4(0)(\tilde{\pi}_\parallel \vec{L}_{p_1} + \vec{L}_{p_1} \tilde{\pi}_\parallel)^\eta + m_3(r)L_{p_2}^\eta + m_4(r)(\tilde{\pi}_\parallel \vec{L}_{p_2})^\eta \right)}_{\frac{\partial \bar{D}_2}{\partial L_{p_1}^\eta}} \left. \right) \\
 & + \int_r \left( \underbrace{m_3(0)L_{p_1}^\eta \bar{D}_1}_{\frac{\partial \bar{D}_1}{\partial L_{p_1}^\eta}} \cdot \underbrace{\bar{D}_2 \left( \frac{1}{2}m_4(0)(\tilde{\pi}_\parallel \vec{L}_{p_2} + \vec{L}_{p_2} \tilde{\pi}_\parallel)^\rho + m_3(r)L_{p_1}^\rho + m_4(r)(\vec{L}_{p_1} \tilde{\pi}_\parallel)^\rho \right)}_{\frac{\partial \bar{D}_2}{\partial L_{p_2}^\rho}} \right) \\
 & + \bar{D}_1 \int_r \bar{D}_2 \left( \underbrace{\left( \frac{1}{2}m_4(0)(\tilde{\pi}_\parallel \vec{L}_{p_1} + \vec{L}_{p_1} \tilde{\pi}_\parallel)^\eta + m_3(r)L_{p_2}^\eta + m_4(r)(\tilde{\pi}_\parallel \vec{L}_{p_2})^\eta \right)}_{\frac{\partial \bar{D}_2}{\partial L_{p_1}^\eta}} \right. \\
 & \left. \cdot \underbrace{\left( \frac{1}{2}m_4(0)(\tilde{\pi}_\parallel \vec{L}_{p_2} + \vec{L}_{p_2} \tilde{\pi}_\parallel)^\rho + m_3(r)L_{p_1}^\rho + m_4(r)(\vec{L}_{p_1} \tilde{\pi}_\parallel)^\rho \right)}_{\frac{\partial \bar{D}_2}{\partial L_{p_2}^\rho}} + \underbrace{m_3(r)\delta^{\eta\rho} + m_4(r)\tilde{\pi}_\parallel^{\eta\rho}}_{\frac{\partial^2 \bar{D}_2}{\partial L_{p_1}^\eta \partial L_{p_2}^\rho} \text{ part-1}} \right) \Big] \\
 & \tag{6.22}
 \end{aligned}$$

With the shift vectors  $\vec{L}_{p_1} = -\vec{k}_1 g_{qp}(t)$  and  $\vec{L}_{p_2} = \vec{k}_1 g_{qp}(t)$ , the above expression has a much simpler form as

$$\begin{aligned}
 \bar{Z}_{12}^{\eta\rho(1)}[\mathbf{L}] = & \mathcal{C}N^{-N}V^{N-2}(2\pi)^3\delta(\vec{k}_1 + \vec{k}_2)g_{pp}^2(t)\bar{D}_1 \int_r \bar{D}_2 \left[ - (m_3(r)\delta^{\eta\rho} + m_4(r)\tilde{\pi}_\parallel^{\eta\rho}) + \right. \\
 & \left. g_{qp}^2(t)k_1^\eta k_1^\rho \left( m_3(0) + m_4(0) - m_3(r) - m_4(r) \right)^2 \right], \\
 & \tag{6.23}
 \end{aligned}$$

where the components become

$$\bar{D}_1 = \exp(g_{qp}^2(t)k_1^2 m_3(0)) \tag{6.24}$$

$$\bar{D}_2 = \exp\left(g_{qp}^2(t)k_1^2 \left(m_4(0) - m_3(r) - m_4(r)\right) - i\vec{k}_1 \cdot \vec{r}\right) \tag{6.25}$$

Next, the expression for  $\bar{Z}_{12}^{\eta\rho(2)}[\mathbf{L}]$  becomes

$$\begin{aligned}
\bar{Z}_{12}^{\eta\rho(2)}[\mathbf{L}] = & i\mathcal{C}N^{-N}V^{N-2}(2\pi)^3\delta(\vec{k}_1 + \vec{k}_2)g_{pp}(t) \left[ \left( F_1^\eta(t) - u_0^\eta(1 - g_{pp}(t)) \right) \cdot \right. \\
& \underbrace{\left( \bar{D}_1 \cdot \int_r \bar{D}_2 \left( \frac{1}{2}m_4(0)(\tilde{\pi}_{\parallel}\vec{L}_{p_2} + \vec{L}_{p_2}\tilde{\pi}_{\parallel})^\rho + m_3(r)L_{p_1}^\rho + m_4(r)(\vec{L}_{p_1}\tilde{\pi}_{\parallel})^\rho \right) + \right.}_{\int_r \frac{\partial \bar{D}_2}{\partial \mathbf{l}_{p_2}^\rho}} \\
& \underbrace{\left. m_3(0)L_{p_2}^\rho \bar{D} \right)}_{\frac{\partial \bar{D}_1}{\partial \mathbf{l}_{p_2}^\rho} \int_r \bar{D}_2} + \left( F_2^\rho(t) - u_0^\rho(1 - g_{pp}(t)) \right) \cdot \left( \underbrace{m_3(0)L_{p_1}^\eta \bar{D}}_{\frac{\partial \bar{D}_1}{\partial \mathbf{l}_{p_1}^\eta} \int_r \bar{D}_2} + \right. \\
& \left. \left. \bar{D}_1 \cdot \int_r \bar{D}_2 \left( \frac{1}{2}m_4(0)(\tilde{\pi}_{\parallel}\vec{L}_{p_1} + \vec{L}_{p_1}\tilde{\pi}_{\parallel})^\eta + m_3(r)L_{p_2}^\eta + m_4(r)(\tilde{\pi}_{\parallel}\vec{L}_{p_2})^\eta \right) \right) \right] \quad (6.26) \\
& \underbrace{\left. \right)}_{\int_r \frac{\partial \bar{D}_2}{\partial \mathbf{l}_{p_1}^\eta}}
\end{aligned}$$

with the same shift vectors plugging in the above equation, it becomes

$$\begin{aligned}
\bar{Z}_{12}^{\eta\rho(2)}[\mathbf{L}] = & i\mathcal{C}N^{-N}V^{N-2}(2\pi)^3\delta(\vec{k}_1 + \vec{k}_2)g_{pp}(t)g_{qp}(t) \\
& \cdot \left( \left( F_1^\eta(t) - u_0^\eta(1 - g_{pp}(t)) \right) k_1^\rho - \left( F_2^\rho(t) - u_0^\rho(1 - g_{pp}(t)) \right) k_1^\eta \right) \quad (6.27) \\
& \cdot \bar{D}_1 \int_r \bar{D}_2 \left( m_3(0) + m_4(0) - m_3(r) - m_4(r) \right).
\end{aligned}$$

With  $\bar{Z}_{12}^{\eta\rho(3)}$  merely being a simple multiplication, define a new function

$$m(r) = m_3(r) + m_4(r) = ((1 - 3\mu^2)b_1 - b_0)\zeta_{pp}(r), \quad (6.28)$$

then we can write down the final expression for the "free" generating functional

$$\begin{aligned}
\bar{Z}_{12}^{\eta\rho} = & \mathcal{C}N^{-N}V^{N-2}(2\pi)^3\delta(\vec{k}_1 + \vec{k}_2)\bar{D}_1 \int_r \bar{D}_2 \left[ -g_{pp}^2(t)(m_3(r)\delta^{\eta\rho} + m_4(r)\tilde{\pi}_{\parallel}^{\eta\rho}) \right. \\
& + g_{pp}^2(t)g_{qp}^2(t)k_1^\eta k_1^\rho (m(0) - m(r))^2 + ig_{pp}(t)g_{qp}(t)\bar{D}_1 \int_r \bar{D}_2 (m(0) - m(r)) \cdot \\
& \left( \left( F_1^\eta(t) - u_0^\eta(1 - g_{pp}(t)) \right) k_1^\rho + \left( F_1^\rho(t) + u_0^\rho(1 - g_{pp}(t)) \right) k_1^\eta \right) + \\
& \left. \left[ u_0^\eta(1 - g_{pp}(t)) - F_1^\eta(t) \right] \left[ u_0^\rho(1 - g_{pp}(t)) + F_1^\rho(t) \right] \right]. \quad (6.29)
\end{aligned}$$

Here we've used the relation  $\vec{F}_1(t) + \vec{F}_2(t) = 0$  ensured by Newton's third law.

## 6.1.2 Three Scalar Momentum-Density Power Spectra

In this section, we derive the final expressions for the three scalar momentum-density power spectra by calculating the three quantities in Equation 6.2-6.4 with the factorized generating functional  $Z^m[\mathbf{L}] = e^{i\langle S_i \rangle} \bar{Z}_{12}$ .

We start with the trace term in Equation 6.2,

$$\begin{aligned} \text{tr}(Z^m[\mathbf{L}]) &= e^{i\langle S_i \rangle} \bar{Z}_{12\eta}^\eta = \mathcal{C} N^{-N} V^{N-2} (2\pi)^3 \delta(\vec{k}_1 + \vec{k}_2) e^{i\langle S_i \rangle} \bar{D}_1 \int_{\mathbf{r}} \bar{D}_2 \cdot \\ &\left[ -g_{pp}^2(t) (3m_3(r) + m_4(r)) + g_{pp}^2 g_{qp}^2 k_1^2 (m(0) - m(r))^2 + \right. \\ &\left. 2ig_{pp}(t) g_{qp}(t) (m(0) - m(r)) \vec{k}_1 \cdot \vec{F}_1 + g_{qp}^2(t) \frac{u_0^2}{\tau_s^2} - \vec{F}_1 \cdot \vec{F}_1 \right], \end{aligned} \quad (6.30)$$

where we obtain the full expression for the trace momentum-density power spectrum as

$$\begin{aligned} \mathcal{P}_{\text{gtr}}(k_1, t) &= g_{pp}^2(t) e^{i\langle S_i \rangle} \mathcal{P}_m(k_1, t) + 2ig_{pp}(t) g_{qp}(t) (\vec{k}_1 \cdot \vec{F}_1) \cdot \\ &e^{i\langle S_i \rangle} (\mathcal{T}_5 + \mathcal{T}_7 + \mathcal{T}_8) + \left( g_{qp}^2(t) \frac{u_0^2}{\tau_s^2} - \vec{F}_1 \cdot \vec{F}_1 \right) \mathcal{P}_g(k_1, t), \end{aligned} \quad (6.31)$$

with  $\mathcal{P}_g(k_1, t)$  being the full nonlinear KFT density power spectrum given in Equation 5.38. Also we've defined the integral  $\mathcal{P}_m(k_1, t)$  as

$$\begin{aligned} \mathcal{P}_m(k_1, t) &= \int_{\mathbf{r}} \left[ -3m_3(r) - m_4(r) + g_{qp}^2(t) k_1^2 (m(r) - m(0))^2 \right] e^{-g_{qp}^2(t) k_1^2 (m(r) - m(0)) - i\vec{k}_1 \cdot \vec{r}} \\ &= \underbrace{\int_{\mathbf{r}} 3b_0 \zeta_{pp}(r) e^{-g_{qp}^2(t) k_1^2 (m(r) - m(0)) - i\vec{k}_1 \cdot \vec{r}}}_{\mathcal{T}_1} \\ &+ \underbrace{\int_{\mathbf{r}} \left[ g_{qp}^2(t) k_1^2 (m^2(r) - 2m(r)m(0)) \right] e^{-g_{qp}^2(t) k_1^2 (m(r) - m(0)) - i\vec{k}_1 \cdot \vec{r}}}_{\mathcal{T}_2} \\ &+ \underbrace{\int_{\mathbf{r}} g_{qp}^2(t) k_1^2 m^2(0) \left[ e^{-g_{qp}^2(t) k_1^2 m(r)} - 1 \right] \cdot e^{g_{qp}^2(t) k_1^2 m(0) - i\vec{k}_1 \cdot \vec{r}}}_{\mathcal{T}_3} \\ &+ \underbrace{\int_{\mathbf{r}} g_{qp}^2(t) k_1^2 m^2(0) e^{g_{qp}^2(t) k_1^2 m(0) - i\vec{k}_1 \cdot \vec{r}}}_{\mathcal{T}_4}, \end{aligned}$$

(6.32)

and the momentum-density power spectra elements as

$$T_5 = - \int_{\mathbf{r}} m(\mathbf{r}) e^{-g_{qp}^2(t) k_1^2 (m(\mathbf{r}) - m(0)) - i \vec{k}_1 \cdot \vec{r}}, \quad (6.33)$$

$$T_7 = \int_{\mathbf{r}} m(0) \left[ e^{-g_{qp}^2(t) k_1^2 m(\mathbf{r})} - 1 \right] \cdot e^{g_{qp}^2(t) k_1^2 m(0) - i \vec{k}_1 \cdot \vec{r}}, \quad (6.34)$$

$$T_8 = \int_{\mathbf{r}} m(0) e^{g_{qp}^2(t) k_1^2 m(0) - i \vec{k}_1 \cdot \vec{r}}. \quad (6.35)$$

To guarantee the trace momentum-density power spectrum  $\mathcal{P}_{\text{gr}}(k_1, t)$  being convergent, we start with analyzing the elements in the integral  $\mathcal{P}_m(k_1, t)$ . First, integrate  $T_1$  over spherical coordinates  $\varphi$  and  $\mu$  to obtain

$$T_1 = 6\pi b_0 \int_0^\infty dr r^2 l_1(r) = 6\pi b_0 \int_0^\infty dr r^2 \zeta_{pp}(r) \int_{-1}^1 d\mu e^{-g_{qp}^2(t) k_1^2 (m(r) - m(0)) - i k_1 r \mu}, \quad (6.36)$$

at finite time  $t$  and wave number  $k_1$ , making use of the asymptotic behavior for  $\zeta_{pp}(r)$  in Equation 4.76, the integrand  $r^2 l_1(r)$  satisfies

$$\lim_{r \rightarrow \infty} r^2 l_1(r) = \lim_{r \rightarrow \infty} r^2 \frac{0.04}{r^{\frac{7}{3}}} \int_{-1}^1 d\mu e^{y(t, \mu)} \cos k_1 r \mu < e^{y(t, 0)} \frac{0.08 |\sin k_1 r|}{k_1 r^{\frac{4}{3}}} \rightarrow 0, \quad (6.37)$$

which guarantees term  $T_1$  converges at large  $r$ . Here we already exploit the fact that  $y(t, \mu) = g_{qp}^2(t) k_1^2 m(0)$  in Equation 5.16 is a negative, monotonously decreasing function in terms of  $\mu^2$ . Similarly, integrate term  $T_2$  over spherical coordinates  $\varphi$  and  $\mu$ ,

$$T_2 = 2\pi \int_0^\infty dr r^2 l_2(r) = -2\pi \int_0^\infty dr g_{qp}^2(t) k_1^2 r^2 \zeta_{pp}(r) (2\zeta_{pp}(0) - \zeta_{pp}(r)) \int_{-1}^1 d\mu ((1 - 3\mu^2) b_1 - b_0)^2 e^{-g_{qp}^2(t) k_1^2 (m(r) - m(0)) - i k_1 r \mu} < 0 \quad (6.38)$$

At finite time  $t$  and wave number  $k_1$ , the integrand  $r^2 l_2(r)$  satisfies

$$\lim_{r \rightarrow \infty} r^2 l_2(r) > -g_{qp}^2 k_1^2 (2b_1 + b_0)^2 \zeta_{pp}(0) e^{y(t, 0)} \frac{0.16 |\sin k_1 r|}{k_1 r^{\frac{4}{3}}} \rightarrow 0 \quad (6.39)$$

which guarantees term  $T_2$  converges at large  $r$ . For term  $T_3$ , again integrate over spherical coordinates  $\varphi$  and  $\mu$ ,

$$T_3 = 2\pi \int_0^\infty dr r^2 l_3(r) = 2\pi \int_0^\infty dr g_{qp}^2(t) k_1^2 r^2 \zeta_{pp}^2(0) \cdot \int_{-1}^1 d\mu \left( (3\mu^2 - 1)b_1 + b_0 \right)^2 \left[ e^{-g_{qp}^2(t) k_1^2 m(r)} - 1 \right] e^{y(t,\mu) - ik_1 r \mu} \quad (6.40)$$

In the limit of  $r \rightarrow \infty$ , the expression in the square brackets satisfies

$$\lim_{r \rightarrow \infty} \left[ e^{-g_{qp}^2(t) k_1^2 m(r)} - 1 \right] = g_{qp}^2(t) k_1^2 \left( (3\mu^2 - 1)b_1 + b_0 \right) \frac{0.04}{r^{\frac{7}{3}}} \rightarrow 0 \quad (6.41)$$

Thus given finite time  $t$  and wave number  $k_1$ , the integrand  $r^2 l_3(r)$  satisfies

$$\lim_{r \rightarrow \infty} r^2 l_3(r) < g_{qp}^4(t) k_1^3 (2b_1 + b_0)^3 \zeta_{pp}^2(0) e^{y(t,0)} \frac{0.08 |\sin k_1 r|}{r^{\frac{4}{3}}} \rightarrow 0 \quad (6.42)$$

which guarantees term  $T_3$  converges at large  $r$ . Now we move on to term  $T_4$  and integrate it over  $\varphi$  and  $\mu$ ,

$$T_4 = 2\pi \int_0^\infty dr r^2 l_4(r) = 2\pi \int_0^\infty dr g_{qp}^2(t) k_1^2 r^2 \zeta_{pp}^2(0) \cdot \int_{-1}^1 d\mu \left( (3\mu^2 - 1)b_1 + b_0 \right)^2 e^{y(t,\mu) - ik_1 r \mu}. \quad (6.43)$$

At the limit of  $r \rightarrow \infty$ , its integrand

$$\lim_{r \rightarrow \infty} r^2 l_4(r) > 2g_{qp}^2(t) (-b_1 + b_0)^2 \zeta_{pp}^2(0) e^{y(t,1)} (k_1 r |\sin k_1 r|) \rightarrow \infty, \quad (6.44)$$

doesn't converge, on the other hand, at very small scales where  $k_1 \rightarrow \infty$ , the integral

$$\int_0^\infty dr r^2 l_4(r) < 2g_{qp}^2(t) (2b_1 + b_0)^2 \zeta_{pp}^2(0) e^{-g_{qp}^2(t) k_1^2 (b_0 - b_1) \zeta_{pp}(0)} \int_0^\infty dr k_1 r \sin k_1 r \rightarrow 0 \quad (6.45)$$

converges to zero exponentially. Here we've plugged in the full expression of  $y(t,0)$ . Since in the following we are mostly interested in the small-scale asymptotic behaviors of the momentum-density power spectra, term  $T_4$  can be ignored for not contributing

to such matter, which in the meantime also guarantees the power spectrum to be convergent on all scales. Through similar analysis, we can further prove that elements  $T_5$  and  $T_7$  are convergent at the limit of  $r \rightarrow \infty$ , and  $T_8$  can be ignored for not contributing to the small-scale analysis.

Therefore we obtain the convergent form of the trace momentum-density power spectrum as

$$\begin{aligned} \bar{\mathcal{P}}_{\text{gtr}}(k_1, t) = & g_{\text{pp}}^2(t) e^{i\langle S_1 \rangle} (T_1 + T_2 + T_3) + 2ig_{\text{pp}}(t)g_{\text{qp}}(t)(\vec{k}_1 \cdot \vec{F}_1) \cdot \\ & e^{i\langle S_1 \rangle} (T_5 + T_7) + \left( g_{\text{qp}}^2(t) \frac{u_0^2}{\tau_s^2} - \vec{F}_1 \cdot \vec{F}_1 \right) \mathcal{P}_g(k_1, t), \end{aligned} \quad (6.46)$$

Now we calculate the divergence term in [Equation 6.3](#)

$$\begin{aligned} \vec{k}_1 \cdot Z^m[\mathbf{L}]\vec{k}_1 = & e^{i\langle S_1 \rangle} k_{1\eta} \bar{Z}_{12}^{\eta\rho} k_{1\rho} = cN^{-N} V^{N-2} (2\pi)^3 \delta(\vec{k}_1 + \vec{k}_2) k_1^2 e^{i\langle S_1 \rangle} \\ & \bar{D}_1 \int_r \bar{D}_2 \left[ -g_{\text{pp}}^2(t) (m_3(r) + m_4(r)) + g_{\text{pp}}^2 g_{\text{qp}}^2 k_1^2 (m(0) - m(r))^2 + \right. \\ & \left. 2ig_{\text{pp}}(t)g_{\text{qp}}(t) (m(0) - m(r)) \vec{k}_1 \cdot \vec{F}_1 + g_{\text{qp}}^2(t) \frac{(\hat{k}_1 \cdot \vec{u}_0)^2}{\tau_s^2} - (\hat{k}_1 \cdot \vec{F}_1)^2 \right], \end{aligned} \quad (6.47)$$

with  $\hat{k}_1 = \frac{\vec{k}_1}{k_1}$  being the unit vector of  $\vec{k}_1$ . We can thus read off the convergent form of the divergence momentum-density power spectrum as

$$\begin{aligned} \bar{\mathcal{P}}_{\text{gdiv}}(k_1, t) = & g_{\text{pp}}^2(t) k_1^2 e^{i\langle S_1 \rangle} (T_5 + T_2 + T_3) + 2ig_{\text{pp}}(t)g_{\text{qp}}(t) k_1^2 (\vec{k}_1 \cdot \vec{F}_1) \cdot \\ & e^{i\langle S_1 \rangle} (T_5 + T_7) + \left( g_{\text{qp}}^2(t) \frac{\langle (\vec{k}_1 \cdot \vec{u}_0)^2 \rangle}{\tau_s^2} - (\vec{k}_1 \cdot \vec{F})^2 \right) \mathcal{P}_g(k_1, t), \end{aligned} \quad (6.48)$$

where we've exploited the conclusions of convergent properties of different momentum-density power spectra elements. And since the direction of wave number  $\vec{k}_1$  is arbitrary, we further modify the expression by introducing the spatial average of the term  $(\vec{k}_1 \cdot \vec{u}_0)^2$  as

$$\langle (\vec{k}_1 \cdot \vec{u}_0)^2 \rangle = \frac{\int d\varphi d\mu (\vec{k}_1 \cdot \vec{u}_0)^2}{4\pi} = \frac{1}{3} k_1^2 u_0^2. \quad (6.49)$$

In the end, we compute the curl quantity in [Equation 6.4](#) as

$$\begin{aligned}
k_1^2 \text{tr}(Z^m[\mathbf{L}]) - \vec{k}_1 \cdot Z^m[\mathbf{L}] \vec{k}_1 &= e^{i\langle S_1 \rangle} \left( k_1^2 \bar{Z}_{12\eta}^\eta - k_{1\eta} \bar{Z}_{12}^{\eta\rho} k_{1\rho} \right) \\
&= \mathcal{C} N^{-N} V^{N-2} (2\pi)^3 \delta(\vec{k}_1 + \vec{k}_2) k_1^2 e^{i\langle S_1 \rangle} \bar{D}_1 \int_r \bar{D}_2 \cdot \\
&\left[ -2g_{pp}^2(t) m_3(r) + g_{qp}^2(t) \frac{u_0^2 - (\hat{k}_1 \cdot \vec{u}_0)^2}{\tau_s^2} - \left( \vec{F}_1 \cdot \vec{F}_1 - (\hat{k}_1 \cdot \vec{F}_1)^2 \right) \right], \tag{6.50}
\end{aligned}$$

then the convergent curl momentum-density power spectrum can be written as

$$\bar{\mathcal{P}}_{\text{gcurl}}(k_1, t) = g_{pp}^2(t) k_1^2 e^{i\langle S_1 \rangle} T_6 + \left( \frac{2g_{qp}^2(t) u_0^2}{3\tau_s^2} - \left( \vec{F}_1 \cdot \vec{F}_1 - (\hat{k}_1 \cdot \vec{F}_1)^2 \right) \right) k_1^2 \mathcal{P}_g(k_1, t), \tag{6.51}$$

with one more new element  $T_6$  being

$$T_6 = -2 \int_r m_3(r) e^{-g_{qp}^2(t) k_1^2 (m(r) - m(0)) - i\vec{k}_1 \cdot \vec{r}}. \tag{6.52}$$

Here we've used the result in [Equation 6.49](#). Thus we finally obtain the three convergent **KFT** scalar momentum-density power spectra in [Equation 6.46](#), [Equation 6.48](#) and [Equation 6.51](#). Due to the complicated forms of the three equations, following the path in [Chapter 5](#), in the following sections, we will analyze the convergent **KFT** scalar momentum-density power spectra step by step. In [Section 6.3](#), we calculate the linear and nonlinear free momentum-density power spectra for freely streaming dust particles and analyze their small-scale asymptotic behaviors by exploiting the new asymptotic method in [Section 6.2](#). In [Section 6.4](#), we further compute the three convergent momentum-density power spectra for both large and small-size particles considering the friction interaction with the constant background gas in the system. In [Section 6.5](#), with both friction and self-gravitational interactions present in the system, we finally perform the analysis of the full **KFT** momentum-density power spectra.

## 6.2 INTERLUDE: ASYMPTOTICS OF CERTAIN TYPES OF INTEGRALS

In [Section 5.2.2](#), we've introduced a new analytical method to calculate the asymptotics at the limit  $k \rightarrow \infty$  for integrals of the form [Equation 5.49](#) which satisfies the criteria [1-3](#). Though the three criteria all provide constraints on the function  $f(x)$ , there is a hidden condition for the function  $g(x)$  that demands it to be a function of the absolute value of  $\vec{x}$  rather than the direction of  $\vec{x}$ . In this Chapter, to calculate and analyze the asymptotics for the three convergent scalar momentum-density power spectra in

Equation 6.46, Equation 6.48 and Equation 6.51, inevitably we need to deal with the momentum-density power spectra elements  $T_1$ ,  $T_2$ ,  $T_3$ ,  $T_5$ ,  $T_6$ ,  $T_7$ . We first write them as

$$T_1 = \int_{\mathbf{r}} 3b_0 \zeta_{pp}(\mathbf{r}) e^{-g_{qp}^2(t) k_1^2 (m(\mathbf{r}) - m(0)) - i\vec{k}_1 \cdot \vec{r}}, \quad (6.53)$$

$$T_2 = \int_{\mathbf{r}} \left[ g_{qp}^2(t) k_1^2 (m^2(\mathbf{r}) - 2m(\mathbf{r})m(0)) \right] e^{-g_{qp}^2(t) k_1^2 (m(\mathbf{r}) - m(0)) - i\vec{k}_1 \cdot \vec{r}}, \quad (6.54)$$

$$T_3 + T_4 = \int_{\mathbf{r}} g_{qp}^2(t) k_1^2 m^2(0) e^{-g_{qp}^2(t) k_1^2 (m(\mathbf{r}) - m(0)) - i\vec{k}_1 \cdot \vec{r}}, \quad (6.55)$$

$$T_5 = - \int_{\mathbf{r}} m(\mathbf{r}) e^{-g_{qp}^2(t) k_1^2 (m(\mathbf{r}) - m(0)) - i\vec{k}_1 \cdot \vec{r}}, \quad (6.56)$$

$$T_6 = -2 \int_{\mathbf{r}} m_3(\mathbf{r}) e^{-g_{qp}^2(t) k_1^2 (m(\mathbf{r}) - m(0)) - i\vec{k}_1 \cdot \vec{r}}, \quad (6.57)$$

$$T_7 + T_8 = \int_{\mathbf{r}} m(0) e^{-g_{qp}^2(t) k_1^2 (m(\mathbf{r}) - m(0)) - i\vec{k}_1 \cdot \vec{r}}, \quad (6.58)$$

since in Equation 6.45, we've proved elements  $T_4$  and similarly  $T_8$  both have negligible small-scale asymptotics, for the convenience of further analysis, here we choose to examine the integrals  $T_3 + T_4$  and  $T_7 + T_8$  as they have identical small scale asymptotic expansions as  $T_3$  and  $T_7$ . Notice the six integrals above all have the same form as Equation 5.49 with one identical  $f(x)$  being

$$f_m(\mathbf{r}) = g_{qp}^2(m(\mathbf{r}) - m(0)) = g_{qp}^2((b_1 - b_0) - 3b_1\mu^2) (\zeta_{pp}(\mathbf{r}) - \zeta_{pp}(0)), \quad (6.59)$$

which has exactly the same expression as  $f(\mathbf{r})$  in Equation 5.52 just with the general propagator  $g_{qp}(t)$  instead of the free one  $g_0(t)$ . However, in each integral, the corresponding function  $g(x)$  no longer only depends on the absolute value of  $\vec{x}$ , but also the direction of  $\vec{x}$  due to the  $\mu$ -dependence of the function  $m(\mathbf{r})$  and  $m_3(\mathbf{r})$ , except element  $T_1$ . Therefore, for the elements  $T_2$  to  $(T_7 + T_8)$ , we need to find a new analytical method to analyze their small-scale asymptotic behaviors.

In this section, we wish to study the asymptotic behavior of a specific Laplace-Fourier type integral

$$P(k) = 2\pi \int_{-1}^1 d\mu ((b_1 - b_0) - 3b_1\mu^2)^2 \int_0^\infty dr r^2 e^{-g_{qp}^2(t) k^2 (m(\mathbf{r}) - m(0)) - i\vec{k} \cdot \vec{r}} \quad (6.60)$$

for  $k \rightarrow \infty$ . According to Konrad [25], we begin with an asymptotic expansion of the  $r$  integral, for which we modify Erdelyi's theorem for Laplace integrals, which states:

**Theorem 1** (Erdelyi). *Let  $I(\lambda)$  be an integral of the form*

$$I(\lambda) = \int_a^b e^{-\lambda f_\lambda(x)} g_\lambda(x) dx \quad (6.61)$$

where  $f_\lambda(x)$  is a real function of the real variable  $x$ , while  $g_\lambda(x)$  may be real or complex. Then if

1.  $f_\lambda(x) > f_\lambda(a)$  for  $x \in (a, b)$  and

$$\inf_{[a+\delta, b)} f_\lambda(x) - f_\lambda(a) > 0 \quad (6.62)$$

for  $\delta > 0$ ;

2.  $f'_\lambda(x)$  and  $g_\lambda(x)$  are continuous in a neighbourhood of  $a$ , except possibly at  $a$ ;
3.  $f_\lambda$  and  $g_\lambda$  admit asymptotic expansions

$$\begin{aligned} f_\lambda(x) &\sim f_\lambda(a) + \sum_{k=0}^{\infty} a_k(x-a)^{k+\alpha} \\ g_\lambda(x) &\sim \sum_{k=0}^{\infty} b_k(x-a)^{k+\beta-1} \end{aligned} \quad (6.63)$$

$f_\lambda$  can be term-wise differentiated,

$$f'_\lambda(x) \sim \sum_{k=0}^{\infty} a_k(k+\alpha)(x-a)^{k+\alpha-1} \quad (6.64)$$

for  $x \rightarrow a^+$  where  $\alpha > 0$  and  $\text{Re}\beta > 0$ ; and

4.  $I(\lambda)$  converges absolutely for sufficiently large  $\lambda$ ; then

the integral  $I(\lambda)$  has the asymptotic expansion

$$I(\lambda) \sim e^{-\lambda f_\lambda(a)} \sum_{n=0}^{\infty} \frac{\Gamma(\nu)c_n}{\lambda^\nu} \quad (6.65)$$

for  $\lambda \rightarrow \infty$  where  $\nu := \frac{n+\beta}{\alpha}$ . The coefficients  $c_n$  can be expressed by  $a_n$  and  $b_n$  as

$$c_n = \frac{1}{\alpha a_0^\nu} \sum_{m=0}^n \frac{b_{n-m}}{m!} d_{m,n} \quad \text{with} \quad d_{m,n} = \lim_{x \rightarrow 0} \frac{d^m}{dx^m} \left( 1 + \sum_{j=1}^{\infty} \frac{a_j}{a_0} x^j \right)^{-\nu} \quad (6.66)$$

For applying Erdelyi's theorem to [Equation 6.60](#), we set  $\lambda := g_{qp}^2(t)k^2$  and identify  $f_\lambda(x)$ ,  $g_\lambda(x)$  as

$$f_\lambda(r) = \frac{f_m(r)}{g_{qp}^2(t)} = \frac{f(r)}{g_0^2(t)} = a_{1\lambda}(r) + \mu^2 a_{2\lambda}(r), \quad g_\lambda(r) = r^2 e^{-ikr\mu}, \quad (6.67)$$

with  $a_{1\lambda}(r) = (b_1 - b_0) (\zeta_{pp}(r) - \zeta_{pp}(0))$  and  $a_{2\lambda}(r) = -3b_1 (\zeta_{pp}(r) - \zeta_{pp}(0))$ . For  $r \rightarrow 0^+$ , according to Equation 5.52, we have

$$f_\lambda(r) \sim \sum_{m=0}^{\infty} a_{2m}(\mu) r^{2m+2}. \quad (6.68)$$

with

$$a_{2m}(\mu) = (b_1 - b_0 - 3\mu^2 b_1) \frac{\bar{\sigma}^{7/3} \Gamma(\frac{3}{2})}{2^{5/6} \pi^2} \frac{\Gamma(\frac{13}{6} + m)}{\Gamma(\frac{5}{2} + m)} \frac{\left(-\frac{\bar{\sigma}^2}{2}\right)^{m+1}}{(m+1)!}, \quad (6.69)$$

and the asymptotic expansion of the function  $g_\lambda(r)$  is

$$g_\lambda(r) \sim \sum_{m=0}^{\infty} b_m(\mu, k) r^{m+3-1} \quad \text{with} \quad b_m(\mu, k) = \frac{(-ik\mu)^m}{m!}. \quad (6.70)$$

We identify  $\alpha = 2$  and  $\beta = 3$  and find

$$I_\mu(\lambda) := \int_0^\infty e^{-\lambda f_\lambda(r)} g_\lambda(r) dr \sim \sum_{n=0}^{\infty} \frac{\Gamma(\frac{n+3}{2}) c_n(\mu, k)}{\lambda^{(n+3)/2}} \quad (6.71)$$

The coefficient  $c_n$  are

$$c_n = \frac{a_0^{-(n+3)/2}}{2} \sum_{m=0}^n \frac{(-ik\mu)^{n-m}}{m!(n-m)!} d_{m,n}(\mu) \quad (6.72)$$

with

$$d_{m,n}(\mu) = \lim_{x \rightarrow 0} \left( 1 + \sum_{j=1}^{\infty} \frac{a_{2j}}{a_0} x^{2j} \right)^{-\frac{n+3}{2}} = a_0^{\frac{n+3}{2}} \lim_{x \rightarrow 0} \left( \frac{a_{1\lambda} + \mu^2 a_{2\lambda}}{x^2} \right)^{-\frac{n+3}{2}} \quad (6.73)$$

Since  $f_\lambda(r)$  is even in  $r$ , all odd derivatives vanish, implying  $d_{2m+1,n}(\mu) = 0$ . Thus in the coefficients  $c_n(\mu, k)$ , only even values of  $m$  contribute to the sum. We further add that, due to the integration over the parameter  $\mu$ , it is sufficient to consider only the real part, which is even in  $\mu$ , thus only terms for even numbers of  $n$ . This brings us to

$$\operatorname{Re}I_\mu(\lambda) \sim \frac{1}{2} \sum_{n=0}^{\infty} \frac{\Gamma(n + \frac{3}{2})}{\lambda^{n + \frac{3}{2}}} \sum_{m=0}^n \frac{(-k^2\mu^2)^{n-m}}{(2m)!(2n-2m)!} \lim_{x \rightarrow 0} \frac{d^{2m}}{dx^{2m}} \left( \frac{a_{1\lambda} + \mu^2 a_{2\lambda}}{x^2} \right)^{-\frac{2n+3}{2}} \quad (6.74)$$

Since we are interested in the expression in the order of  $k$ , after reordering  $n$  and  $m$ , we have

$$\operatorname{Re}I_\mu(g_{qp}^2 k^2) \sim \frac{1}{2k^3} \sum_{m=0}^{\infty} \frac{(-k^2\mu^2)^{-m}}{(2m)!} \tilde{c}_n(\mu^2) \quad (6.75)$$

with

$$\tilde{c}_n(\mu^2) = \lim_{x \rightarrow 0} \frac{d^{2m}}{dx^{2m}} \left[ \frac{x^2/g_{qp}^2}{a_{1\lambda} + \mu^2 a_{2\lambda}} \right]^{\frac{3}{2}} \sum_{n=0}^{\infty} \frac{\Gamma(n + m + \frac{3}{2})}{(2n)!} \left[ \frac{-\mu^2 x^2/g_{qp}^2}{a_{1\lambda} + \mu^2 a_{2\lambda}} \right]^{n+m} \quad (6.76)$$

We now proceed to the  $\mu$ -integral

$$\int_{-1}^1 d\mu \left[ (b_1 - b_0)^2 + 6b_1(b_0 - b_1)\mu^2 + 9b_1^2\mu^4 \right] (-\mu^2)^{-m} \tilde{c}_n(\mu^2), \quad (6.77)$$

Due to the complicated form of the integral, also since our primary interest lies in the expression of the highest order in terms of  $k$ , here we present the final results for the case  $m = 0$ .

Split the above integral into three ones:

$$\begin{aligned} (1) &= (b_1 - b_0)^2 \lim_{x \rightarrow 0} \sum_{n=0}^{\infty} \frac{\Gamma(n + \frac{3}{2})}{(2n)!} \left( \frac{x^2}{g_{qp}^2} \right)^{n + \frac{3}{2}} \left[ \int_{-1}^1 d\mu \frac{(-\mu^2)^n}{(a_{1\lambda} + \mu^2 a_{2\lambda})^{n + \frac{3}{2}}} \right] \\ (2) &= 6b_1(b_1 - b_0) \lim_{x \rightarrow 0} \sum_{n=0}^{\infty} \frac{\Gamma(n + \frac{3}{2})}{(2n)!} \left( \frac{x^2}{g_{qp}^2} \right)^{n + \frac{3}{2}} \left[ \int_{-1}^1 d\mu \frac{(-\mu^2)^{n+1}}{(a_{1\lambda} + \mu^2 a_{2\lambda})^{n + \frac{3}{2}}} \right] \\ (3) &= 9b_1^2 \lim_{x \rightarrow 0} \sum_{n=0}^{\infty} \frac{\Gamma(n + \frac{3}{2})}{(2n)!} \left( \frac{x^2}{g_{qp}^2} \right)^{n + \frac{3}{2}} \left[ \int_{-1}^1 d\mu \frac{(-\mu^2)^{n+2}}{(a_{1\lambda} + \mu^2 a_{2\lambda})^{n + \frac{3}{2}}} \right] \end{aligned} \quad (6.78)$$

Integral (1) has the result as

$$(1) = (b_1 - b_0)^2 \lim_{x \rightarrow 0} \sum_{n=0}^{\infty} \frac{\Gamma(n + \frac{3}{2})}{(2n)!} \left( \frac{x^2}{g_{qp}^2} \right)^{n + \frac{3}{2}} \frac{2 \cdot (-1)^n}{a_{1\lambda}^{n + \frac{3}{2}} (2n + 1)} {}_2F_1 \left( n + \frac{1}{2}, n + \frac{3}{2}, n + \frac{3}{2}, -\frac{a_{2\lambda}}{a_{1\lambda}} \right), \quad (6.79)$$

where  ${}_2F_1(a, b, c, z)$  is the Hypergeometric function. Using Milton Abramowitz [30], we find

$${}_2F_1(a, b, c, z) = {}_2F_1(b, a, c, z); \quad {}_2F_1(a, b, b, z) = (1 - z)^{-a}; \quad (6.80)$$

Thus we can perform the sum in integral (1) as

$$\begin{aligned} (1) &= (b_1 - b_0)^2 \lim_{x \rightarrow 0} \sum_{n=0}^{\infty} \frac{\Gamma(n + \frac{3}{2})}{(2n + 1)!} \left( \frac{x^2}{g_{qp}^2} \right)^{n + \frac{3}{2}} \frac{2 \cdot (-1)^n}{a_{1\lambda}^{n + \frac{3}{2}}} \left( 1 + \frac{a_{2\lambda}}{a_{1\lambda}} \right)^{-n - \frac{1}{2}} \\ &= (b_1 - b_0)^2 \sqrt{\pi} \lim_{x \rightarrow 0} \frac{x^2/g_{qp}^2}{a_{1\lambda}} \left( \frac{x^2/g_{qp}^2}{a_{1\lambda} + a_{2\lambda}} \right)^{\frac{1}{2}} e^{-\frac{x^2/g_{qp}^2}{4(a_{1\lambda} + a_{2\lambda})}} \end{aligned} \quad (6.81)$$

Combining Equation 6.67 and Equation 6.69, we can write  $a_{1\lambda}$  and  $a_{2\lambda}$  to their primary order in the limit of  $x \rightarrow 0$ ,

$$a_{1\lambda} = \frac{b_0 - b_1}{2} \sigma_1^2 x^2; \quad a_{2\lambda} = \frac{3b_1}{2} \sigma_1^2 x^2; \quad (6.82)$$

with  $\sigma_1^2$  given in Equation 5.55, then the final expression for integral (1) becomes

$$(1) = \frac{2(b_0 - b_1)}{g_{qp}^3 \sigma_1^3} \sqrt{\frac{2\pi}{b_0 + 2b_1}} \exp\left(-\frac{1}{2g_{qp}^2 \sigma_1^2 (b_0 + 2b_1)}\right). \quad (6.83)$$

Combining with coefficients in Equation 6.75 and Equation 6.60, the amplitude of the  $k^{-3}$  tail at small scales for  $P(k)$  contributed from integral (1) becomes

$$P^{a1}(t) = \pi \cdot (1) = (b_0 - b_1)^2 \mathcal{P}_f^{(0)}(t), \quad (6.84)$$

with  $\mathcal{P}_f^{(0)}(t)$  being the amplitude for the small-scale  $k_1^{-3}$  slope of the nonlinear density power spectrum given in Equation 5.67. This result makes perfect sense. If we only consider the part of  $P(k)$  including integral (1), then the function would take the form of

$$\begin{aligned} P_1(k) &= 2\pi \int_{-1}^1 d\mu (b_0 - b_1)^2 \int_0^\infty dr r^2 e^{-g_{qp}^2(t)k^2(m(r) - m(0)) - i\vec{k} \cdot \vec{r}} \\ &= (b_0 - b_1)^2 \int_r e^{-g_{qp}^2(t)k^2(m(r) - m(0)) - i\vec{k} \cdot \vec{r}}, \end{aligned} \quad (6.85)$$

which is exactly the same as the first part of  $\mathcal{P}_f(k_1, t)$  in Equation 5.20 but with coefficient  $(b_0 - b_1)^2$ , since the second part of  $\mathcal{P}_f(k_1, t)$  doesn't contribute to the small-scale asymptotics, the amplitude for the  $k^{-3}$  slope at small scales for  $P_1(k)$  is exactly Equation 6.84.

Now we move on to integral (2), after integration we have

$$(2) = 6b_1(b_1 - b_0)\sqrt{\pi} \sum_{n=0}^{\infty} \frac{(-1)^{n+1} 2^3 (2n+1)}{n! (2n+3)} \left( \frac{1}{2g_{qp}^2 \sigma_1^2 (b_0 - b_1)} \right)^{n+\frac{3}{2}} {}_2F_1 \left( n + \frac{3}{2}, n + \frac{3}{2}, n + \frac{5}{2}, \frac{3b_1}{b_1 - b_0} \right). \quad (6.86)$$

Here we've already plugged Equation 6.82. Then the calculation over integral (3) gives

$$(3) = 9b_1^2 \sqrt{\pi} \sum_{n=0}^{\infty} \frac{(-1)^n 2^3 (2n+1)}{n! (2n+5)} \left( \frac{1}{2g_{qp}^2 \sigma_1^2 (b_0 - b_1)} \right)^{n+\frac{3}{2}} {}_2F_1 \left( n + \frac{5}{2}, n + \frac{3}{2}, n + \frac{7}{2}, \frac{3b_1}{b_1 - b_0} \right). \quad (6.87)$$

Due to the complicated form of (2) and (3), Figure 6.1 illustrates the shape of integral results (2) and (3) in Equation 6.86 and Equation 6.87 as functions of propagator  $g_{qp}(t)$ . We can see their curves both have multiple extreme points with values being either negative or positive. And at very large  $g_{qp}(t)$ , the values of both functions approach to zero.

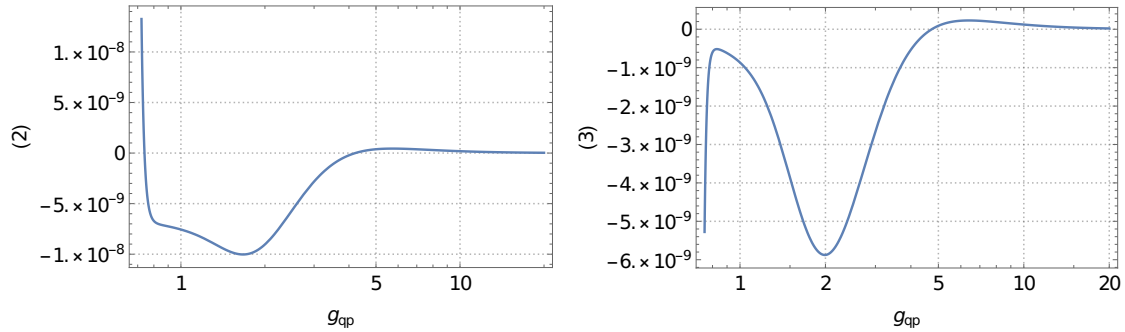


Figure 6.1: *Left panel:* This plot shows the shape of integral (2) in Equation 6.86 as a function of  $g_{qp}(t)$ . *Right panel:* This plot shows the shape of integral (3) in Equation 6.87 as a function of  $g_{qp}(t)$ .

In the end, we obtain the amplitude for the  $k^{-3}$  tail at small scales for  $P(k)$  in Equation 6.60 as

$$P(k) \sim \frac{P^a(t)}{k^3} = \frac{2\pi}{2k^3} \cdot ((1) + (2) + (3)) = \frac{\pi \cdot ((1) + (2) + (3))}{k^3} \quad (6.88)$$

Now we return to the momentum-density power spectra elements in [Equation 6.53-6.58](#), rewritten them as

$$T_1 = 2\pi\alpha_1 \int_{-1}^1 d\mu h_1(\mu) \int_0^\infty dr g_1(r) e^{-g_{qp}^2(t) k_1^2 (m(r) - m(0))}, \quad (6.89)$$

$$T_2 = 2\pi\alpha_2 \int_{-1}^1 d\mu h_2(\mu) \int_0^\infty dr g_2(r) e^{-g_{qp}^2(t) k_1^2 (m(r) - m(0))}, \quad (6.90)$$

$$T_3 + T_4 = 2\pi\alpha_3 \int_{-1}^1 d\mu h_3(\mu) \int_0^\infty dr g_3(r) e^{-g_{qp}^2(t) k_1^2 (m(r) - m(0))}, \quad (6.91)$$

$$T_5 = 2\pi\alpha_5 \int_{-1}^1 d\mu h_5(\mu) \int_0^\infty dr g_5(r) e^{-g_{qp}^2(t) k_1^2 (m(r) - m(0))}, \quad (6.92)$$

$$T_6 = 2\pi\alpha_6 \int_{-1}^1 d\mu h_6(\mu) \int_0^\infty dr g_6(r) e^{-g_{qp}^2(t) k_1^2 (m(r) - m(0))}, \quad (6.93)$$

$$T_7 + T_8 = 2\pi\alpha_7 \int_{-1}^1 d\mu h_7(\mu) \int_0^\infty dr g_7(r) e^{-g_{qp}^2(t) k_1^2 (m(r) - m(0))}, \quad (6.94)$$

with the coefficients and the  $\mu$ -functions being

$$\begin{aligned} \alpha_1 &= 3b_0 \zeta_{pp}(0), & h_1(\mu) &= 1, \\ \alpha_2 &= -g_{qp}^2(t) k_1^2 \zeta_{pp}^2(0), & h_2(\mu) &= (b_1 - b_0 - 3b_1 \mu^2)^2, \\ \alpha_3 &= g_{qp}^2(t) k_1^2 \zeta_{pp}^2(0), & h_3(\mu) &= (b_1 - b_0 - 3b_1 \mu^2)^2, \\ \alpha_5 &= -\zeta_{pp}(0), & h_5(\mu) &= (b_1 - b_0 - 3b_1 \mu^2), \\ \alpha_6 &= \zeta_{pp}(0), & h_6(\mu) &= (2b_0 + b_1 - 3b_1 \mu^2), \\ \alpha_7 &= \zeta_{pp}(0), & h_7(\mu) &= (b_1 - b_0 - 3b_1 \mu^2), \end{aligned} \quad (6.95)$$

and the  $g_\lambda(x)$  functions being

$$\begin{aligned} g_1(r) &= \frac{\zeta_{pp}(r)}{\zeta_{pp}(0)} r^2 e^{-ikr\mu}, & g_5(r) &= \frac{\zeta_{pp}(r)}{\zeta_{pp}(0)} r^2 e^{-ikr\mu}, \\ g_2(r) &= \left( \frac{2\zeta_{pp}(r)}{\zeta_{pp}(0)} - \frac{\zeta_{pp}^2(r)}{\zeta_{pp}^2(0)} \right) r^2 e^{-ikr\mu}, & g_6(r) &= \frac{\zeta_{pp}(r)}{\zeta_{pp}(0)} r^2 e^{-ikr\mu}, \\ g_3(r) &= r^2 e^{-ikr\mu}, & g_7(r) &= r^2 e^{-ikr\mu}. \end{aligned} \quad (6.96)$$

Thus the asymptotic expansions for the  $g_\lambda(x)$  functions above at  $r \rightarrow 0^+$  become

$$g_1(r) \sim \sum_{m=0}^{\infty} b_{1m}(\mu, k) r^{m+3-1}, \quad \text{with} \quad b_{1m} = \frac{\zeta_{pp}(0)}{\zeta_{pp}(0)} b_m = b_m, \quad (6.97)$$

$$g_2(r) \sim \sum_{m=0}^{\infty} b_{2m}(\mu, k) r^{m+3-1}, \quad \text{with} \quad b_{2m} = \left( \frac{2\zeta_{pp}(0)}{\zeta_{pp}(0)} - \frac{\zeta_{pp}^2(0)}{\zeta_{pp}^2(0)} \right) b_m = b_m, \quad (6.98)$$

$$g_3(r) \sim \sum_{m=0}^{\infty} b_{3m}(\mu, k) r^{m+3-1}, \quad \text{with} \quad b_{3m} = b_m, \quad (6.99)$$

$$g_5(r) \sim \sum_{m=0}^{\infty} b_{5m}(\mu, k) r^{m+3-1}, \quad \text{with} \quad b_{5m} = \frac{\zeta_{pp}(0)}{\zeta_{pp}(0)} b_m = b_m, \quad (6.100)$$

$$g_6(r) \sim \sum_{m=0}^{\infty} b_{6m}(\mu, k) r^{m+3-1}, \quad \text{with} \quad b_{6m} = \frac{\zeta_{pp}(0)}{\zeta_{pp}(0)} b_m = b_m, \quad (6.101)$$

$$g_7(r) \sim \sum_{m=0}^{\infty} b_{7m}(\mu, k) r^{m+3-1}, \quad \text{with} \quad b_{7m} = b_m, \quad (6.102)$$

which are all identical with  $g_\lambda(r)$  in Equation 6.70. With the  $f_\lambda(x)$  functions for Equation 6.89-6.94 are the same with  $f_\lambda(r)$  in Equation 6.67, we conclude all  $r$ -integrals in Equation 6.89-6.94 give the same asymptotic result as in Equation 6.75. Furthermore, comparing the six  $\mu$ -functions in Equation 6.95 with the  $\mu$ -dependence in integral Equation 6.77-6.78, then combining with the six coefficients  $\alpha_i$  with  $i = 1, 2, 3, 5, 6, 7$ , we can write down the small-scale asymptotic expansions for all the momentum-density power spectra elements as

$$T_1 \sim \frac{\mathcal{T}_1^0(t)}{k_1^3} = \frac{3b_0\zeta_{pp}(0)}{(b_0 - b_1)^2} \cdot \frac{P^{\alpha 1}(t)}{k_1^3} = \frac{3b_0\zeta_{pp}(0)\mathcal{P}_f^{(0)}(t)}{k_1^3}, \quad (6.103)$$

$$T_2 \sim \frac{\mathcal{T}_2^0(t)}{k} = -g_{qp}^2(t)k_1^2\zeta_{pp}^2(0)\frac{P^\alpha(t)}{k_1^3} = -\frac{\pi g_{qp}^2(t)\zeta_{pp}^2(0)}{k} \cdot ((1) + (2) + (3)), \quad (6.104)$$

$$T_3 \sim \frac{\mathcal{T}_3^0(t)}{k} = g_{qp}^2(t)k_1^2\zeta_{pp}^2(0)\frac{P^\alpha(t)}{k_1^3} = \frac{\pi g_{qp}^2(t)\zeta_{pp}^2(0)}{k} \cdot ((1) + (2) + (3)), \quad (6.105)$$

$$T_5 \sim \frac{\mathcal{T}_5^0(t)}{k} = -\frac{\pi\zeta_{pp}(0)}{k_1^3} \cdot \left( \frac{(1)}{b_1 - b_0} - \frac{(2)}{2(b_0 - b_1)} \right) = \frac{\pi\zeta_{pp}(0)}{(b_0 - b_1)k_1^3} \cdot \left( (1) + \frac{(2)}{2} \right), \quad (6.106)$$

$$T_6 \sim \frac{\mathcal{T}_6^0(t)}{k} = \frac{\pi\zeta_{pp}(0)}{k_1^3} \cdot \left( \frac{2b_0 + b_1}{(b_1 - b_0)^2} (1) - \frac{(2)}{2(b_0 - b_1)} \right) = \frac{\pi\zeta_{pp}(0)}{(b_1 - b_0)k_1^3} \cdot \left( \frac{2b_0 + b_1}{b_1 - b_0} (1) + \frac{(2)}{2} \right), \quad (6.107)$$

$$T_7 \sim \frac{\mathcal{T}_7^0(t)}{k} = \frac{\pi\zeta_{pp}(0)}{k_1^3} \cdot \left( \frac{(1)}{b_1 - b_0} - \frac{(2)}{2(b_0 - b_1)} \right) = -\frac{\pi\zeta_{pp}(0)}{(b_0 - b_1)k_1^3} \cdot \left( (1) + \frac{(2)}{2} \right), \quad (6.108)$$

With three important relations  $T_2 + T_3 = 0$ ,  $T_5 + T_7 = 0$ , and  $T_5 + T_6 = T_1$  at small scales. Therefore, by introducing Erdelyi's theorem for the one-dimensional Laplace integrals then performing the spatial angular integrals afterward, a new analytical method is developed to calculate the small-scale asymptotics for the integrals of the form [Equation 5.49](#), especially for the ones with a more complicated form of  $g(x)$ .

### 6.3 FREE STREAMING PARTICLES

In this section, we ignore the friction interaction in the system, at the limit of  $\tau_s \rightarrow \infty$ , the free momentum propagator  $g_0^m(t, t')$  can be derived from [equation 3.39](#) as

$$\lim_{\tau_s \rightarrow \infty} g_{pp}(t, t') = g_0^m(t, t') = \lim_{\tau_s \rightarrow \infty} e^{-\frac{t-t'}{\tau_s}} = 1, \quad (6.109)$$

we further ignore the self-gravity among dust particles and obtain

$$\vec{f}_j = 0 \quad \text{and} \quad \vec{F}_j = 0, \quad (6.110)$$

combing them with the free propagator  $g_0(t, t')$  given in [Equation 5.40](#) and the free interaction term  $S_{\text{Ifree}}$  given in [Equation 5.41](#), the three free convergent momentum-density power spectra can be read off directly from [Equation 6.46](#), [Equation 6.48](#) and [Equation 6.51](#) as

$$\bar{\mathcal{P}}_{\text{tr}}^{\text{free}}(\mathbf{k}_1, t) = T_{10} + T_{20} + T_{30}, \quad (6.111)$$

$$\bar{\mathcal{P}}_{\text{div}}^{\text{free}}(\mathbf{k}_1, t) = k_1^2 (T_{50} + T_{20} + T_{30}), \quad (6.112)$$

$$\bar{\mathcal{P}}_{\text{curl}}^{\text{free}}(\mathbf{k}_1, t) = k_1^2 T_{60}, \quad (6.113)$$

where  $T_{i0}$  with  $i = 1, 2, 3, 5, 6$  has the same expression as  $T_i$  in [Equation 6.32](#), [Equation 6.33](#) and [Equation 6.52](#) but with the free propagator  $g_0(t)$  instead of the general propagator  $g_{\text{qp}}(t)$ .

In the following section, we first derive the expressions of the three linear free momentum-density power spectra for dust particles by looking for the asymptotic behaviors of the momentum-density power spectra elements  $T_1$  to  $T_6$  at very early evolution time. Then we return to the nonlinear momentum-density power spectra by employing the new asymptotic method introduced in [Section 6.2](#). Furthermore, for each different momentum-density power spectrum, we analyze its small-scale asymptotic behaviors and find evidence for scale-invariant kinetic energy at very small scales in the system.

### 6.3.1 Linear Momentum-Density Power Spectra

At very early times, the free propagator satisfies  $g_0(t) = t \rightarrow 0$ , the exponentials in the momentum-density power spectra elements can thus be Taylor approximated to their first orders,

$$T_{10} \approx T_{\text{lin1}}(\mathbf{k}_1, t) = 3b_0 \int_{\mathbf{r}} \zeta_{\text{pp}}(\mathbf{r}) e^{-i\mathbf{k}_1 \cdot \mathbf{r}}, \quad (6.114)$$

$$T_{20} \approx T_{\text{lin2}}(\mathbf{k}_1, t) = g_0^2(t) k_1^2 \int_{\mathbf{r}} (m^2(\mathbf{r}) - 2m(\mathbf{r})m(0)) e^{-i\mathbf{k}_1 \cdot \mathbf{r}}, \quad (6.115)$$

$$T_{30} \approx T_{\text{lin3}}(\mathbf{k}_1, t) = -g_0^4(t) k_1^4 \int_{\mathbf{r}} m^2(0) m(\mathbf{r}) e^{-i\mathbf{k}_1 \cdot \mathbf{r}}, \quad (6.116)$$

$$T_{50} \approx T_{\text{lin5}}(\mathbf{k}_1, t) = - \int_{\mathbf{r}} m(\mathbf{r}) e^{-i\mathbf{k}_1 \cdot \mathbf{r}}, \quad (6.117)$$

$$T_{60} \approx T_{\text{lin6}}(\mathbf{k}_1, t) = -2 \int_{\mathbf{r}} m_3(\mathbf{r}) e^{-i\mathbf{k}_1 \cdot \mathbf{r}}, \quad (6.118)$$

evidently,  $T_{\text{lin2}}(\mathbf{k}_1, t)$  and  $T_{\text{lin3}}(\mathbf{k}_1, t)$  instantly become negligible compared to the other terms due to the higher orders of  $g_0(t)$  in their expressions. Therefore the three free momentum-density power spectra in [Equation 6.111-6.113](#) can be simplified to their linear form as

$$\bar{\mathcal{P}}_{\text{lin}1}^{\text{free}}(k_1, t) = T_{\text{lin}1}(k_1, t), \quad (6.119)$$

$$\bar{\mathcal{P}}_{\text{lin}2}^{\text{free}}(k_1, t) = k_1^2 T_{\text{lin}5}(k_1, t), \quad (6.120)$$

$$\bar{\mathcal{P}}_{\text{lin}3}^{\text{free}}(k_1, t) = k_1^2 T_{\text{lin}6}(k_1, t). \quad (6.121)$$

Now we integrate  $T_{\text{lin}1}(k_1, t)$ ,  $T_{\text{lin}5}(k_1, t)$  and  $T_{\text{lin}6}(k_1, t)$  over the Spherical coordinates  $\mu$  and  $\varphi$ , then replace  $r$  with  $r_1 = k_1 r$  to obtain

$$T_{\text{lin}1}(k_1, t) = \frac{6\pi b_0}{k_1^3} \int_0^\infty dr_1 r_1^2 \zeta_{\text{pp}} \left( \frac{r_1}{k_1} \right) \frac{2 \sin r_1}{r_1}, \quad (6.122)$$

$$T_{\text{lin}5}(k_1, t) = \frac{2\pi}{k_1^3} \int_0^\infty dr_1 r_1^2 \zeta_{\text{pp}} \left( \frac{r_1}{k_1} \right) \int_{-1}^1 d\mu ((3\mu^2 - 1)b_1 + b_0) \cos r_1 \mu, \quad (6.123)$$

$$T_{\text{lin}6}(k_1, t) = \frac{2\pi}{k_1^3} \int_0^\infty dr_1 r_1^2 \zeta_{\text{pp}} \left( \frac{r_1}{k_1} \right) \int_{-1}^1 d\mu (2b_0 + (1 - 3\mu^2)b_1) \cos r_1 \mu, \quad (6.124)$$

when  $k_1 \rightarrow 0$ , by employing the asymptotic behavior of  $\zeta_{\text{pp}}(r_1/k_1) \propto (k_1/r_1)^{7/3}$  in Equation 4.76, we obtain their large-scale asymptotic behaviors as

$$T_{\text{lin}1}(k_1, t) \sim \frac{c_1}{k_1^{3/2}}, \quad c_1 = 0.975\pi b_0, \quad (6.125)$$

$$T_{\text{lin}5}(k_1, t) \sim \frac{c_5}{k_1^{3/2}}, \quad c_5 = 0.08\pi \frac{4}{21} (7b_0 - 4b_1) \Gamma\left(-\frac{4}{3}\right), \quad (6.126)$$

$$T_{\text{lin}6}(k_1, t) \sim \frac{c_6}{k_1^{3/2}}, \quad c_6 = 0.08\pi \frac{8}{21} (7b_0 + 2b_1) \Gamma\left(-\frac{4}{3}\right). \quad (6.127)$$

While at the limit of  $k_1 \rightarrow \infty$ , we obtain their small-scale asymptotics in Section A.1.2 as

$$\lim_{k_1 \rightarrow \infty} T_{\text{lin}1}(k_1, t) \approx 0, \quad \lim_{k_1 \rightarrow \infty} T_{\text{lin}5}(k_1, t) = -18.85b_1 \frac{2\pi\zeta_0}{k_1^3}, \quad \lim_{k_1 \rightarrow \infty} T_{\text{lin}6}(k_1, t) = 18.85b_1 \frac{2\pi\zeta_0}{k_1^3}. \quad (6.128)$$

where  $\zeta_0$  is a constant given in Equation A.2. Therefore, using Equation 6.119-6.121, we can immediately conclude that, for the linear free trace momentum-density power spectrum  $\bar{\mathcal{P}}_{\text{lin}1}^{\text{free}}(k_1, t)$ , it will develop a  $k_1^{-2/3}$  slope at large scales then continuously decreases exponentially to zero at small scales, as for the linear free divergence and curl momentum-density power spectra  $\bar{\mathcal{P}}_{\text{lin}2}^{\text{free}}(k_1, t)$  and  $\bar{\mathcal{P}}_{\text{lin}3}^{\text{free}}(k_1, t)$ , they will develop

$k_1^{\frac{4}{3}}$  slopes at large scales and  $k_1^{-1}$  tails at small scales. Furthermore, the fact that the expressions in Equation 6.125-6.128 are independent of the evolution time indicates that all asymptotic behaviors of the three linear free momentum-density power spectra are conserved and remain the same at the very early time of evolution.

Figure 6.2 shows the shape of  $\bar{\mathcal{P}}_{\text{lin}1}^{\text{free}}(k_1)$ ,  $\bar{\mathcal{P}}_{\text{lin}2}^{\text{free}}(k_1)$  and  $\bar{\mathcal{P}}_{\text{lin}3}^{\text{free}}(k_1)$  as functions of wave number  $k_1$ . Notice their large and small scale behaviors confirmed our asymptotic analysis. Moreover, notice that the small scale asymptotics of  $T_{\text{lin}5}(k_1)$  and  $T_{\text{lin}6}(k_1)$  in Equation 6.128 indicate the relation of  $\bar{\mathcal{P}}_{\text{lin}2}^{\text{free}}(k_1) + \bar{\mathcal{P}}_{\text{lin}3}^{\text{free}}(k_1) = 0$  at very small scales, this result could then very well explain the small scale asymptotic behavior of  $\bar{\mathcal{P}}_{\text{lin}1}^{\text{free}}(k_1)$ . Since the trace, divergence, curl momentum-density power spectra are derived from Equation 6.2-6.4 which satisfy (6.4)+(6.3)= $k_1^2 \cdot (6.2)$ , thus at small scales, when the linear free divergence momentum-density power spectrum cancel out the linear free curl momentum-density power spectrum, the linear free trace momentum-density power spectrum is bound to become zero as in Equation 6.128.

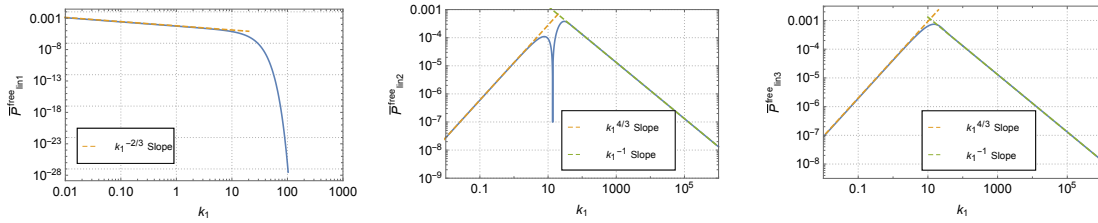


Figure 6.2: This figure shows the shape of absolute values of  $\bar{\mathcal{P}}_{\text{lin}1}^{\text{free}}(k_1)$  (left panel),  $\bar{\mathcal{P}}_{\text{lin}2}^{\text{free}}(k_1)$  (middle panel) and  $\bar{\mathcal{P}}_{\text{lin}3}^{\text{free}}(k_1)$  (right panel) in terms of wavenumber  $k_1$  (blue lines), together with their small scale asymptotic behaviors (yellow dashed lines) and the large scale  $k^{-1}$  asymptotic slopes (green dashed lines) of  $\bar{\mathcal{P}}_{\text{lin}2}^{\text{free}}(k_1)$  and  $\bar{\mathcal{P}}_{\text{lin}3}^{\text{free}}(k_1)$ .

### 6.3.2 Nonlinear Momentum-Density Power Spectra

In this section, we return to the full expressions of the three free convergent momentum-density power spectra in Equation 6.111-6.113 at any given evolution time  $t$ , by analyzing their corresponding power spectra elements  $T_{i0}$  with  $i = 1, 2, 3, 5, 6$ , we conclude their small and large scale asymptotic behaviors, furthermore, the time dependence of their small scale asymptotic behaviors are examined.

#### 6.3.2.1 Momentum-Density Trace Power Spectrum

We start with the free trace momentum-density power spectrum in Equation 6.111. At very large scales where  $k_1 \rightarrow 0$ , the exponentials in the momentum-density power spectra elements  $T_{i0}$  with  $i = 1, 2, 3$  can still be Taylor approximated to their first orders as in Equation 6.114-6.116, with the large scale asymptotics of  $T_{10}$  given in

Equation 6.125, we integrate the other two terms over the Spherical coordinates  $\mu$  and  $\varphi$ , then replace  $r$  with  $r_1 = k_1 r$  to obtain

$$T_{20} \approx T_{\text{lin}2}(k_1, t) = \frac{2\pi g_0^2(t)}{k_1} \int_0^\infty dr_1 r_1^2 \zeta_{\text{pp}} \left( \frac{r_1}{k_1} \right) \left( \zeta_{\text{pp}} \left( \frac{r_1}{k_1} \right) - 2\zeta_{\text{pp}}(0) \right) \cdot \int_{-1}^1 d\mu ((1 - 3\mu^2)b_1 - b_0)^2 \cos r_1 \mu, \quad (6.129)$$

$$T_{30} \approx T_{\text{lin}3}(k_1, t) = 2\pi g_0^4(t) k_1 \zeta_{\text{pp}}^2(0) \int_0^\infty dr_1 r_1^2 \zeta_{\text{pp}} \left( \frac{r_1}{k_1} \right) \cdot \int_{-1}^1 d\mu ((3\mu^2 - 1)b_1 + b_0)^3 \cos r_1 \mu, \quad (6.130)$$

by employing the asymptotic behavior of  $\zeta_{\text{pp}}(r_1/k_1) \propto (k_1/r_1)^{7/3}$  in Equation 4.76, we obtain their large-scale asymptotic behaviors as

$$T_{\text{lin}2}(k_1, t) \sim c_2 k_1^{\frac{4}{3}}, \quad c_2 = 0.16\pi g_0^2(t) \zeta_{\text{pp}}(0) \frac{4}{117} (76b_1^2 - 104b_1 b_0 + 91b_0^2) \Gamma \left( -\frac{7}{3} \right) \\ = -5.167 \times 10^{-9} g_0^2(t), \quad (6.131)$$

$$T_{\text{lin}3}(k_1, t) \sim c_3 k_1^{\frac{10}{3}}, \quad c_3 = 0.08\pi g_0^4(t) \zeta_{\text{pp}}^2(0) \frac{40}{1539} \Gamma \left( -\frac{13}{3} \right) \cdot \\ \left( 640b_1^3 - 4332b_1^2 b_0 + 2964b_1 b_0^2 - 1729b_0^3 \right) \\ = 6.451 \times 10^{-13} g_0^4(t). \quad (6.132)$$

At very small scales where  $k_1 \rightarrow \infty$ , the asymptotic behavior of  $T_{i0}$  with  $i = 1, 2, 3$  are given in Equation 6.103-6.105, but with the general propagator  $g_{\text{qp}}(t)$  in the expressions replaced by the free propagator  $g_0(t)$ .

Figure 6.3 shows the shape of the free momentum-density trace power spectrum  $\bar{\mathcal{P}}_{\text{tr}}^{\text{free}}(k_1, t) = T_{10} + T_{20} + T_{30}$  and its elements  $T_{10}, T_{20}, T_{30}$  as functions of wavenumber  $k_1$  at evolution time  $g_0(t) = t = 2.0$ . We can see their large and small scale asymptotic behaviors match our calculations very well. Furthermore, notice the curves of  $\bar{\mathcal{P}}_{\text{tr}}^{\text{free}}(k_1, t)$  and  $T_{10}$  are almost identical with each other, which can easily be explained by looking into the asymptotic behaviors of  $T_{10}, T_{20}$  and  $T_{30}$ . At very large scales with  $k_1 \rightarrow 0$ , the asymptotic behavior of  $T_{10}$  in Equation 6.125 is significantly larger than the ones of  $T_{20}$  and  $T_{30}$  by Equation 6.131 and Equation 6.132, moreover, at very small scales with  $k_1 \rightarrow \infty$ , the asymptotic behaviors satisfy  $T_{20} + T_{30} = 0$  according to Equation 6.104 and Equation 6.105, combining both conclusions, we immediately realize at both large and small scales, the value of  $T_{10}$  dominates and contributes the most to the free momentum-density trace power spectrum  $\bar{\mathcal{P}}_{\text{tr}}^{\text{free}}(k_1, t)$ .

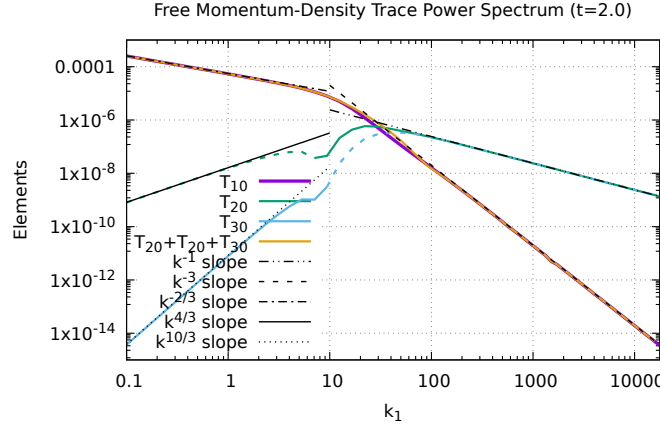


Figure 6.3: This plot shows the free momentum-density trace power spectrum  $\bar{\mathcal{P}}_{\text{tr}}^{\text{free}}(k_1, t) = T_{10} + T_{20} + T_{30}$  (yellow line) and its elements  $T_{10}$  (purple line),  $T_{20}$  (green line),  $T_{30}$  (blue line) in terms of wave number  $k_1$  at evolution time  $g_0(t) = t = 2.0$ , together with their large scales asymptotic behaviors by Equation 6.125, Equation 6.131, Equation 6.132 and small-scale asymptotic behaviors by Equation 6.103-6.105. The negative values of  $T_{20}$  and  $T_{30}$  are represented by the same color dashed lines.

Therefore, we can straightforwardly write down the large-scale asymptotic behaviors for  $\bar{\mathcal{P}}_{\text{tr}}^{\text{free}}(k_1, t)$  as

$$\bar{\mathcal{P}}_{\text{tr}}^{\text{free}}(k_1, t) \sim \frac{c_1}{k_1^{\frac{2}{3}}}, \quad \text{for } k_1 \rightarrow 0, \quad (6.133)$$

with  $c_1$  given in Equation 6.125, and its small-scale asymptotic behavior as

$$\bar{\mathcal{P}}_{\text{tr}}^{\text{free}}(k_1, t) \sim \frac{\bar{\mathcal{P}}_{\text{frtr}}^{(0)}(t)}{k_1^3} = \frac{3b_0\zeta_{\text{pp}}(0)\mathcal{P}^{(0)}(t)}{k_1^3}, \quad \text{for } k_1 \rightarrow \infty, \quad (6.134)$$

where  $\bar{\mathcal{P}}_{\text{frtr}}^{(0)}(t)$  represents the amplitude for the  $k_1^{-3}$  tail of  $\bar{\mathcal{P}}_{\text{tr}}^{\text{free}}(k_1, t)$ , and  $\mathcal{P}^{(0)}(t)$  is the amplitude for the nonlinear free density power spectrum given in Equation 5.59. At the limit of  $k_1 \rightarrow \infty$ , since the separation between two particles becomes negligible, the free momentum-density trace power spectrum actually measures the kinetic energy of dust particles in the system, with  $k_1^3 \cdot \bar{\mathcal{P}}_{\text{tr}}^{\text{free}}(k_1, t)$  being a constant, we conclude a scale-invariant kinetic energy for dust particles at small scales of the system.

Furthermore, since the large scale asymptotic behavior of  $\bar{\mathcal{P}}_{\text{tr}}^{\text{free}}(k_1, t)$  in Equation 6.133 is independent of the evolution time  $t$ , concerning the time dependence of the free momentum-density trace power spectrum at small scales, notice the amplitude  $\bar{\mathcal{P}}_{\text{frtr}}^{(0)}(t)$

is just a constant multiply  $\mathcal{P}^{(0)}(t)$ , we can then immediately write down its maximal amplitude and the corresponding evolution time as in [Equation 5.60](#) being

$$\mathcal{P}_{\max}^{\text{frtr}} = 3b_0\zeta_{\text{pp}}(0) \left(\frac{6\pi}{e}\right)^{3/2} \frac{b_0 + 2b_1}{b_0 - b_1} \approx 4.96 \cdot 10^{-2} \quad \text{at} \quad (6.135)$$

$$t_{\max} = \sigma_1^{-1} \sqrt{\frac{1}{3(b_0 + 2b_1)}} \approx 3.04. \quad (6.136)$$

Therefore, at very large scales, the power spectrum  $\bar{\mathcal{P}}_{\text{tr}}^{\text{free}}(k_1, t)$  is conserved over time, while at very small scales, the change of the amplitude for  $\bar{\mathcal{P}}_{\text{tr}}^{\text{free}}(k_1, t)$  indicates that the kinetic energy of the dust particles in the system first increases until reaches its maximum at time  $t_{\max}$  then continues to decrease as time proceeds.

### 6.3.2.2 Momentum-Density Divergence Power Spectrum

We proceed to the nonlinear free momentum-density divergence power spectrum by [Equation 6.112](#) in this section. At very large scales where  $k_1 \rightarrow 0$ , the asymptotic behaviors of  $T_{i0}$  with  $i = 5, 2, 3$  are given in [Equation 6.126](#), [Equation 6.131](#), [Equation 6.132](#), while at very small scales where  $k_1 \rightarrow \infty$ , their asymptotic behaviors are represented by [Equation 6.104-6.106](#), in which the general propagator  $g_{\text{qp}}(t)$  are replaced by the free propagator  $g_0(t)$ .

The left panel of [Figure 6.4](#) shows the shape of the free momentum-density divergence power spectrum elements  $T_{50}$ ,  $T_{20}$ ,  $T_{30}$  and  $T_{50} + T_{20} + T_{30}$  as functions of wave number  $k_1$  at evolution time  $g_0(t) = t = 2.0$ . Their large and small asymptotic behaviors match our analysis very well as expected. Notice the values of the sum  $T_{50} + T_{20} + T_{30}$  and element  $T_{50}$  are the same for most scales considered, which can also be explained by the negligible large scale asymptotic values of  $T_{20}$ ,  $T_{30}$  in [Equation 6.131-6.132](#) and the small scale asymptotic relation of  $T_{20} + T_{30} = 0$  in [Equation 6.104-6.105](#) as [Figure 6.3](#).

Therefore at very large scales the asymptotic behaviors for  $\bar{\mathcal{P}}_{\text{div}}^{\text{free}}(k_1, t)$  in [Equation 6.112](#) is given by

$$\bar{\mathcal{P}}_{\text{div}}^{\text{free}}(k_1, t) = k_1^2 T_{50} \sim c_5 k_1^{\frac{4}{3}}, \quad \text{for } k_1 \rightarrow 0, \quad (6.137)$$

with  $c_5$  given in [Equation 6.126](#), while at very small scales, its asymptotic behavior becomes

$$\bar{\mathcal{P}}_{\text{div}}^{\text{free}}(k_1, t) = k_1^2 T_{50} \sim \frac{\mathcal{P}_{\text{frdiv}}^{(0)}(t)}{k_1} = \frac{\pi\zeta_{\text{pp}}(0)}{(b_0 - b_1)k_1} \cdot \left( (1) + \frac{(2)}{2} \right), \quad \text{for } k_1 \rightarrow \infty, \quad (6.138)$$

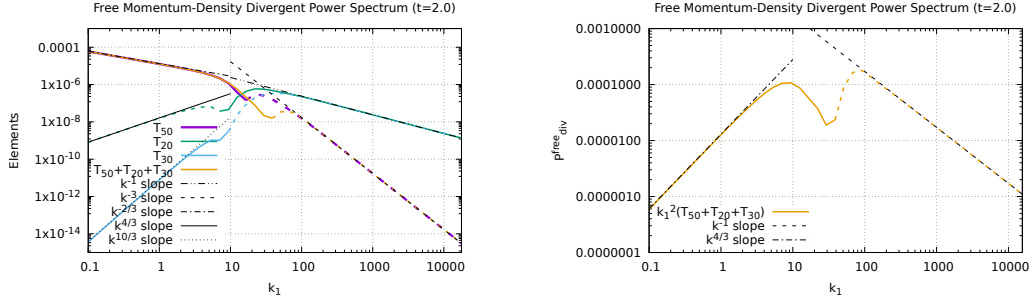


Figure 6.4: *Left panel:* This plot shows the free momentum-density divergence power spectrum elements  $T_{50}$  (purple line),  $T_{20}$  (green line),  $T_{30}$  (blue line) and  $T_{50} + T_{20} + T_{30}$  (yellow line) in terms of wave number  $k_1$  at evolution time  $g_0(t) = t = 2.0$ , together with their large scales asymptotic behaviors by Equation 6.126, Equation 6.131, Equation 6.132 and small-scale asymptotic behaviors by Equation 6.104-6.106. The negative values of  $T_{20}$ ,  $T_{30}$ ,  $T_{50}$  and  $T_{50} + T_{20} + T_{30}$  are represented by the same color dashed lines. *Right panel:* This plot shows the free momentum-density divergence power spectrum  $\bar{\mathcal{P}}_{\text{div}}^{\text{free}}(k_1, t)$  (yellow line) as a function of  $k_1$  at the same evolution time  $g_0(t) = t = 2.0$ , together with its large scale  $k_1^{4/3}$  asymptotic slope (black dash-dotted line) in Equation 6.137 and its small scale  $k_1^{-1}$  asymptotic slope (black dashed line) in Equation 6.138.

with (1) and (2) given in Equation 6.83 and Equation 6.86, in which the general propagator  $g_{\text{qp}}(t)$  is replaced by the free propagator  $g_0(t)$ , see the right panel of Figure 6.4. Since the free momentum-density divergence power spectrum measures the power spectrum for the projections of the momentum-density operator  $\hat{\Pi}$  on the wave vector  $\vec{k}_1$  multiplied by  $k_1^2$ , at the limit  $k_1 \rightarrow \infty$ , we have its small scale asymptotic behavior satisfy  $\frac{\bar{\mathcal{P}}_{\text{div}}^{\text{free}}(k_1, t)}{k_1^2} \cdot k_1^3 = \text{constant}$ , which indicates a scale-invariant momentum-density power in the  $\vec{k}_1$  space.

Since the large scale asymptotic behavior of  $\bar{\mathcal{P}}_{\text{div}}^{\text{free}}(k_1, t)$  in Equation 6.137 is independent of the evolution time  $t$ , we are only interested in the time dependence of its small scale asymptotic behaviors. Due to the complicated shape of (2) in Equation 6.86 and Figure 6.1, instead of taking the analytical derivative of  $\mathcal{P}_{\text{frdiv}}^{(0)}(t)$ , Figure 6.5 shows the shape of it as a function of evolution time  $t$ . We can see it has two extreme points which corresponds to two local maximal and minimal amplitude for the  $k_1^{-3}$  slope of  $\bar{\mathcal{P}}_{\text{div}}^{\text{free}}(k_1, t)$ . The numerical result gives the local maximal  $\mathcal{P}_{\text{frdiv}}^{\text{max}}$  and minimal  $\mathcal{P}_{\text{frdiv}}^{\text{min}}$  at their corresponding evolution times as

$$\mathcal{P}_{\text{frdiv}}^{\text{min}} \approx -0.020 \quad \text{at} \quad t_{\text{min}} \approx 1.55, \quad \text{and} \quad \mathcal{P}_{\text{frdiv}}^{\text{max}} \approx 6.18^{-3} \quad \text{at} \quad t_{\text{max}} \approx 4.12. \quad (6.139)$$

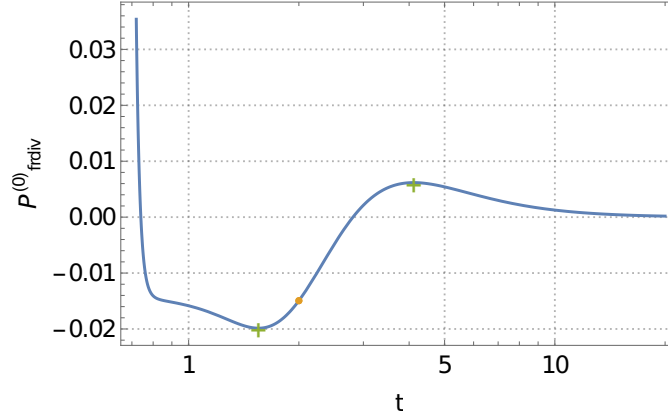


Figure 6.5: This plot shows the shape of amplitude  $\mathcal{P}_{\text{frdiv}}^{(0)}(t)$  in equation 6.138 as a function of evolution time  $t$ . The yellow dot marks its value at evolution time  $t = 2.0$  which corresponds to Figure 6.4. The green cross represents the example extreme points of the curve given in Equation 6.139.

### 6.3.2.3 Momentum-Density Curl Power Spectrum

In the end, we move on to the nonlinear free momentum-density curl power spectrum by Equation 6.113. At very large scales where  $k_1 \rightarrow 0$ , the asymptotic behavior of  $T_{60}$  is given in Equation 6.127, while at very small scales where  $k_1 \rightarrow \infty$ , its asymptotic behavior is represented by Equation 6.107, in which the general propagator  $g_{\text{qp}}(t)$  is replaced by the free propagator  $g_0(t)$ .

Therefore we can immediately write down the large-scale asymptotic behavior for  $\bar{\mathcal{P}}_{\text{curl}}^{\text{free}}(k_1, t)$  in Equation 6.113 as

$$\bar{\mathcal{P}}_{\text{curl}}^{\text{free}}(k_1, t) = k_1^2 T_{60} \sim c_6 k_1^{\frac{4}{3}}, \quad \text{for } k_1 \rightarrow 0, \quad (6.140)$$

with  $c_6$  given in Equation 6.127, while at very small scales, its asymptotic behavior becomes

$$\bar{\mathcal{P}}_{\text{curl}}^{\text{free}}(k_1, t) = k_1^2 T_{60} \sim \frac{\mathcal{P}_{\text{frcurl}}^{(0)}(t)}{k_1} = \frac{\pi \zeta_{\text{pp}}(0)}{(b_1 - b_0) k_1} \cdot \left( \frac{2b_0 + b_1}{b_1 - b_0} (1) + \frac{(2)}{2} \right), \quad \text{for } k_1 \rightarrow \infty, \quad (6.141)$$

with (1) and (2) given in Equation 6.83 and Equation 6.86, in which the general propagator  $g_{\text{qp}}(t)$  is replaced by the free propagator  $g_0(t)$ . Now that the free momentum-density curl power spectrum measures the power spectrum for the projections of the momentum-density operator  $\hat{\Pi}$  perpendicular to the wave vector  $\vec{k}_1$  multiplied by  $k_1^2$ , at the limit  $k_1 \rightarrow \infty$ , we have its small scale asymptotic behavior satisfy

$\frac{\bar{\mathcal{P}}_{\text{curl}}^{\text{free}}(k_1, t)}{k_1^2} \cdot k_1^3 = \text{constant}$ , which indicates a scale-invariant momentum-density power in a space perpendicular to  $\vec{k}_1$ .

Figure 6.6 shows the shape of the free momentum-density curl power spectrum  $\bar{\mathcal{P}}_{\text{curl}}^{\text{free}}(k_1, t)$  (right panel) and its element  $T_{60}$  (left panel) as functions of wave number  $k_1$ . Their large and small asymptotic behaviors match our analysis very well as expected.

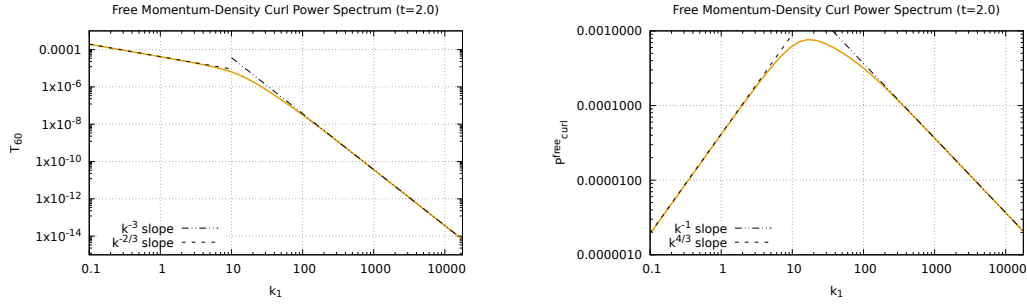


Figure 6.6: *Left panel:* This plot shows the free momentum-density curl power spectrum elements  $T_{60}$  (yellow line) in terms of wave number  $k_1$  at evolution time  $g_0(t) = t = 2.0$ , together with its large scales asymptotic behaviors by Equation 6.127 (black dashed line) and small-scale asymptotic behaviors by Equation 6.107 (black dash-dotted line). *Right panel:* This plot shows the free momentum-density curl power spectrum  $\bar{\mathcal{P}}_{\text{curl}}^{\text{free}}(k_1, t)$  (yellow line) as a function of  $k_1$  at the same evolution time  $g_0(t) = t = 2.0$ , together with its large scale  $k_1^{4/3}$  asymptotic slope (black dashed line) in Equation 6.140 and its small scale  $k_1^{-1}$  asymptotic slope (black dash-dotted line) in Equation 6.141.

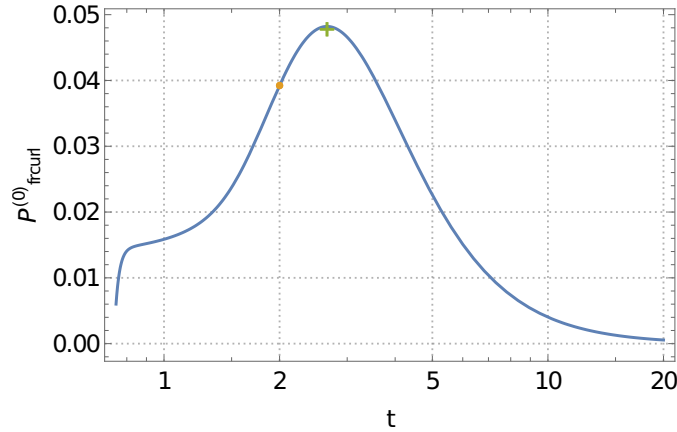


Figure 6.7: This plot shows the shape of amplitude  $\mathcal{P}_{\text{frcurl}}^{(0)}(t)$  in Equation 6.141 as a function of evolution time  $t$ . The yellow dot marks its value at evolution time  $t = 2.0$  which corresponds to Figure 6.6. The green cross represents the example extreme point of the curve given in Equation 6.142.

Since the large scale asymptotic behavior of  $\bar{\mathcal{P}}_{\text{curl}}^{\text{free}}(k_1, t)$  in Equation 6.140 is also independent of the evolution time  $t$ , we only consider the time dependence of its small scale asymptotic behaviors. Due to the complicated shape of (2) in Equation 6.86 and Figure 6.1, Figure 6.7 shows the shape of  $\mathcal{P}_{\text{frcurl}}^{(0)}(t)$  as a function of evolution time  $t$ . We can see it first increases over time and reaches its local maximal amplitude  $\mathcal{P}_{\text{frcurl}}^{\text{max}}$  at time  $t_{\text{max}}$ , then decreases all along as time proceeds to zero. The numerical result gives the local maximal  $\mathcal{P}_{\text{frcurl}}^{\text{max}}$  at its corresponding evolution time as

$$\mathcal{P}_{\text{frcurl}}^{\text{max}} \approx 0.048 \quad \text{at} \quad t_{\text{max}} \approx 2.66. \quad (6.142)$$

#### 6.3.2.4 The Relation of The Three Power Spectra

At the end of this section, we would like to discuss a bit more about the relation among the three free nonlinear momentum-density power spectra. We mentioned in Section 6.3.1 that the quantities in Equation 6.2-6.4 satisfy the relation  $k_1^2 \cdot (6.2) = (6.3) + (6.4)$ , which leads to the relation between  $\bar{\mathcal{P}}_{\text{tr}}^{\text{free}}(k_1, t)$ ,  $\bar{\mathcal{P}}_{\text{div}}^{\text{free}}(k_1, t)$  and  $\bar{\mathcal{P}}_{\text{curl}}^{\text{free}}(k_1, t)$  as

$$k_1^2 \bar{\mathcal{P}}_{\text{tr}}^{\text{free}}(k_1, t) = \bar{\mathcal{P}}_{\text{div}}^{\text{free}}(k_1, t) + \bar{\mathcal{P}}_{\text{curl}}^{\text{free}}(k_1, t), \quad \rightarrow \quad T_{10} = T_{50} + T_{60}. \quad (6.143)$$

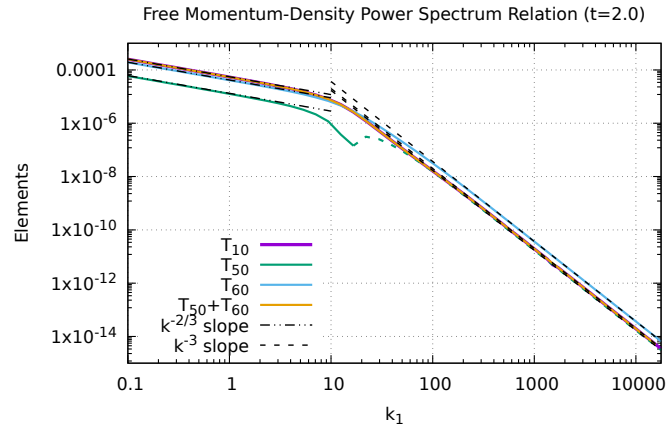


Figure 6.8: This plot shows the free momentum-density power spectra elements  $T_{10}$  (purple line),  $T_{50}$  (green line),  $T_{60}$  (blue line) and sum  $T_{50} + T_{60}$  (yellow line) in terms of wave number  $k_1$  at evolution time  $g_0(t) = t = 2.0$ , together with their large scales asymptotic behaviors by Equation 6.125, Equation 6.126, Equation 6.127 and small-scale asymptotic behaviors by Equation 6.103, Equation 6.106, Equation 6.107. The negative values of  $T_{50}$  is represented by the same color dashed lines.

Figure 6.8 shows the shape of the free momentum-density power spectra elements  $T_{10}$ ,  $T_{50}$ ,  $T_{60}$  and sum  $T_{50} + T_{60}$  as functions of  $k_1$  at evolution time  $g_0(t) = t = 2.0$ . We

can see the curve of sum  $T_{50} + T_{60}$  matches with the curve of element  $T_{10}$  very well, which verifies the relation in Equation 6.143. This result makes perfect sense for the reason that the sum of the power spectra for the momentum-density operator  $\hat{\Pi}$  in  $\vec{k}_1$  space and perpendicular to  $\vec{k}_1$  space should be equal to its total trace power spectrum.

Furthermore, since all the scalar momentum-density power spectra analyzed in this chapter are derived from the quantities in Equation 6.2-6.4, the very same relation will also be satisfied in the following sections.

#### 6.4 FRICTION MOMENTUM-DENSITY POWER SPECTRA

In this section, we still ignore the self-gravitational interaction among dust particles with  $\vec{F}_j = 0$  and  $S_{\text{Ifree}} = 0$ , yet return to the general propagators  $g_{qp}(t, t')$  and  $g_{pp}(t, t')$  in Equation 3.39 to reconsider the friction interaction between the dust particles and the constant background gas field in the system. The three scalar momentum-density power spectra in Equation 6.46, Equation 6.48 and Equation 6.51 thus can be written as

$$\bar{\mathcal{P}}_{\text{ftr}}(k_1, t) = \bar{\mathcal{P}}_{\text{lin1}}(k_1, t) + g_{pp}^2(t)(T_1 + T_2 + T_3), \quad (6.144)$$

$$\bar{\mathcal{P}}_{\text{fdiv}}(k_1, t) = \bar{\mathcal{P}}_{\text{lin2}}(k_1, t) + g_{pp}^2(t)k_1^2(T_5 + T_2 + T_3), \quad (6.145)$$

$$\bar{\mathcal{P}}_{\text{fcurl}}(k_1, t) = \bar{\mathcal{P}}_{\text{lin3}}(k_1, t) + g_{pp}^2(t)k_1^2T_6, \quad (6.146)$$

with

$$\bar{\mathcal{P}}_{\text{lin1}}(k_1, t) = (1 - g_{pp}(t))^2 u_0^2 \mathcal{P}_f(k_1, t), \quad (6.147)$$

$$\bar{\mathcal{P}}_{\text{lin2}}(k_1, t) = \frac{1}{3} k_1^2 \bar{\mathcal{P}}_{\text{lin1}}(k_1, t), \quad (6.148)$$

$$\bar{\mathcal{P}}_{\text{lin3}}(k_1, t) = 2\bar{\mathcal{P}}_{\text{lin2}}(k_1, t), \quad (6.149)$$

where the gravity-free nonlinear density power spectrum  $\mathcal{P}_f(k_1, t)$  is given in Equation 5.20. Here we've used the relation  $g_{qp}(t) = \tau_s(1 - g_{pp}(t))$ .

This section is constructed as follows. We start with deriving the expressions of the three linear gravity-free momentum-density power spectra for very small dust particles. By analyzing the asymptotic behaviors of the propagators at the limit of  $\tau_s \rightarrow 0$ , we find that the three linear gravity-free momentum-density power spectra are completely determined by the corresponding linear gravity-free density power spectrum  $\mathcal{P}_{\text{fin}}(k_1, t)$  in Equation 5.62. Then we return to the three nonlinear gravity-free momentum-density power spectra by calculating the corresponding momentum-density power spectra elements  $T_i$  with  $i = 1, 2, 3, 5, 6$  using the method shown in Section 6.2. Furthermore, by analyzing the time-dependence for the small-scale asymptotic behaviors of the trace power spectra, we find a critical particle size  $\tau_{\text{max}} \approx 3.03$

which corresponds to the maximum small-scale total kinetic energy for dust particles in the system.

#### 6.4.1 Linear Momentum-Density Power Spectra at Small $\tau_s$

We start with very small particles at finite evolution time  $t$ , in the limit of  $\tau_s \rightarrow 0$ , the propagators become

$$\lim_{\tau_s \rightarrow 0} g_{pp}(t) = \lim_{\tau_s \rightarrow 0} \exp\left(-\frac{t}{\tau_s}\right) \rightarrow 0, \quad (6.150)$$

$$\lim_{\tau_s \rightarrow 0} g_{qp}(t) = \lim_{\tau_s \rightarrow 0} \tau_s \left(1 - \exp\left(-\frac{t}{\tau_s}\right)\right) \rightarrow \tau_s, \quad (6.151)$$

therefore the three momentum-density power spectra in Equation 6.144-6.146 are only left with their first terms involving the KFT density power spectrum  $\bar{\mathcal{P}}_f(k_1, t)$  as

$$\bar{\mathcal{P}}_{\text{ftr}}(k_1, t) \approx \bar{\mathcal{P}}_{\text{lin1}}(k_1, t) \approx \bar{\mathcal{P}}_{\text{lin1}}(k_1, t) = (1 - g_{pp}(t))^2 u_0^2 \mathcal{P}_{\text{fin}}(k_1, t), \quad (6.152)$$

$$\bar{\mathcal{P}}_{\text{fdiv}}(k_1, t) \approx \bar{\mathcal{P}}_{\text{lin2}}(k_1, t) \approx \bar{\mathcal{P}}_{\text{lin2}}(k_1, t) = \frac{1}{3} (1 - g_{pp}(t))^2 u_0^2 k_1^2 \mathcal{P}_{\text{fin}}(k_1, t), \quad (6.153)$$

$$\bar{\mathcal{P}}_{\text{fcurl}}(k_1, t) \approx \bar{\mathcal{P}}_{\text{lin3}}(k_1, t) \approx \bar{\mathcal{P}}_{\text{lin3}}(k_1, t) = \frac{2}{3} (1 - g_{pp}(t))^2 u_0^2 k_1^2 \mathcal{P}_{\text{fin}}(k_1, t), \quad (6.154)$$

where the gravity-free linear density power spectrum  $\mathcal{P}_{\text{fin}}(k_1, t)$  for very small particles is given in Equation 5.62 to replace the gravity-free nonlinear density power spectrum  $\mathcal{P}_f(k_1, t)$  at the limit of  $\tau_s \rightarrow 0$ . Using the asymptotic behaviors of  $\mathcal{P}_{\text{fin}}(k_1, t)$  concluded from in Equation 5.62, we can immediately infer that at the limit of  $k_1 \rightarrow 0$ , the linear momentum-density trace power spectrum  $\bar{\mathcal{P}}_{\text{lin1}}(k_1, t)$  develops a  $k_1^{\frac{4}{3}}$  large scale asymptotic behavior, while the linear momentum-density divergence and curl power spectra  $\bar{\mathcal{P}}_{\text{lin2}}(k_1, t)$ ,  $\bar{\mathcal{P}}_{\text{lin3}}(k_1, t)$  develop  $k_1^{\frac{10}{3}}$  large-scale asymptotic slopes, at the limit of  $k_1 \rightarrow \infty$ ,  $\bar{\mathcal{P}}_{\text{lin1}}(k_1, t)$  develops a  $k_1^{-1}$  small-scale asymptotic behavior, while the other two develop  $k_1^1$  small-scale asymptotic slope.

Figure 6.9 shows the shape of the linear momentum-density trace, divergence and curl power spectra with very small friction coefficient  $\tau_s = 0.01$  and  $\tau_s = 0.1$  at evolution time  $t = 10.0$ . We can see their large and small-scale asymptotic behaviors match our analysis very well as predicted. Notice at relatively later evolution time where  $t \gg \tau_s$ , all linear momentum-density power spectra become larger with larger friction coefficients, which indicates that faster momentum-density power accumulation occurs if the system is filled with larger size dust particles. Furthermore, in the linear momentum-density divergence and curl power spectra, we see both power spectra grow proportional to the wave number  $k_1$  at very small scales in the scenario of only averaged friction interaction present in the system, which doesn't make any sense. Therefore, we need to introduce the nonlinear analysis in the following.

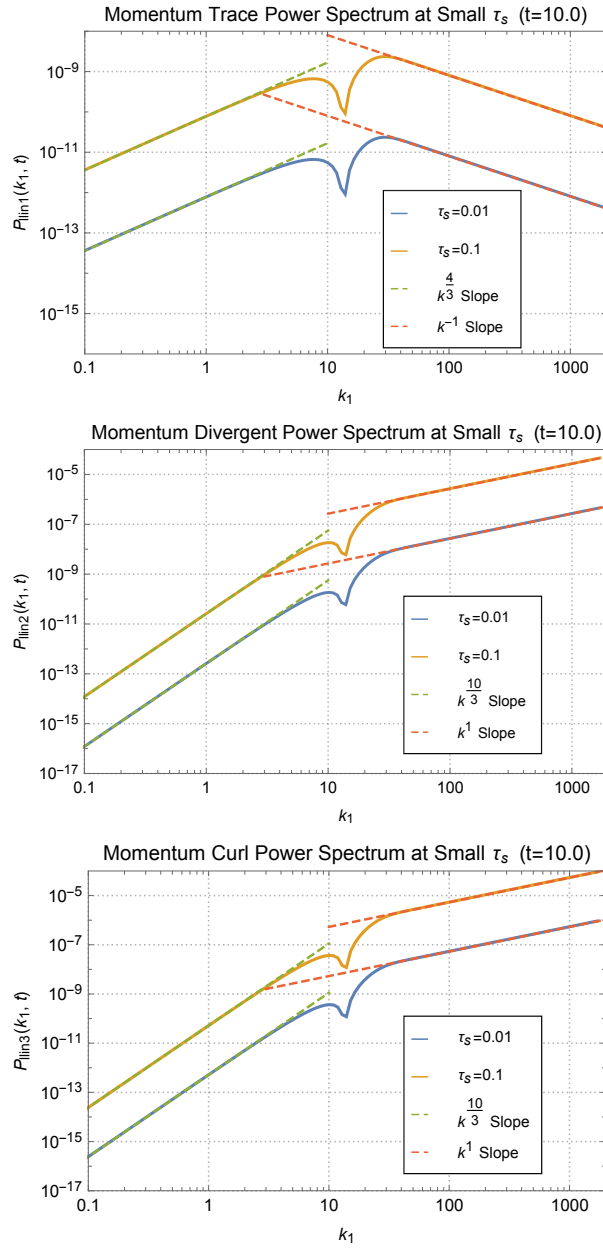


Figure 6.9: This plot shows the shape of the linear momentum-density trace (top panel), divergence (middle panel) and curl (bottom panel) power spectra as functions of wave number  $k_1$  with very small friction coefficient  $\tau_s = 0.01$  (blue lines) and  $\tau_s = 0.1$  (yellow lines) at evolution time  $t = 10.0$ . Their large scales asymptotic behaviors are marked by the green dashed lines, and their small-scale asymptotic behaviors are represented by the red dashed lines.

#### 6.4.2 Nonlinear Momentum-Density Power Spectra at Large $\tau_s$

When the friction coefficient  $\tau_s$  gets larger, the approximation shown above only remains true at a very late stage of evolution. In the limit of  $t \rightarrow \infty$ , the propagators also satisfy

$$\lim_{t \rightarrow \infty} g_{pp}(t) = \lim_{t \rightarrow \infty} \exp\left(-\frac{t}{\tau_s}\right) \rightarrow 0, \quad (6.155)$$

$$\lim_{t \rightarrow \infty} g_{qp}(t) = \lim_{t \rightarrow \infty} \tau_s \left(1 - \exp\left(-\frac{t}{\tau_s}\right)\right) \rightarrow \tau_s. \quad (6.156)$$

Therefore, all three linear momentum-density power spectra we deduce above remain unchanged. However, if we are interested in the momentum-density power spectra at an earlier evolution time where  $t$  is finite, the above approximation no longer holds, we need to return to the nonlinear momentum-density power spectra given in [Equation 6.144-6.146](#).

##### 6.4.2.1 Momentum-Density Trace Power Spectrum

First we discuss the nonlinear momentum-density trace power spectrum  $\bar{\mathcal{P}}_{\text{ftr}}(k_1, t)$  given in [Equation 6.144](#). Since the propagators no longer satisfy [Equation 6.150](#) and [6.151](#), for its first term  $\bar{\mathcal{P}}_{\text{linI}}(k_1, t)$ , we need to return to the nonlinear density power spectrum  $\mathcal{P}_f(k_1, t)$  in [Equation 5.20](#).

[Figure 6.10](#) gives the shape of  $\bar{\mathcal{P}}_{\text{linI}}(k_1, t)$  as a function of wavenumber  $k_1$  with parameters:  $\tau_s = 1.0, t = 2.0$ ;  $\tau_s = 2.0, t = 2.0$ ;  $\tau_s = 3.0, t = 2.0$ ;  $\tau_s = 3.0, t = 3.0$ . Compared to the linear momentum-density trace power spectrum in the top panel of [Figure 6.9](#), notice at small scales, the nonlinear power spectra all develop the steeper  $k_1^{-3}$  slopes.

Using [Equation 6.147](#) and [Equation 5.67](#), their small-scale asymptotic behaviors can directly be written down as

$$\bar{\mathcal{P}}_{\text{linI}}(k_1, t) \sim \frac{\mathcal{P}_{\text{linI}}^{(0)}(t)}{k_1^3}, \quad \text{for } k_1 \rightarrow \infty, \quad (6.157)$$

with the amplitude being

$$\mathcal{P}_{\text{linI}}^{(0)}(t) = \frac{u_0^2}{\tau_s^2 g_{qp}(t) \sigma_1^3 (b_0 - b_1)} \sqrt{\frac{(2\pi)^3}{b_0 + 2b_1}} \exp\left(-\frac{1}{2g_{qp}^2(t) \sigma_1^2 (b_0 + 2b_1)}\right). \quad (6.158)$$

Furthermore, the analysis over the amplitude's time and particle size dependence in [Section B.1](#) shows that the maximum kinetic energy accumulation for dust particles at very small scales caused by the density structure formation in the system

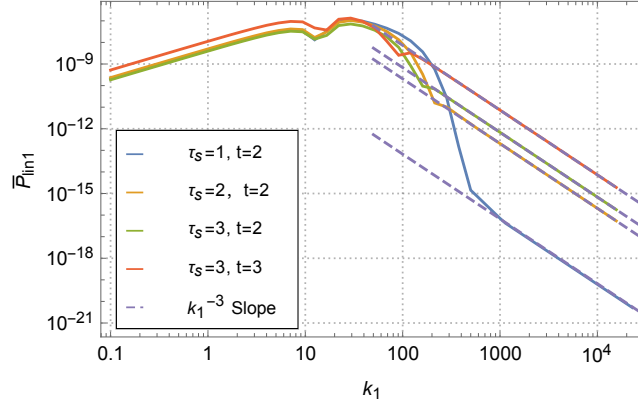


Figure 6.10: This plot gives the shape of the first term in Equation 6.144  $\tilde{\mathcal{P}}_{\text{lin}1}(k_1, t)$  as a function of wave number  $k_1$  with parameters:  $\tau_s = 1.0, t = 2.0$  (blue line);  $\tau_s = 2.0, t = 2.0$  (yellow line);  $\tau_s = 3.0, t = 2.0$  (green line);  $\tau_s = 3.0, t = 3.0$  (red line). At small scales, the  $k_1^{-3}$  slopes are marked by the purple dashed lines.

happens at the very late stage of evolution with the particle size being  $\tau_s = \tau_{s1} \approx 3.03$ , which agrees with the maximum small-scale structure formation result discussed in Section 5.3.3.

Now we move on to the second term in Equation 6.144 and first analyze the corresponding momentum-density trace power spectrum elements  $T_i$  with  $i = 1, 2, 3$ . At very small scales where  $k_1 \rightarrow \infty$ , their asymptotic behaviors are already given in Equation 6.103-6.105. While at very large scales where  $k_1 \rightarrow 0$ , since the only difference between  $T_i$  here and  $T_{i0}$  in Section 6.3 lies in the propagators, we can still use Equation 6.125, Equation 6.131, Equation 6.132 to represent their large scale asymptotic behaviors, yet with the free propagator  $g_0(t)$  in coefficient  $c_2$  and  $c_3$  replaced by the general propagator  $g_{\text{qp}}(t)$ .

Figure 6.11 shows the shape of the momentum-density trace power spectrum elements  $T_1, T_2, T_3$  and  $T_1 + T_2 + T_3$  as a function of wavenumber  $k_1$  with friction coefficient  $\tau_s = 1.0, 2.0, 3.0$  at evolution time  $t = 2.0, 3.0$ . We can see their large and small-scale asymptotic behaviors match our analytical predictions very well. In the meantime, since the values of  $T_2, T_3$  are negligible compared to  $T_1$  at very large scales and the asymptotic behaviors satisfy  $T_2 + T_3 = 0$  at very small scales, the shape of  $T_1 + T_2 + T_3$  is mostly determined by the values of  $T_1$ . Therefore, the large-scale asymptotic behavior of the second term in Equation 6.144 can be written as

$$g_{\text{pp}}^2(t)(T_1 + T_2 + T_3) \sim \frac{g_{\text{pp}}^2(t)c_1}{k_1^{\frac{3}{2}}}, \quad \text{for } k_1 \rightarrow 0, \quad (6.159)$$

at small scales, its asymptotic behavior becomes

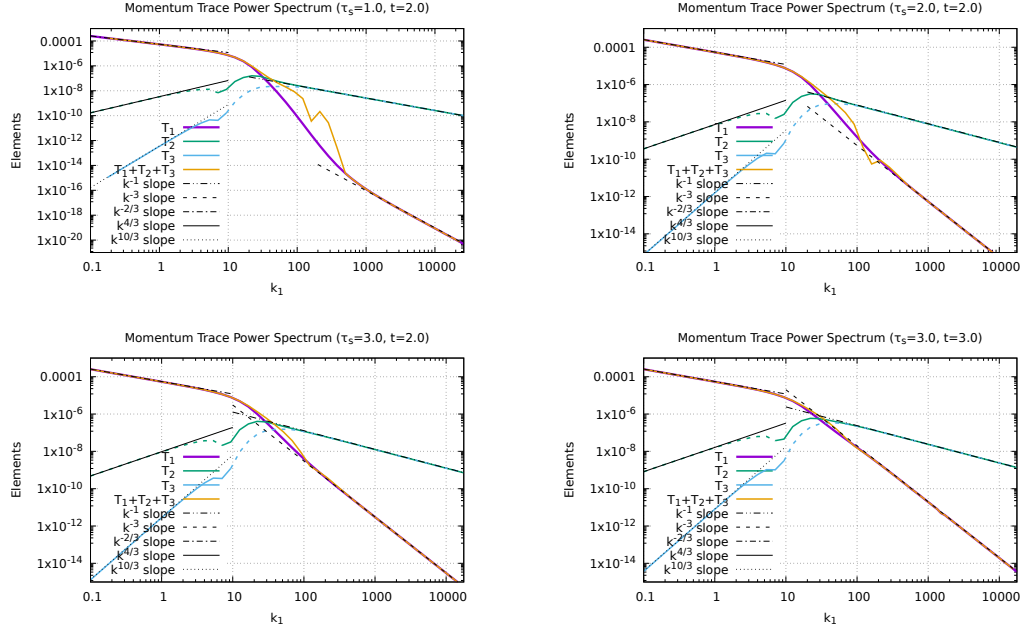


Figure 6.11: These four plots show the momentum-density trace power spectrum elements  $T_1$  (purple line),  $T_2$  (green line),  $T_3$  (blue line) and  $T_1 + T_2 + T_3$  (yellow line) as functions of wave number  $k_1$ , together with their large scales asymptotic behaviors by Equation 6.125, 6.131, 6.132 and small scales asymptotic behaviors by Equation 6.103-6.105, respectively at parameters:  $\tau_s = 1.0, t = 2.0$  (top left);  $\tau_s = 2.0, t = 2.0$  (top right);  $\tau_s = 3.0, t = 2.0$  (bottom left);  $\tau_s = 3.0, t = 3.0$  (bottom right). The negative values of  $T_2$  and  $T_3$  are represented by the same color dashed lines.

$$g_{pp}^2(t)(T_1 + T_2 + T_3) \sim \frac{g_{pp}^2(t)\mathcal{T}_1^0(t)}{k_1^3}, \quad \text{for } k_1 \rightarrow \infty. \quad (6.160)$$

with  $c_1$  given in Equation 6.125 and  $\mathcal{T}_1^0(t)$  given in Equation 6.103. Now we proceed to calculate the total momentum-density trace power spectrum  $\bar{\mathcal{P}}_{\text{fr}}(k_1, t)$  in Equation 6.144. Figure 6.12 shows the shape of  $\bar{\mathcal{P}}_{\text{fr}}(k_1, t)$  as a function of wave number  $k_1$  with friction coefficient  $\tau_s = 1.0, 2.0, 3.0$  and evolution time  $t = 2.0, 3.0$ . As expected, at small scales, the curves developed  $k_1^{-3}$  slopes due to the shape of  $\bar{\mathcal{P}}_{\text{lin1}}(k_1)$  and  $T_1 + T_2 + T_3$ , suggesting a small-scale scale-invariant particles' kinetic energy accumulation in the system.

The amplitude for the  $k_1^{-3}$  slope of  $\bar{\mathcal{P}}_{\text{fr}}(k_1, t)$  can be expressed by Equation 6.158 and 6.160 as

$$\mathcal{P}^{\text{tot}}(t) = \mathcal{P}_{\text{lin1}}^{(0)}(t) + g_{pp}^2(t)\mathcal{T}_1^0(t), \quad (6.161)$$

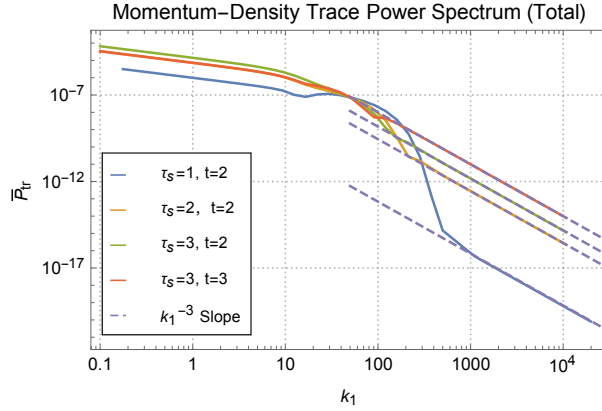


Figure 6.12: This plot shows the total momentum-density trace power spectrum  $\bar{\mathcal{P}}_{\text{fr}}(k_1, t)$  as a function of wave number  $k_1$  at the parameters:  $\tau_s = 1.0, t = 2.0$  (blue line);  $\tau_s = 2.0, t = 2.0$  (yellow line);  $\tau_s = 3.0, t = 2.0$  (green line);  $\tau_s = 3.0, t = 3.0$  (red line). At small scales, the  $k_1^{-3}$  asymptotic behaviors are marked by purple dashed lines.

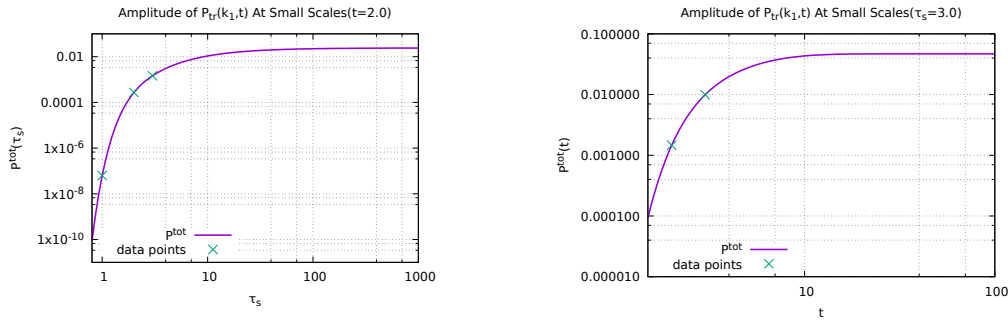


Figure 6.13: This plot shows the amplitude  $\mathcal{P}^{\text{tot}}(t)$  of  $\bar{\mathcal{P}}_{\text{fr}}(k_1, t)$  at small scales as a function of friction coefficient  $\tau_s$  (left panel) and evolution time (right panel). The green points in both plots mark the value of  $\mathcal{P}^{(0)}(t)$  corresponding to the  $\tau_s$  and  $t$  in Figure 6.12.

and its shape as functions of evolution time  $t$  and particle size  $\tau_s$  are shown in Figure 6.13. Further analysis over the time and particle-size dependence of the amplitude  $\mathcal{P}^{\text{tot}}(t)$  is given in Section B.2. The final result surprisingly shows that even considering both contributions from density structure accumulation  $\bar{\mathcal{P}}_{\text{linI}}(k_1, t)$  and particle momentum propagation  $g_{\text{pp}}^2(t)(T_1 + T_2 + T_3)$ , within the particle size range of interests, the maximum total small-scale kinetic energy accumulation in the system still occurs at the same particle size  $\tau_s \approx 3.03$ , suggesting that the largest small-scale structure formation and the maximum small scale kinetic energy accumulation happens at the same time in a system only considering friction interaction with the constant background gas field.

In the end, to study how the second term in Equation 6.144 involving momentum propagator  $g_{pp}(t)$  affects the momentum-density trace power spectrum compared to the contribution from its nonlinear density power spectrum, we define their ratio as

$$\text{ratio}_1(k_1, t) = \frac{g_{pp}^2(t)(T_1 + T_2 + T_3)}{\bar{\mathcal{P}}_{\text{lin1}}(k_1, t)} \quad (6.162)$$

At small scales where  $k_1 \rightarrow \infty$ , it satisfies

$$\begin{aligned} R_1(t) &= \lim_{k_1 \rightarrow \infty} \text{ratio}_1(k_1, t) = \lim_{k_1 \rightarrow \infty} \frac{g_{pp}^2(t)(T_1 + T_2 + T_3)}{\bar{\mathcal{P}}_{\text{lin1}}(k_1, t)} \\ &= \frac{g_{pp}^2(t)\mathcal{T}_1^0(t)}{(1 - g_{pp}(t))^2 u_0^2 \mathcal{P}_f^{(0)}(t)} = \frac{3b_0 \zeta_{pp}(0) g_{pp}^2(t)}{(1 - g_{pp}(t))^2 u_0^2}, \quad (6.163) \end{aligned}$$

with  $\mathcal{P}_f^{(0)}(t)$  given in Equation 5.67 and  $\mathcal{T}_1^0(t)$  given in Equation 6.103.

Figure 6.14 shows the shape of  $\text{ratio}_1(k_1, t)$  as a function of  $k_1$  at different friction coefficient  $\tau_s = 1.0, 2.0, 3.0$  and different evolution time  $t = 2.0, 3.0$ . We can see all curves follow the same pattern where they start with rather large values at large scales and then decrease all along until reach a rather small constant at small scales, meaning the momentum propagation term contributes greatly to the momentum-density trace power spectrum at large scales, as the scales get smaller, its effect becomes weaker.

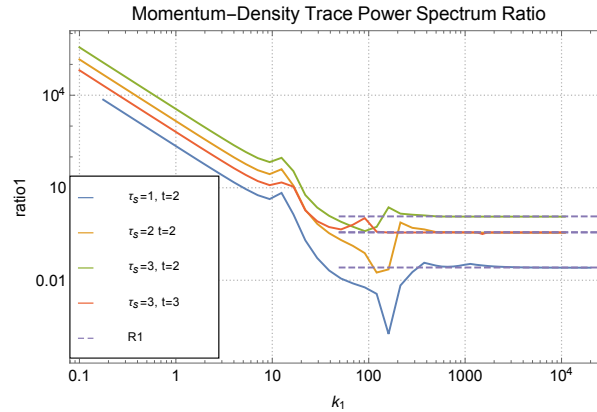


Figure 6.14: This plot shows the momentum-density trace power spectrum ratio  $\text{ratio}_1(k_1, t)$  in Equation 6.162 as a function of wave number  $k_1$  with parameters as:  $\tau_s = 1.0$ ,  $t = 2.0$  (blue line);  $\tau_s = 2.0$ ,  $t = 2.0$  (yellow line);  $\tau_s = 3.0$ ,  $t = 2.0$  (green line);  $\tau_s = 3.0$ ,  $t = 3.0$  (red line). The purple dashed lines represent the asymptotic constant  $R_1$  in Equation 6.163 at small scales.

At small scales, the value of  $R_1$  shows an interesting pattern. Define  $y_1 = \frac{t}{\tau_s}$  and rewrite Equation 6.163 as

$$R_1 = \frac{3b_0\zeta_{pp}(0)}{u_0^2} \frac{1}{(e^{y_1} - 1)^2}. \quad (6.164)$$

We can see the value of  $R_1$  monotonously decrease as  $y_1$  gets larger. Thus, for the four pairs of parameters, we are considering here,  $y_1 = \frac{2}{1}$  has the smallest  $R_1$  and  $y_1 = \frac{2}{3}$  has the largest  $R_1$ , the other two cases should have the same value of  $R_1$  as their  $y_1$  is the same. This pattern implies that at the earlier time of evolution, the momentum propagator dominates the growth of kinetic energy in the system, as time proceeds, it dies out exponentially, and only the density propagator matters at the later stage of evolution.

#### 6.4.2.2 Momentum-Density Divergence Power Spectrum

Now we discuss the nonlinear momentum-density divergence power spectrum  $\bar{\mathcal{P}}_{\text{div}}(k_1, t)$  in Equation 6.145. For calculating its first term  $\bar{\mathcal{P}}_{\text{lin2}}(k_1, t)$  at finite  $t$  and  $\tau_s$ , we need to return to the full expression for the nonlinear density power spectrum  $\mathcal{P}_f(k_1, t)$  in Equation 5.20.

Figure 6.15 gives the shape of  $\bar{\mathcal{P}}_{\text{lin2}}(k_1, t)$  as a function of wave number  $k_1$  with parameters:  $\tau_s = 1.0, t = 2.0$ ;  $\tau_s = 2.0, t = 2.0$ ;  $\tau_s = 3.0, t = 2.0$ ;  $\tau_s = 3.0, t = 3.0$ . Compared to the linear momentum-density divergence power spectrum in the middle panel of Figure 6.9, notice at small scales, the nonlinear power spectrum develops a decreasing  $k_1^{-1}$  slope, which makes a lot more sense for a system only considering friction interaction between dust particles and the constant background gas field, and further proves the necessity for computing the nonlinear solution of the density power spectrum.

Using Equation 6.148 and Equation 5.67, we can write down the small-scale asymptotic behavior for  $\bar{\mathcal{P}}_{\text{lin2}}(k_1, t)$  as

$$\bar{\mathcal{P}}_{\text{lin2}}(k_1, t) \sim \frac{\mathcal{P}_0^{\text{div}}(t)}{k_1}, \quad \text{for } k_1 \rightarrow \infty, \quad (6.165)$$

with its amplitude expressed by

$$\mathcal{P}_0^{\text{div}}(t) = \frac{1}{3}\mathcal{P}_{\text{lin1}}^{(0)}(t), \quad (6.166)$$

where  $\mathcal{P}_{\text{lin1}}^{(0)}(t)$  is given in Equation 6.158. Thus we can borrow all conclusions discussed before on  $\mathcal{P}_{\text{lin1}}^{(0)}(t)$  here to  $\mathcal{P}_0^{\text{div}}(t)$  just with one-third of its values.

Now we move on to the second term in Equation 6.145 and first discuss the corresponding momentum-density power spectra elements  $T_i$  with  $i = 5, 2, 3$ . At very small

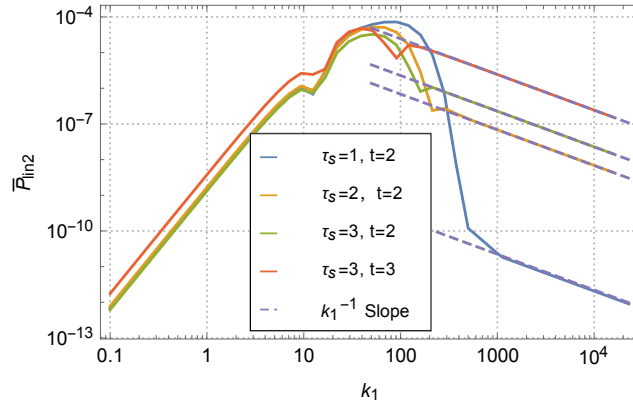


Figure 6.15: This plot gives the shape of the first term in Equation 6.145  $\bar{\mathcal{P}}_{\text{lin}2}(k_1, t)$  as a function of wave number  $k_1$  with parameters:  $\tau_s = 1.0, t = 2.0$  (blue line);  $\tau_s = 2.0, t = 2.0$  (yellow line);  $\tau_s = 3.0, t = 2.0$  (green line);  $\tau_s = 3.0, t = 3.0$  (red line). At small scales, the  $k_1^{-1}$  slopes are marked by the purple dashed lines.

scales where  $k_1 \rightarrow \infty$ , their asymptotic behaviors are already given in Equation 6.106, Equation 6.104, and Equation 6.105.

While at very large scales where  $k_1 \rightarrow 0$ , considering the similarities between  $T_i$  and  $T_{i0}$ , we can still use Equation 6.126, Equation 6.131 and Equation 6.132 to represent the large-scale asymptotics of  $T_5, T_2$  and  $T_3$ , only with the free propagator  $g_0(t)$  in coefficient  $c_2$  and  $c_3$  replace by the general propagator  $g_{\text{qp}}(t)$ .

Figure 6.16 shows momentum-density power spectra elements  $T_5, T_2, T_3$  and  $T_5 + T_2 + T_3$  as a function of wave number  $k_1$  at three different friction coefficients  $\tau_s = 1.0, 2.0, 3.0$  and two different evolution time  $t = 2.0, 3.0$ . We can see their large and small-scale asymptotic behaviors match the analytical predictions very well. In the meantime, since the values of  $T_2, T_3$  are negligible compared to  $T_5$  at very large scales and the asymptotic behaviors satisfy  $T_2 + T_3 = 0$  at very small scales, the shape of  $T_5 + T_2 + T_3$  is mostly determined by the values of  $T_5$ . Therefore, the large-scale asymptotic behavior of the second term in Equation 6.145 can be written as

$$g_{\text{pp}}^2(t)k_1^2(T_5 + T_2 + T_3) \sim g_{\text{pp}}^2(t)c_5k_1^{\frac{4}{3}}, \quad \text{for } k_1 \rightarrow 0, \quad (6.167)$$

at small scales, its asymptotic behavior becomes

$$g_{\text{pp}}^2(t)k_1^2(T_5 + T_2 + T_3) \sim \frac{g_{\text{pp}}^2(t)\mathcal{T}_5^0(t)}{k_1}, \quad \text{for } k_1 \rightarrow \infty. \quad (6.168)$$

with  $c_5$  given in Equation 6.126 and  $\mathcal{T}_5^0(t)$  given in Equation 6.106.

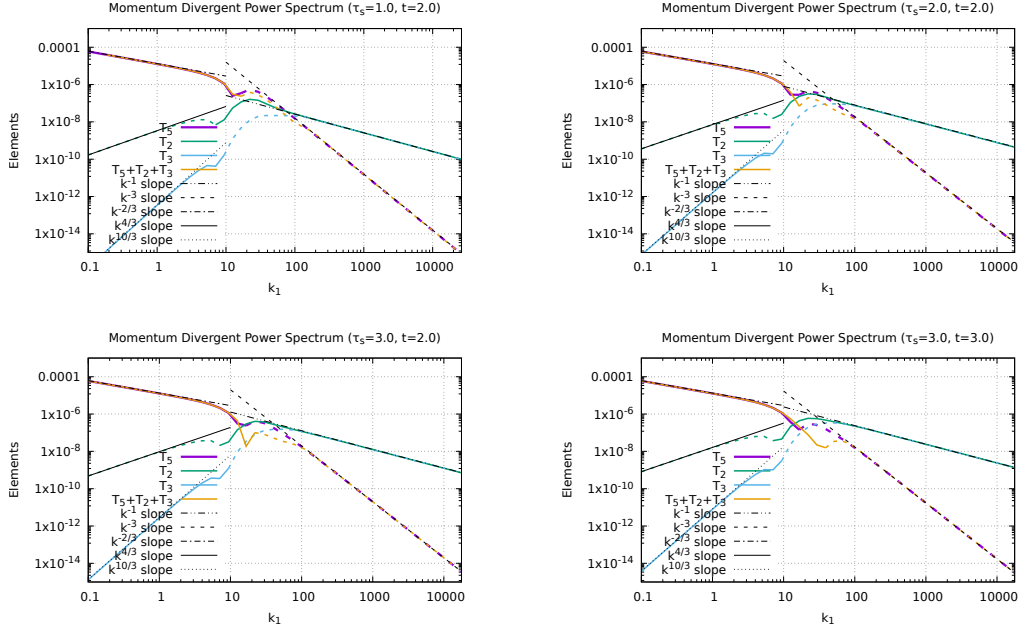


Figure 6.16: These four plots show the momentum-density power spectra elements  $T_5$  (purple line),  $T_2$  (green line),  $T_3$  (blue line) and  $T_5 + T_2 + T_3$  (yellow line) as a function of wave number  $k_1$ , together with their large scales asymptotic behaviors by Equation 6.126, Equation 6.131, Equation 6.132 and small scales asymptotic behaviors by Equation 6.106, Equation 6.104, Equation 6.105 respectively at parameters:  $\tau_s = 1.0, t = 2.0$  (top left);  $\tau_s = 2.0, t = 2.0$  (top right);  $\tau_s = 3.0, t = 2.0$  (bottom left);  $\tau_s = 3.0, t = 3.0$  (bottom right). The negative values of  $T_5$ ,  $T_2$ ,  $T_3$  and  $T_5 + T_2 + T_3$  are represented by the same color dashed lines.

Now we proceed to calculate the total momentum-density divergence power spectrum  $\bar{\mathcal{P}}_{\text{fr}}(k_1, t)$  in Equation 6.145. Figure 6.17 shows the shape of  $\bar{\mathcal{P}}_{\text{div}}(k_1, t)$  as a function of wave number  $k_1$  with friction coefficient  $\tau_s = 1.0, 2.0, 3.0$  and evolution time  $t = 2.0, 3.0$ . As expected, at small scales, the curves developed  $k_1^{-1}$  slopes due to the shape of  $\bar{\mathcal{P}}_{\text{lin2}}(k_1)$  and  $k_1^2(T_5 + T_2 + T_3)$ . Since the momentum-density divergence power spectrum measures the power spectrum for the projections of the momentum-density operator  $\hat{\Pi}$  on the wave vector  $\vec{k}_1$  multiplied by its absolute value squared, with the relation  $\frac{\bar{\mathcal{P}}_{\text{div}}(k_1, t)}{k_1^2} \cdot k_1^3 = \text{constant}$ , we conclude that the momentum-density power spectrum in  $\vec{k}_1$  space is scale-invariant at very small scales.

The amplitude for the  $k_1^{-1}$  slope of  $\bar{\mathcal{P}}_{\text{div}}(k_1, t)$  can be expressed by Equation 6.158 and Equation 6.168 as

$$\mathcal{P}_2^{\text{tot}}(t) = \frac{1}{3}\mathcal{P}_{\text{lin1}}^{(0)}(t) + g_{\text{pp}}^2(t)\mathcal{T}_5^0(t), \quad (6.169)$$

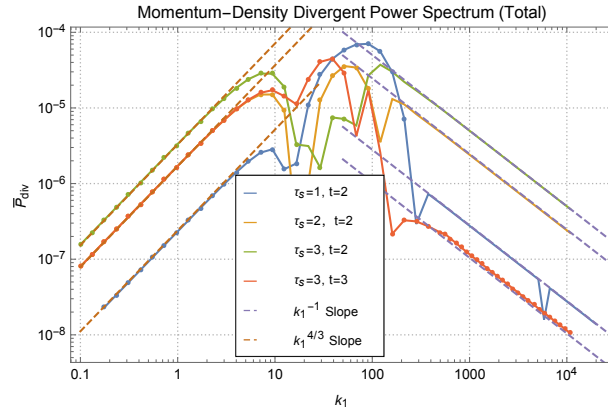


Figure 6.17: This plot shows the total momentum-density divergence power spectrum  $\bar{\mathcal{P}}_{\text{div}}(k_1, t)$  as a function of wave number  $k_1$  at the parameters:  $\tau_s = 1.0, t = 2.0$  (blue line);  $\tau_s = 2.0, t = 2.0$  (yellow line);  $\tau_s = 3.0, t = 2.0$  (green line);  $\tau_s = 3.0, t = 3.0$  (red line), the same color dotted-straight lines represent positive values, otherwise are negative values. At small scales, the  $k_1^{-1}$  asymptotic behaviors are marked by the purple dashed lines. At large scales, the  $k_1^{4/3}$  slopes are marked by the borrow dashed line.

and its shape as functions of evolution time  $t$  and particle size  $\tau_s$  are shown in Figure 6.18.

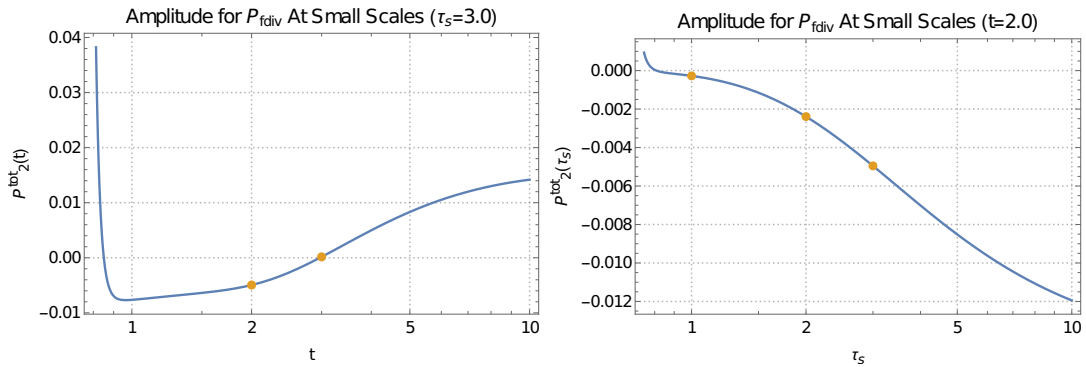


Figure 6.18: This plot shows the amplitude  $\mathcal{P}_2^{\text{tot}}(t)$  of  $\bar{\mathcal{P}}_{\text{div}}(k_1, t)$  at small scales as a function of evolution time  $t$  (left panel) and friction coefficient  $\tau_s$  (right panel). The yellow points in both plots mark the value of  $\mathcal{P}_2^{\text{tot}}(t)$  corresponding to the  $\tau_s$  and  $t$  in Figure 6.17.

Now to study how the second term in Equation 6.145 which involves momentum propagator  $g_{pp}(t)$  affects the total momentum-density divergence power spectrum compared to the first term with the nonlinear density power spectrum, we define their ratio as

$$\text{ratio2}(k_1, t) = \frac{g_{pp}^2(t)k_1^2(T_5 + T_2 + T_3)}{\bar{\mathcal{P}}_{\text{lin2}}(k_1, t)} \quad (6.170)$$

At very small scales where  $k_1 \rightarrow \infty$ ,

$$R_2(t) = \lim_{k_1 \rightarrow \infty} \text{ratio2}(k_1, t) = \frac{9b_0\zeta_{pp}(0)g_{pp}^2(t)\mathcal{T}_5^0(t)}{u_0^2(1 - g_{pp}(t))^2\mathcal{T}_1^0(t)} \quad (6.171)$$

Figure 6.19 shows the shape of  $\text{ratio2}(k_1, t)$  as a function of  $k_1$  at different friction coefficient  $\tau_s = 1.0, 2.0, 3.0$  and different evolution time  $t = 2.0, 3.0$ . We can see all curves follow a very similar pattern where they start with rather large values at very large scales and then decrease as  $k_1$  gets larger, in the end reach different constants at very small scales, meaning the momentum propagation term contributes greatly to the momentum-density divergence power spectrum at large scales, as the scales get smaller, its effect becomes weaker, finally at very small scales, the effect freezes and becomes scale-invariant.

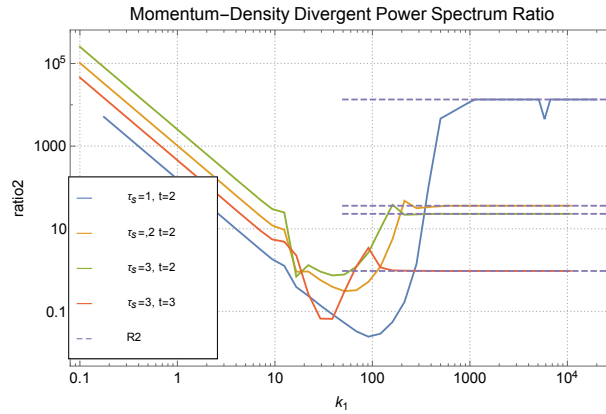


Figure 6.19: This plot shows the momentum-density divergence power spectrum ratio  $\text{ratio2}(k_1, t)$  in Equation 6.170 as a function of wave number  $k_1$  with parameters as:  $\tau_s = 1.0, t = 2.0$  (blue line);  $\tau_s = 2.0, t = 2.0$  (yellow line);  $\tau_s = 3.0, t = 2.0$  (green line);  $\tau_s = 3.0, t = 3.0$  (red line). The purple dashed lines represent the asymptotic constant  $R_2$  in Equation 6.171 at small scales.

### 6.4.2.3 Momentum-Density Curl Power Spectrum

In the end, we discuss the nonlinear momentum-density curl power spectrum  $\bar{\mathcal{P}}_{\text{fcurl}}(k_1, t)$  in Equation 6.146. Same as before, we return to the nonlinear expression for density power spectrum  $\mathcal{P}_f(k_1, t)$  in Equation 5.20 when calculating the first term  $\bar{\mathcal{P}}_{\text{lin3}}(k_1, t)$ .

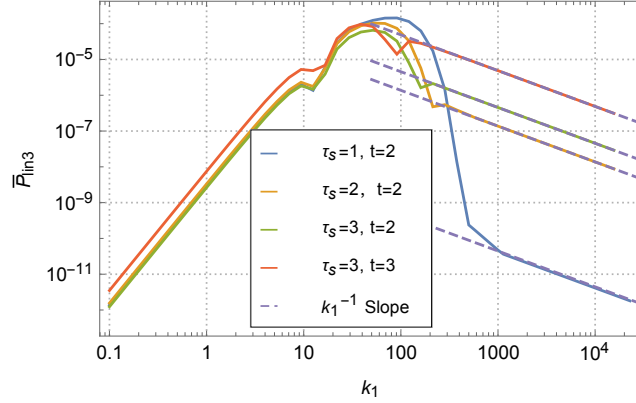


Figure 6.20: This plot gives the shape of the first term in Equation 6.146  $\bar{\mathcal{P}}_{\text{lin}3}(k_1, t)$  as a function of wave number  $k_1$  with parameters:  $\tau_s = 1.0, t = 2.0$  (blue line);  $\tau_s = 2.0, t = 2.0$  (yellow line);  $\tau_s = 3.0, t = 2.0$  (green line);  $\tau_s = 3.0, t = 3.0$  (red line). At small scales, the  $k_1^{-1}$  slopes are marked by the purple dashed lines.

Figure 6.20 gives the shape of  $\bar{\mathcal{P}}_{\text{lin}3}(k_1, t)$  as a function of wave number  $k_1$  with parameters:  $\tau_s = 1.0, t = 2.0$ ;  $\tau_s = 2.0, t = 2.0$ ;  $\tau_s = 3.0, t = 2.0$ ;  $\tau_s = 3.0, t = 3.0$ . Compared to the linear momentum-density curl power spectrum in the bottom panel of Figure 6.9, notice at small scales, the nonlinear power spectrum develops a decreasing  $k_1^{-1}$  slope. Using Equation 6.149 and Equation 5.67, we write down its small scale asymptotics as

$$\bar{\mathcal{P}}_{\text{lin}3}(k_1, t) \sim \frac{\mathcal{P}_0^{\text{curl}}(t)}{k_1}, \quad \text{for } k_1 \rightarrow \infty, \quad (6.172)$$

with the amplitude being

$$\mathcal{P}_0^{\text{curl}}(t) = \frac{2}{3} \mathcal{P}_{\text{lin}1}^{(0)}(t), \quad (6.173)$$

where  $\mathcal{P}_{\text{lin}1}^{(0)}(t)$  is given in Equation 6.158. Therefore we can also borrow all conclusions on  $\mathcal{P}_{\text{lin}1}^{(0)}(t)$  here to  $\mathcal{P}_0^{\text{curl}}(t)$  with two-third of its values.

Now we move to the second term in Equation 6.146 and first calculate the corresponding momentum-density power spectra element  $T_6$ . At very small scales where  $k_1 \rightarrow \infty$ , its asymptotic behavior is already given in Equation 6.107. While at very large scales where  $k_1 \rightarrow 0$ , the similarities of  $T_6$  here and  $T_{60}$  in Section 6.3 suggest that we can directly use Equation 6.127 to represent the large-scale asymptotics of  $T_6$ .

Figure 6.21 shows the momentum-density power spectrum element  $T_6$  as a function of wave number  $k_1$  at three different friction coefficients  $\tau_s = 1.0, 2.0, 3.0$  and two different evolution time  $t = 2.0, 3.0$ . The rather perfect match between the numerical

results and the analytical results indicates our asymptotic analysis gives quite accurate predictions.

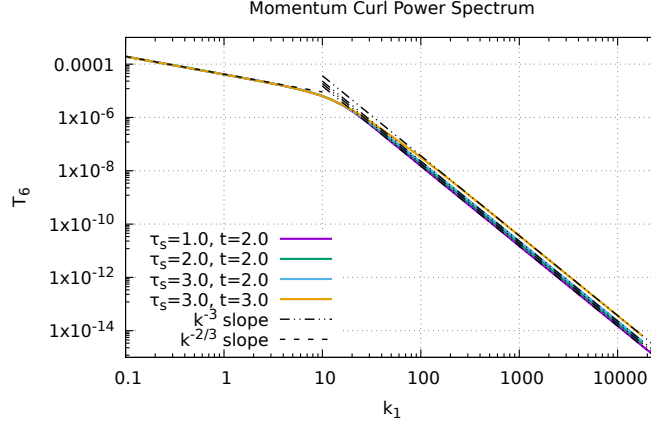


Figure 6.21: This plot shows the momentum-density power spectra element  $T_6$  as a function of wave number  $k_1$  at parameters:  $\tau_s = 1.0, t = 2.0$  (purple line);  $\tau_s = 2.0, t = 2.0$  (green line);  $\tau_s = 3.0, t = 2.0$  (blue line);  $\tau_s = 3.0, t = 3.0$  (yellow line). Their large scale  $k^{-2/3}$  asymptotic behavior is represented by the black dashed line, and their small scale  $k^{-3}$  asymptotic behavior is represented by the black dash-dotted line.

Therefore the second term in Equation 6.146 has the large-scale asymptotics as

$$g_{pp}^2(t)k_1^2T_6 \sim g_{pp}^2c_6k_1^{\frac{4}{3}}, \quad \text{for } k_1 \rightarrow 0, \quad (6.174)$$

and the small-scale asymptotics as

$$g_{pp}^2(t)k_1^2T_6 \sim \frac{g_{pp}^2\mathcal{J}_6^0(t)}{k_1}, \quad \text{for } k_1 \rightarrow \infty, \quad (6.175)$$

with  $c_6$  given in Equation 6.127 and  $\mathcal{J}_6^0(t)$  given in Equation 6.107.

Now we proceed to calculate the total momentum-density curl power spectrum  $\bar{\mathcal{P}}_{\text{fcurl}}(k_1, t)$  in Equation 6.146. Figure 6.22 shows the shape of the total momentum-density curl power spectrum  $\bar{\mathcal{P}}_{\text{fdiv}}(k_1, t)$  as a function of wave number  $k_1$  with friction coefficient  $\tau_s = 1.0, 2.0, 3.0$  and evolution time  $t = 2.0, 3.0$ . As expected, at small scales, the curves developed  $k_1^{-1}$  slopes due to the shape of  $\bar{\mathcal{P}}_{\text{lin3}}(k_1)$  and  $k_1^2T_6$ . Since the momentum-density curl power spectrum measures the power spectrum for the projections of the momentum-density operator  $\hat{\Pi}$  perpendicular to the wave vector  $\vec{k}_1$  multiplied by its absolute value squared, with the relation  $\frac{\bar{\mathcal{P}}_{\text{fcurl}}(k_1, t)}{k_1^2} \cdot k_1^3 = \text{constant}$ , we conclude that the momentum-density power spectrum in the space perpendicular to  $\vec{k}_1$  is scale-invariant at very small scales.

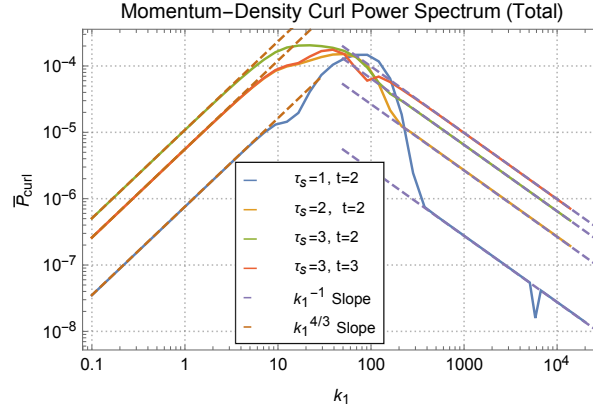


Figure 6.22: This plot shows the total momentum-density divergence power spectrum  $\bar{\mathcal{P}}_{\text{div}}(k_1, t)$  as a function of wave number  $k_1$  at the parameters:  $\tau_s = 1.0, t = 2.0$  (blue line);  $\tau_s = 2.0, t = 2.0$  (yellow line);  $\tau_s = 3.0, t = 2.0$  (green line);  $\tau_s = 3.0, t = 3.0$  (red line), the same color dotted-straight lines represent positive values, otherwise are negative values. At small scales, the  $k_1^{-1}$  asymptotic behaviors are marked by purple dashed lines. At large scales, the  $k_1^{4/3}$  slopes are marked by the borrow dashed line.

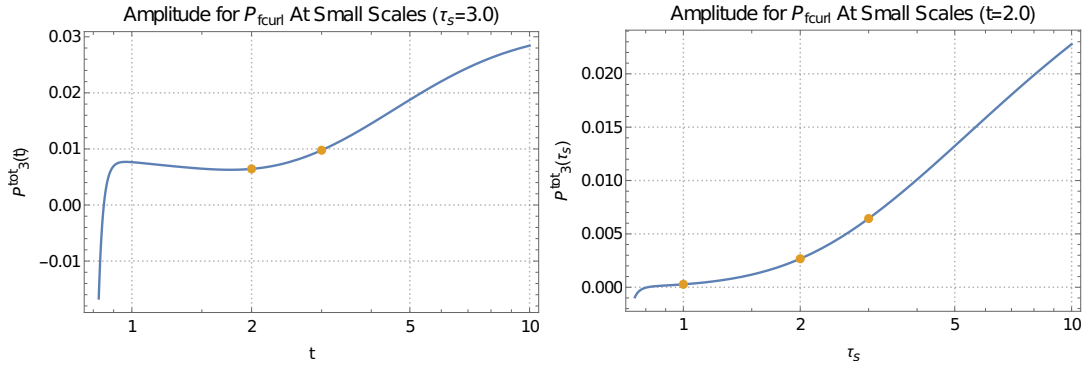


Figure 6.23: This plot shows the amplitude  $\mathcal{P}_3^{\text{tot}}(t)$  of  $\bar{\mathcal{P}}_{\text{curl}}(k_1, t)$  at small scales as a function of evolution time  $t$  (left panel) and friction coefficient  $\tau_s$  (right panel). The yellow points in both plots mark the value of  $\mathcal{P}_3^{\text{tot}}(t)$  corresponding to the  $\tau_s$  and  $t$  in Figure 6.22.

The amplitude for the  $k_1^{-1}$  slope of  $\bar{\mathcal{P}}_{\text{curl}}(k_1, t)$  can be expressed by Equation 6.158 and 6.175 as

$$\mathcal{P}_3^{\text{tot}}(t) = \frac{2}{3}\mathcal{P}_{\text{lin1}}^{(0)}(t) + g_{\text{pp}}^2(t)\mathcal{T}_6^0(t), \quad (6.176)$$

and its shape as functions of evolution time  $t$  and particle size  $\tau_s$  are shown in Figure 6.23.

Now to study how the second term in Equation 6.146 involving momentum propagator  $g_{pp}(t)$  affects the momentum-density curl power spectrum compared to the contribution from its nonlinear density power spectrum, we define their ratio as

$$\text{ratio3}(k_1, t) = \frac{g_{pp}^2(t)T_6}{\bar{\mathcal{P}}_{\text{lin3}}(k_1, t)}. \tag{6.177}$$

At very small scales where  $k_1 \rightarrow \infty$ ,

$$R_3(t) = \lim_{k_1 \rightarrow \infty} \text{ratio3}(k_1, t) = \lim_{k_1 \rightarrow \infty} \frac{g_{pp}^2(t)T_6}{\bar{\mathcal{P}}_{\text{lin3}}(k_1, t)} = \frac{9b_0g_{pp}^2(t)\zeta_{pp}(0)T_6^0(t)}{2(1-g_{pp}(t))^2u_0^2\mathcal{J}^0(t)} \tag{6.178}$$

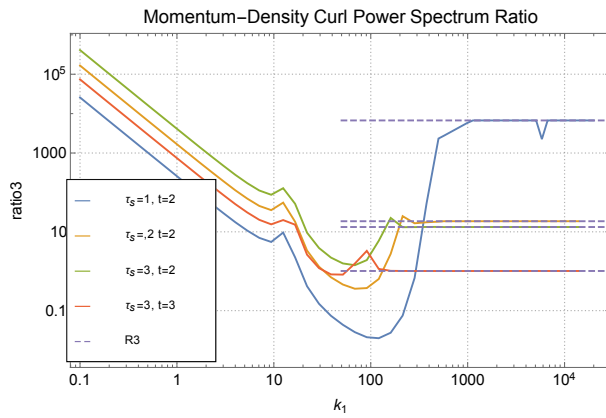


Figure 6.24: This plot shows the momentum-density curl power spectrum ratio  $\text{ratio3}(k_1, t)$  in Equation 6.177 as a function of wave number  $k_1$  with parameters as:  $\tau_s = 1.0$ ,  $t = 2.0$  (blue line);  $\tau_s = 2.0$ ,  $t = 2.0$  (yellow line);  $\tau_s = 3.0$ ,  $t = 2.0$  (green line);  $\tau_s = 3.0$ ,  $t = 3.0$  (red line). The purple dashed lines represent the asymptotic constant  $R_3$  in Equation 6.178 at small scales.

Figure 6.24 shows the shape of  $\text{ratio3}(k_1, t)$  as a function of  $k_1$  at different friction coefficient  $\tau_s = 1.0, 2.0, 3.0$  and different evolution time  $t = 2.0, 3.0$ . We can see all curves follow a very similar pattern where they start with rather large values at very large scales and then decrease as  $k_1$  gets larger, in the end reach different constants at very small scales, meaning the momentum propagation term contributes greatly to the momentum-density curl power spectrum at large scales, as the scales get smaller, its effect becomes weaker, finally at very small scales, the effect freezes and becomes scale-invariant.

#### 6.4.2.4 The Relation of The Three Power Spectra

At the end of this section, we would like to discuss a bit more about the relation among the three nonlinear momentum-density power spectra. We discussed in Section 6.3.2.4

that the quantities in Equation 6.2-6.4 satisfy the relation  $k_1^2 \cdot (6.2) = (6.3) + (6.4)$ , which leads to the relation between  $\bar{\mathcal{P}}_{\text{tr}}(k_1, t)$ ,  $\bar{\mathcal{P}}_{\text{div}}(k_1, t)$ ,  $\bar{\mathcal{P}}_{\text{curl}}(k_1, t)$  in Equation 6.144-6.146 as

$$k_1^2 \bar{\mathcal{P}}_{\text{tr}}(k_1, t) = \bar{\mathcal{P}}_{\text{div}}(k_1, t) + \bar{\mathcal{P}}_{\text{curl}}(k_1, t), \quad (6.179)$$

since the expression of their first terms in Equation 6.147-6.149 satisfy

$$k_1^2 \bar{\mathcal{P}}_{\text{lin1}}(k_1, t) = \bar{\mathcal{P}}_{\text{lin2}}(k_1, t) + \bar{\mathcal{P}}_{\text{lin3}}(k_1, t), \quad (6.180)$$

we obtain the final relation between the momentum-density power spectra elements as

$$T_1 = T_5 + T_6. \quad (6.181)$$

At very small scales, we can already confirm this relation by Equation 6.103, Equation 6.106, and Equation 6.107. While at large scales, the coefficients of  $c_1$ ,  $c_5$ ,  $c_6$  in Equation 6.125-6.127 also satisfy

$$c_1 = c_5 + c_6. \quad (6.182)$$

Figure 6.25 illustrates the relation among the three scalar momentum-density power spectra by showing the momentum-density power spectra elements  $T_1$  (purple line),  $T_5$  (green line),  $T_6$  (blue line) and  $T_5 + T_6$  (yellow line) as a function of wave number  $k_1$  at three different friction coefficients  $\tau_s = 1.0, 2.0, 3.0$  and two different evolution time  $t = 2.0, 3.0$ . The numerical results show that the relation  $T_1 = T_5 + T_6$  is perfectly satisfied, which further verifies the relation of the momentum-density power spectra  $k_1^2 \bar{\mathcal{P}}_{\text{tr}}(k_1, t) = \bar{\mathcal{P}}_{\text{div}}(k_1, t) + \bar{\mathcal{P}}_{\text{curl}}(k_1, t)$ , suggesting that the sum of the power spectrum for the momentum-density operator in  $\vec{k}_1$  space and perpendicular to  $\vec{k}_1$  space exactly equals to its trace power spectrum.

We can further verify this relation by the value of  $\text{ratio}_1(t)$ ,  $\text{ratio}_2(t)$  and  $\text{ratio}_3(t)$ . Rewrite Equation 6.170 and Equation 6.177 as

$$\begin{aligned} \text{ratio}_2(t) &= \frac{g_{\text{pp}}^2(t) k_1^2 (T_5 + T_2 + T_3)}{\frac{1}{3} k_1^2 \bar{\mathcal{P}}_{\text{lin1}}(k_1, t)} = \frac{3g_{\text{pp}}^2(t) (T_5 + T_2 + T_3)}{\bar{\mathcal{P}}_{\text{lin1}}(k_1, t)} \\ \text{ratio}_3(t) &= \frac{g_{\text{pp}}^2(t) k_1^2 T_6}{\frac{2}{3} k_1^2 \bar{\mathcal{P}}_{\text{lin1}}(k_1, t)} = \frac{3g_{\text{pp}}^2(t) T_6}{2\bar{\mathcal{P}}_{\text{lin1}}(k_1, t)} \end{aligned} \quad (6.183)$$

if the relation Equation 6.182 exists, we can write down their relation with Equation 6.162 as

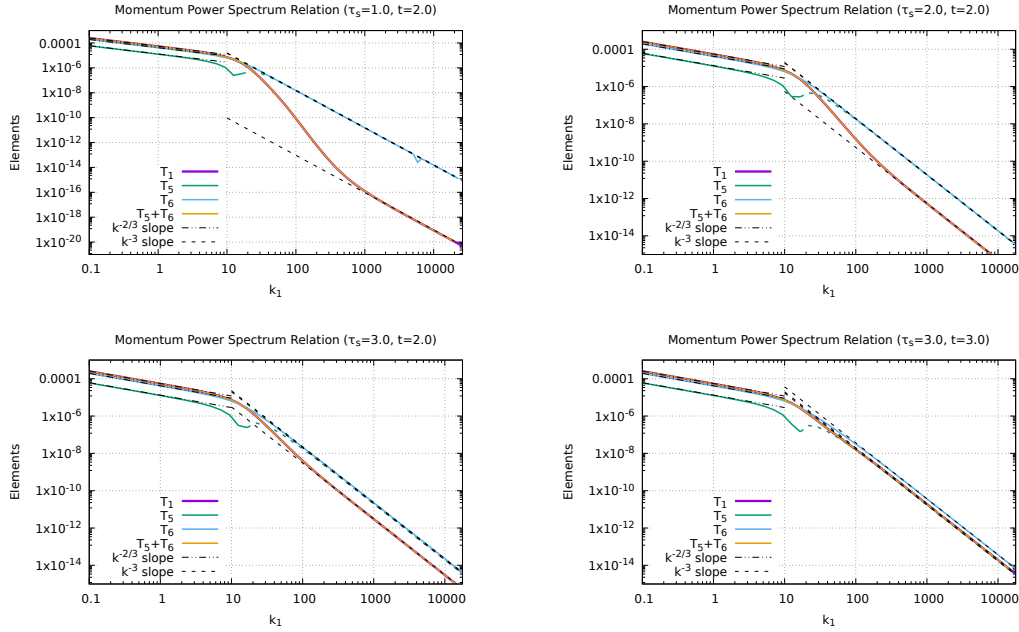


Figure 6.25: These four plots show the momentum-density power spectrum elements  $T_1$  (purple line),  $T_5$  (green line),  $T_6$  (blue line) and  $T_5 + T_6$  (yellow line) as a function of wave number  $k_1$ , together with their  $k^{-2/3}$  large scales asymptotic behaviors by Equation 6.125, Equation 6.126, Equation 6.127 and  $k^{-3}$  small scales asymptotic behaviors by Equation 6.103, Equation 6.106, Equation 6.107 respectively at parameters:  $\tau_s = 1.0, t = 2.0$  (top left);  $\tau_s = 2.0, t = 2.0$  (top right);  $\tau_s = 3.0, t = 2.0$  (bottom left);  $\tau_s = 3.0, t = 3.0$  (bottom right). The negative values of  $T_5$  are represented by the same color dashed lines.

$$\text{ratio}_1(t) = \frac{1}{3}(\text{ratio}_2(t) + 2 \cdot \text{ratio}_3(t)). \quad (6.184)$$

Figure 6.26 shows the shape of  $\text{ratio}_1$  and  $\frac{1}{3}(\text{ratio}_2(t) + 2 \cdot \text{ratio}_3(t))$  as a function  $k_1$  with parameters:  $\tau_s = 1, t = 2$ ;  $\tau_s = 2, t = 2$ ;  $\tau_s = 3, t = 2$ ;  $\tau_s = 3, t = 3$ . We can see the numerical results perfectly confirmed the relation in Equation 6.184, which further verified the relation by Equation 6.182 and Equation 6.179.

## 6.5 GRAVITATIONAL MOMENTUM-DENSITY POWER SPECTRA

With the gravity-free KFT nonlinear momentum-density power spectra  $\bar{\mathcal{P}}_{\text{ftr}}(k_1, t)$ ,  $\bar{\mathcal{P}}_{\text{fdiv}}(k_1, t)$ ,  $\bar{\mathcal{P}}_{\text{fcurl}}(k_1, t)$  in Equation 6.144-6.146 and their linear forms  $\bar{\mathcal{P}}_{\text{lin}i}$  with  $i = 1, 2, 3$  in Equation 6.152-6.154 obtained, we successfully include the friction interaction between the dust particles and the constant background gas field to the KFT framework. In this

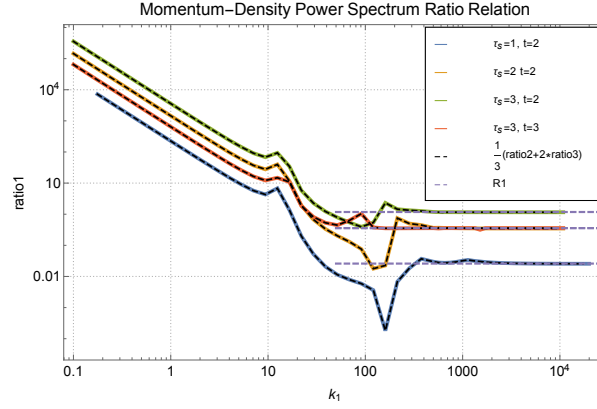


Figure 6.26: This plot shows the shape of ratio1 as a function  $k_1$  with parameters:  $\tau_s = 1, t = 2$  (blue line);  $\tau_s = 2, t = 2$  (green line);  $\tau_s = 3, t = 2$  (yellow line);  $\tau_s = 3, t = 3$  (red line), together with the corresponding values of  $\frac{1}{3}(\text{Ratio2}(t) + 2 \cdot \text{Ratio3}(t))$ . At very small scales, the values of  $R_1$  in Equation 6.163 are marked by the purple dashed lines.

section, we further consider to switch on the self-gravity among dust particles in the system at time  $t_0$  and compute the full nonlinear KFT momentum-density power spectra  $\bar{\mathcal{P}}_{\text{gtr}}(k_1, t)$ ,  $\bar{\mathcal{P}}_{\text{gdiv}}(k_1, t)$ ,  $\bar{\mathcal{P}}_{\text{gcurl}}(k_1, t)$  in Equation 6.46, Equation 6.48, Equation 6.51. Using  $\bar{\mathcal{P}}_{\text{ftr}}(k_1, t)$ ,  $\bar{\mathcal{P}}_{\text{fdiv}}(k_1, t)$ ,  $\bar{\mathcal{P}}_{\text{fcurl}}(k_1, t)$ , we can rewrite them as

$$\begin{aligned} \bar{\mathcal{P}}_{\text{gtr}}(k_1, t) = e^{i\langle S_1 \rangle} & \left( \bar{\mathcal{P}}_{\text{ftr}}(k_1, t) + 2ig_{\text{pp}}(t)g_{\text{qp}}(t)(\vec{k}_1 \cdot \vec{F}_1)(T_5 + T_7) \right. \\ & \left. - \vec{F}_1 \cdot \vec{F}_1 \mathcal{P}_f(k_1, t) \right), \end{aligned} \quad (6.185)$$

$$\begin{aligned} \bar{\mathcal{P}}_{\text{gdiv}}(k_1, t) = e^{i\langle S_1 \rangle} & \left( \bar{\mathcal{P}}_{\text{fdiv}}(k_1, t) + 2ig_{\text{pp}}(t)g_{\text{qp}}(t)k_1^2(\vec{k}_1 \cdot \vec{F}_1)(T_5 + T_7) \right. \\ & \left. - (\vec{k}_1 \cdot \vec{F}_1)^2 \mathcal{P}_f(k_1, t) \right), \end{aligned} \quad (6.186)$$

$$\bar{\mathcal{P}}_{\text{gdiv}}(k_1, t) = e^{i\langle S_1 \rangle} \left( \bar{\mathcal{P}}_{\text{fcurl}}(k_1, t) - \left( k^2 \vec{F}_1 \cdot \vec{F}_1 - (\vec{k}_1 \cdot \vec{F}_1)^2 \right) \mathcal{P}_f(k_1, t) \right), \quad (6.187)$$

with the full expressions for the force terms being

$$\vec{F} \cdot \vec{F} = -\frac{f^2 \hat{G}_0^2}{\pi^2} \left[ \int_{t_0}^t dt' g_{\text{pp}}(t, t') \int_0^\infty dk_2 \left( 1 + \frac{k_2}{k_1} - \left| 1 - \frac{k_2}{k_1} \right| \right) k_2 P(k_2, t') \right]^2, \quad (6.188)$$

$$\vec{k}_1 \cdot \vec{F} = \frac{if\hat{G}_0}{\pi} \int_{t_0}^t dt' g_{\text{pp}}(t, t') \int_0^\infty dk k^2 P(k, t') J\left(\frac{k}{k_1}\right), \quad (6.189)$$

where we've used the expression for  $\vec{f}_1 = \langle \vec{\nabla}_1 \Phi_2 \rangle$  in Equation 5.33 and the definition for  $\vec{F}_1$  in Equation 6.11. And the linear and nonlinear expressions of the mean interaction term  $i\langle S_I \rangle$  are given in Equation 5.83 and Equation 5.90.

This section is constructed as follows. We start with deriving the expressions of the three full linear momentum-density power spectra for very small dust particles. By analyzing their small-scale asymptotic behaviors at the limit of  $k_1 \rightarrow \infty$ , we find that these power spectra are completely determined by their corresponding full linear density power spectrum  $\mathcal{P}_{\text{glin}}(k_1, t)$  in Section 5.4.2 at small scales. Then we return to the three full nonlinear momentum-density power spectra for larger-size particles, by calculating their small-scale asymptotic approximations at  $k_1 \rightarrow \infty$ , we find that their results at very small scales only depend on the mean interaction term and three gravity-free nonlinear momentum-density power spectra in Section 6.4.2.

### 6.5.1 Linear Momentum-Density Power Spectra at Small $\tau_s$

We first derive the full expressions for the three linear momentum-density power spectra with very small friction coefficients  $\tau_s$ . At the limit  $\tau_s \rightarrow 0$ , the propagators satisfy Equation 6.150 and Equation 6.151, therefore we can omit all terms with  $g_{\text{pp}}(t)$  in Equation 6.185-6.187, further approximate all density and momentum-density nonlinear power spectra by their linear expressions to obtain

$$\bar{\mathcal{P}}_{\text{gtr}}(k_1, t) \approx \bar{\mathcal{P}}_{\text{glin1}}(k_1, t) = e^{i\langle S_I \rangle} \left( \bar{\mathcal{P}}_{\text{llin1}}(k_1, t) - \vec{F} \cdot \vec{F} \mathcal{P}_{\text{flin}}(k_1, t) \right), \quad (6.190)$$

$$\bar{\mathcal{P}}_{\text{gdiv}}(k_1, t) \approx \bar{\mathcal{P}}_{\text{glin2}}(k_1, t) = e^{i\langle S_I \rangle} \left( \bar{\mathcal{P}}_{\text{llin2}}(k_1, t) - \left( \vec{k}_1 \cdot \vec{F} \right)^2 \mathcal{P}_{\text{flin}}(k_1, t) \right), \quad (6.191)$$

$$\begin{aligned} \bar{\mathcal{P}}_{\text{gcurl}}(k_1, t) \approx \bar{\mathcal{P}}_{\text{glin3}}(k_1, t) = e^{i\langle S_I \rangle} \left( \bar{\mathcal{P}}_{\text{llin3}}(k_1, t) + \left( \left( \vec{k}_1 \cdot \vec{F} \right)^2 - \right. \right. \\ \left. \left. k_1^2 \left( \vec{F} \cdot \vec{F} \right) \right) \cdot \mathcal{P}_{\text{flin}}(k_1, t) \right). \end{aligned} \quad (6.192)$$

Using the linear expression of the mean interaction term  $i\langle S_I \rangle(k_1, t)$  in the limit of  $\tau_s \rightarrow 0$  at evolution time  $t$  with initial time  $t_0$  given in Equation 5.83, Figure 6.27 shows the shape of  $i\langle S_I \rangle(k, t)$  as a function of  $k_1$  at different particle sizes  $\tau_s = 0.01$ ,  $\tau_s = 0.1$  with different evolution time  $t = 11.0$ ,  $t = 20.0$  at the same initial time  $t_0 = 10.0$  and the same gravitational parameter  $f = 1.0$ . As explained in Section 5.4.2, at the limit of  $k_1 \rightarrow 0$ , the large scale asymptotics of  $i\langle S_I \rangle(k_1, t)$  develops a  $k_1^2$  slope. At the limit of  $k_1 \rightarrow \infty$ , the small scale asymptotics of  $i\langle S_I \rangle(k_1, t)$  reaches their asymptotic constants. In the meantime, since the value of  $i\langle S_I \rangle(k_1, t)$  gets larger with larger  $\tau_s$  and  $t - t_0$ , we can deduce that the three linear momentum-density power spectra become larger with larger particle sizes and longer relative evolution time.

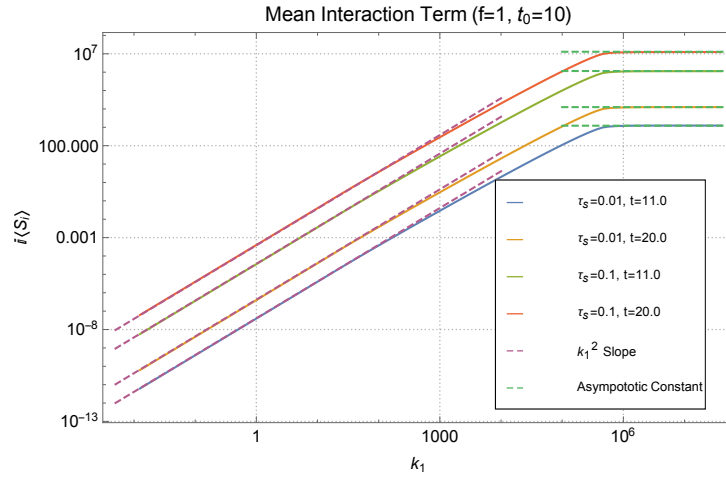


Figure 6.27: This plot shows the shape of  $i(S_1)(k_1, t)$  in Equation 5.83 as a function of  $k_1$  at different particle sizes  $\tau_s = 0.01$  (blue, yellow lines),  $\tau_s = 0.1$  (green, red lines) with different evolution time  $t = 11.0$  (blue, green lines),  $t = 20.0$  (yellow, red lines) at the same initial time  $t_0 = 10.0$  and the same gravitational parameter  $f = 1.0$ . Their large scale  $k_1^2$  asymptotic slopes are marked by the burgundy dashed lines, and their small scale asymptotic constants are represented by the light green dashed lines.

To compute the numerical values of  $\vec{F} \cdot \vec{F}$  and  $\vec{k}_1 \cdot \vec{F}$ , we need to implement the approximated density power spectrum  $P_{\text{inis}}(k_1, t_0)$  at the limit of  $\tau_s \rightarrow 0$  given in Equation 5.77 to replace  $P(k, t')$  in Equation 6.188-6.189, thus the expressions of  $\vec{F} \cdot \vec{F}$  and  $\vec{k}_1 \cdot \vec{F}$  becomes

$$\begin{aligned}
 \vec{F} \cdot \vec{F} &= -\frac{f^2 \hat{G}_0^2}{\pi^2} \left[ \int_{t_0}^t dt' g_{pp}(t, t') \int_0^\infty dk_2 \left( 1 + \frac{k_2}{k_1} - \left| 1 - \frac{k_2}{k_1} \right| \right) k_2 P_{\text{inis}}(k_2, t_0) \right]^2 \\
 &= -\frac{c_0^2 g_{qp}^2(t, t_0) g_{qp}^4(t_0) f^2 \hat{G}_0^2}{\pi^2} \left[ \int_0^\infty dk_2 \left( 1 + \frac{k_2}{k_1} - \left| 1 - \frac{k_2}{k_1} \right| \right) k_2^{\frac{7}{3}} \right. \\
 &\quad \left. \left( 1 - \exp \left( -\frac{c_1}{k_2^{\frac{7}{3}}} \right) \right) \right]^2,
 \end{aligned} \tag{6.193}$$

$$\begin{aligned}
 \vec{k}_1 \cdot \vec{F} &= \frac{if \hat{G}_0}{\pi} \int_{t_0}^t dt' g_{pp}(t, t') \int_0^\infty dk_2 k_2^2 P_{\text{inis}}(k_2, t_0) J \left( \frac{k_2}{k_1} \right) \\
 &= \frac{ic_0 g_{qp}(t, t_0) g_{qp}^2(t_0) f \hat{G}_0}{\pi} \int_0^\infty dk_2 k_2^{\frac{10}{3}} \left( 1 + \frac{k_1^2 - k_2^2}{2k_2 k_1} \ln \frac{k_2 + k_1}{|k_2 - k_1|} \right) \cdot \\
 &\quad \left( 1 - \exp \left( -\frac{c_1}{k_2^{\frac{7}{3}}} \right) \right).
 \end{aligned} \tag{6.194}$$

Notice that the integrals in both terms are not convergent for  $k_2 \rightarrow \infty$ , therefore we borrow the same cutoff scale  $k_m$  as in [Equation 5.87](#) here and obtain their large scales asymptotics at the limit of  $k_1 \rightarrow 0$  as

$$\begin{aligned}
 \vec{F} \cdot \vec{F} &\approx -\frac{4c_0^2 g_{qp}^2(t, t_0) g_{qp}^4(t_0) f^2 \hat{G}_0^2}{\pi^2} \left[ \int_0^{k_m} dk_2 k_2^{\frac{7}{3}} \left( 1 - \exp \left( -\frac{c_1}{k_2^{\frac{7}{3}}} \right) \right) \right]^2 \\
 &= -\frac{4c_0^2 g_{qp}^2(t, t_0) g_{qp}^4(t_0) f^2 \hat{G}_0^2}{\pi^2} \left( \frac{3k_m^{10/3}}{10} - \frac{3c_1^{10/7}}{7} \Gamma \left( -\frac{10}{7}, \frac{c_1}{k_m^{7/3}} \right) \right)^2 \\
 &\approx -\frac{4c_0^2 c_1^2 g_{qp}^2(t, t_0) g_{qp}^4(t_0) f^2 \hat{G}_0^2 k_m^2}{\pi^2},
 \end{aligned} \tag{6.195}$$

$$\begin{aligned}
 \vec{k}_1 \cdot \vec{F} &\approx \frac{2ic_0 g_{qp}(t, t_0) g_{qp}^2(t_0) f \hat{G}_0 k_1^2}{3\pi} \int_0^\infty dk_2 k_2^{\frac{4}{3}} \left( 1 - \exp \left( -\frac{c_1}{k_2^{\frac{7}{3}}} \right) \right) \\
 &= \frac{2ic_0 g_{qp}(t, t_0) g_{qp}^2(t_0) f \hat{G}_0 k_1^2}{3\pi} \left( \frac{3k_m^{7/3}}{7} - \frac{3}{7} \left( e^{-\frac{c_1}{k_m^{7/3}}} k_m^{7/3} - c_1 \Gamma \left( 0, \frac{c_1}{k_m^{7/3}} \right) \right) \right) \\
 &\approx \frac{2ic_0 c_1 g_{qp}(t, t_0) g_{qp}^2(t_0) f \hat{G}_0 k_1^2}{7\pi} \left( 1 - \gamma_e - \ln \left( \frac{c_1}{k_m^{7/3}} \right) \right).
 \end{aligned} \tag{6.196}$$

with  $\gamma_e$  being the Euler Gamma constant, here we already use the Taylor expansion for the incomplete Gamma function  $\Gamma(a, z)$  at the limit of  $z \rightarrow 0$ . And at very small scales  $k_1 \rightarrow \infty$ , we have

$$\begin{aligned} \vec{F} \cdot \vec{F} &\approx -\frac{4c_0^2 g_{qp}^2(t, t_0) g_{qp}^4(t_0) f^2 \hat{G}_0^2}{\pi^2 k_1^2} \left[ \int_0^{k_m} dk_2 k_2^{\frac{10}{3}} \left( 1 - \exp\left(-\frac{c_1}{k_2^{\frac{7}{3}}}\right) \right) \right]^2 \\ &= -\frac{4c_0^2 g_{qp}^2(t, t_0) g_{qp}^4(t_0) f^2 \hat{G}_0^2}{\pi^2 k_1^2} \left( \frac{3k_m^{13/3}}{13} - \frac{3c_1^{13/7} \Gamma\left(-\frac{13}{7}, \frac{c_1}{k_m^{7/3}}\right)}{7} \right)^2 \end{aligned} \quad (6.197)$$

$$\begin{aligned} &\approx -\frac{c_0^2 c_1^2 g_{qp}^2(t, t_0) g_{qp}^4(t_0) f^2 \hat{G}_0^2 k_m^4}{\pi^2 k_1^2}, \\ \vec{k}_1 \cdot \vec{F} &\approx \frac{2ic_0 g_{qp}(t, t_0) g_{qp}^2(t_0) f \hat{G}_0}{\pi} \int_0^\infty dk_2 k_2^{\frac{10}{3}} \left( 1 - \exp\left(-\frac{c_1}{k_2^{\frac{7}{3}}}\right) \right) \\ &\approx \frac{ic_0 c_1 g_{qp}(t, t_0) g_{qp}^2(t_0) f \hat{G}_0 k_m^2}{\pi}. \end{aligned} \quad (6.198)$$

Figure 6.28 shows the shape of  $\vec{F} \cdot \vec{F}$  and  $\vec{k}_1 \cdot \vec{F}$  as functions of wavenumber  $k_1$  at the initial time  $t_0 = 10.0$  and gravitational parameter  $f = 1.0$  with different particle size  $\tau_s = 0.01$ ,  $\tau_s = 0.1$  and different relative evolution time  $t - t_0 = 1.0$ ,  $t - t_0 = 10.0$ . We can see the curves of  $\vec{F} \cdot \vec{F}$  reach their asymptotic constants at very large scales as shown in Equation 6.195, and develop the  $k_1^{-2}$  slopes at very small scales as shown in Equation 6.197. While the curves of  $\vec{k}_1 \cdot \vec{F}$  develop the large scale  $k_1^2$  asymptotic behaviors at the limit of  $k_1 \rightarrow 0$  and reach their small scale asymptotic constant at the limit of  $k_1 \rightarrow \infty$ , which also agrees with our predictions in Equation 6.196 and Equation 6.198.

In the meantime, the comparison between different curves shows that the values of  $\vec{F} \cdot \vec{F}$  and  $\vec{k}_1 \cdot \vec{F}$  grow larger with larger  $\tau_s$ , meaning that the self-gravitational interaction becomes stronger with larger size particles present in the system. On the other hand, notice when we switch on the self-gravity at the very late stage of friction evolution time where  $t_0 \gg \tau_s$ , different relative evolution times  $t - t_0$  don't change the values of  $\vec{F} \cdot \vec{F}$  and  $\vec{k}_1 \cdot \vec{F}$  for the same size particles.

Now we return to the full expression of linear scalar momentum-density power spectra, at very small scales where  $k_1 \rightarrow \infty$ , preserving the terms with higher order  $k_1$ , we obtain the asymptotics as

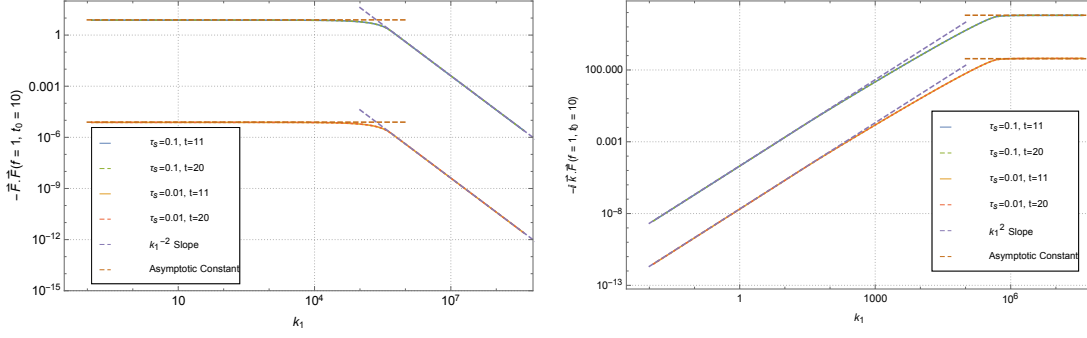


Figure 6.28: This plot shows the shape of  $\vec{F} \cdot \vec{F}$  (left panel) and  $\vec{k}_1 \cdot \vec{F}$  (right panel) in Equation 6.193 and Equation 6.194 as functions of wavenumber  $k_1$  at the initial time  $t_0 = 10.0$  and gravitational parameter  $f = 1.0$  with different parameters:  $\tau_s = 0.1$ ,  $t - t_0 = 1.0$  (blue lines);  $\tau_s = 0.1$ ,  $t - t_0 = 10.0$  (green dashed lines);  $\tau_s = 0.01$ ,  $t - t_0 = 1.0$  (yellow lines);  $\tau_s = 0.01$ ,  $t - t_0 = 10.0$  (red dashed lines). At large scales, their asymptotic behaviors are marked by the purple dashed lines, and at small scales, their asymptotic behaviors are marked by brown dashed lines.

$$\begin{aligned} \bar{\mathcal{P}}_{\text{glin1}}(k_1, t) &= e^{i\langle S_1 \rangle} \left( \bar{\mathcal{P}}_{\text{lin1}}(k_1, t) - \vec{F} \cdot \vec{F} \mathcal{P}_{\text{flin}}(k_1, t) \right) \\ &\approx e^{i\langle S_1 \rangle} \left[ (1 - g_{\text{pp}}(t))^2 u_0^2 \mathcal{P}_{\text{flin}}(k_1, t) + \right. \\ &\quad \left. \frac{c_0^2 c_1^2 g_{\text{qp}}^2(t, t_0) g_{\text{qp}}^4(t_0) f^2 \hat{G}_0^2 k_m^4}{\pi^2} \frac{\mathcal{P}_{\text{flin}}(k_1, t)}{k_1^2} \right] \end{aligned} \quad (6.199)$$

$$\begin{aligned} \bar{\mathcal{P}}_{\text{glin2}}(k_1, t) &= e^{i\langle S_1 \rangle} \left( \bar{\mathcal{P}}_{\text{lin2}}(k_1, t) - (\vec{k}_1 \cdot \vec{F})^2 \mathcal{P}_{\text{flin}}(k_1, t) \right) \\ &\approx e^{i\langle S_1 \rangle} \left[ \frac{1}{3} (1 - g_{\text{pp}}(t))^2 u_0^2 k_1^2 \mathcal{P}_{\text{flin}}(k_1, t) + \right. \\ &\quad \left. \frac{c_0^2 c_1^2 g_{\text{qp}}^2(t, t_0) g_{\text{qp}}^4(t_0) f^2 \hat{G}_0^2 k_m^4}{\pi^2} \mathcal{P}_{\text{flin}}(k_1, t) \right] \end{aligned} \quad (6.200)$$

$$\begin{aligned} \bar{\mathcal{P}}_{\text{glin3}}(k_1, t) &= e^{i\langle S_1 \rangle} \left( \bar{\mathcal{P}}_{\text{lin3}}(k_1, t) + \left( (\vec{k}_1 \cdot \vec{F})^2 - k_1^2 (\vec{F} \cdot \vec{F}) \right) \mathcal{P}_{\text{flin}}(k_1, t) \right) \\ &\approx \frac{2}{3} (1 - g_{\text{pp}}(t))^2 u_0^2 k_1^2 \mathcal{P}_{\text{glin}}(k_1, t), \end{aligned} \quad (6.201)$$

suggesting that the small-scale asymptotic behaviors of the full linear momentum-density power spectra are simply given by  $\bar{\mathcal{P}}_{\text{glini}}(k_1, t) \sim \exp(i\langle S_1 \rangle) \cdot \bar{\mathcal{P}}_{\text{lini}}(k_1, t)$  with

$i = 1, 2, 3$ , which completely determined by the linear full density power spectrum  $\mathcal{P}_{\text{glin}}(k_1, t)$  calculated in Section 5.4.2.

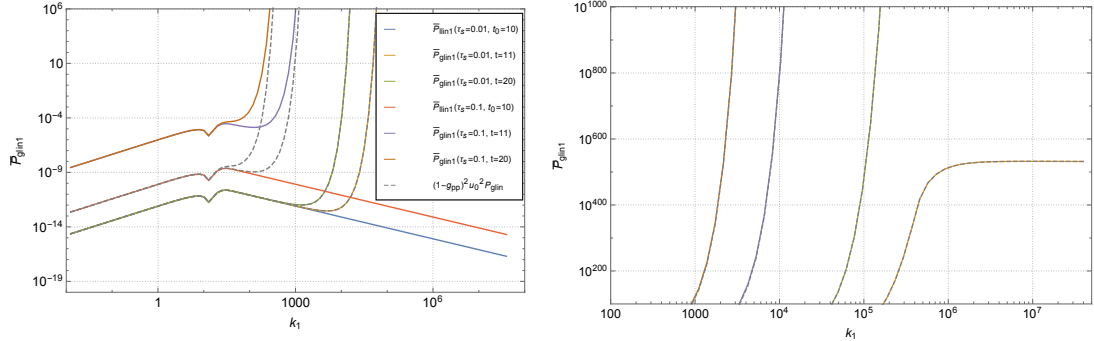


Figure 6.29: These two plots shows the shape of the full linear momentum-density trace power spectra  $\bar{\mathcal{P}}_{\text{glin1}}(k_1, t)$  as functions of wave number  $k_1$  with parameters:  $\tau_s = 0.01$ ,  $t = 11.0$  (yellow line);  $\tau_s = 0.01$ ,  $t = 20.0$  (green line);  $\tau_s = 0.1$ ,  $t = 11.0$  (purple line);  $\tau_s = 0.1$ ,  $t = 20.0$  (brown line), together with their corresponding initial trace power spectrum  $\bar{\mathcal{P}}_{\text{lin1}}(k_1, t)$  in Equation 6.152 at initial time  $t_0 = 10.0$  (blue, red lines) at the same gravitational parameter  $f = 1.0$ . The gray dashed line marks the curve of  $(1 - g_{\text{pp}}(t))^2 u_0^2 \mathcal{P}_{\text{glin}}(k_1, t)$ . The right panel plot shows the zoom plot of  $\bar{\mathcal{P}}_{\text{glin1}}(k_1, t)$  at higher values.

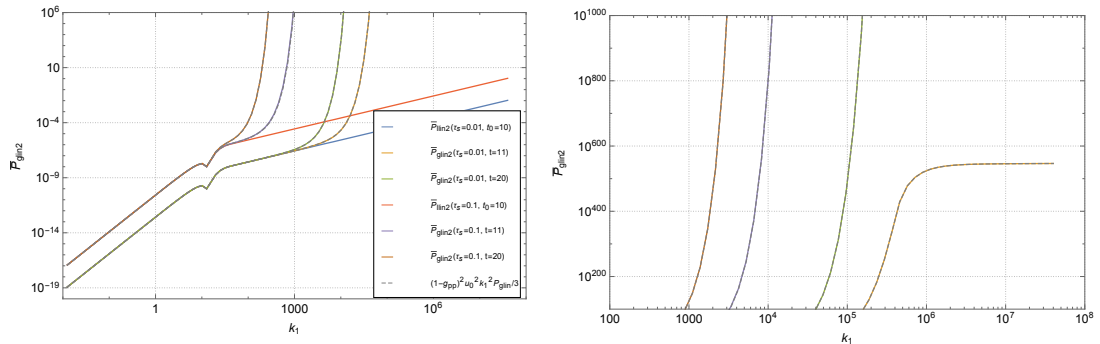


Figure 6.30: These two plots show the shape of the full linear momentum-density divergence power spectra  $\bar{\mathcal{P}}_{\text{glin2}}(k_1, t)$  as functions of wave number  $k_1$  with parameters:  $\tau_s = 0.01$ ,  $t = 11.0$  (yellow line);  $\tau_s = 0.01$ ,  $t = 20.0$  (green line);  $\tau_s = 0.1$ ,  $t = 11.0$  (purple line);  $\tau_s = 0.1$ ,  $t = 20.0$  (brown line), together with their corresponding initial divergence power spectrum  $\bar{\mathcal{P}}_{\text{lin2}}(k_1, t)$  in Equation 6.153 at initial time  $t_0 = 10.0$  (blue, red lines) at the same gravitational parameter  $f = 1.0$ . The gray dashed line marks the curve of  $\frac{1}{3}(1 - g_{\text{pp}}(t))^2 u_0^2 k_1^2 \mathcal{P}_{\text{glin}}(k_1, t)$ . The right panel plot shows the zoom plot of  $\bar{\mathcal{P}}_{\text{glin2}}(k_1, t)$  at higher values.

Figure 6.29-6.31 show the shape of  $\bar{\mathcal{P}}_{\text{glin1}}(k_1, t)$ ,  $\bar{\mathcal{P}}_{\text{glin2}}(k_1, t)$ ,  $\bar{\mathcal{P}}_{\text{glin3}}(k_1, t)$  as functions of wavenumber  $k_1$  with very small particle sizes  $\tau_s = 0.01$ ,  $\tau_s = 0.1$  at different evolution time  $t = 11.0$ ,  $t = 20.0$  with the same initial time  $t_0 = 10.0$  and the same

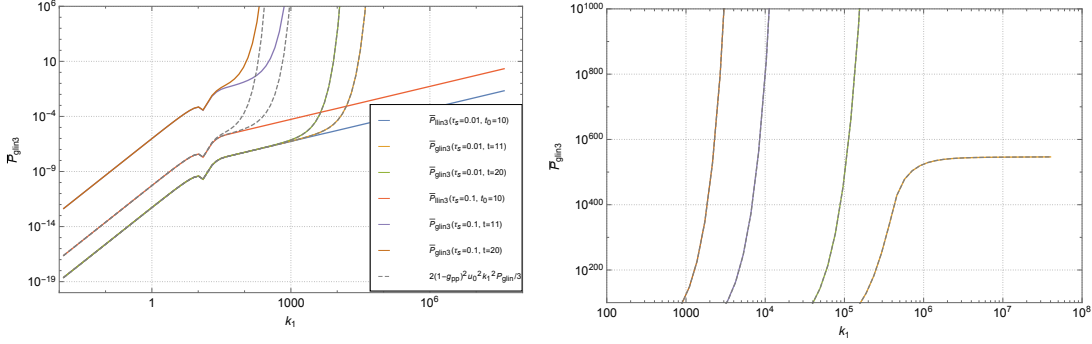


Figure 6.31: This plot shows the shape of the full linear momentum-density curl power spectra  $\bar{\mathcal{P}}_{\text{glin}3}(k_1, t)$  as functions of wave number  $k_1$  with parameters:  $\tau_s = 0.01$ ,  $t = 11.0$  (yellow line);  $\tau_s = 0.01$ ,  $t = 20.0$  (green line);  $\tau_s = 0.1$ ,  $t = 11.0$  (purple line);  $\tau_s = 0.1$ ,  $t = 20.0$  (brown line), together with their corresponding initial curl power spectrum  $\bar{\mathcal{P}}_{\text{lin}3}(k_1, t)$  in Equation 6.154 at initial time  $t_0 = 10.0$  (blue, red lines) at the same gravitational parameter  $f = 1.0$ . The gray dashed line marks the curve of  $\frac{2}{3}(1 - g_{\text{pp}}(t))^2 u_0^2 k_1^2 \mathcal{P}_{\text{glin}}(k_1, t)$ . The right panel plot shows the zoom plot of  $\bar{\mathcal{P}}_{\text{glin}3}(k_1, t)$  at higher values.

gravitational parameter  $f = 1.0$ . We can see that at small to middle scales, all three power spectra increase significantly compared to their initial gravity-free linear power spectra, even at a very early time of switching on the self-gravity among dust particles, and the power caused by the gravitational attraction grows much stronger as time proceeds. Moreover, the perfect match between the gray dashed curves and their corresponding  $\bar{\mathcal{P}}_{\text{glin}i}(k_1, t)$  with  $i = 1, 2, 3$  at small and middle scales in all three right-panel plots confirms our conclusions in Equation 6.199-6.201, and further implies that as the system going through gravitational collapse, the momentum energy in the system also grows exponentially, which agrees with our intuition and makes perfect sense.

### 6.5.2 Nonlinear Momentum-Density Power Spectra at Large $\tau_s$

Now we proceed to the three full nonlinear momentum-density power spectra with larger particle size  $\tau_s$  in Equation 6.185-6.187.

First, using the nonlinear expression of the mean interaction term  $i\langle S_I \rangle(k_1, t)$  at evolution time  $t$  with initial time  $t_0$  given in Equation 5.90, Figure 6.32 shows the shape of  $i\langle S_I \rangle(k_1, t)$  as a function of  $k_1$  at different particle sizes  $\tau_s = 1, 2, 3$  with different initial time  $t_0 = 2.0, 3.0$ , at the same evolution time  $t = 10.0$  and the same gravitational parameter  $f = 1.0$ . As explained in Section 5.4.3, at the limit of  $k_1 \rightarrow 0$ , the large scale asymptotics of  $i\langle S_I \rangle(k_1, t)$  develops a  $k_1^2$  slope. At the limit of  $k_1 \rightarrow \infty$ , the small scale asymptotics of  $i\langle S_I \rangle(k_1, t)$  reaches their asymptotic constants. In the meantime, since the value of  $i\langle S_I \rangle(k_1, t)$  gets larger with larger  $\tau_s$ , we can deduce that the three nonlinear momentum-density power spectra become larger with larger particle sizes.

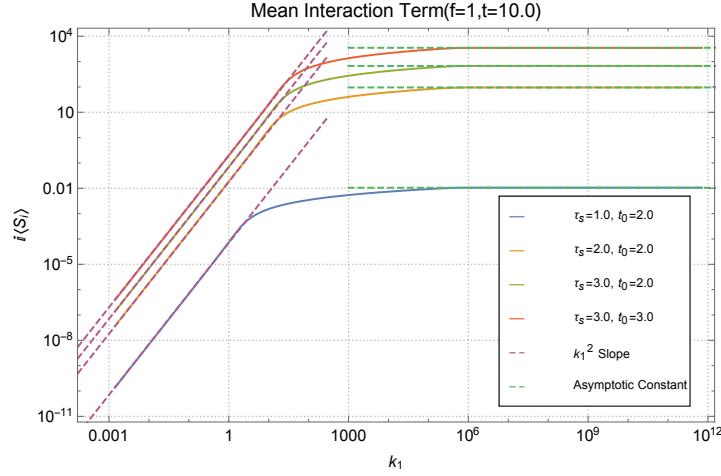


Figure 6.32: This plot shows the shape of  $i(S_1)(k_1, t)$  in Equation 5.90 as a function of  $k_1$  at different particle sizes  $\tau_s = 1$  (blue line),  $\tau_s = 2$  (yellow line),  $\tau_s = 3.0$  (green line) with different initial time  $t_0 = 2.0$  (blue, yellow, green lines),  $t = 3.0$  (red lines) at the same evolution time time  $t = 10.0$  and the same gravitational parameter  $f = 1.0$ . Their large scale  $k_1^2$  asymptotic slopes are marked by the burgundy dashed lines, and their small scale asymptotic constants are represented by the light green dashed lines.

Next, to calculate the numerical values of  $\vec{F} \cdot \vec{F}$  and  $\vec{k}_1 \cdot \vec{F}$ , we implement the approximated density power spectrum  $P_{\text{ini}}(k_1, t_0)$  given in Equation 5.81 to replace  $P(k, t')$  in Equation 6.188-6.189, thus their full expressions become

$$\begin{aligned}
 \vec{F} \cdot \vec{F} &= -\frac{f^2 \hat{G}_0^2}{\pi^2} \left[ \int_{t_0}^t dt' g_{pp}(t, t') \int_0^\infty dk_2 \left( 1 + \frac{k_2}{k_1} - \left| 1 - \frac{k_2}{k_1} \right| \right) k_2 P_{\text{ini}}(k_2, t_0) \right]^2 \\
 &= -\frac{c_0^2 g_{qp}^2(t, t_0) g_{qp}^4(t_0) f^2 \hat{G}_0^2}{\pi^2} \left[ \int_0^\infty dk_2 \left( 1 + \frac{k_2}{k_1} - \left| 1 - \frac{k_2}{k_1} \right| \right) k_2^{\frac{7}{3}} \cdot \right. \\
 &\quad \left. \left( 1 - \exp \left( -\frac{c_2}{k_2^{\frac{13}{3}}} \right) \right) \right]^2,
 \end{aligned} \tag{6.202}$$

$$\begin{aligned}
\vec{k}_1 \cdot \vec{F} &= \frac{if\hat{G}_0}{\pi} \int_{t_0}^t dt' g_{pp}(t, t') \int_0^\infty dk_2 k_2^2 P_{ini}(k_2, t_0) J\left(\frac{k_2}{k_1}\right) \\
&= \frac{ic_0 g_{qp}(t, t_0) g_{qp}^2(t_0) f\hat{G}_0}{\pi} \int_0^\infty dk_2 k_2^{\frac{10}{3}} \left(1 + \frac{k_1^2 - k_2^2}{2k_2 k_1} \ln \frac{k_2 + k_1}{|k_2 - k_1|}\right) \cdot \\
&\quad \left(1 - \exp\left(-\frac{c_2}{k_2^{\frac{13}{3}}}\right)\right). \quad (6.203)
\end{aligned}$$

At very small scales where  $k_1 \rightarrow \infty$ , the two expressions above are not convergent, thus here we continue to employ the cutoff scale  $k_m$  in Equation 5.87 as before, the asymptotic behaviors of  $\vec{F} \cdot \vec{F}$  and  $\vec{k}_1 \cdot \vec{F}$  at small scales are given as follow,

$$\begin{aligned}
\vec{F} \cdot \vec{F} &\approx -\frac{4c_0^2 g_{qp}^2(t, t_0) g_{qp}^4(t_0) f^2 \hat{G}_0^2}{\pi^2 k_1^2} \left[ \int_0^{k_m} dk_2 k_2^{\frac{10}{3}} \left(1 - \exp\left(-\frac{c_2}{k_2^{\frac{13}{3}}}\right)\right) \right]^2 \\
&= -\frac{4c_0^2 g_{qp}^2(t, t_0) g_{qp}^4(t_0) f^2 \hat{G}_0^2}{\pi^2 k_1^2} \left[ \frac{3k_m^{13/3}}{13} - \frac{3}{13} \left( e^{-\frac{c_2}{k_m^{13/3}}} k_m^{13/3} - c_2 \Gamma\left(0, \frac{c_2}{k_m^{13/3}}\right) \right) \right]^2 \\
&\approx -\frac{36c_0^2 c_2^2 g_{qp}^2(t, t_0) g_{qp}^4(t_0) f^2 \hat{G}_0^2}{169\pi^2 k_1^2} \left(1 - \gamma_e - \ln\left(\frac{c_2}{k_m^{13/3}}\right)\right)^2 = \frac{\alpha_{ff}}{k_1^2}, \quad (6.204)
\end{aligned}$$

$$\begin{aligned}
\vec{k}_1 \cdot \vec{F} &\approx \frac{2ic_0 g_{qp}(t, t_0) g_{qp}^2(t_0) f\hat{G}_0}{\pi} \int_0^{k_m} dk_2 k_2^{\frac{10}{3}} \left(1 - \exp\left(-\frac{c_2}{k_2^{\frac{13}{3}}}\right)\right) \\
&\approx \frac{6ic_0 g_{qp}(t, t_0) g_{qp}^2(t_0) f\hat{G}_0}{13\pi} \left(1 - \gamma_e - \ln\left(\frac{c_2}{k_m^{13/3}}\right)\right) = \alpha_{kf}. \quad (6.205)
\end{aligned}$$

At large scales where  $k_1 \rightarrow 0$ , we have their asymptotic behaviors as

$$\begin{aligned}
\vec{F} \cdot \vec{F} &\approx -\frac{4c_0^2 g_{qp}^2(t, t_0) g_{qp}^4(t_0) f^2 \hat{G}_0^2}{\pi^2} \left[ \int_0^{k_m} dk_2 k_2^{\frac{7}{3}} \left( 1 - \exp\left(-\frac{c_2}{k_2^{\frac{13}{3}}}\right) \right) \right]^2 \\
&= -\frac{4c_0^2 g_{qp}^2(t, t_0) g_{qp}^4(t_0) f^2 \hat{G}_0^2}{\pi^2} \left[ \frac{3k_m^{10/3}}{10} - \frac{3c_2^{10/13}}{13} \Gamma\left(-\frac{10}{13}, \frac{c_2}{k_m^{13/3}}\right) \right]^2 \quad (6.206) \\
&\approx -\frac{9c_0^2 c_2^{20/13} g_{qp}^2(t, t_0) g_{qp}^4(t_0) f^2 \hat{G}_0^2}{25\pi^2} \Gamma^2\left(\frac{3}{13}\right) = \beta_{ff},
\end{aligned}$$

$$\begin{aligned}
\vec{k}_1 \cdot \vec{F} &\approx \frac{2ic_0 g_{qp}(t, t_0) g_{qp}^2(t_0) f \hat{G}_0 k_1^2}{3\pi} \int_0^{k_m} dk_2 k_2^{\frac{4}{3}} \left( 1 - \exp\left(-\frac{c_2}{k_2^{\frac{13}{3}}}\right) \right) \\
&= \frac{2ic_0 g_{qp}(t, t_0) g_{qp}^2(t_0) f \hat{G}_0 k_1^2}{3\pi} \left[ \frac{3k_m^{7/3}}{7} - \frac{3c_2^{7/13}}{13} \Gamma\left(-\frac{7}{13}, \frac{c_2}{k_m^{13/3}}\right) \right] \quad (6.207) \\
&\approx \frac{2ic_0 c_2^{7/13} g_{qp}(t, t_0) g_{qp}^2(t_0) f \hat{G}_0 k_1^2}{7\pi} \Gamma\left(\frac{6}{13}\right) = \beta_{kf} k_1^2.
\end{aligned}$$

Here we've introduced the coefficients  $\beta_{ff}$ ,  $\alpha_{kf}$ ,  $\beta_{ff}$  and  $\beta_{kf}$  to help abbreviate the above expressions.

Figure 6.33 shows the shape of  $\vec{F} \cdot \vec{F}$  and  $\vec{k}_1 \cdot \vec{F}$  in Equation 6.202 and Equation 6.203 as functions of wavenumber  $k_1$  at the evolution time  $t = 10.0$  and gravitational parameter  $f = 1.0$  with different particle size  $\tau_s = 1, 2, 3$  and different initial time  $t_0 = 2.0, 3.0$ . We can see the curves of  $\vec{F} \cdot \vec{F}$  reach their asymptotic constants at very large scales as shown in Equation 6.206, and develop the  $k_1^{-2}$  slopes at very small scales as shown in Equation 6.204. While the curves of  $\vec{k}_1 \cdot \vec{F}$  develop the large scale  $k_1^2$  asymptotic behaviors at the limit of  $k_1 \rightarrow 0$  and reach their small scale asymptotic constant at the limit of  $k_1 \rightarrow \infty$ , which also agrees with our predictions in Equation 6.207 and Equation 6.205.

In the meantime, the comparison between different curves shows that the values of  $\vec{F} \cdot \vec{F}$  and  $\vec{k}_1 \cdot \vec{F}$  get larger with larger  $\tau_s$ , meaning that the self-gravitational interaction becomes stronger with larger size particles present in the system. On the other hand, notice when we switch on the self-gravity between particles at the relatively earlier stage of friction evolution time where  $t_0 \sim \tau_s$ , relatively large  $t_0$  which corresponds to relatively weaker friction interaction in the system will lead to a stronger self-gravitational interaction even with short relative evolution time  $t - t_0$ , which can also be seen in the mean interaction plot in Figure 6.32.

In the end, we analyze the terms in Equation 6.185 and Equation 6.186 with the momentum-density power spectra element  $T_5 + T_7$ . Since the behaviors of  $T_5$  are analyzed before, see Section 6.4.2.2, here we focus on the other element  $T_7$  defined in Equation 6.34. At very small scales where  $k_1 \rightarrow \infty$ , the asymptotic behavior of  $T_7$  is

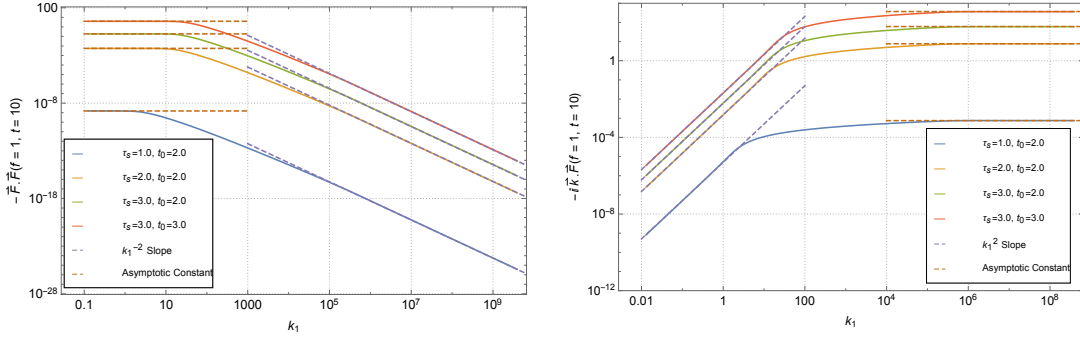


Figure 6.33: This plot shows the shape of  $\vec{F} \cdot \vec{F}$  (left panel) and  $\vec{k}_1 \cdot \vec{F}$  (right panel) in Equation 6.202 and Equation 6.203 as functions of wavenumber  $k_1$  at the evolution time  $t = 10.0$  and gravitational parameter  $f = 1.0$  with different parameters:  $\tau_s = 1.0$ ,  $t_0 = 2.0$  (blue lines);  $\tau_s = 2.0$ ,  $t_0 = 2.0$  (yellow lines);  $\tau_s = 3.0$ ,  $t_0 = 2.0$  (green lines);  $\tau_s = 3.0$ ,  $t_0 = 3.0$  (red lines). Their  $k_1^{-2}$  and  $k_1^2$  asymptotic slopes are marked by the purple dashed lines, and their asymptotic constants are marked by brown dashed lines.

derived in Section 6.2 and given in Equation 6.108. While at very large scales where  $k_1 \rightarrow 0$ , we can Taylor expand the exponential in  $T_7$  to its first order and substitute  $r \rightarrow r_1/k_1$  to obtain

$$T_7 = -\frac{2\pi g_{qp}^2(t)\zeta_{pp}(0)}{k_1} \int_0^\infty dr_1 r_1^2 \zeta_{pp} \left( \frac{r_1}{k_1} \right) \int_{-1}^1 d\mu \left( (1 - 3\mu^2)b_1 - b_0 \right)^2 \cos r_1 \mu \approx c_7 k_1^{\frac{4}{3}} \quad (6.208)$$

with the coefficient

$$c_7 = 0.08\pi g_{qp}^2(t)\zeta_{pp}(0) \frac{4}{117} (91b_0^2 - 104b_0b_1 + 76b_1^2) \Gamma\left(-\frac{7}{3}\right) = -2.52 \times 10^{-9} g_{qp}^2(t). \quad (6.209)$$

The left panel of Figure 6.34 shows the momentum-density power spectra element  $T_7$  as a function of wave number  $k_1$  at different particle size  $\tau_s = 1, 2, 3$  and different evolution time  $t = 2.0, 3.0$ . We can see their larger and small-scale asymptotic behaviors match our predictions in Equation 6.208 and Equation 6.108 very well. Furthermore, since at small scales the relation  $T_5 + T_7 = 0$  is satisfied by Equation 6.106, and at large scales, the coefficient  $c_5$  in Equation 6.126 is far larger than  $c_7$  in Equation 6.209, we can deduce the asymptotic behaviors of  $T_5 + T_7$  satisfy

$$T_5 + T_7 \sim \frac{c_5}{k_1^{\frac{5}{2}}}, \quad \text{for } k_1 \rightarrow 0, \quad \text{and} \quad T_5 + T_7 \sim 0, \quad \text{for } k_1 \rightarrow \infty. \quad (6.210)$$

These behaviors are illustrated in the right panel of [Figure 6.34](#). In this plot, the curves of elements  $T_5$  and  $T_7$  are given at the same time with the particle size being  $\tau_s = 2.0$  and evolution time being  $t = 2.0$ . We can see at small scales their asymptotic behaviors cancel each other very well which proves the relation  $T_5 + T_7$  is satisfied, and at large scales, the values of  $T_5$  are far larger than  $T_7$ , which verifies the large scales asymptotic of  $T_5 + T_7$  given in [Equation 6.210](#).

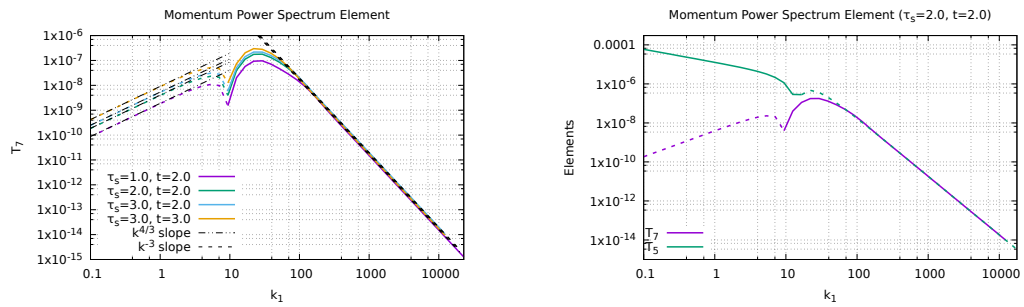


Figure 6.34: *Left panel*: This plot shows the momentum-density power spectra element  $T_7$  as a function of wave number  $k_1$  at parameters:  $\tau_s = 1.0, t = 2.0$  (purple line);  $\tau_s = 2.0, t = 2.0$  (green line);  $\tau_s = 3.0, t = 2.0$  (blue line);  $\tau_s = 3.0, t = 3.0$  (yellow line). The negative values of  $T_7$  at different  $\tau_s$  and  $t$  are represented by the same color dashed lines. Their large scale  $k_1^{\frac{4}{3}}$  asymptotic behaviors are represented by the black dash-dotted lines, and their small scale  $k_1^{-3}$  asymptotic behaviors are represented by the black dashed lines. *Right panel*: This plot shows the shape of momentum-density elements  $T_5$  (green line) and  $T_7$  (purple line) at the same time as functions of  $k_1$  with parameters  $\tau_s = 2.0$  and  $t = 2.0$ . Their negative values are represented by the same color dashed lines.

Now we return to the full expression of the three scalar momentum-density power spectra, at very small scales where  $k_1 \rightarrow \infty$ , using the [Equation 6.161](#), [6.169](#), [6.176](#), [5.67](#), [6.204](#) and [6.205](#), preserving only the higher order of  $k_1$  dependence, we have the asymptotic behaviors as

$$\begin{aligned}\bar{\mathcal{P}}_{\text{gr}}(\mathbf{k}_1, t) &\approx e^{i\langle S_I \rangle} \left( \bar{\mathcal{P}}_{\text{ftr}}(\mathbf{k}_1, t) - \vec{\mathbf{F}}_1 \cdot \vec{\mathbf{F}}_1 \mathcal{P}_f(\mathbf{k}_1, t) \right) \\ &= e^{i\langle S_I \rangle} \left( \frac{\mathcal{P}_f^{\text{tot}}(t)}{k_1^3} - \frac{\alpha_{ff}}{k_1^2} \cdot \frac{\mathcal{P}_f^{(0)}}{k_1^3} \right) \approx e^{i\langle S_I \rangle} \bar{\mathcal{P}}_{\text{ftr}}(\mathbf{k}_1, t),\end{aligned}\quad (6.211)$$

$$\begin{aligned}\bar{\mathcal{P}}_{\text{gdiv}}(\mathbf{k}_1, t) &\approx e^{i\langle S_I \rangle} \left( \bar{\mathcal{P}}_{\text{fdiv}}(\mathbf{k}_1, t) - \left( \vec{\mathbf{k}}_1 \cdot \vec{\mathbf{F}} \right)^2 \mathcal{P}_f(\mathbf{k}_1, t) \right) \\ &= e^{i\langle S_I \rangle} \left( \frac{\mathcal{P}_f^{\text{tot}}(t)}{k_1} - \alpha_{kf}^2 \cdot \frac{\mathcal{P}_f^{(0)}}{k_1^3} \right) \approx e^{i\langle S_I \rangle} \bar{\mathcal{P}}_{\text{fdiv}}(\mathbf{k}_1, t),\end{aligned}\quad (6.212)$$

$$\begin{aligned}\bar{\mathcal{P}}_{\text{gcurl}}(\mathbf{k}_1, t) &\approx e^{i\langle S_I \rangle} \left( \bar{\mathcal{P}}_{\text{fcurl}}(\mathbf{k}_1, t) + \left( \left( \vec{\mathbf{k}}_1 \cdot \vec{\mathbf{F}} \right)^2 - k_1^2 \left( \vec{\mathbf{F}} \cdot \vec{\mathbf{F}} \right) \right) \mathcal{P}_f(\mathbf{k}_1, t) \right) \\ &= e^{i\langle S_I \rangle} \left( \frac{\mathcal{P}_f^{\text{tot}}(t)}{k_1} + \left( \alpha_{ff} - \alpha_{kf}^2 \right) \cdot \frac{\mathcal{P}_f^{(0)}}{k_1^3} \right) \approx e^{i\langle S_I \rangle} \bar{\mathcal{P}}_{\text{fcurl}}(\mathbf{k}_1, t),\end{aligned}\quad (6.213)$$

suggesting that the small-scale asymptotic behaviors of the full nonlinear momentum-density power spectra are simply given by  $\bar{\mathcal{P}}_{g*}(\mathbf{k}_1, t) \sim \exp(i\langle S_I \rangle) \cdot \bar{\mathcal{P}}_{f*}(\mathbf{k}_1, t)$  with  $*$  = tr, div, curl, which completely determined by the mean gravitational interaction and their corresponding gravity-free nonlinear momentum-density power spectra  $\bar{\mathcal{P}}_{f*}(\mathbf{k}_1, t)$  calculated in [Section 6.4.2](#). Furthermore, since the mean interaction term  $i\langle S_I \rangle$  reaches a constant at very small scales, the asymptotic behaviors of  $\bar{\mathcal{P}}_{g*}(\mathbf{k}_1, t)$  can finally be represented as

$$\bar{\mathcal{P}}_{\text{gr}}(\mathbf{k}_1, t) \sim \text{constant} \cdot \frac{\mathcal{P}_f^{\text{tot}}(t)}{k_1^3}, \quad \text{for } k_1 \rightarrow \infty, \quad (6.214)$$

$$\bar{\mathcal{P}}_{\text{gdiv}}(\mathbf{k}_1, t) \sim \text{constant} \cdot \frac{\mathcal{P}_f^{\text{tot}}(t)}{k_1}, \quad \text{for } k_1 \rightarrow \infty, \quad (6.215)$$

$$\bar{\mathcal{P}}_{\text{gcurl}}(\mathbf{k}_1, t) \sim \text{constant} \cdot \frac{\mathcal{P}_f^{\text{tot}}(t)}{k_1}, \quad \text{for } k_1 \rightarrow \infty, \quad (6.216)$$

indicating that even with the self-gravitational interaction present in the system, the total kinetic energy accumulation of dust particles still remains scale-invariant at very small scales, the same conclusion also suits for the power spectra of the momentum-density operators in  $\hat{\mathbf{k}}_1$  and perpendicular to  $\hat{\mathbf{k}}_1$  space.

[Figure 6.35-6.37](#) show the shape of  $\bar{\mathcal{P}}_{\text{gr}}(\mathbf{k}_1, t)$ ,  $\bar{\mathcal{P}}_{\text{gdiv}}(\mathbf{k}_1, t)$ ,  $\bar{\mathcal{P}}_{\text{gcurl}}(\mathbf{k}_1, t)$  as functions of wavenumber  $k_1$  with particle sizes  $\tau_s = 1$ ,  $\tau_s = 2$ ,  $\tau_s = 3$  at different initial time  $t_0 = 2.0$ ,  $t_0 = 3.0$  with the same evolution time  $t = 10.0$  and the same gravitational parameter  $f = 1.0$ . We can see that except for the plots corresponding to particle size  $\tau_s = 1.0$  which has very small mean interaction values, at small to middle scales, all

three nonlinear momentum-density power spectra with  $\tau_s = 2.0$ ,  $\tau_s = 3.0$  increase significantly compared to their initial gravity-free nonlinear power spectra. Moreover, the rather similar shapes and values of the gray dashed curves and their corresponding  $\bar{\mathcal{P}}_{g*}(k_1, t)$  with  $* = \text{tr}, \text{div}, \text{curl}$  at small and middle scales in all plots confirms our conclusions in Equation 6.211-6.213, and further implies that as the system going through gravitational collapse, the accumulation of the momentum energy in the system is also immense.

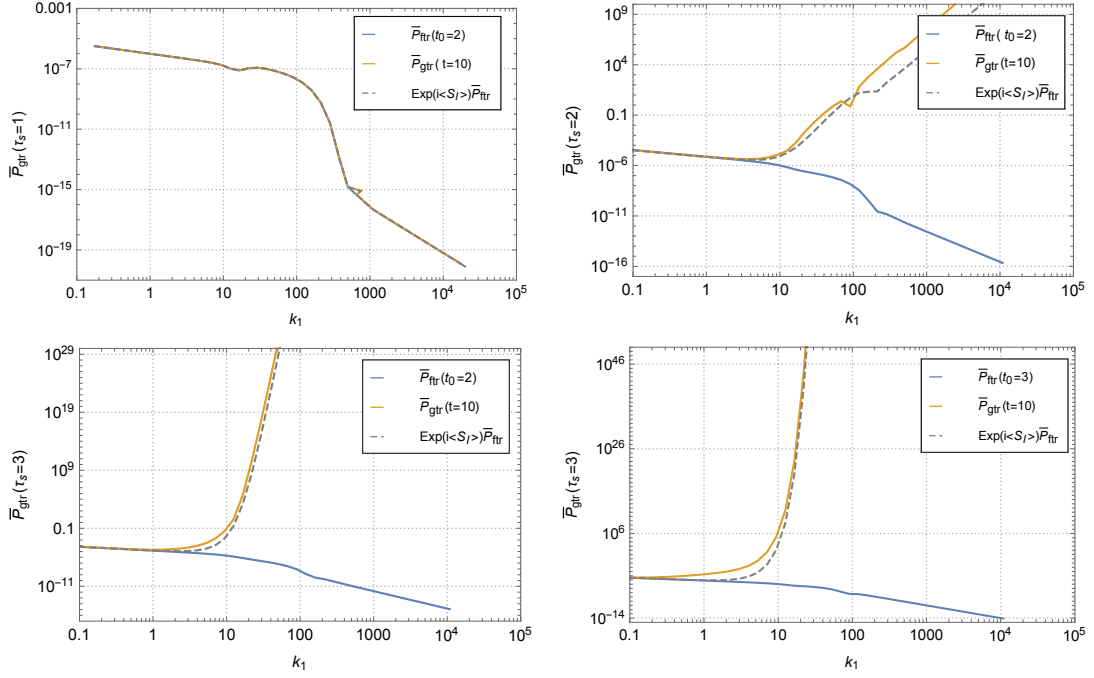


Figure 6.35: These four plots show the full nonlinear momentum-density trace power spectra  $\bar{\mathcal{P}}_{\text{gr}}(k_1, t)$  as functions of wave number  $k_1$  at evolution time  $t = 10.0$  (yellow lines) with parameters  $\tau_s = 1.0, t_0 = 2.0$ ;  $\tau_s = 2.0, t_0 = 2.0$ ;  $\tau_s = 3.0, t_0 = 2.0$ ;  $\tau_s = 3.0, t_0 = 3.0$  with the same gravitational parameter  $f = 1.0$ . Their corresponding initial trace power spectrum  $\bar{\mathcal{P}}_{\text{tr}}(k_1, t)$  in Equation 6.144 at initial times  $t_0$  are marked by blue lines. The gray dashed lines mark the curve of  $\exp(i\langle S_I \rangle) \cdot \bar{\mathcal{P}}_{\text{tr}}(k_1, t)$ .

## 6.6 SUMMARY AND DISCUSSION

In this Chapter, building on the simplified dust trajectories of Chapter 3 and their initial probability distribution function in phase space (iPDF) in Chapter 4, we apply the KFT method to planetary formation and give a full review of the three momentum-density power spectra of the dust particles. This chapter started with modifying the momentum factorized generating functional  $Z^m[\mathbf{L}]$ , by generalizing the mean-field

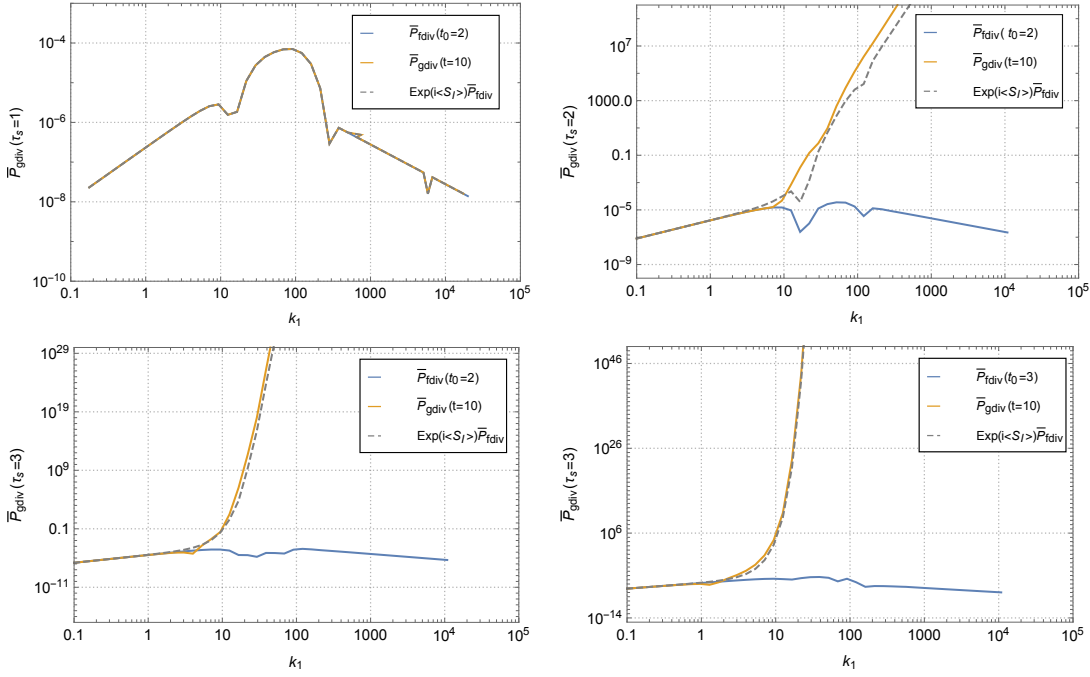


Figure 6.36: These four plots show the full nonlinear momentum-density divergence power spectra  $\bar{\mathcal{P}}_{\text{gdiv}}(k_1, t)$  as functions of wave number  $k_1$  at evolution time  $t = 10.0$  (yellow lines) with parameters  $\tau_s = 1.0, t_0 = 2.0$ ;  $\tau_s = 2.0, t_0 = 2.0$ ;  $\tau_s = 3.0, t_0 = 2.0$ ;  $\tau_s = 3.0, t_0 = 3.0$  with the same gravitational parameter  $f = 1.0$ . Their corresponding initial trace power spectra  $\bar{\mathcal{P}}_{\text{fdiv}}(k_1, t)$  in Equation 6.145 at initial times  $t_0$  are marked by blue lines. The gray dashed lines mark the curve of  $\exp(i\langle S_I \rangle) \cdot \bar{\mathcal{P}}_{\text{fdiv}}(k_1, t)$ .

approach and averaging the self-gravitational forces  $\vec{f}_j(t)$  over the phase space coordinates, we pulled the momentum-density operators in front of the integral and expressed the factorized generating functional as in Equation 6.1. Then the three relative scalar quantities were defined in Equation 6.2-6.4 for computing trace of the momentum-density power spectrum as well as the power spectra for the divergence and the curl of the momentum density.

In the first section, we reviewed the derivation of the three full nonlinear momentum-density power spectra for dust particles considering both the friction with the constant background gas field and their self-gravitational interaction with each other. By analyzing the matrix components of the new "free" generating functional  $\bar{Z}_{12}[\mathbf{L}]$  in Equation 6.6 and combing it with the mean interaction term  $e^{i\langle S_I \rangle}$ , we calculated the three scalar quantities defined in Equation 6.2-6.4. Furthermore, we defined and analyzed the momentum-density power spectra elements  $T_i$  with  $i = 1, \dots, 8$  to obtain the final convergent momentum-density trace, divergence and curl power spectra in Equation 6.46, Equation 6.48 and Equation 6.51.

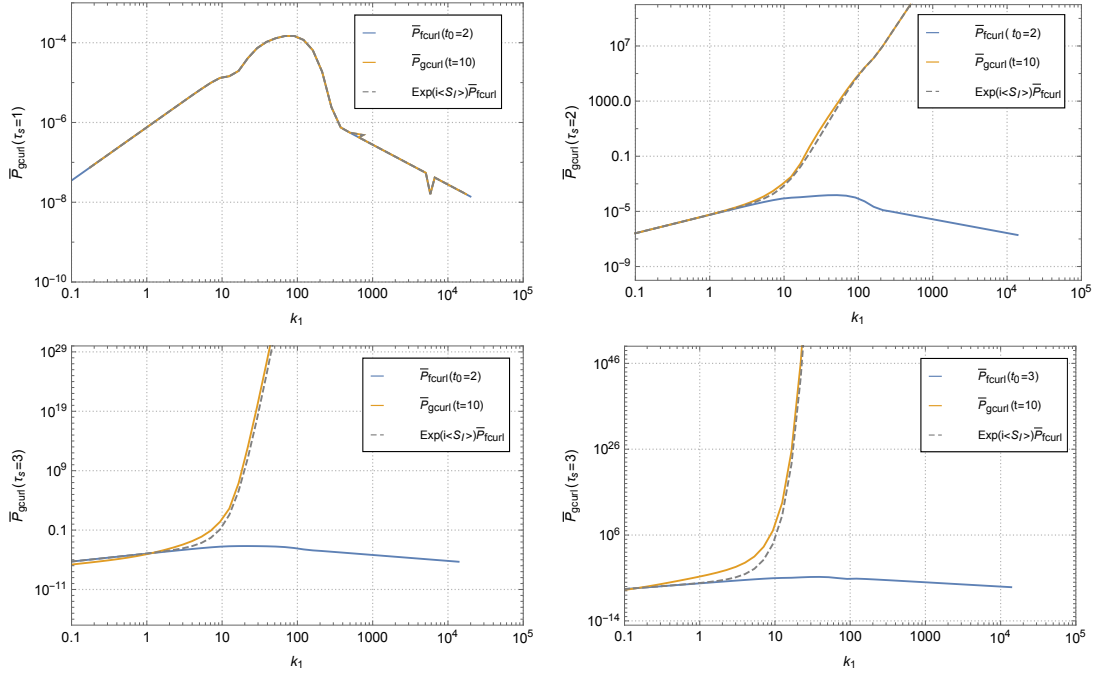


Figure 6.37: These four plots show the full nonlinear momentum-density curl power spectra  $\bar{\mathcal{P}}_{\text{gcurl}}(k_1, t)$  as functions of wave number  $k_1$  at evolution time  $t = 10.0$  (yellow lines) with parameters  $\tau_s = 1.0, t_0 = 2.0$ ;  $\tau_s = 2.0, t_0 = 2.0$ ;  $\tau_s = 3.0, t_0 = 2.0$ ;  $\tau_s = 3.0, t_0 = 3.0$  with the same gravitational parameter  $f = 1.0$ . Their corresponding initial trace power spectrum  $\bar{\mathcal{P}}_{\text{fcurl}}(k_1, t)$  in Equation 6.146 at initial times  $t_0$  are marked by blue lines. The gray dashed lines mark the curve of  $\exp(i\langle S_I \rangle) \cdot \bar{\mathcal{P}}_{\text{fcurl}}(k_1, t)$ .

In the second section, due to the complicated  $\mu$ -dependence in the integrals of the momentum-density power spectra and their elements  $T_i$ , to analyze their small-scale asymptotic behavior, we reviewed a new method for the asymptotic analysis of a specific Laplace-Fourier type integral in three dimensions in Equation 6.60, based on a modification of Erdelyi's theorem for one-dimensional Laplace integrals. By applying Erdelyi's theorem to the  $r$ -integral of Equation 6.60, we computed its  $\mu$ -dependent small-scale asymptotic series in Equation 6.75. Next, we proceeded with the first term of the series which has the highest order in  $k_1$ , and gave the final expressions for the three different  $\mu$ -integrals involved in Equation 6.60. In the end, we compared the momentum-density power spectra elements with integral Equation 6.60 and obtained their small-scale asymptotic behavior in Equation 6.103-6.108.

In the third section, we ignored the friction ( $\tau_s \rightarrow \infty$ ) and self-gravitational interaction in the system and reviewed the linear and nonlinear free KFT momentum-density power spectra for dust particles. First, we derived the expressions of the three linear free momentum-density power spectra  $\bar{\mathcal{P}}_{\text{lin1}}^{\text{free}}(k_1, t)$ ,  $\bar{\mathcal{P}}_{\text{lin2}}^{\text{free}}(k_1, t)$ ,  $\bar{\mathcal{P}}_{\text{lin3}}^{\text{free}}(k_1, t)$  for the freely

streaming particles at a very early evolution time ( $t \rightarrow 0$ ) by Taylor approximating the corresponding momentum-density power spectra elements  $T_{i0}$  with  $i = 1, 2, 3, 5, 6$  to first order. Further asymptotic analysis of their large and small scale behavior suggested that all results on the asymptotic behavior of the three linear free momentum-density power spectra are conserved and satisfy the relation  $k_1^2 \bar{\mathcal{P}}_{\text{lin}1}^{\text{free}}(k_1) = \bar{\mathcal{P}}_{\text{lin}2}^{\text{free}}(k_1) + \bar{\mathcal{P}}_{\text{lin}3}^{\text{free}}(k_1)$  at very small scales. Then we applied the new analytical asymptotic method introduced in the second section to analyze the nonlinear free momentum-density power spectra  $\bar{\mathcal{P}}_{\text{tr}}^{\text{free}}(k_1, t)$ ,  $\bar{\mathcal{P}}_{\text{div}}^{\text{free}}(k_1, t)$ ,  $\bar{\mathcal{P}}_{\text{curl}}^{\text{free}}(k_1, t)$ , and showed that the nonlinear structure in the system changed the small scale asymptotic behavior of the momentum-density trace power spectrum to a  $k^{-3}$  tail, which indicated a scale-invariant kinetic energy accumulation below a characteristic length scale for freely streaming particles. Furthermore, we concluded that the nonlinear free power spectra of the divergence and the curl of the momentum density both developed  $k_1^{-1}$  small-scale asymptotic behavior, which also implies scale-invariant momentum-density power accumulation in  $\vec{k}_1$  and perpendicular to  $\vec{k}_1$  space at very small scales. These are mathematically rigorous conclusions that depend only on the number of spatial dimensions and general properties of the initial correlation functions. In the end, we analyzed the relation of the three free nonlinear momentum-density power spectra and confirmed the relation  $k_1^2 \bar{\mathcal{P}}_{\text{tr}}^{\text{free}}(k_1, t) = \bar{\mathcal{P}}_{\text{div}}^{\text{free}}(k_1, t) + \bar{\mathcal{P}}_{\text{curl}}^{\text{free}}(k_1, t)$  at all scales considered in the system.

In the fourth section, we still ignored the self-gravitational interaction among dust particles and reviewed the linear and nonlinear **KFT** momentum-density power spectra for dust particles undergoing friction with the constant background gas field. First, we derived the three linear momentum-density power spectrum  $\bar{\mathcal{P}}_{\text{lin}1}(k_1, t)$ ,  $\bar{\mathcal{P}}_{\text{lin}2}(k_1, t)$ ,  $\bar{\mathcal{P}}_{\text{lin}3}(k_1, t)$  for very small dust particles  $\tau_s \rightarrow 0$  and concluded that they are completely determined by the corresponding linear gravity-free density power spectrum  $\mathcal{P}_{\text{flin}}(k_1, t)$  in Equation 5.62. The resulting  $k_1^1$  small-scale asymptotic behavior of  $\bar{\mathcal{P}}_{\text{lin}2}(k_1, t)$ ,  $\bar{\mathcal{P}}_{\text{lin}3}(k_1, t)$  with only averaged friction did not make any sense and provided more evidence for the necessity of a nonlinear density power spectrum. Next, we computed the three nonlinear momentum-density power spectra  $\bar{\mathcal{P}}_{\text{fr}}(k_1, t)$ ,  $\bar{\mathcal{P}}_{\text{div}}(k_1, t)$ ,  $\bar{\mathcal{P}}_{\text{curl}}(k_1, t)$  for larger dust particles at finite evolution time individually and found the same  $k^{-3}$  small-scale nonlinear asymptotic behavior for the trace power spectrum and  $k_1^{-1}$  small-scale nonlinear asymptotic behavior for the divergence and curl power spectrum, which implies the same scale-invariant total kinetic energy accumulation, and momentum-density power accumulation parallel and perpendicular to  $\vec{k}_1$  at very small scales. Moreover, we analyzed the dependence of the small-scale asymptotic tail of the trace of the momentum-density power spectrum  $\bar{\mathcal{P}}_{\text{fr}}(k_1, t)$  on particle size and time within the range of particle size we care for. Mathematically rigorously, we found a critical particle size  $\tau_s \approx 3.03$ , at which the system shows both the maximal small-scale kinetic energy accumulation and the strongest small scale structure formation. At the end of this section, we also analyzed the relation of the three nonlinear momentum-

density power spectra and verified the relation  $k_1^2 \bar{\mathcal{P}}_{\text{ftr}}(k_1, t) = \bar{\mathcal{P}}_{\text{fdiv}}(k_1, t) + \bar{\mathcal{P}}_{\text{fcurl}}(k_1, t)$  for all scales in the system.

In the end, we switched on self-gravity among dust particles at evolution time  $t_0$  and considered both friction and gravitational interactions in the system to calculate the full linear and nonlinear KFT momentum-density power spectra. We start with deriving the expressions of the three full linear momentum-density power spectra  $\bar{\mathcal{P}}_{\text{glin1}}(k_1, t)$ ,  $\bar{\mathcal{P}}_{\text{glin2}}(k_1, t)$ ,  $\bar{\mathcal{P}}_{\text{glin3}}(k_1, t)$  for very small dust particles where  $\tau_s \rightarrow 0$ . By implementing the approximated density power spectrum  $\mathcal{P}_{\text{inis}}(k_1, t_0)$  in Equation 5.77 and borrowing the cutoff scale  $k_m$  from Equation 5.87. The analysis of their small-scale asymptotic behavior at the limit of  $k_1 \rightarrow \infty$  shows that the force terms  $\vec{F}_1 \cdot \vec{F}_1$  and  $\vec{k}_1 \cdot \vec{F}_1$  are negligible and these power spectra are completely determined by their corresponding full linear density power spectrum  $\mathcal{P}_{\text{glin}}(k_1, t)$  in Section 5.4.2 at small scales. Then we return to the three full nonlinear momentum-density power spectra  $\bar{\mathcal{P}}_{\text{gtr}}(k_1, t)$ ,  $\bar{\mathcal{P}}_{\text{gdiv}}(k_1, t)$ ,  $\bar{\mathcal{P}}_{\text{gcurl}}(k_1, t)$  for larger particles, by implementing the corresponding approximated density power spectrum  $\mathcal{P}_{\text{ini}}(k_1, t_0)$  in Equation 5.81 and still applying the cutoff scale  $k_m$ , the calculations of their small-scale asymptotic approximations at  $k_1 \rightarrow \infty$  shows that the force terms  $\vec{F}_1 \cdot \vec{F}_1$  and  $\vec{k}_1 \cdot \vec{F}_1$  remain negligible. Combining with the small-scale asymptotic relation  $T_5 + T_7 = 0$  shown in Equation 6.106 and Equation 6.108, we concluded that the three nonlinear momentum-density power spectra only depend on the mean interaction term and three gravity-free nonlinear momentum-density power spectra in Section 6.4.2 at very small scales. In particular, since the mean interaction term  $i\langle S_I \rangle$  for large particles reaches its asymptotic constant at very small scales, the  $k_1^{-3}$  asymptotic behavior for the trace power spectrum and the  $k_1^{-1}$  asymptotic slope for the divergence and curl power spectra are preserved, which further suggests that even with self-gravitational interaction considered in the system, the total kinetic energy accumulation, and the momentum-density power accumulation in parallel and perpendicular to  $\vec{k}_1$  remain scale invariant at very small scales. Notice that as discussed in Chapter 5, the preserved small-scale asymptotics of the momentum-density power spectra is completely determined by the asymptotic constants of the mean interaction term  $i\langle S_I \rangle$  which results from choosing a constant cutoff scale  $k_m$ . Nevertheless, these results still provide a lower limit for the momentum-density power accumulation in the system. Furthermore, the significant power increase at small to intermediate scales for both linear and nonlinear momentum-density power spectra with self-gravitational interaction in the system implies that as the system undergoes gravitational collapse, the accumulation of the momentum-density power in the system is also enormous.

## CONCLUSIONS AND DISCUSSIONS

---

In this work, we made the first attempt to apply kinetic field theory ([KFT](#)) to planetesimal formation and analytically investigated the formation of structures by collisionless dust particles with correlated positions and momenta in protoplanetary disks ([PPDs](#)) at the limit of large and especially small scales.

As a statistical, kinetic theory for classical particle ensembles in or out of equilibrium, [KFT](#) encodes the dynamics of a classical particle ensemble in a generating functional  $Z$  which is completely specified by the initial probability distribution of particles in phase space and their equation of motion. Therefore, our first main result is to obtain a suitable equation of motion for dust particles in a general [PPD](#) by considering their friction with a constant background gas field and the self-gravitational interaction among themselves. The friction caused by different azimuthal velocities of gas and dust due to the distinguishing internal pressure of gas initiates the planetesimal formation through the streaming instability ([SI](#)) between the two systems. For very small particles well-coupled to the gas field, we neglect the feedback of the dust onto the gas and assume the lower azimuthal velocity of the gas is locally stable. Therefore we limit ourselves to a prescribed constant background gas velocity field. Furthermore, the gravitational instability of a [PPD](#) by surpassing the local Hill density provides another important mechanism for planetesimal formation.

For future work, it is well possible to go beyond the scope of this thesis and study more complicated interactions between dust particles. [KFT](#) could still be a rather useful tool once the additional functional determinant of the equation of motion introduced to the generating functional is properly solved. And this question itself would be of great interest to the development of [KFT](#) since the solution could vastly expand its applications into more areas.

Our next important result derived by applying [KFT](#) to planetesimal formation is the development of a new scheme to obtain the initial probability distribution function in phase space ([iPDF](#)) for dust particles from a 3-dimensional [SI](#) local shearing sheet simulation in a general [PPD](#). By Gaussianizing the density field, we derive the final expression of the [iPDF](#) using a multivariate Gaussian distribution. Furthermore, a pipeline is developed to extract the covariance matrices of the dust ensemble embedded in its expression, and the correlation operator of the [iPDF](#) is accordingly simplified to a constant due to the significantly larger values of the density covariance matrix compared to the momentum-density cross-covariance matrix. With this approximation, the expression of the [iPDF](#) reduced to a multivariate Gaussian distribution describing solely the initial momenta of the dust particles. We can interpret this outcome both conceptually and

observationally. From a theoretical point of view, Gaussian random fields are ubiquitous and they are a natural consequence of many processes due to the central limit theorem. In cosmology, the vast cosmic webs consisting of cosmic sheets and filaments provide evidence of the structure formation originating from a Gaussian random field. [Figure 7.1](#) shows a recent capture of the spiral galaxy IC 5332, where the visible filamentary structures verify the wide-spread existence of Gaussian random fields in the universe. Therefore, we are convinced that this work based on Gaussianized density and momenta fields is fairly valid.



Figure 7.1: The spiral galaxy IC 5332, as captured by the James Webb Space Telescope's Mid-Infrared Instrument.

Although in this thesis the simulation data suggests only Gaussianizing the density field, for other types of simulation data that show non-Gaussian momentum distributions, we can still employ the same method and Gaussianize them in a similar manner as long as the new Gaussianized fields relate with the original ones by monotonic functions. And even better, since there will only be additional integrations over delta distributions, the final expression of the [iPDF](#) stays in the very same form. Furthermore, we isotropize the momentum covariance matrix and provide a simple mathematical so-

lution for rotating it into the position and wave vector space, which serves quite an essential purpose for computing the final **KFT** power spectra.

Applying **KFT** to planetesimal formation, we extract important structure and kinetic information of a general **PPD** with the initial setup modeled according to the simulation by analyzing the 2-point **KFT** density and momentum-density power spectra for dust particles. One of our main results rests on applying two novel asymptotic methods developed by Konrad [25] to prove, in two different scenarios, the inevitable development of a universal  $k^{-3}$  small-scale asymptotic behavior for the nonlinear power spectrum of the density and the trace of the nonlinear momentum-density power spectrum, suggesting scale-invariant structure formation and kinetic energy accumulation below a characteristic and time-dependent length scale in a **PPD** filled with either free dust particles or dust particles experiencing friction with a background gas of constant density and velocity. These are significant and mathematically rigorous conclusions that depend only on the number of spatial dimensions and the form of the initial correlation functions.

We also calculate the time-dependent characteristic wave number above which the density power spectrum converges to the  $k^{-3}$  slope for freely streaming particles. Its decreasing slope in the right panel of [Figure 5.5](#) shows that structure formation rapidly proceeds towards small scales first and then slows down, which suggests that the  $k^{-3}$  tails are typically way below the resolution limit of numerical simulations at early evolution times.

Furthermore, the analysis of the amplitude for the small-scale  $k^{-3}$  tails show a critical particle size of  $\tau_s \approx 3.03$  which corresponds to the strongest structure formation and the maximal kinetic energy accumulation at small scales of a system when considering only the friction between dust particles and the constant background gas. Adding the self-gravitational interaction to such a system, the stronger attractive interaction would help trap larger size particles at small scales which pushes this critical particle size to larger values.

Moreover, using the mean-field approach developed in the **KFT** framework, we find that the averaged self-gravitational interaction term reaches an asymptotic constant at very small scales, which leads to the same  $k^{-3}$  asymptotic tail for the power spectrum of the density and the trace of the nonlinear momentum-density power spectrum considering both friction and self-gravitational interactions in the system. However, this result sensitively depends on the chosen form of the cutoff scale  $k_m$  and the approximations made for the density power spectrum at any evolution time  $P(k, t')$  in the mean interaction term. Nevertheless, the results given in this work still provide a lower limit for gravitational aggregation and suggest that the total structure formation and kinetic energy accumulation caused by the self-gravitational interaction will always be scale-invariant or increasing at smaller scales. For further work, it is worth exploring different and improved schemes for calculating the interaction terms within **KFT**, which also lies right in the center of the development of the theory itself.

In the end, we discuss the “meter-size barrier” problem. By calculating the averaged dust density growth in the system and setting the collapse criteria to  $\delta^2 = 10^{14}$ , we find the relation  $\tau_s^3(t - t_0)f = 2.60 \times 10^{-8}$  to determine the collapse moment in a PPD with the initial setup modeled according to the simulation. Furthermore, by setting the dust density to the critical Hill density ( $f = 1$ ) and the evolution time as the averaged lifetime of a PPD ( $t = 10^6$ ), we obtain the minimum particle size  $\tau_s^g = 2.96 \times 10^{-5}$  to ensure a final gravitational collapse in the system, which greatly lowers the limit  $10^{-3}$  set by simulations and becomes much closer to the lower end of the “meter-size barrier”. In Windmark, F. et al. [42], the likelihood for a few lucky winner particles to reach planetesimal size, which benefit from the mass transfer in particle-particle collisions, is estimated. By this work, we provide evidence that as long as the particles grow to the minimum particle size of around  $10^{-5}$  by the particle coagulation process, the accumulated self-gravitational interaction over a long evolution time could already be sufficient for such smaller particles to successfully “jump the barrier” and achieve gravitational collapse, which significantly increases the chances to find the lucky winners in PPDs and helps to understand the formation of countless planets and asteroids in nature.

There are several directions we can follow to continue this work in the future. One of them concerns the numerical verification of the conclusions derived in this thesis. In Chapter 4, we have already seen that the initial density power spectrum of dust particles shows signs of developing a  $k^{-3}$  tail at very small scales. By developing better simulation methods with higher resolution while still preserving the statistically isotropic nature of a system, it is well possible to numerically verify the small-scale  $k^{-3}$  asymptotic behavior of the nonlinear density power spectrum for dust particles.

Furthermore, in this thesis, we have assumed a background gas distribution with constant density and velocity that captures one of the most important features of the gas and greatly simplifies the dust particle trajectories in a general PPD. However, one of the limitations of this model is the lack of possible turbulence in the gas, which is supposed to help intermediate-size dust aggregates form clusters and more efficiently grow to larger sizes. Thus the development of a more sophisticated model of the background gas which describes eddies and their cascade processes in PPDs is a necessary future step to obtain more realistic results comparable to simulations and conclusions for applying KFT to planetesimal formation.

Moreover, though considering fixed gas backgrounds has the advantage of simplifying the gas and dust interactions, ignoring the back reaction of dust particles onto gas could be simplistic, especially at high densities. One possible approach to overcome this shortcoming is to turn to resummed kinetic field theory within the framework of KFT, which was initially developed to study both baryons and dark matter in the cosmic picture, see Lilow et al. [26], Geiss et al. [15], Geiss et al. [14]. Generalizing and applying this theory to planetesimal formation could provide a feasible method for considering dynamic interactions between dust and gas in PPDs.

In the end, we would like to briefly discuss other possible interactions that could be included in [KFT](#) for dust particles. For example, to better understand the dust coagulation process, it is possible to develop a feasible scheme to describe particle-particle collisions in the equation of motion by sampling an additional averaged force term from internal particle collisions that occur in various local simulations. Furthermore, many studies have shown that the magnetorotational instability caused by the presence of a weak magnetic field and a partially ionized gaseous shear flow can lead to a repulsive force that transfers angular momentum from the inner to outer volume elements and further to an unstable flow with turbulent motion, see Balbus and Hawley [2], Balbus and Hawley [3] and Davis, Stone, and Pessah [10]. Therefore, concerning the weakly ionized areas in a [PPD](#), [KFT](#) could as well offer some analytical insight into structure formation once the weak magnetic force is properly included into the equation of motion for dust particles.

To summarize, in this work, we have successfully developed the full scheme of applying [KFT](#) to planetesimal formation and extracted some important structure and kinetic information for dust particles in [PPDs](#). With the possible future steps to follow, we are confident to conclude that the novel kinetic field theory ([KFT](#)) offers insights and is becoming a new extraordinary tool for studying planetesimal formation.



Part III

APPENDIX



## MORE DISCUSSIONS OVER KFT POWER SPECTRA

---

### A.1 SMALL-SCALE ASYMPTOTICS OF LINEAR POWER SPECTRA

In this section, we provide detailed calculations for the integrals in the expressions of the linear density power spectrum  $\mathcal{P}_{\text{lin}}(k_1, t)$ ,  $\mathcal{P}_{\text{flin}}(k_1, t)$  and the linear free momentum-density power spectra elements  $T_{\text{lin}i}$  with  $i = 1, 5, 6$  to find their rigorous small-scale asymptotic behaviors.

#### A.1.1 Linear Density Power spectrum

We start with the linear free density power spectrum  $\mathcal{P}_{\text{lin}}(k_1, t)$  in [Equation 5.46](#),

$$\begin{aligned} \mathcal{P}_{\text{lin}}(k_1, t) &= -\frac{4\pi g_0^2(t)\zeta_0}{k_1} I_{\text{lin}0}(k_1), \quad \text{with} \\ I_{\text{lin}0}(k_1) &= \int_0^\infty dr_1 \left( \frac{6b_1 \sin(r_1)}{r_1} - 6b_1 \cos(r_1) - (b_0 + 2b_1)r_1 \sin(r_1) \right) \cdot \\ &\quad {}_1F_1 \left( \frac{7}{6}, \frac{3}{2}, -\frac{\bar{\sigma}^2 r_1^2}{2k_1^2} \right), \end{aligned} \quad (\text{A.1})$$

where we've denoted the coefficient of the averaged initial momentum correlation function  $\zeta_{\text{pp}}(r)$  in [Equation 4.66](#) as

$$\zeta_0 = \frac{1}{2^{\frac{5}{6}}\pi^2} \bar{\sigma}^{\frac{7}{3}} \Gamma \left( \frac{7}{6} \right), \quad (\text{A.2})$$

The analytical integration result of  $I_{\text{lin}0}(k_1)$  can be obtained as

$$I_{\text{lin}0}(k_1) = 8.67 \cdot 10^{-5} - 2.41 \cdot 10^{-7} k_1^{\frac{7}{3}} e^{-4.74 \cdot 10^{-3} k_1^2} - 9.35 \cdot 10^{-5} \Gamma \left( \frac{7}{6}, 4.74 \cdot 10^{-3} k_1^2 \right), \quad (\text{A.3})$$

at the limit of  $k_1 \rightarrow 0$ , we have its first order Taylor series as

$$\lim_{k_1 \rightarrow 0} I_{\text{lin}0}(k_1) \approx 8.67 \cdot 10^{-5} - 2.41 \cdot 10^{-7} k_1^{\frac{7}{3}} - 9.35 \cdot 10^{-5} \Gamma \left( \frac{7}{6} \right) = -2.41 \cdot 10^{-7} k_1^{\frac{7}{3}}, \quad (\text{A.4})$$

while at the limit of  $k_1 \rightarrow \infty$ , its first order Taylor expansion becomes

$$\begin{aligned} \lim_{k_1 \rightarrow \infty} I_{\text{lin}0}(k_1) &\approx 8.67 \cdot 10^{-5} - e^{-4.74 \cdot 10^{-3} k_1^2} \left( 2.41 \cdot 10^{-7} k_1^{\frac{7}{3}} + 9.35 \cdot 10^{-5} (4.74 \cdot 10^{-3} k_1^2)^{\frac{1}{6}} \right) \\ &\approx 8.67 \cdot 10^{-5}. \end{aligned} \tag{A.5}$$

Figure A.1 shows the shape of  $I_{\text{lin}0}(k_1)$  in Equation A.3 as a function of wavenumber  $k_1$ . We can see at large scales where  $k_1$  is small, it develops a  $k_1^{7/3}$  slope as in Equation A.4, and at small scales where  $k_1$  is large, the curve reaches its asymptotic constant as in Equation A.5.

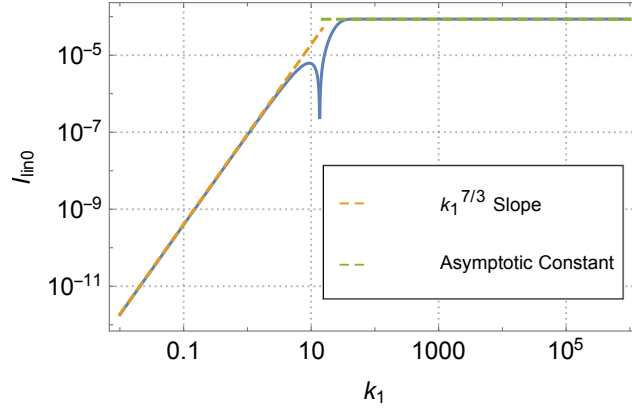


Figure A.1: This plot shows the shape of integral  $I_{\text{lin}0}(k_1)$  in (A.3) as a function of wavenumber  $k_1$  (blue line), together with its large scale  $k_1^{7/3}$  asymptotic behavior (yellow dashed line) and small scale asymptotic constant (green dashed line).

Therefore, the linear free density power spectrum which takes the form of  $\mathcal{P}_{\text{lin}}(k_1, t) \propto I_{\text{lin}0}(k_1)/k_1$  naturally develops a  $k_1^{4/3}$  slope at large scales and a  $k_1^{-1}$  slope at small scales. As for  $\mathcal{P}_{\text{flin}}(k_1, t)$  in Equation 5.62, its identical  $k_1$ -dependence as  $\mathcal{P}_{\text{lin}}(k_1, t)$  with a different propagator  $g_{\text{qp}}(t)$  indicates that the above conclusions also apply to it.

### A.1.2 Linear Free Momentum-Density Power Spectra Elements

In this section, we analyze the asymptotic behaviors of the linear free Momentum-Density Power Spectra Elements  $T_{\text{lin}i}$  with  $i = 1, 5, 6$  in Equation 6.122-6.124. First rewrite them as

$$T_{\text{lin}1}(k_1, t) = \frac{12\pi b_0 \zeta_0}{k_1^3} I_{\text{lin}1}(k_1), \quad (\text{A.6})$$

$$T_{\text{lin}5}(k_1, t) = \frac{2\pi \zeta_0}{k_1^3} I_{\text{lin}5}(k_1), \quad (\text{A.7})$$

$$T_{\text{lin}6}(k_1, t) = \frac{2\pi \zeta_0}{k_1^3} I_{\text{lin}6}(k_1), \quad (\text{A.8})$$

with the  $k_1$  functions being

$$I_{\text{lin}1}(k_1) = \int_0^\infty dr_1 r_1 \sin r_1 \cdot {}_1F_1\left(\frac{7}{6}, \frac{3}{2}, -\frac{\bar{\sigma}^2 r_1^2}{2k_1^2}\right), \quad (\text{A.9})$$

$$I_{\text{lin}5}(k_1) = \int_0^\infty dr_1 r_1^2 \cdot {}_1F_1\left(\frac{7}{6}, \frac{3}{2}, -\frac{\bar{\sigma}^2 r_1^2}{2k_1^2}\right) \psi_5(r_1), \quad (\text{A.10})$$

$$I_{\text{lin}6}(k_1) = \int_0^\infty dr_1 r_1^2 \cdot {}_1F_1\left(\frac{7}{6}, \frac{3}{2}, -\frac{\bar{\sigma}^2 r_1^2}{2k_1^2}\right) \psi_6(r_1), \quad (\text{A.11})$$

and  $\psi_i(r_1)$  being the  $\mu$  integrations in [Equation 6.123](#) and [Equation 6.124](#) as

$$\begin{aligned} \psi_5(r_1) &= \int_{-1}^1 d\mu ((3\mu^2 - 1)b_1 + b_0) \cos r_1 \mu \\ &= \frac{\sin r_1}{r_1} \left(2b_0 + 4b_1 - \frac{12b_1}{r_1^2}\right) + \frac{12b_1}{r_1^2} \cos r_1, \end{aligned} \quad (\text{A.12})$$

$$\begin{aligned} \psi_6(r_1) &= \int_{-1}^1 d\mu ((1 - 3\mu^2)b_1 + 2b_0) \cos r_1 \mu, \\ &= \frac{4 \sin r_1}{r_1} \left(b_0 - b_1 + \frac{3b_1}{r_1^2}\right) - \frac{12b_1}{r_1^2} \cos r_1. \end{aligned} \quad (\text{A.13})$$

Plugging them in [Equation A.10](#) and [Equation A.11](#), the final results for the  $k_1$  functions  $I_{\text{lin}i}$  with  $i = 1, 5, 6$  are given as

$$I_{\text{lin}1}(k_1) = 6.58 \cdot 10^{-3} k_1^{7/3} e^{-4.74 \cdot 10^{-3} k_1^2}, \quad (\text{A.14})$$

$$\begin{aligned} I_{\text{lin}5}(k_1) &= k_1^{7/3} e^{-4.74 \cdot 10^{-3} k_1^2} (1.32 \cdot 10^{-2} b_0 + \\ &2.63 \cdot 10^{-2} b_1) + 20.32 b_1 \Gamma\left(\frac{7}{6}, 4.74 \cdot 10^{-3} k_1^2\right) - 18.85 b_1, \end{aligned} \quad (\text{A.15})$$

$$\begin{aligned} I_{\text{lin}6}(k_1) &= 2.63 \cdot 10^{-2} (b_0 - b_1) k_1^{7/3} e^{-4.74 \cdot 10^{-3} k_1^2} + \\ &18.85 b_1 - 20.32 b_1 \Gamma\left(\frac{7}{6}, 4.74 \cdot 10^{-3} k_1^2\right). \end{aligned} \quad (\text{A.16})$$

At the limit of  $k_1 \rightarrow 0$ , the  $k_1$  functions can be approximated by their first order Taylor expansion as

$$\lim_{k_1 \rightarrow 0} I_{\text{lin}1}(k_1) \approx 6.58 \cdot 10^{-3} k_1^{7/3}, \quad (\text{A.17})$$

$$\begin{aligned} \lim_{k_1 \rightarrow 0} I_{\text{lin}5}(k_1) &\approx k_1^{7/3} (1.32 \cdot 10^{-2} b_0 + 2.63 \cdot 10^{-2} b_1) + 20.32 b_1 \Gamma\left(\frac{7}{6}\right) - 18.85 b_1 \\ &= k_1^{7/3} (1.32 \cdot 10^{-2} b_0 + 2.63 \cdot 10^{-2} b_1) \end{aligned} \quad (\text{A.18})$$

$$\lim_{k_1 \rightarrow 0} I_{\text{lin}6}(k_1) \approx 2.63 \cdot 10^{-2} (b_0 - b_1) k_1^{7/3}. \quad (\text{A.19})$$

While at the limit of  $k_1 \rightarrow \infty$ , the Taylor approximations of the  $k_1$  functions become

$$\lim_{k_1 \rightarrow \infty} I_{\text{lin}1}(k_1) \approx 0, \quad (\text{A.20})$$

$$\lim_{k_1 \rightarrow \infty} I_{\text{lin}5}(k_1) \approx 20.32 b_1 (4.74 \cdot 10^{-3} k_1^2)^{\frac{1}{6}} e^{-4.74 \cdot 10^{-3} k_1^2} - 18.85 b_1 \approx -18.85 b_1, \quad (\text{A.21})$$

$$\lim_{k_1 \rightarrow \infty} I_{\text{lin}6}(k_1) \approx 18.85 b_1. \quad (\text{A.22})$$

Figure A.2 shows the shape of absolute values of  $I_{\text{lin}1}(k_1)$ ,  $I_{\text{lin}5}(k_1)$  and  $I_{\text{lin}6}(k_1)$  as functions of wave number  $k_1$ . At very large scales where  $k_1$  is small, we can see all three plots show the development of  $k_1^{7/3}$  slope as expected. While at very small scales where  $k_1$  is large, the curves in the middle and right panels reach their asymptotic constants as Equation A.21 and Equation A.22, while in the left panel,  $I_{\text{lin}1}(k_1)$  continuously decreases sharply and presumably will reach zero quickly as predicted in Equation A.20.

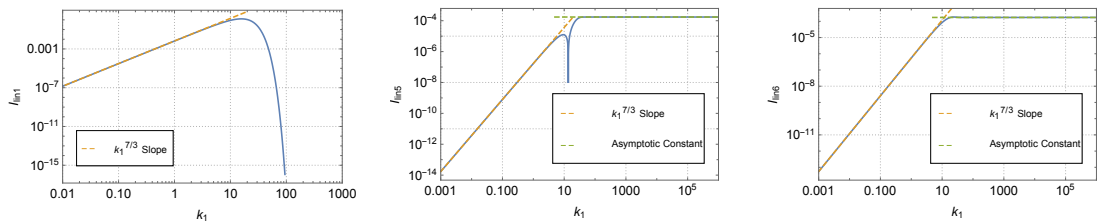


Figure A.2: This figure shows the shape of absolute values of  $I_{\text{lin}1}(k_1)$  (left panel),  $I_{\text{lin}5}(k_1)$  (middle panel) and  $I_{\text{lin}6}(k_1)$  (right panel) in terms of wavenumber  $k_1$  (blue lines), together with their small scale  $k_1^{7/3}$  asymptotic behaviors (yellow dashed lines) and the large scale asymptotic constants (green dashed lines) of  $I_{\text{lin}5}(k_1)$  and  $I_{\text{lin}6}(k_1)$ .

Now we return to the linear free momentum-density power spectra elements  $T_{\text{lin}1}(k_1, t)$ ,  $T_{\text{lin}5}(k_1, t)$  and  $T_{\text{lin}6}(k_1, t)$  in Equation A.6-A.8. Since they all satisfy  $T_{\text{lin}i}(k_1, t) \propto$

$I_{\text{lin}i}(k_1)/k_1^3$  with  $i = 1, 5, 6$ , we can immediately conclude that, all  $T_{\text{lin}i}(k_1, t)$  develop  $k_1^{-\frac{2}{3}}$  slopes at large scales, while at small scales,  $T_{\text{lin}5}(k_1, t)$  and  $T_{\text{lin}6}(k_1, t)$  both develop  $k_1^{-3}$  slopes, and  $T_{\text{lin}1}(k_1, t)$  continuously decreases to zero.

## A.2 VERIFY MODIFIED NONLINEAR DENSITY POWER SPECTRUM

In this section, we further discuss in more detail the evidence of ignoring part of  $\mathcal{P}(k_1, t)$  in Equation 5.12 and rewriting the expression of the nonlinear KFT density power spectrum in the form of  $\mathcal{P}_f(k_1, t)$  by Equation 5.20.

Now we return to its full expression in Equation 5.15 and mark the second integral as  $\mathcal{P}_{\text{diff}}(k_1, t)$

$$\mathcal{P}_{\text{diff}}(k_1, t) = \int_{\mathbf{r}} e^{g_{\text{qp}}^2(t)k_1^2(m_1(0)+\mu^2m_2(0))} e^{-ik_1r\mu} \quad (\text{A.23})$$

First the asymptotic behaviour of  $\mathcal{P}_{\text{diff}}(k_1, t)$  at large and small  $k_1$  is analyzed. Using the definition of  $y(t, \mu)$  in Equation 5.16, when  $k_1 \rightarrow \infty$ , at finite evolution time  $t$ ,  $\mathcal{P}_{\text{diff}}(k_1, t)$  becomes

$$\begin{aligned} \lim_{k_1 \rightarrow \infty} \mathcal{P}_{\text{diff}}(k_1, t) &= \lim_{k_1 \rightarrow \infty} \int_{\mathbf{r}} e^{y(t, \mu)k_1^2} e^{-ik_1r\mu} = \lim_{k_1, R \rightarrow \infty} 2\pi \int_{-1}^1 d\mu e^{y(t, \mu)k_1^2} \int_0^R dr r^2 \cos(k_1 r \mu) \\ &< \lim_{k_1, R \rightarrow \infty} 2\pi R^3 \int_{-1}^1 d\mu e^{y(t, \mu)k_1^2} < \lim_{k_1, R \rightarrow \infty} 4\pi R^3 \int_0^1 d\mu e^{y(t, 0)k_1^2} \\ &= \lim_{k_1, R \rightarrow \infty} 4\pi R^3 e^{y(t, 0)k_1^2} \rightarrow 0 \end{aligned} \quad (\text{A.24})$$

where  $R$  represents the upper integrating limit. We have used here that  $y(t, \mu)$  is a negative, monotonically decreasing function of  $\mu^2$  with a maximum at  $y(t, 0)$ . Since exponential function increases much faster than polynomial functions,  $\mathcal{P}_{\text{diff}}(k_1, t)$  will be 0 at large  $k_1$ . On the other hand, if  $k_1 \rightarrow 0$ , it becomes

$$\begin{aligned} \lim_{k_1 \rightarrow 0} \mathcal{P}_{\text{diff}}(k_1, t) &= \lim_{k_1 \rightarrow 0} \int_{\mathbf{r}} e^{y(t, \mu)k_1^2} e^{-ik_1r\mu} = \lim_{k_1 \rightarrow 0, R \rightarrow \infty} 2\pi \int_0^R dr r^2 \int_{-1}^1 d\mu \cos(k_1 r \mu) \\ &= \lim_{k_1 \rightarrow 0, R \rightarrow \infty} 4\pi \int_0^R dr r^2 j_0(k_1 r) \rightarrow \infty, \end{aligned} \quad (\text{A.25})$$

where  $j_0(k_1 r)$  is the 0-th order Spherical Bessel function. Now that the asymptotic behavior of  $\mathcal{P}_{\text{diff}}(k_1, t)$  is clear, to further study how these behaviors change with

different scales and simplify the analysis, for the freely streaming particles where  $\lim_{\tau_s \rightarrow \infty} g_{qp}(t, t') = g_0(t, t')$ , we perform the analytical integral

$$\mathcal{P}_{\text{diff}}(k_1, t) = 2\pi \int_0^\infty dr r^2 l_0(r) \quad (\text{A.26})$$

with

$$l_0(r) = \frac{\sqrt{\pi} \exp\left(g_0^2(t) k_1^2 m_1(0) + \frac{k_1^2 r^2}{4g_0^2(t) k_1^2 m_2(0)}\right)}{2\sqrt{g_0^2(t) k_1^2 m_2(0)}} \left[ \operatorname{erf}\left(\frac{k_1 r - i2g_0^2(t) k_1^2 m_2(0)}{2\sqrt{g_0^2(t) k_1^2 m_2(0)}}\right) - \operatorname{erf}\left(\frac{k_1 r + i2g_0^2(t) k_1^2 m_2(0)}{2\sqrt{g_0^2(t) k_1^2 m_2(0)}}\right) \right] \quad (\text{A.27})$$

Figure A.3 shows the shape of  $r^2 l_0(r)$  at evolution time  $t = 4\pi$  respectively at  $k_1 = 1.0$  and  $k_1 = 50.0$ . At scale  $k_1 = 1.0$ , the continuously increasing shape of  $r^2 l_0(r)$  suggests its integral will be infinitely large, which matches the result in Equation A.25. At scale  $k_1 = 50.0$ , the shape of  $r^2 l_0(r)$  resembles a delta function, while the extremely small absolute value of the function suggests its integral will approximately be 0, which also agrees with the result in Equation A.24.

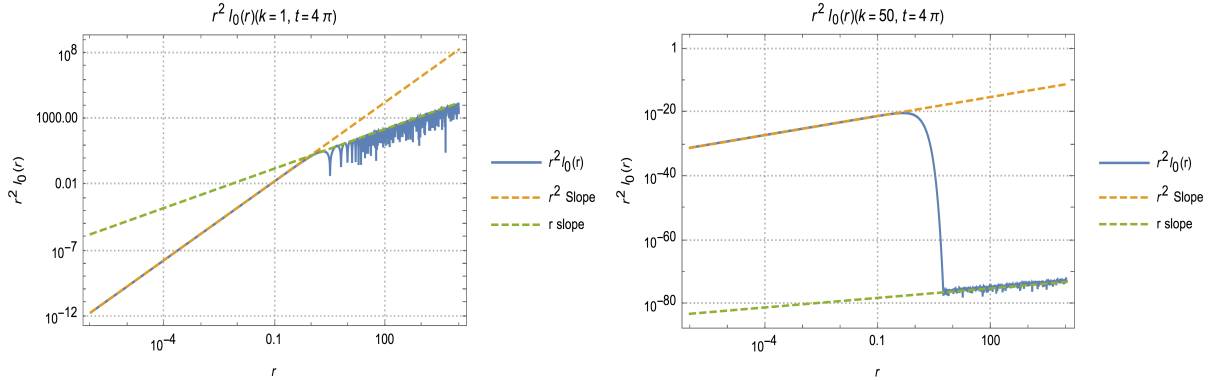


Figure A.3: These 2 plots illustrate the function of  $r^2 l_0(r)$  respectively at  $k_1 = 1.0$  and  $k_1 = 50.0$  at time  $t = 4\pi$  (blue lines). The orange dashed lines represent the  $r^2$  slope. The green dashed lines represent the  $r$  slope.

Now to illustrate the effect of neglecting  $\mathcal{P}_{\text{diff}}(k_1, t)$  on the nonlinear free KFT density power spectrum, we return to the expression in Equation 5.12 and define the full nonlinear free KFT density power spectrum as

$$\mathcal{P}_0(k_1, t) = \int_{\mathbf{r}} e^{-g_0^2(t) k_1^2 ((m_1(\mathbf{r}) - m_1(0)) + \mu^2 (m_2(\mathbf{r}) - m_2(0)))} e^{-i k_1 \cdot \mathbf{r} \mu} . \quad (\text{A.28})$$

Figure A.4 shows the shape of  $\mathcal{P}_0(k_1, t)$  and  $\mathcal{P}_{\text{free}}(k_1, t)$  in Equation 5.42 at evolution time  $t = 4\pi$  with their small scale  $k^{-3}$  asymptotic behaviour. At smaller  $k_1$ , the value of  $\mathcal{P}_0(k_1, t)$  is indeed larger than  $\mathcal{P}_{\text{free}}(k_1, t)$  and shows rapidly increasing sign. However, at large  $k_1$ , there is barely any difference between the two curves and they merge very well, which indicates  $\mathcal{P}_{\text{diff}}(k_1, t)$  doesn't contribute nor affect the shape of the KFT density power spectrum at small scales and the  $k^{-3}$  result reserves.

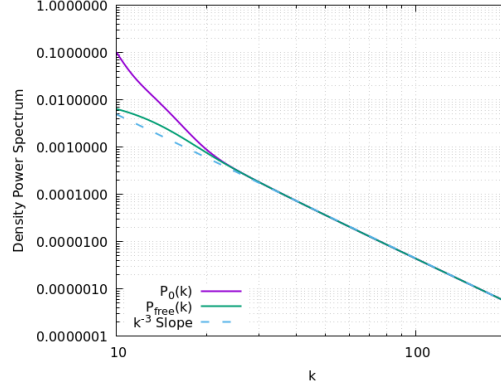


Figure A.4: This plot compares the nonlinear density power spectrum  $\mathcal{P}_0(k_1, t)$  (purple line) with  $\mathcal{P}_{\text{free}}(k_1, t)$  (green line) together with their asymptotic behaviour at large scales (blue dashed line).

To examine the relative difference between the two curves, Figure A.5 shows the final results of

$$\frac{\mathcal{P}_{\text{diff}}(k_1, t)}{\mathcal{P}_{\text{free}}(k_1, t)} = \frac{\mathcal{P}_0(k_1, t) - \mathcal{P}_{\text{free}}(k_1, t)}{\mathcal{P}_{\text{free}}(k_1, t)} \tag{A.29}$$

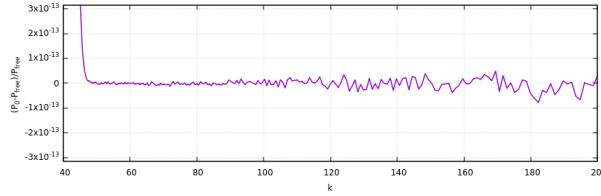


Figure A.5: This plot shows the relative difference between  $\mathcal{P}_0(k_1, t)$  and  $\mathcal{P}_{\text{free}}(k_1, t)$  defined in Equation A.29.

Indeed at around  $k_1 = 50$ , the relative difference between the two becomes negligible, which agrees with Figure A.3. Since we are much more interested in the small-scale behavior, we can say it's safe to ignore  $\mathcal{P}_{\text{diff}}(k_1, t)$  when calculating KFT nonlinear free density power spectrum without compromising our main results. Furthermore, since the free propagator takes the special form  $g_0(t, t') = t - t'$ , the above result further

indicates that the effect of  $\mathcal{P}_{\text{diff}}(k_1, t)$  on the gravity-free nonlinear KFT density power spectrum  $\mathcal{P}_f(k_1, t)$  is also negligible at small scales for any random value of  $g_{\text{qp}}(t)$ .

## SMALL-SCALE ASYMPTOTICS OF MOMENTUM-DENSITY TRACE POWER SPECTRUM

---

### B.1 TIME AND PARTICLE SIZE DEPENDENCE OF $\bar{\mathcal{P}}_{\text{lin1}}(k_1, t)$

In this section, we analyze the time and particle-size dependence of the small-scale asymptotic behavior for  $\bar{\mathcal{P}}_{\text{lin1}}(k_1, t)$  in Equation 6.147.

We can see in Figure 6.10 that as the friction coefficient and evolution time get larger, the amplitude  $\mathcal{P}_{\text{lin1}}^{(0)}(t)$  for the  $k_1^{-3}$  slope of  $\bar{\mathcal{P}}_{\text{lin1}}(k_1, t)$  at small scales also becomes larger. To determine the largest amplitude and its corresponding friction coefficient  $\tau_s$  and evolution time  $t$ , we first perform  $\frac{\partial \mathcal{P}_{\text{lin1}}^{(0)}(t)}{\partial g_{\text{qpt}}} \frac{\partial g_{\text{qpt}}}{\partial t} = 0$  to obtain its maximal  $P_t^0(\tau_s)$  and the corresponding evolution time  $t_m^0$  as

$$P_t^0(\tau_s) = \frac{u_0^2 (2\pi)^{\frac{3}{2}} e^{-\frac{1}{2}}}{\tau_s^2 \sigma_1^2 (b_0 - b_1)} = \frac{0.68}{\tau_s^2}, \quad t_m^0 = -\tau_s \ln \left( 1 - \frac{g_{\text{qpt}}}{\tau_s} \right) \quad (\text{B.1})$$

with

$$g_{\text{qpt}} = \sqrt{\frac{1}{\sigma_1^2 (b_0 + 2b_1)}} \approx 5.26 \quad (\text{B.2})$$

Notice the expression of  $t_m^0$  sets a limit for  $\tau_s$ . In the case of  $\tau_s > g_{\text{qpt}}$ ,  $t_m^0$  exists and monotonously decrease as  $\tau_s$  gets larger, as well as the largest amplitude  $P_t^0(\tau_s)$ . While if  $\tau_s < g_{\text{qpt}}$ ,  $t_m^0$  and  $P_t^0(\tau_s)$  don't exist and the amplitude for the  $k_1^{-3}$  tail at small scales increases monotonously as time proceed, as shown in the right panel of Figure B.1. This behavior shows that when the given particle size is relatively smaller, their small-scale kinetic energy caused by structure formation will always accumulate with time, however, when the given particle size is larger than  $g_{\text{qpt}}$ , then their kinetic energy at small scales will first accumulate then dissipate as time proceeds.

Now we perform  $\frac{\partial \mathcal{P}_{\text{lin1}}^{(0)}(t)}{\partial \tau_s} = 0$  and get the maximal amplitude for  $k_1^{-3}$  slope as

$$P_m^0 = \mathcal{P}_{\text{lin1}}^{(0)}(\tau_{s_m}, t) \quad (\text{B.3})$$

with  $\tau_{s_m}$  being its corresponding friction coefficient and satisfies

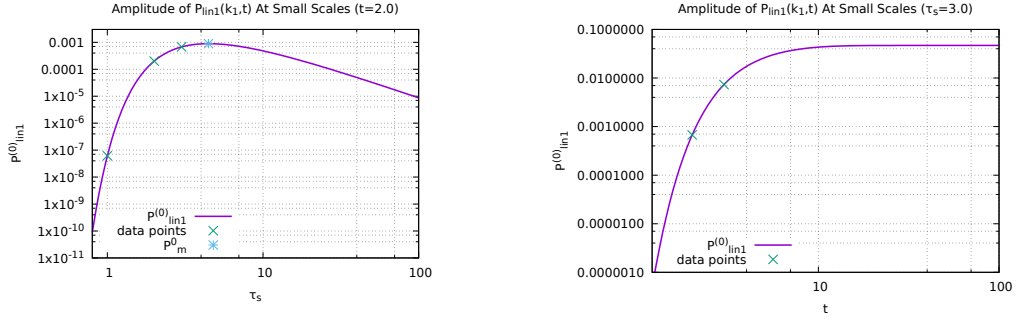


Figure B.1: This plot shows the amplitude  $\mathcal{P}_{\text{lin1}}^{(0)}(t)$  of  $\bar{\mathcal{P}}_{\text{lin1}}(k_1, t)$  at small scales as a function of friction coefficient  $\tau_s$  (left panel) and evolution time (right panel). The green points in both plots mark the value of  $\mathcal{P}^{(0)}(t)$  corresponding to the  $\tau_s$  and  $t$  in [Figure 6.10](#). The blue point in the left panel represents the maximal point of this curve by [Equation B.3](#) and [Equation B.4](#).

$$\frac{3e^{\frac{t}{\tau_{sm}}} - \left(3 + \frac{t}{\tau_{sm}}\right)}{e^{\frac{t}{\tau_{sm}}} - \left(1 + \frac{t}{\tau_{sm}}\right)} = \frac{1}{g_{qp}^2(t)\sigma_1^2(b_0 + 2b_1)} \quad (\text{B.4})$$

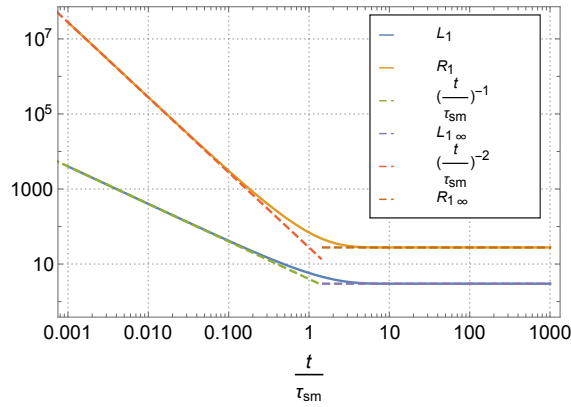


Figure B.2: This plot shows the shape of  $L_1\left(\frac{t}{\tau_{sm}}\right)$  (blue line) and  $R_1\left(\frac{t}{\tau_{sm}}\right)$  (yellow line) as a function of  $\frac{t}{\tau_{sm}}$ . At small  $\frac{t}{\tau_{sm}}$ ,  $L_1$  is proportional to  $\left(\frac{t}{\tau_{sm}}\right)^{-1}$  (green dashed line) and  $R_1$  is proportional to  $\left(\frac{t}{\tau_{sm}}\right)^{-2}$  (red dashed line). At large  $\frac{t}{\tau_{sm}}$ ,  $L_1$  reaches its asymptotic constant at  $L_{1\infty}$  in [Equation B.5](#) (purple dashed line) and  $R_1$  reaches its asymptotic constant at  $R_{1\infty}$  in [Equation B.5](#) (brown dashed line).

Now we mark the LHS of Equation B.4 as  $L_1\left(\frac{t}{\tau_{\text{sm}}}\right)$ , the RHS of Equation B.4 as  $\frac{R_1\left(\frac{t}{\tau_{\text{sm}}}\right)}{\tau_{\text{sm}}^2}$ , Figure B.2 shows the shape of  $L_1\left(\frac{t}{\tau_{\text{sm}}}\right)$  and  $R_1\left(\frac{t}{\tau_{\text{sm}}}\right)$  as a function of  $\frac{t}{\tau_{\text{sm}}}$ . We can see the value of  $R_1$  is always larger than  $L_1$  and at the limit of  $\frac{t}{\tau_{\text{sm}}} \rightarrow \infty$ , they both reach to their asymptotic constant  $L_{1\infty}$  and  $R_{1\infty}$  as

$$L_{1\infty} = 3, \quad R_{1\infty} = \frac{1}{\sigma_1^2(b_0 + 2b_1)} \quad (\text{B.5})$$

This asymptotic behavior also sets a lower limit for  $\tau_s$ . Define

$$\tau_{\text{s1}} = \sqrt{\frac{R_1}{L_1}} = \sqrt{\frac{1}{3\sigma_1^2(b_0 + 2b_1)}} \approx 3.03, \quad (\text{B.6})$$

when  $\tau_s < \tau_{\text{s1}}$ ,  $\tau_{\text{sm}}$  doesn't exist, and at any given time the amplitude for the  $k_1^{-3}$  tail monotonously increases as the size of dust particles gets larger yet still smaller than  $\tau_{\text{s1}}$ . While if  $\tau_s \geq \tau_{\text{s1}}$ , then  $\tau_{\text{sm}}$  exists and its value depends on the evolution time  $t$ , for example, for evolution time  $t = 2.0$ ,  $\tau_{\text{sm}}$  has the value of 4.47, see the left panel of Figure B.1. In this case,  $\mathcal{P}_{\text{lin1}}^{(0)}(t)$  first increases as the dust particles' size gets larger, then decreases after  $\tau_s$  reaches  $\tau_{\text{sm}}$ .

Combining both time and particle size dependence results of  $\mathcal{P}_{\text{lin1}}^{(0)}(t)$  above, we conclude that for particle size  $\tau_s > g_{\text{qpt}}$ , the maximal amplitude of the  $k_1^{-3}$  slope always decreases as  $\tau_s$  gets larger, see Equation B.1, and for particle size  $\tau_s < \tau_{\text{s1}}$ , the maximal amplitude for the  $k_1^{-3}$  occurs at evolution time  $t \rightarrow \infty$  and it monotonously decrease as  $\tau_s$  gets smaller, see Figure B.3.

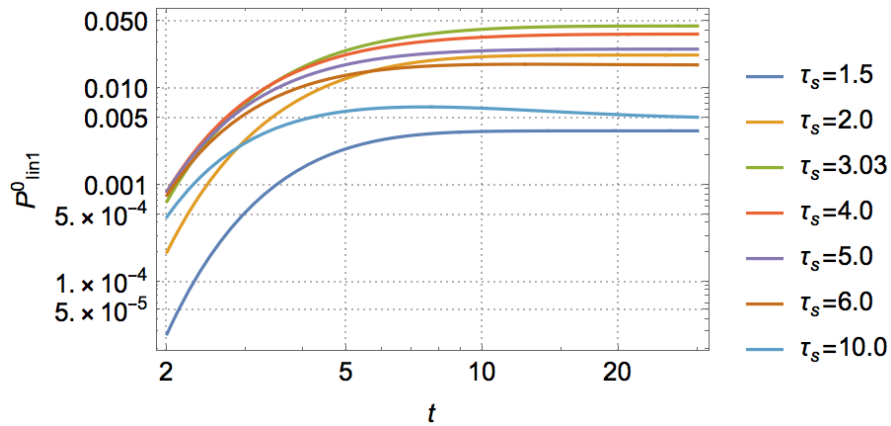


Figure B.3: This plot shows the shape of amplitude  $\mathcal{P}_{\text{lin1}}^{(0)}(t)$  as a function of evolution time  $t$  at different particle size  $\tau_s$ .

Thus to find the maximal small-scale kinetic energy accumulation for dust particles and its corresponding time and particle size, we need to look for the particles at size range  $\tau_{s1} \leq \tau_s \leq g_{qp}t$ . For this range particles, their maximal amplitude of the  $k_1^{-3}$  slope always occur at the limit of  $t \rightarrow \infty$ , thus return to the expression of  $\mathcal{P}_{\text{lin1}}^{(0)}(t)$  in Equation 6.158, we have

$$\lim_{t \rightarrow \infty} \mathcal{P}_{\text{lin1}}^{(0)}(t) = \mathcal{P}_{\text{lin1}}^{\tau_0}(\tau_s) = \frac{u_0^2}{\tau_s^3 \sigma_1^3 (b_0 - b_1)} \sqrt{\frac{(2\pi)^3}{b_0 + 2b_1}} \exp\left(-\frac{1}{2\tau_s^2 \sigma_1^2 (b_0 + 2b_1)}\right). \quad (\text{B.7})$$

By performing  $\frac{\partial \mathcal{P}_{\text{lin1}}^{\tau_0}(\tau_s)}{\partial \tau_s} = 0$ , we obtain its maximal amplitude and the corresponding particle size as

$$\mathcal{P}_{\text{max}}^{\tau_0} = u_0^2 \left(\frac{6\pi}{e}\right)^{\frac{3}{2}} \frac{b_0 + 2b_1}{b_0 - b_1} \approx 0.046, \quad \tau_s^{\text{max}} = \sqrt{\frac{1}{3\sigma_1^2 (b_0 + 2b_1)}} \equiv \tau_{s1} \approx 3.03. \quad (\text{B.8})$$

This result is further verified by Figure B.3. Therefore, we conclude the maximum small-scale particle kinetic energy accumulation caused by the structure formation occurs at the very late stage of evolution time with the particle size being  $\tau_s = \tau_s^{\text{max}} \approx 3.03$ .

## B.2 TIME AND PARTICLE SIZE DEPENDENCE OF $\bar{\mathcal{P}}_{\text{ftr}}(k_1, t)$

In this section, we analyze the time and particle-size dependence of the small-scale asymptotic behavior for  $\bar{\mathcal{P}}_{\text{ftr}}(k_1, t)$  in Equation 6.144.

We can see in Figure 6.12 that as the friction coefficient and evolution time get larger, the amplitude  $\mathcal{P}^{\text{tot}}(t)$  for the  $k_1^{-3}$  slope of  $\bar{\mathcal{P}}_{\text{ftr}}(k_1, t)$  at small scales also becomes larger. To determine the largest amplitude and its corresponding friction coefficient  $\tau_s$  and evolution time  $t$ , we rewrite  $\mathcal{P}^{\text{tot}}(t)$  as

$$\mathcal{P}^{\text{tot}}(t) = \left(1 + \frac{3b_0 \zeta_{pp}(0) \tau_s^2 g_{pp}^2(t)}{u_0^2 g_{qp}^2(t)}\right) \mathcal{P}_{\text{lin1}}^{(0)}(t). \quad (\text{B.9})$$

and define constants

$$a_1 = \frac{u_0^2}{\sigma_1^3 (b_0 - b_1)} \sqrt{\frac{(2\pi)^3}{b_0 + 2b_1}}, \quad a_2 = \frac{1}{2\sigma_1^2 (b_0 + 2b_1)}, \quad a_3 = \frac{3b_0 \zeta_{pp}(0)}{u_0^2} a_1. \quad (\text{B.10})$$

First require  $\frac{\partial \mathcal{P}^{\text{tot}}(t)}{\partial t} = 0$  to find the maximum amplitude  $\mathcal{P}_m^{\text{tot}}(t_m, \tau_s)$  for the  $k_1^{-3}$  tail at small scales and its corresponding evolution time  $t_m$ , denote  $y = \frac{t_m}{\tau_s}$ , we have

$$2a_1 a_2 + \frac{2a_2 a_3}{(e^y - 1)^2} = \tau_s^2 (a_1 + 2(a_3 - a_1)e^{-y} + (a_1 + a_3)e^{-2y}). \quad (\text{B.11})$$

Now we mark the LHS of Equation B.11 as  $L^{\text{tot}}(y)$  and the RHS of Equation B.11 as  $\tau_s^2 R^{\text{tot}}(y)$ , at the limit of  $y \rightarrow \infty$ , both functions reach their asymptotic constants at

$$L_\infty^{\text{tot}} = \lim_{y \rightarrow \infty} L^{\text{tot}}(y) = 2a_1 a_2, \quad R_\infty^{\text{tot}} = \lim_{y \rightarrow \infty} R^{\text{tot}}(y) = a_1. \quad (\text{B.12})$$

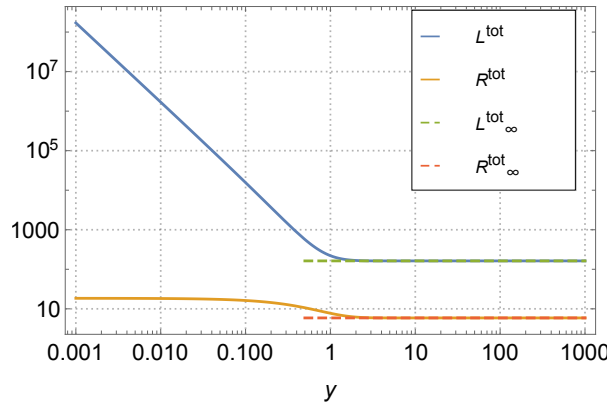


Figure B.4: This plot shows shape of  $L^{\text{tot}}(y)$  (blue line) and  $R^{\text{tot}}(y)$  (yellow line). At large  $y$ , both curves reach their asymptotic constant  $L_\infty^{\text{tot}}$  (green dashed line) and  $R_\infty^{\text{tot}}$  (red dashed line).

Figure B.4 shows the shape of  $L^{\text{tot}}(y)$  and  $R^{\text{tot}}(y)$  and their asymptotic constant at large  $y$ , it's clear that  $L^{\text{tot}}(y)$  is always larger than  $R^{\text{tot}}(y)$  and their asymptotic constants also set a limit for  $\tau_s$ . Define

$$\tau_{s1} = \sqrt{\frac{L_\infty^{\text{tot}}}{R_\infty^{\text{tot}}}} = \sqrt{\frac{1}{\sigma_1^2(b_0 + 2b_1)}} \equiv g_{\text{qpt}} \approx 5.26 \quad (\text{B.13})$$

when  $\tau_s < \tau_{s1}$ ,  $t_m$  doesn't exist and the amplitude  $\mathcal{P}^{\text{tot}}(t)$  for the  $k_1^{-3}$  tail at small scales will monotonously increase as time proceeds. While if  $\tau_s > \tau_{s1}$ , then  $\mathcal{P}_m^{\text{tot}}(t_m, \tau_s)$  and  $t_m$  both exist and the amplitude  $\mathcal{P}^{\text{tot}}(t)$  first increases to its maximal then decreases after evolution time  $t_m$ .

Now we are interested in the relation between the maximum amplitude  $\mathcal{P}_m^{\text{tot}}(t, \tau_{sm})$  for  $k_1^{-3}$  tail and its corresponding size of the particles  $\tau_{sm}$ , thus we require  $\frac{\partial \mathcal{P}^{\text{tot}}(t)}{\partial \tau_s} = 0$  and get

$$\frac{2a_2 e^{2z} (e^z - 1 - z)}{(e^z - 1)^3} \left( a_1 + \frac{a_3}{(e^z - 1)^2} \right) = -\tau_{sm}^2 \left( \frac{a_1 (z + 3 - 3e^z)}{e^z - 1} + \frac{a_3 (2ze^z - 3e^z + z + 3)}{(e^z - 1)^3} \right) \quad (\text{B.14})$$

with  $z = \frac{t}{\tau_{sm}}$ . Now we employ the same scheme as before to analyze this equation, mark the LHS of Equation B.14 as  $L^\tau(z)$  and the RHS as  $\tau_{sm}^2 R^\tau(z)$ . Figure B.5 show the shape of  $L^\tau(z)$  and  $R^\tau(z)$ . We can see at any value of  $z > 0$ ,  $L^\tau(z)$  is always larger than  $R^\tau(z)$ , at large  $z$ , both function reach their asymptotic constants as

$$L_\infty^\tau = 2a_1 a_2, \quad R_\infty^\tau = 3a_1. \quad (\text{B.15})$$

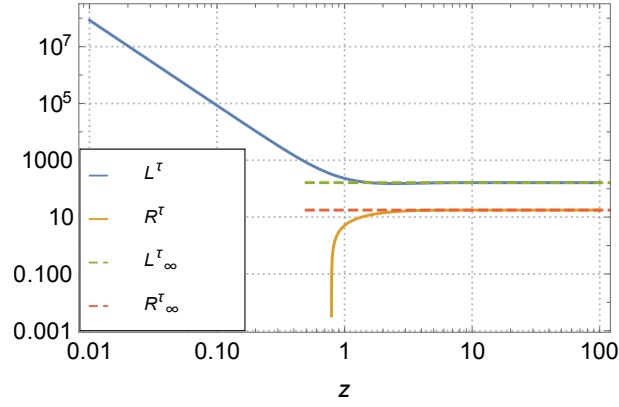


Figure B.5: This plot shows shape of  $L^\tau(z)$  (blue line) and  $R^\tau(z)$  (yellow line). At large  $z$ , both curves reach their asymptotic constant  $L_\infty^\tau$  (green dashed line) and  $R_\infty^\tau$  (red dashed line).

And these two constants set a different limit for the friction coefficient  $\tau_s$ . Define

$$\tau_{s2} = \sqrt{\frac{L_\infty^\tau}{R_\infty^\tau}} = \sqrt{\frac{1}{3\sigma_1^2(b_0 + 2b_1)}} \equiv \tau_{s1} \approx 3.03 \quad (\text{B.16})$$

If  $\tau_s < \tau_{s2}$ , then the maximum amplitude for  $k_1^{-3}$  tail doesn't exist and at any evolution time  $t$ , the amplitude always increases as the size of the particle grows larger while still smaller than  $\tau_{s2}$ . On the other hand, if  $\tau_s > \tau_{s2}$ , then the maximal amplitude exists, and its corresponding particle size  $\tau_{sm}$  depends on the evolution time  $t$ .

Now to find the absolute maximum amplitude of  $\mathcal{P}^{\text{tot}}(t)$  and its corresponding evolution time  $t$  and particle size  $\tau_s$ , Figure B.6 shows the shape of  $\mathcal{P}^{\text{tot}}(t)$  as a function of  $t$

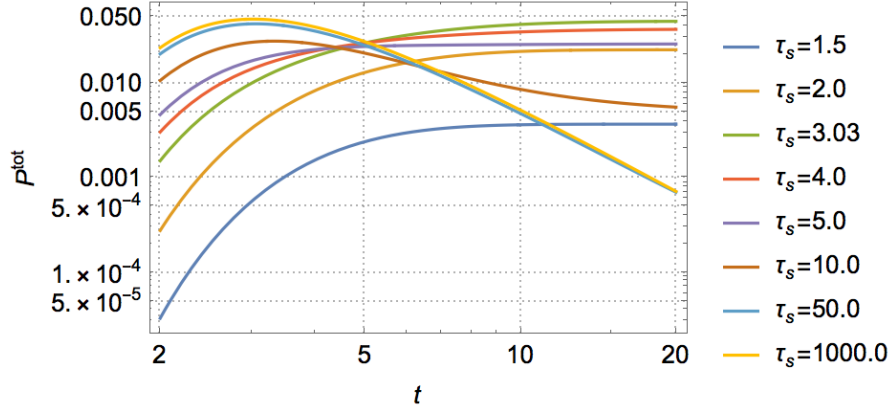


Figure B.6: This plot shows shape of  $\mathcal{P}^{\text{tot}}(t)$  as a function of  $t$  at different particle sizes  $\tau_s$ .

at various particle sizes  $\tau_s$ . We can see that when  $\tau_s < \tau_{s1}$ , the curves of  $\mathcal{P}^{\text{tot}}(t)$  indeed increase monotonously and reach their maximals at very late evolution time as predicted. Furthermore, notice at this range of particle size, the values of  $\lim_{t \rightarrow \infty} \mathcal{P}^{\text{tot}}(t)$  further reach their maximal at particle size  $\tau_s = \tau_{s2} \approx 3.03$ . This result can be better understood by considering the behavior of  $\mathcal{P}^{\text{tot}}(t)$  at the limit of  $t \rightarrow \infty$ ,

$$\lim_{t \rightarrow \infty} \mathcal{P}^{\text{tot}}(t) = \lim_{t \rightarrow \infty} \left( 1 + \frac{3b_0 \zeta_{pp}(0) \tau_s^2 g_{pp}^2(t)}{u_0^2 g_{qp}^2(t)} \right) \mathcal{P}_{\text{lin1}}^{(0)}(t) = \lim_{t \rightarrow \infty} \mathcal{P}_{\text{lin1}}^{(0)}(t) = \mathcal{P}_{\text{lin1}}^{\tau_0}(\tau_s), \quad (\text{B.17})$$

where we've used the asymptotic behavior of the propagators in Equation 6.155-6.156. Since  $\mathcal{P}_{\text{lin1}}^{\tau_0}(\tau_s)$  has its maximal as in Equation B.7, for the particle size  $\tau_s < \tau_{s1}$ , the absolute maximal amplitude  $\mathcal{P}_{\text{max}}^{\tau_0}$  for the  $k_1^{-3}$  slope at very small scales occurs at very late evolution time with particle size  $\tau_s = \tau_{s2} \approx 3.03$ .

While with  $\tau_s > \tau_{s1}$ , notice the curves start increasing at an earlier evolution time and could reach even larger amplitude than  $\mathcal{P}_{\text{max}}^{\tau_0}$  at very large  $\tau_s$ . To quantify this result, we calculate the asymptotic behavior of  $\mathcal{P}^{\text{tot}}(t)$  at the limit of  $\tau_s \rightarrow \infty$  as

$$\lim_{\tau_s \rightarrow \infty} \mathcal{P}^{\text{tot}}(t) = \mathcal{P}_{t0}^{\text{tot}}(t) = \frac{3b_0 \zeta_{pp}(0)}{t^3 \sigma_1^3 (b_0 - b_1)} \sqrt{\frac{(2\pi)^3}{b_0 + 2b_1 + 1}} \exp\left(-\frac{1}{2t^2 \sigma_1^2} (b_0 + 2b_1)\right), \quad (\text{B.18})$$

it reaches its maximal value  $\mathcal{P}_{t0}^{\text{max}}$  at time  $t_{\text{max}}$  as

$$\mathcal{P}_{t0}^{\text{max}} = 3b_0 \zeta_{pp}(0) \left(\frac{6\pi}{e}\right)^{\frac{3}{2}} \frac{b_0 + 2b_1}{b_0 - b_1} \approx 4.87 \cdot 10^{-2}, \quad t_{\text{max}} = \sqrt{\frac{1}{3\sigma_1^2 (b_0 + 2b_1)}} \approx 3.03 \quad (\text{B.19})$$

Since the values  $\mathcal{P}_{t_0}^{\max} > \mathcal{P}_{\max}^{\tau_0}$ , the absolute maximal amplitude of  $\mathcal{P}^{\text{tot}}(t)$  for  $k_1^{-3}$  slope at small scales for any particle size  $\tau_s$  becomes  $\mathcal{P}_{t_0}^{\max}$  corresponds to free particles at evolution time  $t = t_{\max}$ . However, since we are more interested in a system filled in smaller size dust particles for instance  $\tau_s < 10.0$  with the friction interaction presence, we can still conclude that the maximal value of  $\mathcal{P}^{\text{tot}}(t)$  is exactly  $\mathcal{P}_{\max}^{\tau_0}$  which corresponds to particles at size  $\tau_s \approx 3.03$  at the very late stage of evolution.

## BIBLIOGRAPHY

---

- [1] Sean M. Andrews, Katherine A. Rosenfeld, Adam L. Kraus, and David J. Wilner. "THE MASS DEPENDENCE BETWEEN PROTOPLANETARY DISKS AND THEIR STELLAR HOSTS." In: *The Astrophysical Journal* 771.2 (2013), p. 129. DOI: [10.1088/0004-637X/771/2/129](https://doi.org/10.1088/0004-637X/771/2/129). URL: <https://dx.doi.org/10.1088/0004-637X/771/2/129>.
- [2] Steven A. Balbus and John F. Hawley. "A Powerful Local Shear Instability in Weakly Magnetized Disks. I. Linear Analysis." In: 376 (July 1991), p. 214. DOI: [10.1086/170270](https://doi.org/10.1086/170270).
- [3] Steven A. Balbus and John F. Hawley. "A Powerful Local Shear Instability in Weakly Magnetized Disks. I. Linear Analysis." In: 376 (July 1991), p. 214. DOI: [10.1086/170270](https://doi.org/10.1086/170270).
- [4] Matthias Bartelmann, Felix Fabis, Daniel Berg, Elena Kozlikin, Robert Lilow, and Celia Viermann. "A microscopic, non-equilibrium, statistical field theory for cosmic structure formation." In: *New Journal of Physics* 18.4 (2016), p. 043020. DOI: [10.1088/1367-2630/18/4/043020](https://doi.org/10.1088/1367-2630/18/4/043020). URL: <https://doi.org/10.1088/1367-2630/18/4/043020>.
- [5] Matthias Bartelmann, Felix Fabis, Elena Kozlikin, Robert Lilow, Johannes Dombrowski, and Julius Mildenerger. "Kinetic field theory: effects of momentum correlations on the cosmic density-fluctuation power spectrum." In: *New Journal of Physics* 19.8 (2017), p. 083001. DOI: [10.1088/1367-2630/aa7e6f](https://doi.org/10.1088/1367-2630/aa7e6f). URL: <https://doi.org/10.1088/1367-2630/aa7e6f>.
- [6] Matthias Bartelmann, Elena Kozlikin, Robert Lilow, Carsten Littek, Felix Fabis, Ivan Kostyuk, Celia Viermann, Lavinia Heisenberg, Sara Konrad, and Daniel Geiss. *Cosmic Structure Formation with Kinetic Field Theory*. 2019. arXiv: [1905.01179](https://arxiv.org/abs/1905.01179) [astro-ph.CO].
- [7] A. Brandenburg and W. Dobler. "Hydromagnetic turbulence in computer simulations." In: *Computer Physics Communications* 147.1 (2002). Proceedings of the Europhysics Conference on Computational Physics Computational Modeling and Simulation of Complex Systems, pp. 471–475. ISSN: 0010-4655. DOI: [https://doi.org/10.1016/S0010-4655\(02\)00334-X](https://doi.org/10.1016/S0010-4655(02)00334-X). URL: <http://www.sciencedirect.com/science/article/pii/S001046550200334X>.
- [8] Paola D'Alessio, Jorge Canto, Nuria Calvet, and Susana Lizano. "Accretion Disks around Young Objects. I. The Detailed Vertical Structure." In: *The Astrophysical Journal* 500.1 (1998), p. 411. DOI: [10.1086/305702](https://doi.org/10.1086/305702). URL: <https://dx.doi.org/10.1086/305702>.

- [9] Shankar P. Das and Gene F. Mazenko. "Field Theoretic Formulation of Kinetic Theory: Basic Development." In: *Journal of Statistical Physics* 149.4 (2012), pp. 643–675. ISSN: 1572-9613. DOI: [10.1007/s10955-012-0610-y](https://doi.org/10.1007/s10955-012-0610-y). URL: <https://doi.org/10.1007/s10955-012-0610-y>.
- [10] Shane W. Davis, James M. Stone, and Martin E. Pessah. "SUSTAINED MAGNETOROTATIONAL TURBULENCE IN LOCAL SIMULATIONS OF STRATIFIED DISKS WITH ZERO NET MAGNETIC FLUX." In: *The Astrophysical Journal* 713.1 (2010), p. 52. DOI: [10.1088/0004-637X/713/1/52](https://dx.doi.org/10.1088/0004-637X/713/1/52). URL: <https://dx.doi.org/10.1088/0004-637X/713/1/52>.
- [11] C. Dominik and A. G. G. M. Tielens. "The Physics of Dust Coagulation and the Structure of Dust Aggregates in Space." In: *The Astrophysical Journal* 480.2 (1997), pp. 647–673. DOI: [10.1086/303996](https://doi.org/10.1086/303996). URL: <https://doi.org/10.1086%2F303996>.
- [12] Paul S. Epstein. "On the Resistance Experienced by Spheres in their Motion through Gases." In: *Phys. Rev.* 23 (6 1924), pp. 710–733. DOI: [10.1103/PhysRev.23.710](https://link.aps.org/doi/10.1103/PhysRev.23.710). URL: <https://link.aps.org/doi/10.1103/PhysRev.23.710>.
- [13] Matteo Frigo and Steven G. Johnson. "The Design and Implementation of FFTW3." In: *Proceedings of the IEEE* 93.2 (2005). Special issue on "Program Generation, Optimization, and Platform Adaptation", pp. 216–231.
- [14] Daniel Geiss, Ivan Kostyuk, Robert Lilow, and Matthias Bartelmann. "Resummed kinetic field theory: a model of coupled baryonic and dark matter." In: *Journal of Cosmology and Astroparticle Physics* 2021.01 (2021), p. 046. DOI: [10.1088/1475-7516/2021/01/046](https://dx.doi.org/10.1088/1475-7516/2021/01/046). URL: <https://dx.doi.org/10.1088/1475-7516/2021/01/046>.
- [15] Daniel Geiss, Robert Lilow, Felix Fabis, and Matthias Bartelmann. "Resummed Kinetic Field Theory: using Mesoscopic Particle Hydrodynamics to describe baryonic matter in a cosmological framework." In: *Journal of Cosmology and Astroparticle Physics* 2019.05 (2019), p. 017. DOI: [10.1088/1475-7516/2019/05/017](https://dx.doi.org/10.1088/1475-7516/2019/05/017). URL: <https://dx.doi.org/10.1088/1475-7516/2019/05/017>.
- [16] Chushiro Hayashi. "Structure of the Solar Nebula, Growth and Decay of Magnetic Fields and Effects of Magnetic and Turbulent Viscosities on the Nebula." In: *Progress of Theoretical Physics Supplement* 70 (Jan. 1981), pp. 35–53. ISSN: 0375-9687. DOI: [10.1143/PTPS.70.35](https://academic.oup.com/ptps/article-pdf/doi/10.1143/PTPS.70.35/5320828/70-35.pdf). eprint: <https://academic.oup.com/ptps/article-pdf/doi/10.1143/PTPS.70.35/5320828/70-35.pdf>. URL: <https://doi.org/10.1143/PTPS.70.35>.
- [17] R. C. Hogan and J. N. Cuzzi. "Cascade model for particle concentration and enstrophy in fully developed turbulence with mass-loading feedback." In: *Phys. Rev. E* 75 (5 2007), p. 056305. DOI: [10.1103/PhysRevE.75.056305](https://link.aps.org/doi/10.1103/PhysRevE.75.056305). URL: <https://link.aps.org/doi/10.1103/PhysRevE.75.056305>.

- [18] Philip F. Hopkins. “A simple phenomenological model for grain clustering in turbulence.” In: *Monthly Notices of the Royal Astronomical Society* 455.1 (Oct. 2015), pp. 89–111. ISSN: 0035-8711. DOI: [10.1093/mnras/stv2226](https://doi.org/10.1093/mnras/stv2226). eprint: <http://oup.prod.sis.lan/mnras/article-pdf/455/1/89/3062153/stv2226.pdf>. URL: <https://doi.org/10.1093/mnras/stv2226>.
- [19] Emmanuel Jacquet, Steven Balbus, and Henrik Latter. “On linear dust–gas streaming instabilities in protoplanetary discs.” In: *Monthly Notices of the Royal Astronomical Society* 415.4 (Aug. 2011), pp. 3591–3598. ISSN: 0035-8711. DOI: [10.1111/j.1365-2966.2011.18971.x](https://doi.org/10.1111/j.1365-2966.2011.18971.x). eprint: <http://oup.prod.sis.lan/mnras/article-pdf/415/4/3591/4916118/mnras0415-3591.pdf>. URL: <https://doi.org/10.1111/j.1365-2966.2011.18971.x>.
- [20] A. Johansen, H. Klahr, and Th. Henning. “High-resolution simulations of planetesimal formation in turbulent protoplanetary discs.” In: *A&A* 529 (2011). DOI: [10.1051/0004-6361](https://doi.org/10.1051/0004-6361/201015979). URL: <https://doi.org/10.1051/0004-6361/201015979>.
- [21] A. Johansen and A. Youdin. “Protoplanetary Disk Turbulence Driven by the Streaming Instability: Nonlinear Saturation and Particle Concentration.” In: *The Astrophysical Journal* 662.1 (2007), pp. 627–641. DOI: [10.1086/516730](https://doi.org/10.1086/516730). URL: <https://doi.org/10.1086/516730>.
- [22] Anders Johansen, Mordecai-Mark Mac Low, Pedro Lacerda, and Martin Bizarro. “Growth of asteroids, planetary embryos, and Kuiper belt objects by chondrule accretion.” In: *Science Advances* 1.3 (2015), e1500109. DOI: [10.1126/sciadv.1500109](https://doi.org/10.1126/sciadv.1500109). eprint: <https://www.science.org/doi/pdf/10.1126/sciadv.1500109>. URL: <https://www.science.org/doi/abs/10.1126/sciadv.1500109>.
- [23] Kataoka, Akimasa, Tanaka, Hidekazu, Okuzumi, Satoshi, and Wada, Koji. “Fluffy dust forms icy planetesimals by static compression.” In: *A&A* 557 (2013), p. L4. DOI: [10.1051/0004-6361/201322151](https://doi.org/10.1051/0004-6361/201322151). URL: <https://doi.org/10.1051/0004-6361/201322151>.
- [24] Johannes Kepler. *Ioannis Kepleri harmonices mundi libri V : quorum primus harmonicus ... quartus metaphysicus, psychologicus et astrologicus geometricus ... secundus architectonicus ... tertius proprie ... quintus astronomicus & metaphysicus ... : appendix habet comparationem huius operis cum harmonices Cl. Ptolemaei libro III cumque Roberti de Fluctibus ... speculationibus harmonicis, operi de macrocosmo & microcosmo insertis*. 1619. DOI: [10.3931/e-rara-8723](https://doi.org/10.3931/e-rara-8723).
- [25] Sara Konrad. “Cosmic Structure Formation in the Limit of Small Scales within Kinetic Field Theory.” In: (2020). DOI: [10.11588/heidok.00029253](https://doi.org/10.11588/heidok.00029253). URL: <http://www.ub.uni-heidelberg.de/archiv/29253>.

- [26] Robert Lilow, Felix Fabis, Elena Kozlikin, Celia Viermann, and Matthias Bartelmann. "Resummed Kinetic Field Theory: general formalism and linear structure growth from Newtonian particle dynamics." In: *Journal of Cosmology and Astroparticle Physics* 2019.04 (2019), pp. 001–001. DOI: [10.1088/1475-7516/2019/04/001](https://doi.org/10.1088/1475-7516/2019/04/001). URL: <https://doi.org/10.1088/1475-7516/2019/04/001>.
- [27] Carsten Littek. *Kinetic Field Theory: Momentum-Density Correlations and Fuzzy Dark Matter*, (PhD Dissertation). 2018. URL: <http://www.ub.uni-heidelberg.de/archiv/25108>.
- [28] Geoffrey W. Marcy, R. Paul Butler, Eric Williams, Lars Bildsten, James R. Graham, Andrea M. Ghez, and J. Garrett Jernigan. "The Planet around 51 Pegasi\*." In: *The Astrophysical Journal* 481.2 (1997), p. 926. DOI: [10.1086/304088](https://doi.org/10.1086/304088). URL: <https://dx.doi.org/10.1086/304088>.
- [29] Mayor, Michel and Queloz, Didier. "A Jupiter-mass companion to a solar-type star." In: *Nature* 378 (1995), pp. 355–359. DOI: [10.1038/378355a0](https://doi.org/10.1038/378355a0). URL: <https://doi.org/10.1038/378355a0>.
- [30] Irene A. Stegun Milton Abramowitz. *Handbook of Mathematical Functions. with Formulas, Graphs and Mathematical Tables*. 1972.
- [31] Yoshitsugu Nakagawa, Minoru Sekiya, and Chushiro Hayashi. "Settling and growth of dust particles in a laminar phase of a low-mass solar nebula." In: *Icarus* 67.3 (1986), pp. 375–390. ISSN: 0019-1035. DOI: [https://doi.org/10.1016/0019-1035\(86\)90121-1](https://doi.org/10.1016/0019-1035(86)90121-1). URL: <https://www.sciencedirect.com/science/article/pii/0019103586901211>.
- [32] Satoshi Okuzumi, Hidekazu Tanaka, Hiroshi Kobayashi, and Koji Wada. "RAPID COAGULATION OF POROUS DUST AGGREGATES OUTSIDE THE SNOW LINE: A PATHWAY TO SUCCESSFUL ICY PLANETESIMAL FORMATION." In: *The Astrophysical Journal* 752.2 (2012), p. 106. DOI: [10.1088/0004-637X/752/2/106](https://doi.org/10.1088/0004-637X/752/2/106). URL: <https://dx.doi.org/10.1088/0004-637X/752/2/106>.
- [33] Paszun, D. and Dominik, C. "Collisional evolution of dust aggregates. From compaction to catastrophic destruction." In: *A&A* 507.2 (2009), pp. 1023–1040. DOI: [10.1051/0004-6361/200810682](https://doi.org/10.1051/0004-6361/200810682). URL: <https://doi.org/10.1051/0004-6361/200810682>.
- [34] Enikős Regős and Alexander S. Szalay. "Density and velocity correlations of peaks from random Gaussian fluctuations." In: *Monthly Notices of the Royal Astronomical Society* 272.2 (Jan. 1995), pp. 447–461. ISSN: 0035-8711. DOI: [10.1093/mnras/272.2.447](https://doi.org/10.1093/mnras/272.2.447). eprint: <https://academic.oup.com/mnras/article-pdf/272/2/447/18539554/mnras272-0447.pdf>. URL: <https://doi.org/10.1093/mnras/272.2.447>.
- [35] J. L. Russell. "Kepler's Laws of Planetary Motion: 1609–1666." In: *The British Journal for the History of Science* 2.1 (1964), 1–24. DOI: [10.1017/S0007087400001813](https://doi.org/10.1017/S0007087400001813).

- [36] Andreas Schreiber. “Diffusion Limited Planetesimal Formation. Why asteroid and Kuiper-belt objects share a characteristic size.” In: (2018). DOI: [10.11588/heidok.00024579](https://doi.org/10.11588/heidok.00024579). URL: <http://www.ub.uni-heidelberg.de/archiv/24579>.
- [37] Seizinger, A., Speith, R., and Kley, W. “Compression behavior of porous dust agglomerates.” In: *A&A* 541 (2012), A59. DOI: [10.1051/0004-6361/201218855](https://doi.org/10.1051/0004-6361/201218855). URL: <https://doi.org/10.1051/0004-6361/201218855>.
- [38] H. Sigurgeirsson and A. M. Stuart. “A model for preferential concentration.” In: *Physics of Fluids* 14.12 (2002), pp. 4352–4361. DOI: [10.1063/1.1517603](https://doi.org/10.1063/1.1517603). eprint: <https://doi.org/10.1063/1.1517603>. URL: <https://doi.org/10.1063/1.1517603>.
- [39] Jacob B. Simon, Philip J. Armitage, Rixin Li, and Andrew N. Youdin. “THE MASS AND SIZE DISTRIBUTION OF PLANETESIMALS FORMED BY THE STREAMING INSTABILITY. I. THE ROLE OF SELF-GRAVITY.” In: *The Astrophysical Journal* 822.1 (2016), p. 55. DOI: [10.3847/0004-637X/822/1/55](https://doi.org/10.3847/0004-637X/822/1/55). URL: <https://dx.doi.org/10.3847/0004-637X/822/1/55>.
- [40] Celia Viermann, Felix Fabis, Elena Kozlikin, Robert Lilow, and Matthias Bartelmann. “Nonequilibrium statistical field theory for classical particles: Basic kinetic theory.” In: *Phys. Rev. E* 91 (6 2015), p. 062120. DOI: [10.1103/PhysRevE.91.062120](https://doi.org/10.1103/PhysRevE.91.062120). URL: <https://link.aps.org/doi/10.1103/PhysRevE.91.062120>.
- [41] Wada, Koji, Tanaka, Hidekazu, Okuzumi, Satoshi, Kobayashi, Hiroshi, Suyama, Toru, Kimura, Hiroshi, and Yamamoto, Tetsuo. “Growth efficiency of dust aggregates through collisions with high mass ratios.” In: *A&A* 559 (2013), A62. DOI: [10.1051/0004-6361/201322259](https://doi.org/10.1051/0004-6361/201322259). URL: <https://doi.org/10.1051/0004-6361/201322259>.
- [42] Windmark, F., Birnstiel, T., Güttler, C., Blum, J., Dullemond, C. P., and Henning, Th. “Planetesimal formation by sweep-up: how the bouncing barrier can be beneficial to growth.” In: *A&A* 540 (2012), A73. DOI: [10.1051/0004-6361/201118475](https://doi.org/10.1051/0004-6361/201118475). URL: <https://doi.org/10.1051/0004-6361/201118475>.
- [43] A. Youdin and A. Johansen. “Protoplanetary Disk Turbulence Driven by the Streaming Instability: Linear Evolution and Numerical Methods.” In: *The Astrophysical Journal* 662.1 (2007), pp. 613–626. DOI: [10.1086/516729](https://doi.org/10.1086/516729). URL: <https://doi.org/10.1086%2F516729>.
- [44] Andrew N. Youdin and Jeremy Goodman. “Streaming Instabilities in Protoplanetary Disks.” In: *The Astrophysical Journal* 620.1 (2005), pp. 459–469. DOI: [10.1086/426895](https://doi.org/10.1086/426895). URL: <https://doi.org/10.1086%2F426895>.



## COLOPHON

This document was typeset using the typographical look-and-feel `classicthesis` developed by André Miede. The style was inspired by Robert Bringhurst's seminal book on typography "*The Elements of Typographic Style*". `classicthesis` is available for both  $\LaTeX$  and  $\text{LyX}$ :

<https://bitbucket.org/amiede/classicthesis/>

Happy users of `classicthesis` usually send a real postcard to the author, a collection of postcards received so far is featured here:

<http://postcards.miede.de/>

*Final Version* as of March 16, 2023 (`classicthesis`).